Paleomagnetic and rock magnetic study of North Pacific Ocean and South China Sea sediments

A thesis submitted for the degree of Doctor of Philosophy of

The Australian National University

By

Congcong Gai

December 2020

Australian National University | RESEARCH SCHOOL OF EARTH SCIENCES

DECLARATION OF AUTHORSHIP

The work presented in the thesis is my own, and has been generated by me as the result of my own original research. I confirm that:

- this work was done wholly while in a candidature for the degree of Doctor of Philosophy;
- where I have consulted the published work of others, this is always clearly attributed;
- where I have quoted from the work of others, the source is always given. With the exception of such quotations, this thesis is entirely my own work;
- where the thesis is based on work done by myself jointly with others, I have made clear exactly what was done by others and what I have contributed myself;
- part of this work has been published as:

Gai, C., Liu, Q., Roberts, A.P., Chou, Y., Zhao, X., Jiang, Z., Liu, J., 2020. East Asian monsoon evolution since the late Miocene from the South China Sea. *Earth Planet. Sci. Lett.* 530, 115960. https://doi.org/10.1016/j.epsl.2019.115960

Signed: Congcong GAI

Date: 2020/12/17

Acknowledgements

I would first like to thank Andrew Roberts. It is Andrew that provided me the chance to study at the Australian National University. I thank Andrew for his excellent supervision and encouragement. He is always saying that he is an impatient person, but he revises my manuscripts carefully again and again without any complaint. I thank David Heslop for his helpful suggestions and reminding me to be rigorous. Thanks also to Xiang Zhao and Pengxiang Hu for their feedback on my experimental results and for their hospitality and consideration.

During my stay at the Institute of Geology and Geophysics, Chinese Academy of Sciences, I thank Qingsong Liu for providing me with this project. Qingsong can always inspire me during discussion. Without his support, I could not have finished my study smoothly. I also thank the professors and technicians in the paleomagnetism and geochronology laboratory: Rixiang Zhu, Yongxin Pan, Chenglong Deng, Huafeng Qin, and Shuangchi Liu. I am also grateful to my colleagues: Chunsheng Jin, Zhaoxia Jiang, Zongqi Duan, Youliang Su, and Jianxing Liu.

During my stay at the Southern University of Science and Technology, I thank all the staff and colleagues in the Centre for Marine Magnetism: Qingsong Liu, Yu-Min Chou, Deting Yang, Peng Han, Yi Zhong, Xiaodong Jiang, Yuanjie Li, Jiabo Liu, Wanyi Wang, Yang Zhou, Huihui Yang, Wei Liu, Haosen Wang, Wei Cao, Dunfan Wang, Weijie Zhang, Yanan Zhang, Wei Zheng and Hai Li.

I thank the China Scholarship Council for financial support and the International Ocean Discovery Program and the First Institute of Oceanography, Ministry of Natural Resources, China, for the precious samples that formed the basis for my work.

Thanks to my friends: Yao Qian, Yang Wu, Yingxin Kou, Song Zhao, Jiade Wu, Victor Piedrahita Velez, Felicity, Jackie, Pedro, Thomas, Qianqian Han, Pengfei Qin, Xinyu Zou, and Shuaichi Liu. Thanks for the friendship through these years.

At last, a special thanks to my parents and my boyfriend for their selfless love and support.

Abstract

Magnetism plays an important role in marine science. On the one hand, paleomagnetism helps us to understand ancient geomangetic field behaviour that can also facilitate geochronological studies. On the other hand, rock magnetism can provide valuable information concerning paleoenvironmental and paleoclimatic processes. However, magnetic particles in marine sediments are influenced by multiple geological and environmental processes, and commonly occur in mixed magnetic mineral assemblages, which complicates magnetic parameter interpretation. Therefore, to apply environmental magnetism in marine science, it is crucial to be able to discriminate magnetic signals in marine sediments and to relate these signals to relevant processes. In this study, detailed paleomagnetic and rock magnetic studies have been performed on sediments from the North Pacific Ocean (NPO) and the South China Sea (SCS). The main conclusions of this work are as follows. Magnetite is the dominant magnetic mineral throughout SCS Hole U1431D, and its remanence is used to reconstruct a magnetostratigraphic time framework for the past ~6.5 Ma. A single authigenic greigite-bearing interval is identified at 130.5-132.0 mbsf, whose age is estimated at ~2.53-2.55 Ma is associated with oceanographic changes that coincided with intensification of northern hemisphere glaciation. Sedimentary magnetic parameters are affected mainly by the East Asian monsoon and are used to indicate monsoon evolution over the past 6.5 Ma. The summer and winter monsoon were stable before 5 Ma. The summer monsoon intensified from 5 Ma to 3.8 Ma, when it started to weaken. The winter monsoon weakened at 5 Ma, and then intensified after 3.8 Ma, finally stabilizing at 0.6 Ma. Spectral analyses indicate that there was a direct response of the summer monsoon to low-latitude insolation between 6.5 and 3.2 Ma. Since 3.2 Ma, both low-latitude insolation and high-latitude global ice volume have influenced summer monsoon evolution. In NPO core NP02, three visible tephra layers are identified, and can be correlated to the To-Of, Spfa-1, and Kt-3 tephra layers. Together with a radiocarbon date, an initial age model was reconstructed over the ~22-57 ka interval for core NP02. Magnetic analyses suggest that the remanence is carried by detrital vortex state and biogenic single domain magnetite. These two components record similar relative paleointensity (RPI) patterns, and the fidelity of the core NP02 RPI record is further verified by comparison with other RPI stacks and records. Therefore, the RPI-assisted chronology is used to date the studied NPO sediments by tuning the initial core NP02 age model using RPI variations. Hard isothermal remanent magnetization (HIRM) is dominated by the hematite concentration and is used as a proxy for Asian-sourced dust content. Low dust contents are identified at ~25, 39, 48, and 55 ka, which can be linked to Heinrich events 2, 4, 5, and 5a, and are likely caused by southward shifts of the westerlies associated with Atlantic meridional overturning circulation (AMOC) slowdowns. AMOC slowdowns increase the meridional temperature gradient and, therefore, lead to intensified and southward-shifted westerlies. In this situation, the main westerly axis shifts away from the NP02 core site and, therefore, low dust contents are recorded at this site.

Key words: North Pacific Ocean, South China Sea, paleomagnetism, rock magnetism, East Asian monsoon, westerlies

Table of Contents

4. East Asian monsoon evolution since the late Miocene from the South China Sea 64

5. Recording fidelity of relative paleointensity characteristics in the North Pacific Ocean 97

Chapter 1

Introduction

1.1. Motivation and objectives of this thesis

Magnetism plays an important role in marine science because magnetic techniques have the advantage of being rapid, sensitive, and non-destructive. More significantly, magnetic techniques can shed light on issues that cannot be resolved by other chemical and physical methods (Oldfield, 1991). Characteristics of magnetic particles, including their concentration, domain state, and mineralogy, are related to primary geological and/or subsequent environmental changes (Liu et al., 2012), while the remanence of magnetic particles contains information about the geomagnetic field, which helps us to understand field behaviour that can also facilitate geochronological studies. However, magnetic particle assemblages in marine sediments can be complex and may not provide unambiguous information concerning environmental change or geomagnetic field history.

Magnetic particles in marine sediments occur commonly in mixed mineral assemblages, which complicates magnetic parameter interpretation. For example, a first-order reversal curve (FORC) diagram for a mixture of single domain (SD) and multidomain (MD) magnetite could be interpreted misleadingly as evidence for SD particles alone because the characteristics of MD particles only become apparent in FORCs when they make up more than 80% of the mixture (Harrison et al., 2018). For mixed hematite-magnetite assemblages, the signal due to hematite can be suppressed strongly because the saturation magnetization of hematite is about two orders of magnitude lower than that of magnetite (Thompson and Oldfield, 1986; Roberts et al., 2020). Furthermore, environmental processes can also lead to ambiguous magnetic parameter interpretation. For example, increased hematite concentrations in the South China Sea (SCS) have been related either to a weakened East Asian summer monsoon or to increased terrigenous input from the Red and Mekong Rivers (Kissel et al., 2016; Q.

Chen et al., 2017; M. Li et al., 2018). Therefore, to apply environmental magnetism in marine science, it is crucial to be able to discriminate magnetic signals in marine sediments and to relate these signals to relevant processes.

The North Pacific Ocean (NPO) is the largest ocean in the northern hemisphere, and the SCS is the largest marginal sea of the NPO. Connected through the Luzon Strait (Qu et al., 2006), the NPO and SCS have distinct marine contexts. Sedimentation rates in the NPO are relatively low, which tends to lead to oxic diagenesis, including the low-temperature oxidation of magnetite (Johnson et al., 1975). In contrast, the SCS usually has moderate to high sedimentation rates due to high fluvial inputs from surrounding landmasses (Liu and Stattegger, 2014; Liu et al., 2016), with episodic non-steady state reductive diagenesis tending to influence magnetic mineral assemblages (e.g., M. Li et al., 2018; Gai et al., 2020). Moreover, the dominant climatic systems in the NPO and the SCS are different. Westerlies prevail in the NPO while the East Asian monsoon dominates the SCS (e.g., Rea et al., 1985; Wang et al., 1999). Different environmental conditions in the two regions lead to different magnetic mineral characteristics, which have been used widely in environmental magnetic studies (e.g., Yamazaki and Ioka, 1997; Kissel et al., 2003; M. Li et al., 2018; Zhang et al., 2018; Gai et al., 2020).

The NPO and the SCS are the study areas for this Ph.D. project. The main research objectives are as follows.

1. To construct a magnetostratigraphy for SCS sediments to provide a chronological framework to enable assessment of magnetic proxies for East Asian monsoon variations and to explore forcing of the East Asian monsoon on orbital timescales.

2. To examine the feasibility of developing relative-paleointensity (RPI) assisted chronologies for dating NPO sediments.

3. To seek reliable magnetic proxies for dust variations sourced from the Asian continent and deposited in the NPO to elucidate the potential controlling factors of dust production, transportation, and deposition, and to explore forcing mechanisms of westerlies on millennial timescales.

1.2. Thesis structure

There are seven chapters in this thesis. Chapter 1 is an introduction to the research topic. In this chapter, the motivations for my work and my research objectives are presented. It also provides a background to the NPO and the SCS, which includes water mass circulation, sedimentary characteristics, climatic influences, and discussion of previous magnetic studies of the studied regions. Chapter 2 is a review of the principles and theory of paleomagnetic studies, which provide the basis for constructing paleomagnetism-dependent chronologies. It also provides a summary of magnetic parameters and an introduction to the three important magnetic minerals used in my research. Chapter 3 is a presentation of the methods used in my research. All magnetic and non-magnetic experimental procedures used in this thesis are described in this chapter. Chapter 4 is a study of East Asian monsoon records from the SCS. A refined magnetostratigraphy is presented for IODP (International Ocean Discovery Program) Hole U1431D for the last 6.5 Ma, and magnetic parameters are assessed in terms of their usefulness as East Asian monsoon proxies. An East Asian monsoon record since the late Miocene is presented, and orbital forcing of the East Asian summer monsoon is explored. Chapter 5 is a study of a gravity piston core from the NPO for which both bulk magnetic measurements and representations of individual magnetic mineral components are examined in relation to assessing the feasibility of developing a RPI-assisted chronology for NPO sediments. Chapter 6 is a study of the forcing mechanisms of the westerlies on millennial timescales using the NPO gravity piston core samples described in Chapter 5. The age model reconstructed in Chapter 5 is further tuned using the RPI variations, and potential factors that may influence dust variations to the NPO are discussed. Chapter 7 is a synthesis of Chapters 4 to 6. It is a summary of the primary findings of the research presented in this thesis and includes a discussion of potential future work.

1.3. Study regions

1.3.1. The NPO

The NPO is a deep ocean in which sediments are usually deposited below the calcite compensation depth (CCD). The Mariana Trench is the deepest oceanic trench on Earth, which can reach depths >10,000 m. Western boundary currents (e.g., the Kuroshio Current) transfer warm water vapour and heat to the northern hemisphere mid-latitudes, which makes the NPO a source of summer monsoon precipitation (e.g., Qiu, 2002; Sakamoto et al., 2005; Smirnov et al., 2014). The prevailing westerlies transport eolian dust from central Asia to the NPO (Rea et al., 1985; Rea and Leinen, 1988; Rea, 1994; Zhao et al., 2006; Maher et al., 2010). Long-range atmospheric transportation not only influences the marine ecological environment by promoting productivity in Fe-limited NPO surface waters via Fe inputs from dust (Martin and Fitzwater, 1988), but it also provides a natural laboratory to study sedimentary processes from land (source) to the ocean (sink) (e.g., Gao et al., 1992; Jones et al., 2000; W. Zhang et al., 2016; Wan et al., 2020). In this section, I first summarize water mass circulation and the sedimentary characteristics of the NPO, then I review studies of the northern hemisphere westerlies in relation to the potential of using sedimentary sequences with relatively high sedimentation rates to understand the long-term evolution of the westerlies and their forcing. Finally, I summarize previous magnetic studies of the NPO.

Water mass circulation

NPO circulation is discussed in terms of surface, mid-depth, and deep circulation. Surface circulation in the NPO is complex, so I only discuss here the western NPO, where my studied cores are located. In the western NPO, surface circulation can be divided into three latitudinal regions (Figure 1.1): the subtropical gyre (30-10° N), the Kuroshio Current and Kuroshio Extension (42-30° N), and the subarctic region (>42° N). The subtropical gyre has a persistent thermocline with a sea surface salinity of 32-34.5‰ and sea surface temperatures of 15-29 °C in winter and 25-30 °C in summer (Kawahata et al., 1999). The subarctic region has a permanent halocline at 100-200 m depths with sea surface salinity of 33-33.5‰ (Kawahata et al., 1999). The Oyashio Current in this region is an important western boundary current. It flows along the east coast of Kamchatka and brings cold, high-nutrient surface water to the NPO. The Kuroshio Current and Kuroshio Extension separate the subtropical and subarctic zones. The Kuroshio Current is warm and saline. It flows along the southeastern coast of the Japanese islands and then deflects to the east, away from central Japan. The Kuroshio Current carries a large amount of heat from the equatorial to mid-latitudinal Pacific, which generates a warm climate over much of the NPO (Barkley, 1970). The Kuroshio Extension is a dynamic mixed zone where the Oyashio and Kuroshio Currents meet. It has pronounced latitudinal sea surface temperature and salinity gradients.

Mid-depth circulation consists mainly of self-consistent gyre circulation of North Pacific Intermediate Water (NPIW), which flows from subarctic North Pacific regions to the Indonesian archipelago (You, 2003). The salinity minimum layer (~34-34.3‰) is confined to the NPO subtropical gyre (Sverdrup et al., 1942). Modern NPIW originates from the Okhotsk Sea and is distributed widely across the NPO at ~300-800 m water depths (Talley, 1993; Yasuda, 1997). In contrast, during the Last Glacial Maximum, NPIW originated dominantly from the Bering Sea and expanded down to a depth of ~2000 m (Worne et al., 2019).

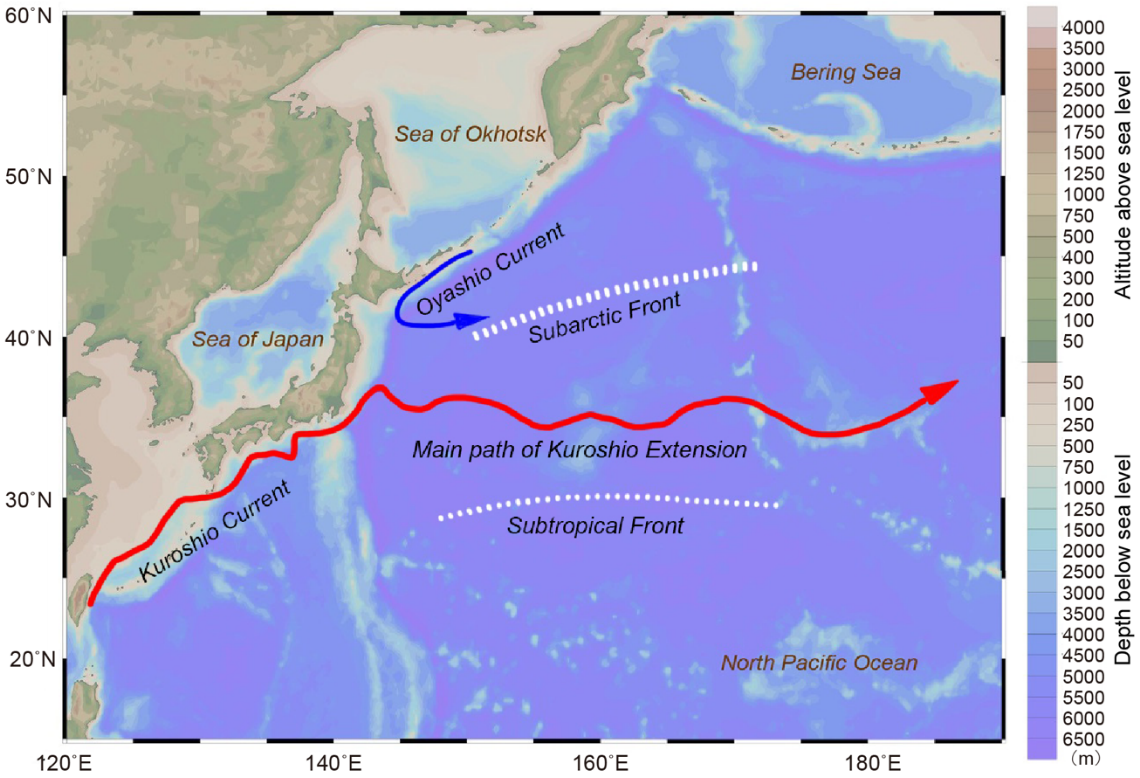

Figure 1.1 Surface water distribution in the western NPO. Currents and fronts are based on Mizuno and White (1983) and Zhang and Hanawa (1993).

In the modern NPO, there is no deep water formation *in situ*; deep water originates from the Southern Ocean. Below ~2000 m, deep-water movements are sluggish, and the water has uniform properties with temperature and salinity ranging from 1.2 to 2.2 °C and 34.65 to 34.75‰, respectively (Pickard and Emery, 1964).

Sedimentary characteristics

To first order, NPO sedimentary provinces follow the general form of the basin. In western and northern regions, sediments are characterized by clay mixed with biogenic material and tephra (Horn et al., 1970). Western NPO sediments originate from central Asia and the Japan-Kuril archipelago, while northern NPO sediments are sourced from the Aleutian-Alaskan province (Horn et al., 1970; Rea et al., 1985). Tephra in the western and northern regions also have distinct characteristics. Tephra in the western NPO are white, which indicate high-SiO_2 magmas related to subduction zones, while tephra in the northern NPO are brown, which represent low-SiO_2 basaltic magmas sourced from nearby volcanoes (Ninkovich et al., 1966; Horn et al., 1969; Gersonde, 2012). In the central NPO basin, sediments are composed of red clay with colours ranging from light grey to light brownish-grey (Horn et al., 1970).

The northern westerlies

Westerlies are the prevailing winds that blow from west to east between latitudes of 30° and 60° in both hemispheres (Toggweiler, 2009). Westerlies are a major component of the global atmospheric circulation system and play an essential role in transporting heat and moisture and balancing the energy distribution between low- and high-latitude regions (e.g., An et al., 2012; Boex et al., 2013; Mölg et al., 2014; Shao et al., 2011). Simulated climatological and geological results suggest that the main westerly axis generally lies around 38° to 40°N (Rea and Leinen, 1988; Zhao et al., 2006). In historic times, the main westerly axis has shifted poleward since the 1960s (Archer and Caldeira, 2008; Chen and Held, 2007). Shifts and changes in westerly strength are mainly forced by the temperature gradient between low and high latitudes (Davis and Brewer, 2009), which can be affected by the height and baroclinicity of the tropopause (Rivière, 2011;

Vallis et al., 2015), stratospheric temperature gradients (Chen et al., 2007), surface temperature gradients (Son and Lee, 2005), and water vapour and related latent heating (Sha et al., 2020). As for long-term variations, the southern hemisphere westerlies are modulated by precession, with stronger westerlies during precession minima, and *vice versa* (Lamy et al., 2019). However, the long-term behaviour of the northern hemisphere westerlies is still not well understood.

Studies of long-term northern hemisphere westerly variations rely mainly on terrestrial and marginal sea sediments. For example, increased sediment grain size in the central Chinese Loess Plateau (CLP) suggests intensification of westerlies over the late Cenozoic, which has been linked to development of northern hemisphere ice sheets (Sun et al., 2008). Eolian flux and geochemical records from Lake Qinghai have an anti-phase relationship between the westerlies and the Asian summer monsoon since 32 ka, which indicates that westerlies dominated the last glaciation, while the Asian summer monsoon prevailed in the Holocene (An et al., 2012). Sediment provenance shifts in the Japan Sea over the past 60 ka suggest that the main westerly axis was located to the south/north of the Tibetan Plateau during stadials/interstadials (Nagashima et al., 2011). However, unambiguous proxy indicators for the westerlies are not easy to obtain because these regions are also affected by monsoon circulation (e.g., Tian et al., 2013; Seo et al., 2014; Wang et al., 2018).

Relatively continuously deposited and undisturbed NPO deep-sea sediments preserve environmental records from which past westerly behaviour can be inferred. Eolian dust, which originates from Asian interior arid regions, is transported to the NPO by the westerlies (Rea et al., 1985; Rea and Leinen, 1988; Rea, 1994; Zhao et al., 2006; Maher et al., 2010), and dominates the major detrital component of sediments (Windom, 1969; Ferguson et al., 1970). Studies from the NPO indicate that larger dust fluxes usually occurred in glacial stages (e.g., Hovan et al., 1989, 1991; Serno et al., 2017), and coarser grain sizes are associated with stronger westerlies (Rea, 1994). Periodic changes have been recognized in Quaternary dust records, such as Milankovitch periodicities (eccentricity, obliquity, and precession), and 52 kyr signals (Janecek and Rea, 1984; Pisias and Leinen, 1984; Morley et al., 1987; Hovan et al., 1991). The 100-kyr and 41-kyr signals dominate the dust flux and grain size records, respectively (Rea, 1994), while the 52 kyr signal has been interpreted to result from nonlinear interactions between external insolation forcing and internal climate feedback mechanisms (Hovan et al., 1991). However, NPO sediments are usually deposited at low sedimentation rates, which hampers detailed understanding of variations and mechanisms of the northern westerlies and age model uncertainties can be significant. To better address this issue, sites with relatively high sedimentation rates should be targetted to understand the long-term behaviour of the westerlies.

Magnetic studies of the NPO

NPO sediments are usually deposited below the CCD, which impedes application of radiocarbon dating and continuous oxygen isotope stratigraphy for developing sedimentary age models. As an alternative, paleomagnetism can play a significant role in reconstructing time frameworks for sedimentary sequences. Ninkovich et al. (1966) and Opdyke and Foster (1970) made pioneering paleomagnetic investigations of the paleomagnetic stratigraphy of many NPO sediment cores north of 20° N and found that sedimentation rates increased from central to marginal regions, which may be attributed to increased deposition of tephra and glacial detritus toward the marginal regions (Ninkovich et al., 1966; Opdyke and Foster, 1970). A significant natural remanent magnetization (NRM) instability was also observed in red clay from the central NPO

(Kent and Lowrie, 1974; Johnson et al., 1975; Prince et al., 1980), which was interpreted as a viscous remanent magnetization (VRM) associated with low-temperature oxidation of magnetite. Since the 1990s, development of RPI-assisted chronologies has facilitated late Quaternary studies (Roberts et al., 1997; Yamazaki, 1999; Kiefer et al., 2001; Yamamoto et al., 2007; Shin et al., 2019), and paleomagnetism has become a widely used method in climatic and oceanographic studies.

Rock magnetic studies of NPO sediments have been used to explore Asian eolian dust variability. Hematite and goethite are weakly magnetic antiferromagnetic minerals that have been used as dust content proxies in the NPO since Doh et al. (1988). However, interpretation of the climatic significance of eolian dust is controversial. For example, increased hematite contents at ~2.5 Ma and over the past 800 ka have been attributed to progressive Asian continental aridification (Yamazaki and Ioka, 1997; Yamazaki, 2009). In contrast, Zhang et al. (2020) suggested that enhanced eolian dust fluxes are caused by increased sediment availability associated with increased snow and glacial meltwater. In this case, increased eolian dust inputs reflect phases in which a relatively more humid Asian environment provided renewable sources of erodible silt that could then be deflated as dust in subsequent arid phases.

1.3.2. The SCS

The SCS is located at the junction of the Eurasian, Pacific, and Indo-Australian plates; it is the largest marginal sea of the NPO with water exchanging through the Luzon Strait (Qu et al., 2000, 2006; Li et al., 2015a). The SCS is influenced by the East Asian monsoon and is highly sensitive to terrigenous inputs and air-sea interactions (e.g., Chang et al., 2000; Wan et al., 2007; Wang et al., 2009; Liu et al., 2016), which makes it a focus of ocean-climate studies. Over the past two decades, 19 international research cruises have taken place in the SCS and more than two thousand exploratory boreholes have been drilled (Wang et al., 2014a), which have contributed to improving our understanding of the SCS. In this section, I first discuss water mass circulation and the source-to-sink sedimentation pattern of the SCS, and then I review the East Asian monsoon and discuss challenges in East Asian monsoon studies. Finally, I review magnetic studies of the SCS.

Water mass circulation

Similar to the NPO, water mass circulation in the SCS can be divided into three patterns by water depth: surface (above 600 m), mid-depth (600-1200 m), and deep circulation (below 1200 m) (Chao et al., 1996). The surface circulation is controlled mainly by the East Asian monsoon. There is a basin-wide cyclonic gyre during winter monsoon seasons, while during summer monsoon seasons there is a weakened cyclonic gyre and a strong anti-cyclonic gyre in the north and south, respectively (Wyrtki, 1961) (Figure 1.2). Western boundary currents are also strong in the SCS. The currents flow southward along the entire western boundary during the winter monsoon season and they flow northward in the southern SCS during the summer monsoon season (Wang and Li, 2009). In summer, the Summer Southeast Vietnam Offshore Current, which is derived from western boundary currents at about 12° N, flows eastward and divides the SCS into the northern and southern parts (Wang et al., 2006). Currents are cyclonic and anticyclonic to the north and south of the Summer Southeast Vietnam Offshore Current, respectively. In the northern SCS, the Kuroshio Current also plays a role in water circulation. A branch of the Kuroshio Current splits from the main flow path at about 21° N, and transports water at 300 to 500 m depths westward along the continental slope of the northern SCS (Shaw and Chao, 1994; Centurioni et al., 2004).

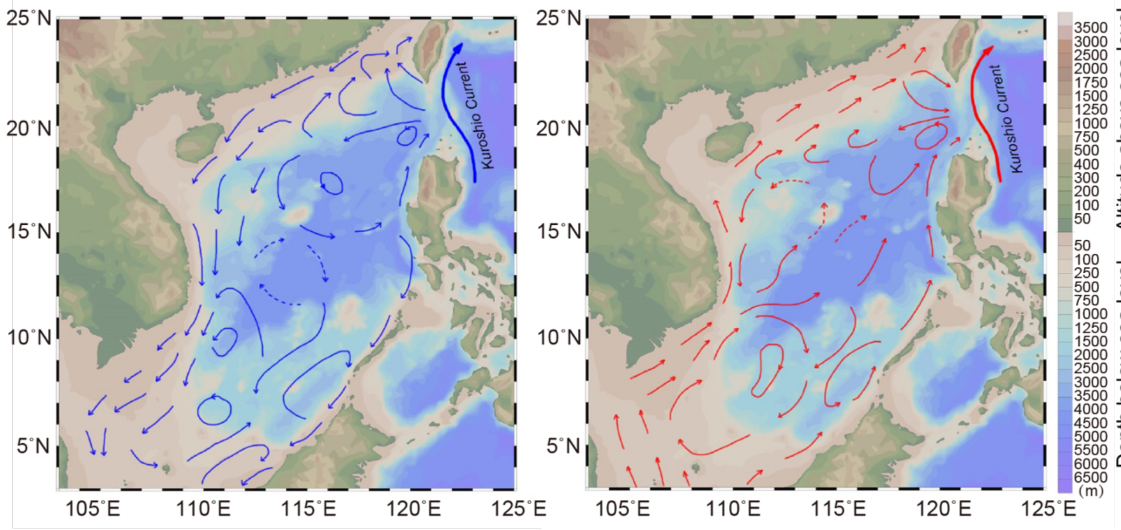

Figure 1.2 Surface circulation of the modern SCS in winter (left) and summer (right). Currents are based on Fang et al. (1998).

SCS deep circulation is dominated by cyclonic currents. The Luzon Strait is the only deep passage that connects the SCS with the NPO (Qu et al., 2006), and deep Pacific water flows into the Luzon Strait through the Taitung Canyon and the Bashi Channel with mean transports of about 0.4 Sv and 1.2 Sv, respectively (Zhao et al., 2014) (Figure 1.3).

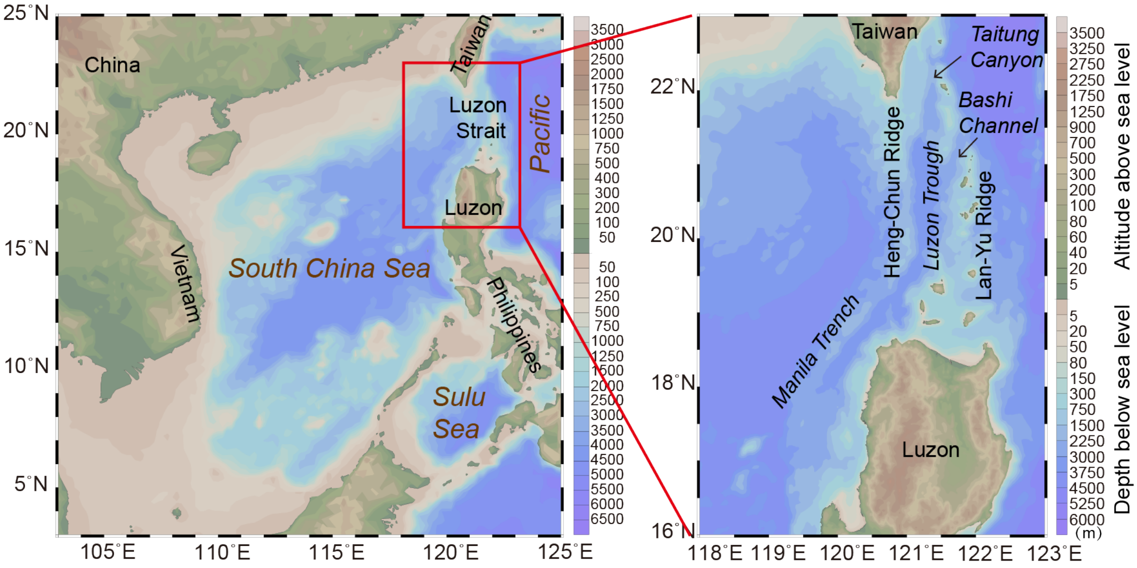

Figure 1.3 Bathymetry of the SCS (left) and Luzon Strait (right).

Restricted by the complex bottom topography, deep water flowing from the Taitung Canyon and the Bashi Channel converges and then flows southward along the Luzon Trough to finally enter the SCS. After entering the SCS, the deep water first turns northwestward and then southwestward along the continental margin offshore of southeast China (Qu et al., 2006). For mid-depth circulation, water flows out of the SCS through the northern Luzon Strait (Chao et al., 1996; Qu et al., 2000; Chen et al., 2001).

Clay minerals and source-to-sink pattern

The SCS is dominated by terrigenous sediments and receives >700 Mt of suspended sediment annually. Fluvial sediments are sourced from several of the largest rivers in the world (i.e., the Mekong, Red, and Pearl Rivers) and small mountain rivers (e.g., the Kao-Ping and Cho-Shui Rivers in SW Taiwan) (Liu and Stattegger, 2014; Liu et al., 2016). The large fluvial sediment flux makes the SCS an ideal natural laboratory to study regional terrigenous input and sedimentary evolution. Based on the spatial distribution of clay minerals, eight sedimentary provinces are recognised as described below (Liu et al., 2016) (Figure 1.4).

Province A (northeastern SCS): illite and chlorite contents are up to 80%, with minor smectite and kaolinite contributions. These minerals represent a Taiwan-sourced clay mineral fraction with a mixture of smectite from Luzon Island.

Province B (eastern SCS): smectite contents are high (63%) compared to the other three clay minerals and represent Luzon-sourced material.

Province C (northwestern SCS) and Province D (southern SCS): all four clay mineral contents are moderate, which indicates clay mineral mixing from different sources.

Province E (Gulf of Thailand): smectite is dominant, with minor kaolinite and illite contents and nearly negligible chlorite content. This pattern is consistent with a Middle Thailand origin.

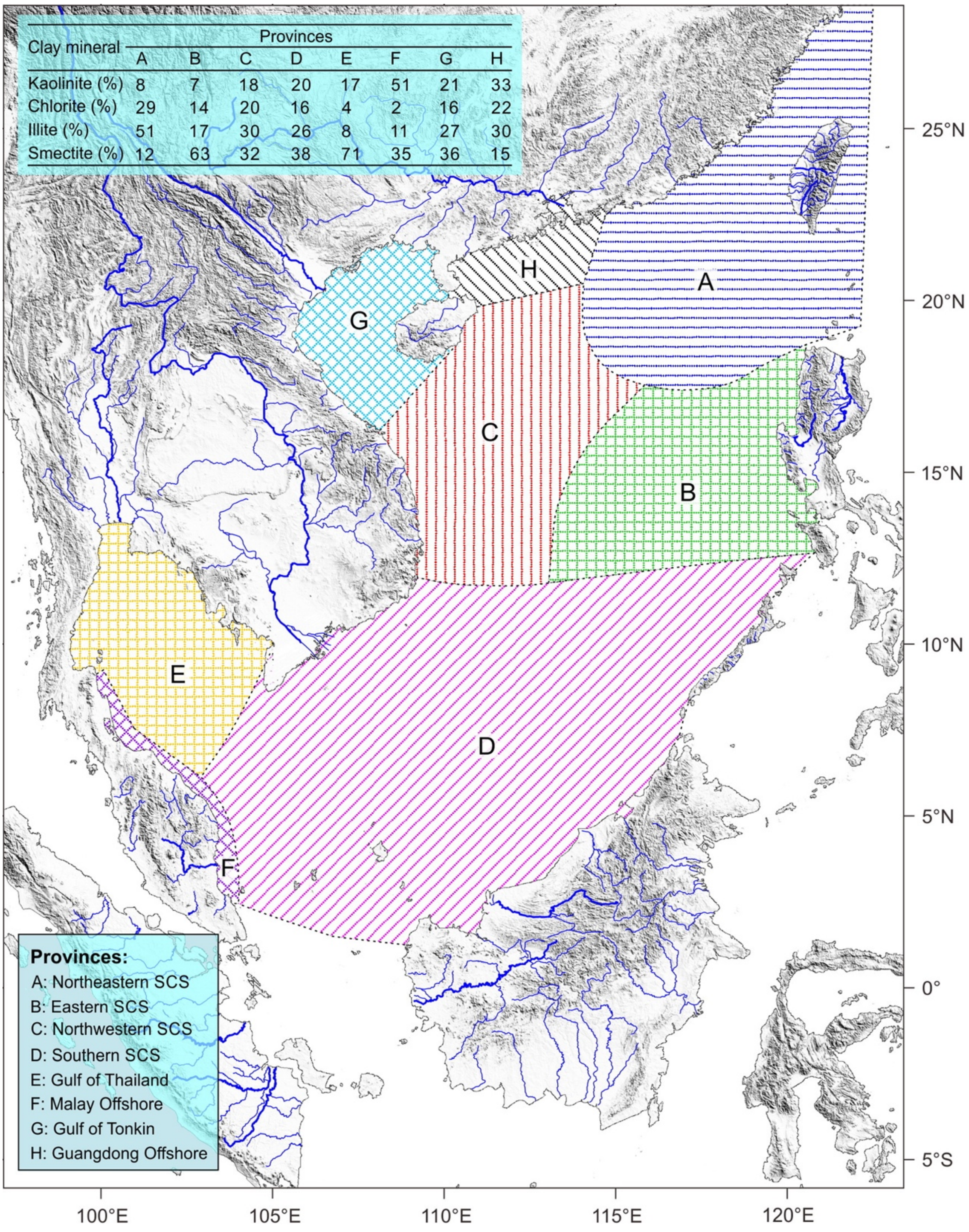

Clay mineral	Provinces A	B	C	D	E	F	G	H
Kaolinite (%)	8	7	18	20	17	51	21	33
Chlorite (%)	29	14	20	16	4	2	16	22
Illite (%)	51	17	30	26	8	11	27	30
Smectite (%)	12	63	32	38	71	35	36	15

Figure 1.4 Distribution of clay mineral assemblages in SCS surface sediments (Liu et al., 2016).

Province F (offshore of Malay Peninsula): kaolinite (51%) and smectite (35%) contents are dominant, which indicates a dominantly Malay Peninsula kaolinite source together with a mixture of smectite from other sources.

Province G (Gulf of Tonkin): all four clay mineral contents are moderate, with similar abundances to the Red River sediments.

Province H (offshore of Guangdong): kaolinite content (33%) is slightly higher compared to the other three clay mineral types, which suggests that the Pearl River is the dominant clay mineral source.

The sediment transportation pattern in the SCS is associated closely with water circulation patterns. In the northern SCS, the smectite distribution is controlled mainly by surface currents under the influence of the SCS branch of the Kuroshio Current. Illite and chlorite are transported to the continental slope and basin by near-bottom contour currents and/or deep water, while they are transported to the continental shelf by the Guangdong Coastal Current during winter (Z. Liu et al., 2010; Liu et al., 2016). In the eastern SCS, high smectite contents may be caused by rapid chemical weathering of volcanic rocks on the seafloor. In the southern and western SCS, sediments are mixed, and transportation patterns cannot be identified (Liu et al., 2016).

East Asian monsoon

The monsoon concept was first proposed by Halley (1687) and Hadley (1735), who suggested that the monsoon was caused by the heat contrast between oceans and continental regions. With the development of satellite technology in the mid-1970s, monsoon observations, including rainfall and winds, have been extended into data-scarce oceans (Wang et al., 2014c). The 1990s saw dramatic progress in paleomonsoon studies from marine sediments to which the Ocean Drilling Program (ODP) made important contributions. ODP Leg 108 in the equatorial Atlantic Ocean, Leg 117 in the western Arabian Sea, Leg 160 in the eastern Mediterranean Sea, and Leg 184 in the SCS have improved our understanding of variability in different paleomonsoon systems (e.g., Anderson and Prell, 1993; deMenocal, 1995; Larrasoaña et al., 2003; Wan et al., 2007).

Located to the east of the Tibetan Plateau, the East Asian monsoon plays a unique role among regional components of the climate system because it is the only subtropical monsoon (other regional monsoons are tropical). The zonal thermal contrast between the Asian continent and the NPO generates a pressure gradient, which, together with Earth's rotation, gives rise to a wet summer season with southerly flows and a dry winter with northerly flows in the East Asian monsoon region. In recent decades, East Asian monsoonal climates have been studied systematically from loess/paleosol sequences, stalagmites, and marine sediments over different timescales (e.g., An et al., 1991; Wang et al., 1999, 2001). The East Asian monsoon can be dated back to the Eocene (J. Li et al., 2018; Xie et al., 2020), and it has been found to have a multi-stage evolution with considerable variability both in space and in time (e.g., Clift et al., 2002; Wan et al., 2007; Sun et al., 2010). Although much progress has been achieved, there are still critical issues to resolve, such as finding reliable proxies and reconstructing continuous pre-Quaternary East Asian monsoon records to understand longer-term drivers of monsoon variability on orbital timescales.

East Asian monsoon proxies can be divided into two groups: direct wind-related proxies, which indicate the direction and intensity of winds, and indirect rainfall-related proxies associated with monsoonal precipitation or upper ocean structure changes (Wang et al., 2005 and references therein) (Table 1.1). Quartz grain size (QGS) of eolian deposits on the CLP and the upper water structure in the SCS are frequently used wind-related proxies for East Asian monsoon reconstruction. For example, QGS from red clay sequences has been employed as a winter monsoon proxy. Its variations have been interpreted to suggest that the winter monsoon wind intensity was relatively strong during the 7-4.2 Ma interval, which then weakened until 2.75 Ma, followed by a gradual increase and stabilization over the last 1.25 Ma (Sun et al., 2010). In the SCS, sea surface temperature variations suggest that the winter monsoon increased in steps at ~ 3.1, 2.7, 2.1, 1.6, 0.9, and 0.5 Ma, respectively (Li et al., 2004; Huang et al., 2005). For the summer monsoon, oxygen isotope variations in stalagmites from southern China have been regarded as a rainfall proxy, which can provide high-resolution records over the past 640 ka (Wang et al., 2001, 2008; Cheng et al., 2016).

Table 1.1 Simplified synthesis of East Asian monsoon proxies (Wang et al., 2005).

	Process	Proxy	Archive
Wind-related proxies	Wind transportation	Eolian dust, quartz grain size	Loess and marine sediments
		Wind-borne pollen	
	Wind-driven upwelling	Phytoplankton and zooplankton	Marine sediments
		Carbon flux-indicative benthic foraminifera	
	Surface ocean structure	Productivity-indicative proxies	
		Horizontal sea surface temperature gradient	
		Thermocline depth based on microfossils	
Rain-related proxies	River run-off	Sea surface salinity based on plankton	Marine sediments
		Stratification-induced laminated deposits	
	Precipitation	Lake level	Lacustrine deposits
		Salinity	
		Pollen-based vegetation, charcoal	
		$\delta^{18}O$, trace elements	Stalagmite
		^{10}Be, $\delta^{13}C_{organic}$	Loess deposits
	Weathering and pedogenesis	Clay minerals	Marine, lacustrine, and loess deposits
		Chemical weathering and pedogenesis indices	
		Magnetic susceptibility	

As shown in Table 1.1, diverse proxies are used to reconstruct East Asian monsoon evolution. However, these proxies do not always indicate similar East Asian monsoon variabilities (e.g., Wang et al., 2003; Gai et al., 2020), which leads to debate on which proxies are representative of the East Asian monsoon. For example, Wang et al. (2001)

suggested that lower $\delta^{18}O$ of stalagmites from southern China indicate a stronger East Asian summer monsoon. However, Pausata et al. (2011) argued that stalagmite $\delta^{18}O$ from southern China is influenced by water vapour exported from India; their climate model reproduced $\delta^{18}O$ enrichment over Northern India and East Asia during Heinrich events, which suggests that stalagmite $\delta^{18}O$ from southern China is a rainfall-related proxy for the Indian summer monsoon rather than the East Asian summer monsoon. Considering the inconsistency between stalagmite $\delta^{18}O$ variations and other independent late Quaternary paleoclimate proxies, Maher and Thompson (2012) suggested that stalagmite $\delta^{18}O$ variations indicate moisture source changes rather than rainfall changes. The complex interplay of physical, chemical, and biological processes in nature, therefore, make proxies ambiguous – East Asian monsoon signals can be suppressed, distorted, or even masked by various processes – which complicates proxy interpretation. Therefore, to better understand proxy records of East Asian monsoon variability, potential complicating processes must be considered and components related to the East Asian monsoon must be discriminated from unrelated processes to develop reliable monsoon proxies.

Another issue is the paucity of continuous pre-Quaternary East Asian monsoon records, which hampers understanding of the long-term evolution and possible orbital forcing of the East Asian monsoon. Compared with terrestrial archives, marine sediments are more continuous and well-preserved. Therefore, marine sediments, especially SCS sediments that have a significant East Asian monsoonal climate influence, have the potential to improve this situation.

Magnetic studies of the SCS

Magnetic studies of the SCS have focused mainly on paleomagnetic or rock magnetic applications. Paleomagnetism is a commonly used and effective method for reconstructing time frameworks in marine sediments (e.g., Aksu and Mudie, 1985; Lanci et al., 2005; van Peer et al., 2017). In the SCS, Wang et al. (1993) analysed paleomagnetic results for three cores from the southernmost SCS and found that sedimentation rates decrease as water-depth increases. Kissel et al. (2003) established a ~1.2-Ma magnetostratigraphy for ODP Site 1146 and observed that low magnetic mineral contents and coarser magnetic particles occur during cold periods, and *vice versa*. Yang et al. (2009) presented a rock magnetic pattern consistent with that revealed by Kissel et al. (2003) for the past ~85 ka based on a geomagnetic RPI record from northern SCS piston cores. Wu et al. (2014, 2017) reconstructed new magnetostratigraphic age models for ODP Sites 1148 and 1143 to provide precise time frameworks back to 23 Ma and 4.6 Ma, respectively, which benefits understanding of long-term tectonic and environmental studies in the SCS. Zhang et al. (2019) obtained a high-resolution astronomically-tuned magnetostratigraphy from the northern SCS and further reconstructed terrigenous inputs to the SCS.

Rock magnetism has been applied to SCS sediments to study terrigenous sediment transportation. Sediments sourced from Taiwan indicate a co-existence of detrital pyrrhotite and magnetite, with authigenic greigite forming through post-depositional diagenetic processes (Kao et al., 2004; Horng and Chen, 2006; Horng and Roberts, 2006; Horng and Huh, 2011; Horng et al., 2012). Magnetic susceptibility variations of the fine-grained surface sediment fraction indicate that northern and southern SCS sediments are sourced mainly from large rivers, while eastern SCS sediments are derived from the island arc, with the sediment distribution pattern controlled dominantly by currents (J. Liu et al., 2010). Kissel et al. (2016, 2017, 2018) reported the magnetic properties of sediments collected from the main rivers that flow into the SCS. They suggested that the magnetic mineralogy of the Pearl River, and rivers in Luzon and Sumatra are magnetite-dominated; Taiwan is magnetite- and pyrrhotite-dominated; southwestern Borneo is magnetite-dominated with some iron sulphides, while other parts of Borneo have high hematite contents; the Mekong River and Malay Peninsula are hematite-dominated; the Red River carries a mixture of magnetite and hematite. Moreover, these authors also pointed out that magnetite- and pyrrhotite-dominated sediments are transported to the northern SCS, while hematite-rich sediments are transported to the southern SCS, so that the hematite concentration is higher toward the southern SCS. Based on the results of Kissel et al. (2017), the long-term increase in pyrrhotite concentration in the northern SCS over the past 400 ka is interpreted to be the result of progressively enhanced contributions from Taiwan (Q. Chen et al., 2017), and increased hematite concentrations in the northwestern SCS over the ~32-15 ka interval are interpreted to result from enhanced Red River terrigenous inputs (M. Li et al., 2018).

Chapter 2

Fundamentals of paleomagnetism and rock magnetism

2.1. Paleomagnetism

The geomagnetic field varies over a wide range of timescales from micropulsations (<1 s to minutes) to superchrons (>10 Myr) (Roberts, 2008). Geomagnetic field behaviour has only been observed directly over the past few centuries, so paleomagnetic measurements are needed to understand long-term field behaviour. In this section, I concentrate on geochoronology, which is among the most widely used applications of paleomagnetism. I first introduce basic definitions that are used frequently in paleomagnetic studies, including components of the geomagnetic field vector, the geocentric axial dipole (GAD) hypothesis, virtual geomagnetic poles (VGPs), and geomagnetic polarity. I then review two paleomagnetic dating methods; magnetostratigraphy (based on geomagnetic reversals) and RPI-assisted chronology (based on geomagnetic field intensity variations).

2.1.1. Basic definitions

Components of the geomagnetic field vector

In paleomagnetism, the direction of the geomagnetic field vector, $\boldsymbol{H}$, can be described by two components: H_v and H_h (Figure 2.1). The vertical component of the geomagnetic field is given by:

$$H_v = H \sin I, \tag{2.1}$$

where I is the inclination, or the vertical angle between the horizontal and $\boldsymbol{H}$, which ranges from -90° to 90° and is defined as positive downward. The horizontal component of the geomagnetic field is given by:

$$H_h = H \cos I. \tag{2.2}$$

The declination, *D*, is the azimuthal angle between the horizontal component of ***H*** and geographic north, which ranges from 0° to 360° and is defined as positive clockwise from north. The horizontal component, H_h, can be further described by the north component H_N and east component H_E, respectively, which are given by:

$$H_N = H \cos I \cos D, \text{ and} \tag{2.3}$$

$$H_E = H \cos I \sin D. \tag{2.4}$$

The total geomagnetic field intensity is given by:

$$H = \sqrt{{H_N}^2 + {H_E}^2 + {H_v}^2}. \tag{2.5}$$

In paleomagnetic studies, the field direction is generally of greatest interest, thus, declination and inclination are determined. In paleointensity studies, it is not only the direction but also the magnitude of the vector – given by the field intensity – that is the focus of investigation. Applications of geomagnetic field components are introduced in Subsections 2.1.3 and 2.1.4.

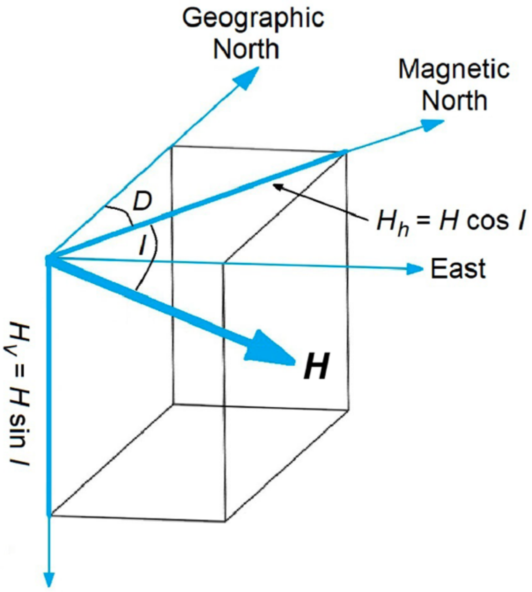

Figure 2.1 Definitions of parameters used to define components of the geomagnetic field vector (modified from McElhinny (1973)).

The GAD hypothesis

The GAD hypothesis assumes that the time-averaged magnetic field is produced by a single magnetic dipole at the centre of the Earth that is aligned with Earth's rotation axis (McElhinny, 1973). In the GAD hypothesis, the geomagnetic field inclination can be determined from the relationship:

$$\tan I = 2\tan\lambda, \tag{2.6}$$

where λ is the geographic latitude, which ranges from -90° to 90° and is defined as positive at northern latitudes. The relationship between I and λ is essential to paleomagnetic applications, including studies of field behaviour and to support paleo-continental reconstructions (e.g., Opdyke and Henry, 1969; Schneider and Kent, 1990; Enkin et al., 1992; Dupont-Nivet et al., 2005; Meert, 2009; Seton et al., 2012; Wang et al., 2016).

Virtual geomagnetic poles, VGPs

A VGP is the position on Earth that corresponds to the pole associated with a given paleomagnetic direction assuming a dipolar field (Butler, 1992). A VGP can be calculated from the geomagnetic field direction observed at a single location. At a location with latitude λ_o and longitude φ_o, if the paleomagnetic direction (D, I) is known, the latitude and longitude of the VGP (λ_p, φ_p) can be calculated using (Butler, 1992):

$$\sin\lambda_p = \sin\lambda_o\sin\lambda + \cos\lambda_o\cos\lambda\cos D, \tag{2.7}$$

$$\varphi_p = \varphi_o + \beta \text{ (if } \sin\lambda \geq \sin\lambda_o\sin\lambda_p\text{), and} \tag{2.8}$$

$$\varphi_p = \varphi_o + \beta + 180 \text{ (if } \sin\lambda < \sin\lambda_o\sin\lambda_p\text{), where} \tag{2.9}$$

$$\tan\lambda = (1/2)\tan I\text{, and} \tag{2.10}$$

$$\sin\beta = \cos\lambda\sin D/\cos\lambda_p. \tag{2.11}$$

Geomagnetic polarity

The geomagnetic field can switch polarity (Brunhes, 1906; Matuyama, 1929). When the polarity is in the same state as at present, that is, when the field points to geographic south, it is called normal polarity; when the polarity is in the opposite state, it is called reversed polarity (Cox et al., 1963). Geomagnetic polarity intervals have durations that range from 10^4 to 10^7 yr (Cox, 1968, 1969). Geomagnetic polarity reversals are discussed in more detail in Subsection 2.1.3.

2.1.2. Magnetic remanences in nature

For natural samples, the remanence that is held before any laboratory treatment is imparted is called the NRM. The NRM is controlled by the geomagnetic field and by geological processes during its acquisition and subsequent modification. The NRM usually consists of several components. The component that is acquired at the time of rock formation is termed a primary component or characteristic remanent magnetization (ChRM), while any component that is acquired during subsequent geological processes is a secondary component. Various mechanisms can produce different types of NRM, including a thermal remanent magnetization (TRM), depositional remanent magnetization (DRM), chemical remanent magnetization (CRM), VRM, and less commonly, an isothermal remanent magnetization (IRM).

A TRM is acquired by cooling from above the Curie temperature (T_C) in a weak magnetic field. Thermally excited transitions among different magnetic microstates become more difficult to pass at lower temperatures, and transitions cease below the blocking temperature (T_B), so that the rock acquires a TRM (Dunlop and Özdemir, 1997). Most igneous rocks and some high-grade metamorphic rocks acquire their NRMs in the form of a TRM. The total TRM can be regarded as the sum of several components that are acquired over distinct temperature intervals, and each component can be called a partial TRM (pTRM). For SD particles, pTRMs follow laws of additivity, reciprocity, and independence (Thellier, 1938). PTRMs are vector quantities, and the total TRM is the vector sum of all pTRMs that can be described as:

$$\mathrm{TRM} = \sum_n pTRM_n, \tag{2.12}$$

which is the additivity law. Reciprocity suggests that a pTRM acquired in a certain temperature interval during cooling in a magnetic field can be demagnetized completely over the same temperature interval in zero field. The direction and magnitude of a pTRM that is acquired in a certain temperature interval should not be affected by another pTRM that is acquired in a non-overlapping temperature interval, which is the independence law.

Unlike igneous rocks, magnetic particles in sediments are already magnetized before deposition. They can rotate to align with the magnetic field direction, and finally be deposited to produce a DRM. A DRM is usually much weaker than the saturation magnetization, which can be explained by different mechanisms in different conditions. In freshwater environments with magnetically isolated particles, the low DRM intensity has been argued to result from the misaligning effects of Brownian motion (Collinson, 1965; Stacey, 1972). In marine environments where magnetic particles form composite flocs, the size of flocs has been suggested to exert a dominant control on DRM intensity (Katari and Bloxham, 2001; Tauxe et al., 2006). Likewise, the presence of small magnetic inclusions within larger silicate host minerals has been argued to contribute to the lower efficiency of a DRM (e.g., Chang et al., 2016b).

A CRM is acquired during the growth or alteration of magnetic particles below T_B in a magnetic field. A CRM has a lower magnitude than a TRM, but its stability is similar to a TRM (Thompson and Oldfield, 1986). A CRM usually occurs as a secondary NRM while TRM and DRM are usually responsible for a primary NRM.

A VRM is acquired gradually during exposure to a weak magnetic field and is a secondary NRM. From a paleomagnetic viewpoint, VRMs are usually undesirable and progressive demagnetization is used to remove such secondary components. An IRM is acquired by short-term exposure to a strong magnetic field. Lightning strikes, which generate a strong local magnetic field by an intense current, is the most frequently cited mechanism for IRM acquisition in nature (Matsuzaki et al., 1954; Graham, 1961). The geomagnetic field is too weak to produce an IRM, therefore, a natural IRM is not commonly present. Rather, an IRM is usually of interest as a laboratory-produced remanence (see Subsection 2.2.2).

2.1.3. Polarity reversals and magnetostratigraphy

Geomagnetic polarity reversals have been recorded in various rocks and sediments, such as lava flows, terrestrial and marine sediments, and seafloor magnetic anomalies (e.g., Vogt et al., 1971; Champion et al., 1988; Guo et al., 2002; Wu et al., 2014). Radiometric dating results indicate that polarity reversals occur synchronously throughout the world (Cox et al., 1963; Cox, 1969), which enables development of a consistent geomagnetic polarity timescale (GPTS) (e.g., Cande and Kent, 1995; Channell et al., 1995; Lowrie and Kent, 2004; Gradstein et al., 2012). Geomagnetic polarity reversals identified in stratigraphic sequences can be correlated to the GPTS, which is called magnetostratigraphy or magnetic polarity stratigraphy (Opdyke and Channell, 1996). General principles to ensure a high-quality magnetostratigraphy include (Van der Voo, 1990; Opdyke and Channell, 1996; Tauxe, 2010): having independent stratigraphic age constraints; isolating a ChRM from stepwise alternating-field (AF)/thermal demagnetization data with least-squares analysis (Kirschvink, 1980), so that the average ChRM direction can be compared with the expected GAD field; separating directional data into clear normal or reversed polarity zones with antipodal reversals; documenting a polarity pattern that can be correlated to the GPTS; and field tests, such as the fold test or the conglomerate test, are desirable for assessing the age of the magnetization.

2.1.4. Paleointensity and RPI-assisted chronology

In theory, the mechanisms by which rocks are magnetized will produce magnetizations that are approximately linearly related to the geomagnetic field strength (Figure 2.2). Therefore, the assumption is:

$$M_{NRM} \cong \alpha_{anc} H_{anc}, \text{ and} \tag{2.13}$$

$$M_{lab} \cong \alpha_{lab} H_{lab}, \tag{2.14}$$

where M_{NRM} and M_{lab} are natural and laboratory remanent magnetizations, respectively, H_{anc} and H_{lab} are ancient and laboratory field intensities, respectively, and α_{anc} and α_{lab} are dimensionless constants of proportionality. If the two constants α_{anc} and α_{lab} are the same, then the ancient field intensity can be determined as:

$$H_{anc} = M_{NRM} H_{lab} / M_{lab}. \tag{2.15}$$

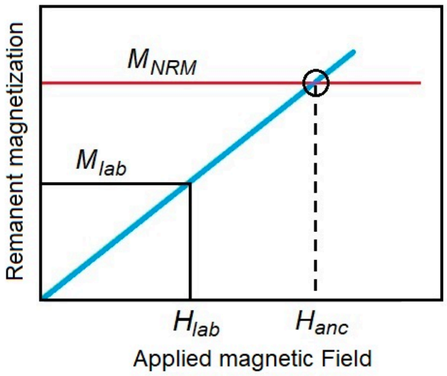

Figure 2.2 Illustration of the bases for making paleointensity estimations.

However, in practice, recovering accurate paleointensities is not simple. For example, the constants α_{anc} and α_{lab} may not be identical because the NRM may have multiple components with different constants of proportionality that result from acquisition of NRM components at different times (Tauxe and Yamazaki, 2015).

TRMs from igneous rocks and baked sediments provide the best records for absolute paleointensity studies. However, it is difficult to reproduce the original magnetization mechanisms in the laboratory and only a small fraction of igneous rocks give useful paleointensity data (Tauxe, 1993). Therefore, sedimentary sequences are an attractive alternative for studies of continuous paleointensity variations. However, in contrast to igneous rocks, the proportionality constant α_{anc} for a DRM cannot be determined because the DRM is affected by the ambient field, magnetic mineralogy, the concentration and grain size of magnetic minerals, flocculation of magnetic and other particles, etc. (Tauxe, 1993; Tauxe et al., 2006; Roberts et al., 2013). Levi and Banerjee (1976) developed a method to estimate RPI in sediments by normalizing the NRM with an artificial laboratory-induced magnetization. RPI variations have since been established and used extensively as a chronological tool in marine sediments (e.g., Guyodo and Valet, 1996, 1999; Valet et al., 2005; Yamamoto et al., 2007; Channell et al., 2009, 2016a). Common criteria for RPI studies include that magnetite should be the dominant remanence-carrier, changes in magnetite concentration should be less than one order of magnitude, and the grain size of magnetite should be in the 1-15 μm range (King et al., 1983; Tauxe, 1993). However, a sound theoretical basis for remanence acquisition is lacking. Also, these requirements are based on the assumption that bulk magnetic properties are due to a single magnetic particle assemblage without considering that magnetic minerals in sediments almost always represent a mixture rather than a single magnetic component. Recent studies suggest that different populations of magnetite within the same sample may respond differently to the magnetic field (Roberts et al., 2012; Yamazaki et al., 2013; Ouyang et al., 2014; L. Chen et al., 2017). Therefore, detailed assessment of grain-size characteristics and the normalized remanence behaviour of each remanence-bearing component should be considered in sedimentary RPI studies.

2.2. Rock magnetic parameters

Characteristics of magnetic particles, including their concentration, domain state, and mineralogy, are related to their geological origin and/or to subsequent environmental changes (Liu et al., 2012). Therefore, rock magnetism can help to better understand geological processes and environmental change. In this section, I first introduce the fundamental types of magnetic behaviours, and then I present parameters that are related to magnetic mineral concentration and domain state, respectively. Finally, I summarize the magnetic characteristics of three magnetic minerals that are important in my research: magnetite, hematite, and greigite.

2.2.1. Basic magnetic properties

There are five fundamental types of magnetic properties: diamagnetism, paramagnetism, ferromagnetism, antiferromagnetism, and ferrimagnetism (Butler, 1992). Each type gives rise to different magnetic responses in natural samples, as outlined below.

Diamagnetism

Diamagnetism is extremely weak compared to other magnetic properties. It is a property of all materials and is independent of temperature. In an applied magnetic field, diamagnetic materials acquire a small induced magnetization in a direction opposite to the applied field. The magnetization is lost when the field is removed. Many common natural minerals and compounds, such as quartz, calcite, feldspar, and water are diamagnetic (Thompson and Oldfield, 1986).

Paramagnetism

Paramagnetism involves partial alignment of magnetic moments in iron atoms parallel to the applied field direction (Dunlop and Özdemir, 1997). When there is no applied field, spin magnetic moments are in arbitrary directions due to thermal energy and, therefore, the total magnetic moment is zero. The paramagnetic magnetization is, thus, a function of applied field and thermal energy (Thompson and Oldfield, 1986). Carbonates, silicates, and most iron sulphides are paramagnetic minerals (Dunlop and Özdemir, 1997).

Ferromagnetism

Ferromagnetism is significantly different from paramagnetism and diamagnetism. Unlike the former two magnetic behaviours, which are induced or temporary (that is, the magnetic moment disappears when the applied field is removed), ferromagnetic materials have a spontaneous magnetization that results from exchange energy that has a quantum mechanical origin (Thompson and Oldfield, 1986). The exchange energy produces parallel coupling of magnetic moments, so that the spontaneous magnetization is strong (Figure 2.3). Ferromagnetic materials can record the direction of an applied field.

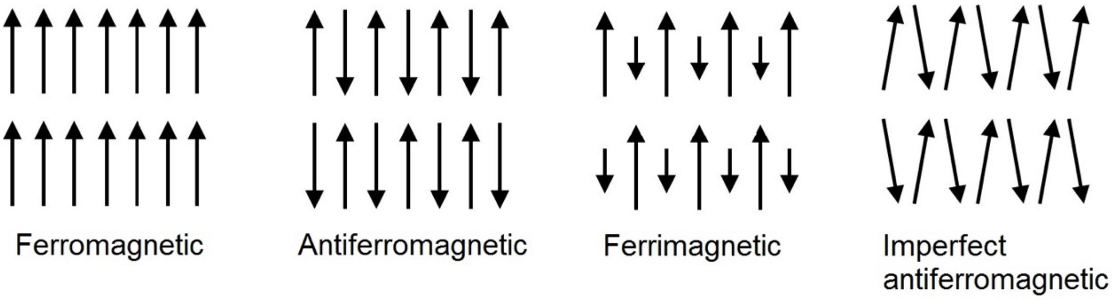

Figure 2.3 Alignment of magnetic moments in ferromagnetic, antiferromagnetic, ferrimagnetic, and imperfect antiferromagnetic materials (redrawn from Thompson and Oldfield (1986)).

Antiferromagnetism and ferrimagnetism

Antiferromagnetism and ferrimagnetism are more relevant than ferromagnetism in naturally occurring magnetic minerals. Magnetic moments of these materials have parallel coupling within a layer (such as in ferromagnetic minerals), but adjacent layers have antiparallel coupling. If these so-called magnetic sublattices have identical magnetic moments, the bulk magnetization is zero and the magnetic structure is antiferromagnetic. When the sublattices have different magnetic moments, the magnetic structure is ferrimagnetic (Thompson and Oldfield, 1986) (Figure 2.3). Modification of the purely antiparallel sublattice magnetizations in antiferromagnetic materials can produce a weak net magnetization due to spin canting or lattice defects. These magnetization types are referred to as canted-antiferromagnetism and defect-antiferromagnetism, respectively (Dunlop and Özdemir, 1997) (Figure 2.3). Such materials can be referred to generically as imperfect antiferromagnets.

2.2.2. Concentration-indicative magnetic parameters

In this section, I summarize magnetic parameters that are used commonly to assess magnetic mineral concentration variations, including the magnetic susceptibility, anhysteretic remanent magnetization, isothermal remanent magnetization, and saturation magnetization.

Magnetic susceptibility, χ

χ is one of the most widely used magnetic properties. The simplest definition of χ is that it is the ratio between the strength of the induced magnetization (***M***) and the strength of the applied field (***H***). χ can be written as:

$$\chi = \boldsymbol{M}/\boldsymbol{H}. \tag{2.16}$$

χ for diamagnetic materials is negative because the magnetization is directed antiparallel to the applied field. χ for paramagnetic materials (χ_p) follows the Curie law:

$$\chi_p = C/T, \tag{2.17}$$

where C and T are the Curie constant and absolute temperature, respectively. Diamagnetic and paramagnetic materials have a simple linear relationship between ***M*** and ***H***, whereas ferromagnetic, imperfect antiferromagnetic, and ferrimagnetic materials have a more complex relationship between ***M*** and ***H***, including an internal demagnetizing field ($\boldsymbol{H_d}$) (Weiss, 1907), which is given by:

$$\boldsymbol{H_d} = -N_d\boldsymbol{M}, \tag{2.18}$$

where $\boldsymbol{N_d}$ is the demagnetizing factor. $\boldsymbol{N_d}$ increases with increasing ***M***. For this reason, ferrimagnetic materials are relatively easy to saturate in laboratory applied fields; χ for ferrimagnetic materials is measured commonly from the initial magnetization curve near the origin and is calculated by the slope of ***M*** and ***H***, which is also termed the low-field magnetic susceptibility. For natural samples that contain mixtures of magnetic minerals, a high-field magnetic susceptibility (χ_{high}) is calculated from hysteresis loops at fields higher than that required to saturate ferrimagnetic components. When ferrimagnetic components are saturated, their magnetization no longer increases with increased applied field and the ferrimagnetic susceptibility is zero. Therefore, χ_{high} is affected by diamagnetic, paramagnetic, and antiferromagnetic components. If antiferromagnetic components are removed, for example, by the citrate-bicarbonate-dithionite method prior to magnetic measurements (Mehra and Jackson, 1958; Verosub et al., 1993; Hunt et al., 1995), χ_{high} will be dominated by diamagnetic and paramagnetic components, and the ferrimagnetic susceptibility (χ_{ferri}) can be determined by:

$$\chi_{ferri} = \chi - \chi_{high}. \tag{2.19}$$

In addition to reflecting variations in the concentration and mineralogy of ferrimagnetic minerals, χ_{ferri} is influenced by grain size. At room temperature, SD particles have the lowest χ values; χ for superparamagnetic (SP) particles is enhanced with increasing grain size, reaching a maximum just below the SP-stable SD (SSD) threshold size. For particles larger than the SD threshold size, Thompson and Oldfield (1986) showed that χ for crushed magnetite increases with grain size; in contrast, Heider et al. (1996) observed that χ for synthetic magnetite with a diameter >20 μm is independent of grain size. They attributed the findings of Thompson and Oldfield (1986) to potential contamination by small particles produced by crushing.

χ of magnetic particles near the SP-SSD boundary is also sensitive to the applied field frequency; increased applied field frequency can change particles from the SP to SSD state and decrease χ significantly (Mullins and Tite, 1973; Worm, 1998). Therefore, a frequency-dependent susceptibility (χ_{fd}) can be used to indicate the magnetic particle concentration across a narrow grain size range at the SP-SSD boundary (Liu et al., 2005b). χ_{fd} is defined as:

$$\chi_{fd} = \chi_{lf} - \chi_{hf}, \tag{2.20}$$

where χ_{lf} and χ_{hf} are measured at low and high frequencies (e.g., 470 and 4,700 Hz for the Bartington Instruments magnetic susceptibility meter), respectively.

Anhysteretic remanent magnetization, ARM

ARM is acquired when magnetic particles are subjected to an AF of gradually decreasing amplitude in the presence of a small direct current (DC) bias field. ARM is then measured when both the AF and DC fields are zero. ARM is proportional to the DC bias field used to impart the ARM for applied field magnitudes similar to that of Earth's (Patton and Fitch, 1962), and is often referred to as the ARM susceptibility (χ_{ARM}):

$$\chi_{ARM} = ARM/DC\ field. \tag{2.21}$$

SD particles have the highest ARM (King et al., 1982), so ARM is often used as an indicator of fine magnetic particle concentrations. Liu et al. (2005b) suggested that an ARM demagnetized after 20 mT is more reliable for quantifying fine particles because the contribution of MD particles can be further suppressed by this demagnetization. However, ARM acquisition can be affected strongly by magnetic mineral concentration, with higher magnetite concentrations reducing ARM acquisition efficiency (Sugiura, 1979; King et al., 1983). Moreover, ARM intensities may not be reproducible among laboratories due to differences in experimental conditions, such as AF decay rates (Sagnotti et al., 2003).

Isothermal remanent magnetization, IRM

In the laboratory, IRM is usually imparted by exposing a sample to a strong DC field at room temperature. In a sufficiently strong field, magnetic moments are reoriented into similar directions to produce the maximum remanence, which is termed the saturation

IRM (SIRM). In the laboratory, a DC field of 1 T or 1.5 T is often used to impart a SIRM. When the mineralogy and magnetic grain size are relatively constant, SIRM can be used to indicate magnetic particle concentration. It should be noted that goethite cannot be saturated even in the highest available applied fields (e.g., Rochette et al., 2005). The S-ratio was introduced by Stober and Thompson (1979) to evaluate the relative concentrations of ferrimagnetic and imperfect antiferromagnetic particles. The S-ratio is usually defined as (Bloemendal et al., 1992):

$$\text{S-ratio} = (1 - IRM_{-0.3\,T}/SIRM)/2, \tag{2.22}$$

where $IRM_{-0.3\,T}$ is the IRM imparted in a DC field of -0.3 T. A higher S-ratio (close to unity) suggests a higher proportion of ferrimagnetic particles, and *vice versa*. To evaluate the imperfect antiferromagnetic particle concentration, Robinson (1986) proposed a parameter named the hard IRM (HIRM), which is defined as:

$$\text{HIRM} = (SIRM + IRM_{-0.3\,T})/2. \tag{2.23}$$

However, interpretations of the S-ratio and HIRM should recognise that these parameters are affected by the distribution of coercivities. To help address this issue, Liu et al. (2007) proposed a parameter (L-ratio), which is defined as:

$$L\text{-ratio} = IRM_{AF@0.3\,T}/IRM_{AF@0.1\,T}, \tag{2.24}$$

where $IRM_{AF@0.1\,T}$ and $IRM_{AF@0.3\,T}$ represent remanences after AF demagnetization of an IRM that was imparted in a 1 T DC field with peak AFs of 0.1 T and 0.3 T, respectively. The L-ratio enables semi-quantitative identification of coercivity variations, and it is suggested that the S-ratio and HIRM can be interpreted as indicators of the relative and absolute concentrations of high coercivity magnetic minerals only when the L-ratio is relatively stable (Q. Liu et al., 2007). It should be noted that all of these parameters have limitations and that relative and absolute quantification of weakly magnetized minerals, such as hematite and goethite, is challenging (Roberts et al., 2020).

Saturation magnetization, Ms

In a sufficiently strong magnetic field, the electronic spins of magnetic particles are aligned parallel to the applied field and the induced magnetization will no longer increase. The resulting magnetization is the saturation magnetization, M_s, which is independent of grain size. This independence on grain size makes M_s an excellent concentration-indicative parameter (e.g., Meena et al., 2011; Dytłow et al., 2019).

2.2.3. Domain state-indicative magnetic parameters

The magnetization of magnetic particles is controlled dominantly by three energies: the exchange energy, the magnetocrystalline anisotropy energy, and the magnetostatic energy. Magnetic particles seek a state that minimizes the total energy. Weiss (1907) proposed the concept of magnetic domains to explain how magnetic particles can produce a lower total energy configuration. SD particles have only one domain and are efficient remanent magnetization carriers. With increasing grain size, the spin structure of magnetic particles evolves from uniaxial to flower, to single vortex, to multi-vortex, and finally to MD states (Nagy et al., 2017; Roberts et al., 2017). For magnetic particles with extremely small grain sizes, the thermal energy is of the same order as the magnetic energy, so they do not have a stable remanent magnetization. These extremely small magnetic particles have so-called SP behaviour; for magnetite, this corresponds to particles with sizes smaller than 20-25 nm (Maher, 1988; Dearing et al., 1996; Worm, 1998). In general, the smaller the grain size, the fewer domains. Therefore, magnetic parameters that reflect domain state variations are also grain-size indicative, such as hysteresis parameters, FORC diagrams, and ratios of different concentration-indicative parameters. Mathematical unmixing methods can also be used for domain state diagnosis.

Roberts et al. (2019) evaluated ten methods for domain state diagnosis, which provides useful guidance on this subject.

Hysteresis loops

The field dependence of magnetization for uniaxial SD magnetite particles is illustrated in Figure 2.4. For demagnetized particles, the magnetization increases with the initial magnetic field increase, and gradually reaches M_s, where the magnetization no longer increases with increasing applied field. This magnetization process follows the path 0→1 in Figure 2.4. SD particles undergo coherent rotation of the magnetic moment toward the magnetic field, and the intensity of the saturating field equals the magnetostatic energy barrier for SD particles. MD particles are magnetized by domain wall displacement, nucleation, annihilation, and/or domain rotation (Dunlop and Özdemir, 1997). As the magnetic field decreases, the magnetization decreases gradually along the path 1→2 in Figure 2.4. When the field is removed, a saturation remanence (M_{rs}) remains. The phenomenon of an irreversible magnetization as depicted in the loop shown in Figure 2.4 is known as hysteresis. The ratio of M_{rs}/M_s is used frequently to indicate the efficiency in acquiring a remanent magnetization. Randomly oriented uniaxial SD particle assemblages have a M_{rs}/M_s of 0.5 (Stoner and Wohlfarth, 1948), and MD particles have much lower M_{rs}/M_s values due to internal cancellation of magnetic moments (Néel, 1955a). To force the magnetization back to zero, a reversed magnetic field must be applied. With the increasing reversed field, the magnetization decreases along the path 2→3 in Figure 2.4. When the magnetization decreases to zero, the reversed field value is the so-called coercivity or coercive force (B_c). B_c depends on the microcoercivity of magnetic particles, and is independent of the particle concentration. To complete a hysteresis loop, magnetic particles are further saturated in the reversed direction followed by switching the field in a positive direction and saturating the sample again to describe a full hysteresis loop.

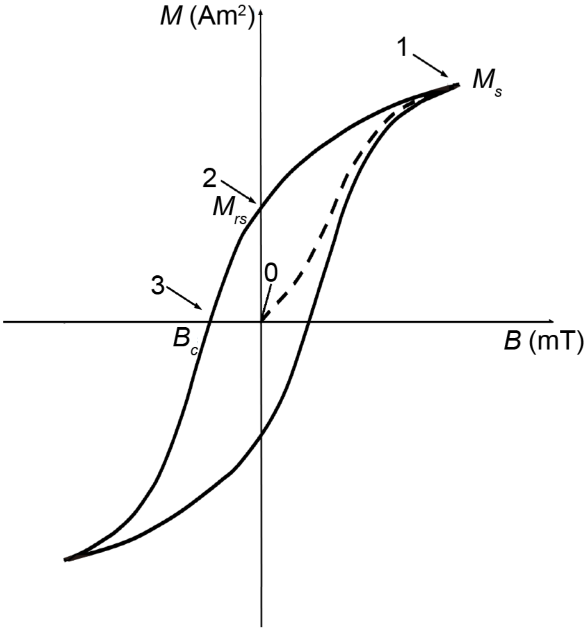

Figure 2.4 Illustration of hysteresis characteristics for uniaxial SD magnetite particles (modified from Dunlop (1984)).

Compared with SD and MD particles, SP particles have a much more steeply rising curve that saturates at relatively low magnetic fields with a completely reversible pathway and no hysteresis. Even a small proportion of SP particles can dominate the induced magnetization of a sample (Dunlop and Özdemir, 1997). SP particles are thermally activated; lowering the measurement temperature can enable detection of hysteresis as particles become magnetically stable.

Natural samples usually contain mixtures of magnetic minerals or mixtures of the same mineral with different grain size distributions. Complicated hysteresis loops shapes can occur, such as wasp-waisted (constricted middles) and potbellied loops (spreading middles and slouching shoulders) (Jackson et al., 1990; Roberts et al., 1995; Tauxe et al., 1996).

First-order reversal curve (FORC) diagrams

To measure a FORC, a sample should be saturated in a positive applied field, and, then, the applied field is decreased to a reversal value, B_a. A FORC is defined as the magnetization curve acquired when the applied field returns from B_a to the positive saturation field (Figure 2.5a). This measurement is repeated for different reversal fields to acquire a suite of FORCs (Figure 2.5b). The magnetization at the field B_b ($B_b > B_a$), which starts at a reversal field of B_a, is denoted by $M(B_a, B_b)$ (Figure 2.5a), and the FORC distribution is defined as the mixed second derivative:

$$\rho(B_a, B_b) = -\partial^2 M(B_a, B_b)/\partial B_a \partial B_b. \tag{2.25}$$

For convenience, the coordinates are changed from $\{B_a, B_b\}$ to $\{B_u, B_c\}$ (Figure 2.5c), where:

$$B_u = (B_a + B_b)/2, \text{ and} \tag{2.26}$$

$$B_c = (B_a - B_b)/2, \tag{2.27}$$

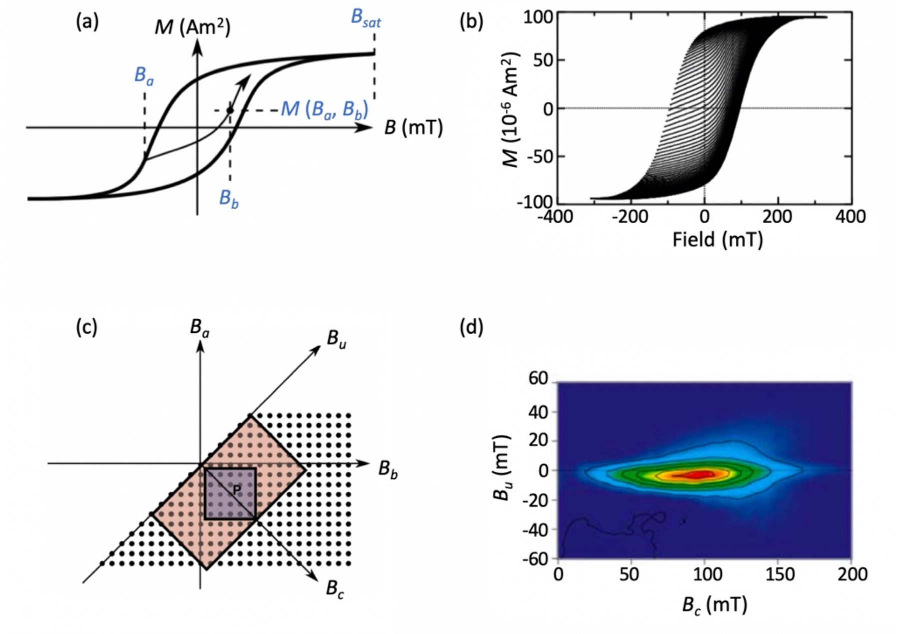

Figure 2.5 Illustrations of the FORC technique (modified from Harrison and Feinberg (2008)). (a) Definition of a FORC. (b) A set of FORCs from a single clinopyroxene that contains magnetite inclusions. (c) A $\{B_a, B_b\}$ plot with superimposed $\{B_u, B_c\}$ coordinate axes. (d) A FORC diagram derived from the FORCs shown in (b).

Therefore, a FORC diagram is a contour plot of a FORC distribution with B_u and B_c on the vertical and horizontal axes, respectively (Figure 2.5d). The behaviour of SD particles in a FORC diagram can be interpreted via the Preisach-Néel model (Preisach, 1935; Néel, 1955a). The vertical, B_i, and horizontal, B_c, axes of FORC diagrams indicate magnetostatic interactions and coercivity, respectively (Pike et al., 1999; Roberts et al., 2000). For non-interacting SD particles, such as magnetofossils in sediments, FORC diagrams have a ridge-like distribution along the B_c axis with little or no vertical spread (Pike et al., 1999; Egli et al., 2010) (Figure 2.6a). For interacting SD particles, FORC diagrams contain a dominant peak centered at the mean coercivity of the magnetic particles and have large vertical spread (Pike et al., 1999; Roberts et al., 2000) (Figure

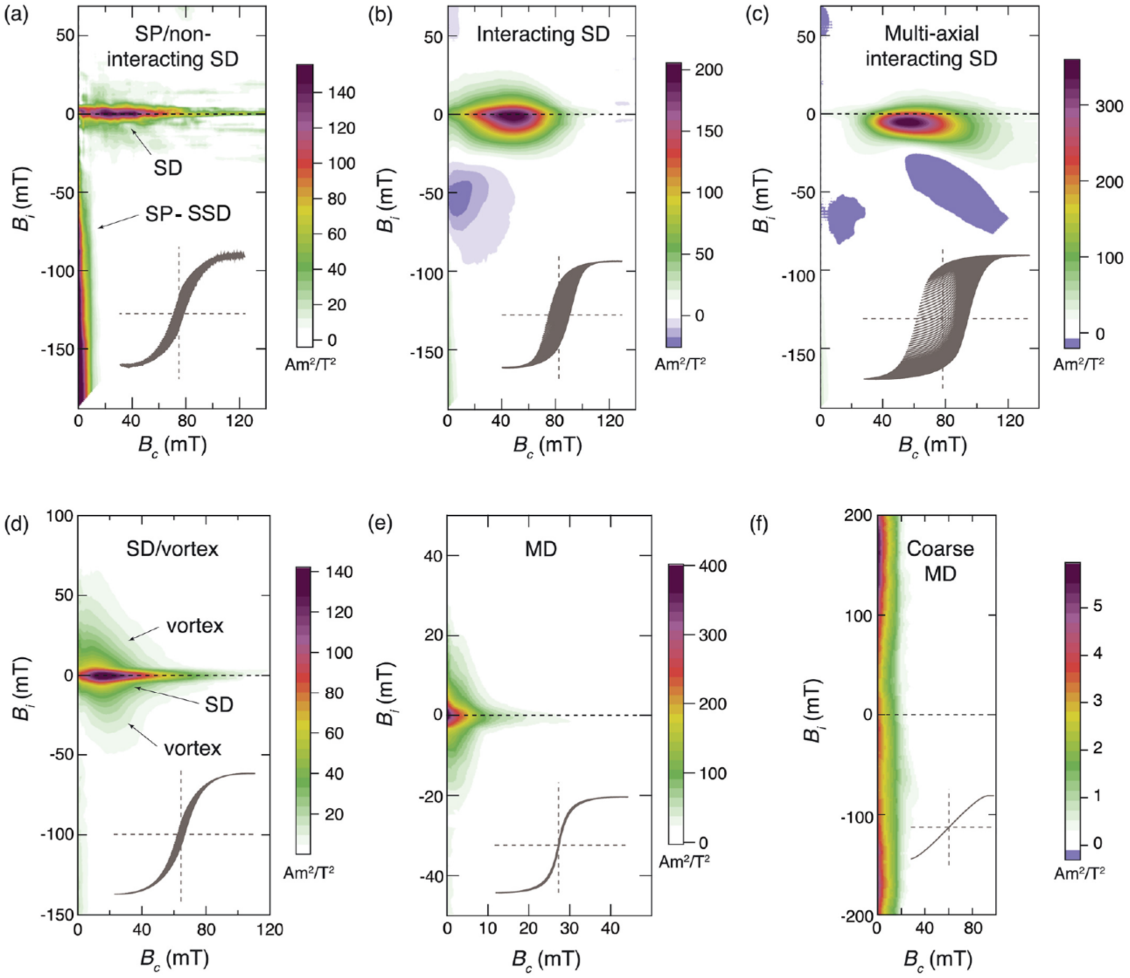

Figure 2.6 Representative FORC diagrams for magnetic particles with different domain states (modified from Roberts et al. (2018a)).

2.6b). Moreover, FORC diagrams can also provide information about magnetic anisotropy types. SD particles with uniaxial anisotropy have a negative peak along the B_i axis (Muxworthy et al., 2004; Newell, 2005) (Figure 2.6b). SD particles with cubic anisotropy have two negative peaks; one along the B_i axis and one below the main positive peak with elongation at -45°, respectively (Harrison and Lascu, 2014) (Figure 2.6c). In contrast to SD particles, magnetization reversal in MD particles is more complex, and includes domain wall pinning, nucleation and annihilation, and domain wall interactions, and thus the vertical B_i distribution of FORC diagrams reflects these processes rather than inter-particle interactions as is the case with SD particles (Pike et al., 2001a). In a classical one-dimensional domain wall pinning model (Néel, 1955b), FORC diagrams of MD particles have a vertical elongated peak with contours spreading near the origin, with the FORC distribution decreasing with increasing B_c (Pike et al., 2001a) (Figure 2.6f). However, geological samples are more complex and cannot be fully explained by this domain wall pinning model. FORC diagrams for geological MD particles have contours that diverge away from the origin (Roberts et al., 2000; Pike et al., 2001a) (Figure 2.6e). The behaviour of single-vortex particles is explained by vortex nucleation and annihilation (Pike and Fernandez, 1999); therefore, the vertical B_i axis of FORC diagrams reflects distributions of vortex nucleation and annihilation fields (Pike and Fernandez, 1999; Roberts et al., 2017). FORC diagrams for single-vortex particles are characterized by two peaks, and sometimes an additional butterfly structure is also present (Figure 2.7). The two peaks are in the upper and lower half planes, respectively, while the butterfly structure lies along the B_c axis and is composed of a circular negative region superimposed on an elongated horizontal positive region (Pike and Fernandez, 1999; Dumas et al., 2007; Roberts et al., 2014). FORC diagrams for multi-vortex particles have a broad and asymmetric central peak (Roberts et al., 2000, 2017; Muxworthy and Dunlop, 2002; Lascu et al., 2018) (Figure 2.6d). In principle, SP particles have no hysteresis and should make no contribution to FORC diagrams. However, FORC measurements are so rapid that particles with grain sizes near the SP-SSD boundary can produce slightly irreversible hysteresis loops due to thermal relaxation (Pike et al., 2001b). FORC diagrams for SP particles near the SP-SSD boundary generate a secondary peak centered about the origin as well as a nearly vertical distribution along the lower B_i axis (Pike et al., 2001b) (Figure 2.6a).

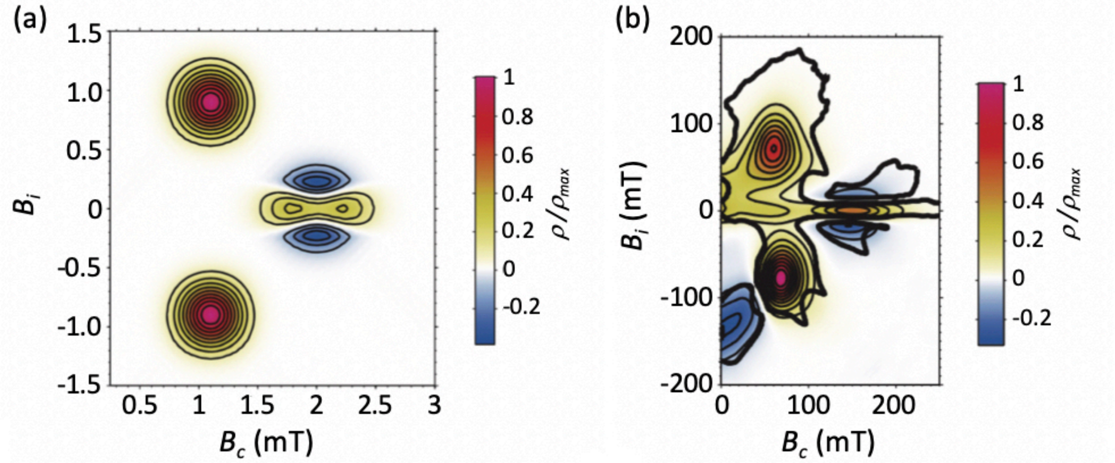

Figure 2.7 FORC diagrams for a single-vortex (a) model (Pike and Fernandez, 1999) and (b) synthetic samples (Dumas et al., 2007). This figure is modified from Roberts et al. (2014).

Apart from conventional FORC diagrams as discussed above, Zhao et al. (2017) further improved FORC measurements to produce additional FORC-like diagrams, including transient FORC, remanent FORC, and induced FORC diagrams. These FORC-like diagrams improve discrimination of magnetic signatures associated with each domain state, which benefits interpretation of complex magnetic mineral mixtures (Zhao et al., 2017; Hu et al., 2018).

Ratios of concentration-indicative parameters and bivariate diagrams

Magnetic particles with different grain sizes are controlled by different magnetization processes, so ratios of different concentration-indicative parameters can provide information on grain size, such as ARM/SIRM and χ_{ARM}/χ (e.g., Oldfield and Yu, 1994; Katz et al., 1998; W. Zhang et al., 2007; Xie et al., 2013; Irurzun et al., 2020). ARM increases in fine SD particles, while SIRM is relatively independent of size for coarse vortex state and MD particles. After excluding concentration effects, ARM/SIRM has a broadly inverse relationship with grain size, as is the case for χ_{ARM}/χ. However, the presence of SP particles will cause relatively high χ and low ARM values, which complicates interpretation (Liu et al., 2012).

Apart from parameter ratios, many bivariate diagrams have been proposed as indicators of magnetic grain size variations. The Day diagram, which divides magnetic domain states into SD, pseudo single domain, and MD zones based on the values of B_{cr}/B_c (coercivity of remanence, B_{cr}) and M_{rs}/M_s is the most widely used tool for inferring domain state in rock magnetism (Day et al., 1977). However, Roberts et al. (2018b) argued that the Day diagram is fundamentally ambiguous in discriminating domain state because its interpretation overlooks at least some of ten issues that contribute ambiguity, such as magnetic mineralogy, mineral stoichiometry, magnetic anisotropy, etc. Similarly, the Néel, Borradaile, and Fabian diagrams are based on hysteresis parameters and loop shapes (Néel, 1955b; Borradaile and Lagroix, 2000; Fabian, 2003), which do not provide sufficient information for domain state diagnosis except when a single magnetic component is present (Roberts et al., 2019). In contrast, the Lascu and Egli diagrams combine hysteresis parameters and ARM to identify domain state (Egli, 2004a; Lascu et al., 2010), and are more effective than the other methods discussed by Roberts et al. (2019).

Mathematical unmixing

The most widely used methods for identifying domain states involve mathematical unmixing of IRM acquisition/demagnetization curves and FORC diagrams. Unmixing of IRM acquisition/demagnetization curves can enable quantification of the coercivity distribution of magnetic particles. To measure an IRM acquisition curve, a sample is subjected to a stepwise increasing applied field and its remanent magnetization is measured after each applied field increase (Figure 2.8a). Robertson and France (1994) first observed that IRM acquisition curves can be fitted by a combination of cumulative log Gaussian (CLG) functions, and an individual CLG function can be expressed as:

$$IRM(B) = SIRM/DP(2\pi)^{1/2} \times \int_{-\infty}^{\infty} \exp\left[\left(\log(B) - \log\left(B_{1/2}\right)\right)^2/2(DP)^2\right] d(\log(B)). \tag{2.28}$$

At any given applied field, B, a CLG function can be characterized by three parameters: SIRM, $B_{1/2}$, and the dispersion parameter (DP). These parameters are used to describe the CLG function height, the applied field at which half of the SIRM is acquired, and the coercivity dispersion, respectively; the latter two parameters are independent of the magnetic mineral concentration (Robertson and France, 1994). When decomposing IRM acquisition/demagnetization curves, the SIRM, $B_{1/2}$, and DP are adjusted interactively to optimize curve-fitting. To obtain a robust interpretation, Kruiver et al. (2001) suggested that IRM acquisition curves should be analyzed with the linear acquisition, gradient of acquisition, and standardized acquisition plots simultaneously (Figure 2.8). An initial SIRM can be estimated easily from the linear acquisition plot, while the initial $B_{1/2}$ and

DP can be estimated from the gradient of acquisition plot. Therefore, the curve-fitting process is more straightforward. Considering that interactive minimization of pre-defined statistics is time-consuming, Heslop et al. (2002) facilitated curve fitting with an automated procedure based on the expectation-maximization algorithm (Dempster et al., 1977). However, geological samples and models often contain skewed coercivity distributions, which are inconsistent with the log Gaussian distribution (Robertson and France, 1994; Egli, 2003; Heslop et al., 2004). Therefore, an IRM unmixing method that employs skewed generalized Gaussian (SGG) distributions was developed, which is suitable for a broader family of coercivity distributions (Egli, 2003, 2004a, 2004b, 2004c). Furthermore, Heslop and Dillon (2007) developed a non-negative matrix factorization-based algorithm (Lee and Seung, 2001) to unmix sets of IRM curves. This algorithm can identify shapes and abundances of individual components based solely on data set variation and makes the unmixing process nonparametric (Heslop and Dillon, 2007).

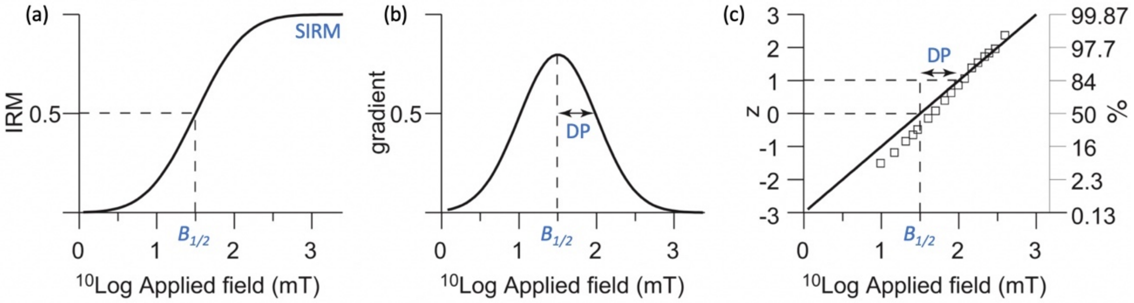

Figure 2.8 Illustrations of (a) an IRM acquisition curve, called a linear acquisition plot, (b) a gradient of acquisition plot, and (c) an IRM standardized acquisition plot (modified from Kruiver et al. (2001)).

Suites of FORC diagrams can be unmixed using principal component analysis (PCA) (Jolliffe, 2002). Lascu et al. (2015) introduced PCA to unmix quantitatively sets of FORC diagrams into linear combinations of end-member (EM) FORC diagrams. However, sum-normalized FORCs are only sensitive to the irreversible magnetization component and include subjective EM choice (Lascu et al., 2015). Harrison et al. (2018) developed an improved FORC-PCA algorithm that considers both reversible and irreversible contributions, and improved objectivity for EM selection.

2.2.4. Magnetic minerals

Iron is the fourth most abundant element in Earth's crust, and is a common element in rock-forming minerals (McDonough and Sun, 1995). Based on the degree of oxidation, magnetic minerals can be divided as iron oxides, oxyhydroxides, and sulphides. In this section, I introduce three common magnetic minerals that are important for the studies included here: magnetite, hematite, and greigite.

Magnetite

Magnetite is the most important magnetic mineral on Earth, and occurs commonly in sediments and rocks. Magnetite is a cubic mineral with an inverse spinel structure and lattice constant a = 8.396 Å (Gorter, 1954) (Figure 2.9). There are two important temperature-dependent magnetic transitions for magnetite. One is the T_C at 580 °C, when thermal energy overcomes the exchange interaction so that magnetite becomes paramagnetic at higher temperatures (Dunlop and Özdemir, 1997); the other is the Verwey transition (T_V) at 120 K, below which the crystal lattice of magnetite changes

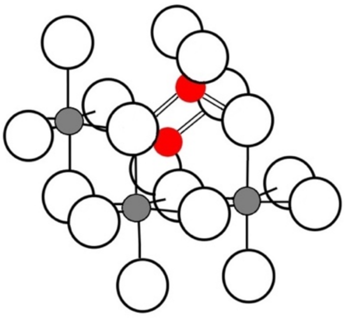

Figure 2.9 Ball-and-stick crystallographic model for magnetite. Red, grey, and white balls represent Fe^{3+}, Fe^{2+}, and O^{2-}, respectively (modified from Cornell and Schwertmann (2003)).

from cubic to monoclinic (Verwey, 1939). For equidimensional SD and MD particles, as the crystal lattice changes across T_V, the magnetic susceptibility and remanent magnetization also change abruptly because they are dominantly controlled by crystal anisotropy, which is the basis for low-temperature demagnetization. Other important magnetic properties of magnetite are summarized in Table 2.1.

Table 2.1 Magnetic and crystallographic properties of magnetite.

	Value	Reference
Saturation magnetization, M_s	92 Am^2/kg	Thompson and Oldfield (1986)
Saturation remanence, M_{rs}	10 Am^2/kg	Thompson and Oldfield (1986)
Susceptibility, χ	5.2-6.7 × 10^{-4} m^3/kg	Heider et al. (1996)
Easy axis of magnetization	<111>	
Magnetocrystalline anisotropy, K_1	-1.35 × 10^4 J/m^3	Dunlop and Özdemir (1997)
Magnetostriction constant, λ_s	35.8 × 10^{-6}	Dunlop and Özdemir (1997)
Crystal structure	Inverse spinel	Gorter (1954)
Lattice constant	$a = 8.396$ Å	Gorter (1954)
High-temperature transition	$T_c = 580$ °C	Dunlop and Özdemir (1997)
Low-temperature transition	$T_v = 120$ K	Verwey (1939)

Magnetite in nature can also have a biogenic origin (Bellini, 1963; Blakemore, 1975). Magnetotactic bacteria are a group of prokaryotes that can synthesize chain-aligned, nano-sized magnetite crystals (Bazylinski and Frankel, 2004). Biogenic magnetite is produced via biomineralization and has regular morphologies, such as octahedra, hexagonal prisms, and teardrop shapes (Figure 2.10). Recent studies suggest that biogenic magnetite morphology can be used to indicate past sedimentary oxygenation variations with teardrop-shaped magnetite preferentially found in less oxygenated environments (e.g., Usui et al., 2017; Yamazaki et al., 2019; Yamazaki, 2020). The T_V of biogenic magnetite can be suppressed to ~95 K (Moskowitz et al., 1993; Kosterov, 2003); which makes it useful as a diagnostic indicator to distinguish the origin of magnetite (e.g., Weiss et al., 2004; Pan et al., 2005; Chang et al., 2016a).

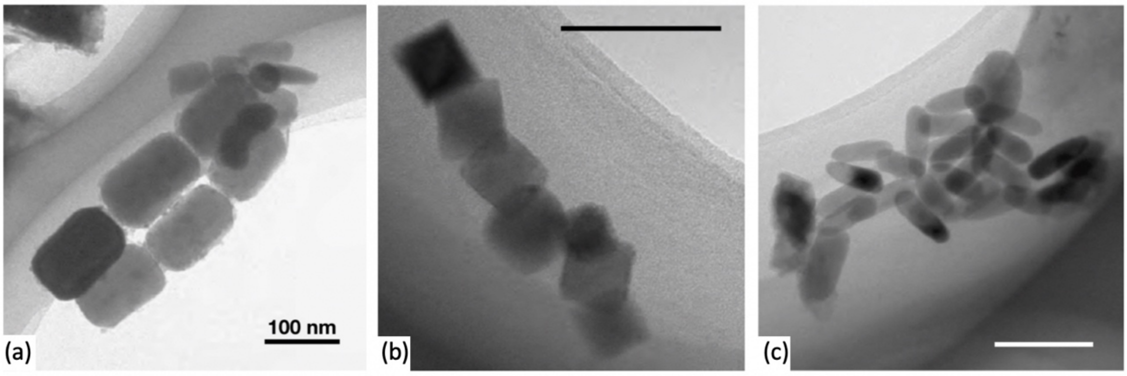

Figure 2.10 Transmission electron microscope images of biogenic magnetite with different morphologies from Yamazaki et al. (2019). (a) Hexagonal prisms, (b) octahedra, and (c) teardrop groups.

Hematite

Hematite is the most stable magnetic mineral in oxidizing environments. It is a hexagonal mineral with a corundum structure and lattice constant a = 5.038 Å and c = 13.772 Å (Pauling and Hendricks, 1925; Blake et al., 1966) (Figure 2.11); hematite can also be indexed in the rhombohedral structure and unit cell a = 5.427 Å and α = 55.3°. There are also two important temperature-dependent magnetic transitions for hematite. One is the Néel temperature (T_N) at ~675 °C (Dunlop and Özdemir, 1997), and the other is the Morin transition (T_M) at 250 K, where the magnetic moment for hematite changes from being parallel to the basal plane above T_M to perpendicular to the basal plane below T_M (Morin, 1950). Hematite is weakly magnetic with magnetization resulting from the spin-canted antiferromagnetism and an isotropic component that is called the defect moment. Spin-canted antiferromagnetism is lost across T_M while the defect moment persists (Dunlop and Özdemir, 1997). The coercivity of hematite ranges from ~1 mT (in large MD particles) to hundreds of mT (in SD particles); its high coercivity results from magnetoelastic anisotropy (Stacey, 1963). Other important magnetic properties of hematite are summarized in Table 2.2. Unlike the well-studied magnetite, there are still some important unknowns for hematite. For example, the upper SD threshold size has not been determined clearly for hematite. Banerjee (1971) suggested that the grain size of SD hematite ranges from 27.5 nm to 15 μm from his own magnetic experimental data and based on published data from Chevallier and Mathieu (1943). Dekkers and Linssen (1989) indicated an upper SD threshold size of 1.0-0.5 μm, and that annealing can shift the threshold to 2.1-1.0 μm due to decreased polycrystallinity in hematite. Other workers have proposed that the upper SD threshold in hematite may have a larger size range. For example, Eaton and Morrish (1969) indicated that synthetic hematite crystals can be in the SD state up to sizes of some hundreds of micrometers, and Kletetschka and Wasilewski (2002) argued for a threshold size of about 0.1 mm. Özdemir and Dunlop (2014) suggested from a broad compilation of B_c values for hematite that the proposed thresholds of 15 μm and 100 μm suggested by Banerjee (1971) and Kletetschka and Wasilewski (2002) are both questionable. They suggested that the SD to MD threshold size likely exceeds 15 μm, and that there is no strong evidence for such a threshold at ≈100 μm. The size at which this threshold occurs has been inferred from B_c data and

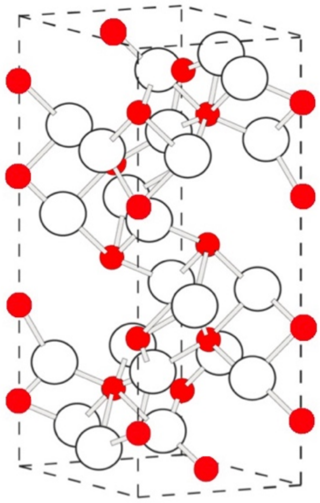

Figure 2.11 Ball-and-stick crystallographic model for hematite. Red and white balls represent Fe^{3+} and O^{2-}, respectively (modified from Cornell and Schwertmann (2003)).

remains an open question that needs to be constrained by direct domain observations (Özdemir and Dunlop, 2014). The fact that the upper threshold size for SSD behaviour occurs at such a large particle size compared to ferrimagnetic minerals indicates that most hematite in natural samples subjected to paleomagnetic analyses is likely to be in the SD state.

Table 2.2 Magnetic and crystallographic properties of hematite.

	Value	Reference
Saturation magnetization, M_s	0.4 Am^2/kg	de Boer and Dekkers (1998)
Saturation remanence, M_{rs}	0.2 Am^2/kg	Thompson and Oldfield (1986)
Susceptibility, χ	6×10^{-6} m^3/kg	Thompson and Oldfield (1986)
Easy axis of magnetization	(0001)	
Magnetocrystalline anisotropy, K_1	1.2×10^6 J/m^3 (c-axis)	Dunlop and Özdemir (1997)
Magnetostriction constant, λ_s	8×10^{-6}	Dunlop and Özdemir (1997)
Crystal structure	Rhombohedral	Pauling and Hendricks (1925)
Lattice constants	a = 5.038 Å, c = 13.772 Å	Blake et al. (1966)
High-temperature transition	T_N = 675 °C	Dunlop and Özdemir (1997)
Low-temperature transition	T_M = 250 K	Morin (1950)

Greigite

Greigite is an iron sulphide that forms under sulphidic redox conditions as a precursor to pyrite (Berner, 1970, 1984; Roberts and Turner, 1993; Roberts, 1995; Wilkin and Barnes, 1997; Benning et al., 2000). Greigite is a cubic mineral with an inverse spinel structure and lattice constant a = 9.872 Å (Skinner et al., 1964; Chang et al., 2008) (Figure 2.12). Unlike magnetite or hematite, greigite does not have a low-temperature magnetic transition, and the high-temperature magnetic properties are complex and irreversible. When heated in air, an inflection in thermomagnetic curves occurs between 200 °C and 300 °C and a secondary peak decays at ~580 °C, which corresponds to the thermal decomposition of greigite to form magnetite as a heating product (e.g., Krs et al., 1992; Roberts, 1995; Chang et al., 2008; Liu et al., 2014; Gai et al., 2020). Although the T_C of greigite has not been determined due to its thermal decomposition between 200 °C and 300 °C, Chang et al. (2008) suggested that it must exceed 350 °C based on results from a series of thermomagnetic cycles measured to progressively higher temperatures. Greigite can also acquire a gyroremanent magnetization (GRM) during AF demagnetization above 50 mT (e.g., Snowball, 1997; Rowan and Roberts, 2006; Fu et al., 2008; Liu et al., 2014; Gai et al., 2020), which can provide a diagnostic indicator for greigite identification although this behaviour is not always observed (Roberts et al., 2011). Other important magnetic properties of greigite are summarized in Table 2.3. In nature, greigite is identified widely as SD particles in lacustrine and marine sediments (e.g., Rowan and Roberts, 2006; Blanchet et al., 2009; Roberts et al., 2011; Reinholdsson et al., 2013; M. Li et al., 2018; Musgrave et al., 2019; Gai et al., 2020). Supplies of reactive iron, sulphate, and organic matter are required for the formation and preservation of greigite (Morse et al., 1987). Based on detailed scanning electron microscope observations, Roberts and Weaver (2005) suggested that sedimentary greigite can be transformed by at least five mechanisms with available reactants (i.e., iron and sulphur) during diagenesis. These mechanisms include neoformation of greigite on pyrite surfaces (Jiang et al., 2001), within detrital silicate sheets (Canfield et al., 1992), on authigenic clay mineral surfaces (Jiang et al., 2001), and greigite growths on siderite (Sagnotti et al., 2005) and gypsum

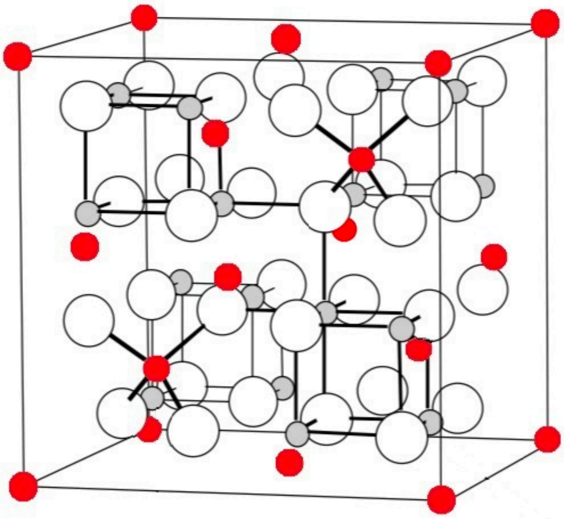

Figure 2.12 Ball-and-stick crystallographic model for greigite. Red, grey, and white balls are Fe^{3+}, Fe^{2+}, and S^{2-}, respectively (modified from García and Subías (2004)).

surfaces (Florindo et al., 2007) to produce late diagenetic magnetizations. Like magnetite, greigite can also be produced via biomineralization (Farina et al., 1990; Mann et al., 1990; Watson et al., 2000). However, identifying greigite magnetofossils is difficult due to their less regular crystal morphology compared to magnetite produced by magnetotactic becteria (Pósfai et al., 2001; Chang et al., 2014); extracelluar greigite occurs mainly in the magnetically unstable SP state and its geological significance is not well-understood (Watson et al., 2000; Roberts, 2015).

Table 2.3 Magnetic and crystallographic properties of greigite.

	Value	Reference
Saturation magnetization, M_s	67.16 Am^2/kg	Li et al. (2014)
Susceptibility, χ	3.2×10^{-4} m^3/kg	Roberts et al. (2011)
Easy axis of magnetization	<111> or <100>	Winklhofer et al. (2014)
Magnetocrystalline anisotropy, K_1	-23…-15 × 10^3 J/m^3 (<111>) 10-17 × 10^3 J/m^3 (<100>)	Winklhofer et al. (2014)
Crystal structure	Inverse spinel	Skinner et al. (1964)
Lattice constant	$a = 9.872$ Å	Chang et al. (2008)
High-temperature transition	$T_c > 350$ °C	Chang et al. (2008)

Magnetite and greigite are ferrimagnetic, while hematite is an imperfect antiferromagnetic mineral. Here, we have concentrated on relatively theoretical characteristics of magnetic minerals and their magnetic properties. Experimental procedures for determining magnetic parameters used in this thesis are described in Chapter 3, and their geochronological and geological applications in the SCS and NPO are discussed further in Chapters 4 to 6.

2.2.5 Diagenetic magnetic mineral alteration

Magnetic minerals are sensitive to diagenetic oxidation and reduction reactions, so that diagenetic modification of magnetic minerals in sediments can vary from subtle to pervasive (Roberts, 2015). As in shown in Figure 2.13, in a water or sedimentary column, electron acceptors react with organic matter is in the following order: oxygen, nitrate, manganese oxides, iron oxides, sulphate, and organic matter itself; the corresponding reaction products are: Mn^{2+}, Fe^{2+}, H_2S, and CH_4. According to the redox reaction sequence, diagenetic zones can be divided into oxic, suboxic, and anoxic zones, in which organic matter reacts with oxygen → nitrate → manganese oxides → iron → sulphate → methane, respectively. Meanwhile, dissolved Mn^{2+}, Fe^{2+}, H_2S, and CH_4 in pore water favours authigenic mineral formation. In terms of magnetic minerals, the order of authigenic formation in different diagenetic zones is indicated in Figure 2.13.

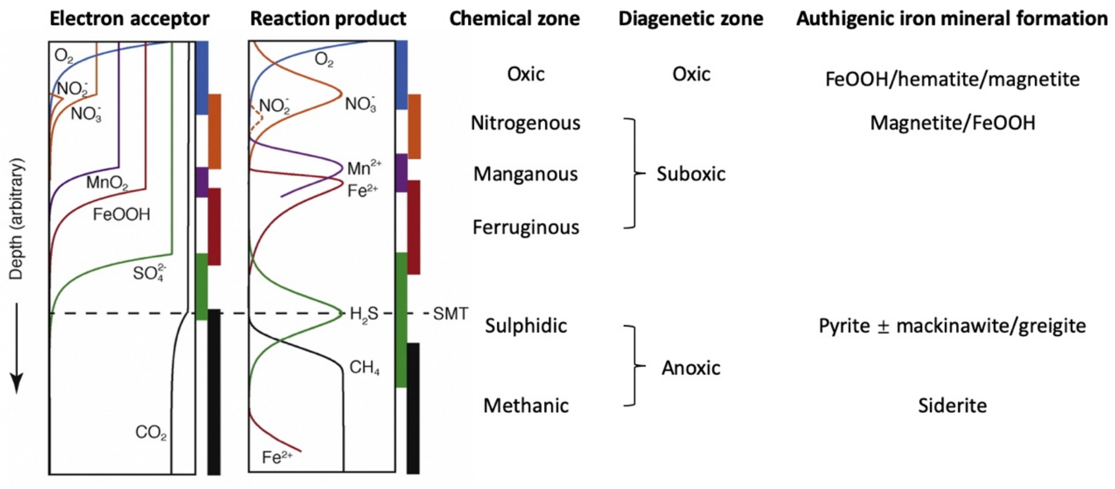

Figure 2.13 Sedimentary redox-driven diagenetic zones with respect to (arbitrary) depth (modified from Roberts, 2015). SMT = sulphate-methane transition.

Chapter 3

Materials and methods

In this chapter, characteristics of the studied cores and experimental procedures for this Ph.D. research are described. Experimental results and their interpretation are discussed in the subsequent three chapters.

3.1. The NPO

3.1.1. Core description

Sediment core NP02 (40.48° N, 150.10° E) is a 4.35-m gravity piston core that was recovered from the North Pacific abyssal plain at a water depth of 5,177 m, downwind of Asian dust source areas. The sediments were deposited below the CCD, which has led to poor foraminiferal preservation. Sediments are dominated by grey clay with occasional intercalated volcanic ash layers. For magnetic analyses, 208 cubic samples (8 cm^3) were taken continuously from the working half of core NP02. For trace element, rare earth element (REE), and clay mineral analyses, samples were selected at 4-cm stratigraphic intervals.

3.1.2. Magnetic measurements

Magnetic remanences were measured using a 2-G Enterprises Model 760R cryogenic magnetometer that is equipped with an in-line AF demagnetizer. The NRM was measured and was then AF demagnetized to a maximum peak field of 100 mT with logarithmically spaced field steps of 0.1-7.7 mT. ChRM inclinations were determined from the stepwise demagnetization data using the anchored PCA method (Kirschvink, 1980). Core NP02 is not oriented, therefore, the mean ChRM declination was calculated following Fisher (1953) and a common azimuthal rotation was applied to all samples to yield an adjusted mean declination of 0°. An ARM was imparted in a 100 mT peak AF with a 0.05 mT DC bias field, and was then AF demagnetized to a maximum peak field of 100 mT with a uniform step interval of 10 mT. An IRM was imparted in DC fields of 1 T, -0.1 T, and -0.3 T, which are defined as the SIRM, $IRM_{-0.1\ T}$, and $IRM_{-0.3\ T}$, respectively. The HIRM and L-ratio were calculated using equations (2.23) and (2.24), respectively.

Magnetic susceptibility and temperature-dependent magnetic susceptibility (χ-T, mass specific) curves for representative samples were measured at a frequency of 967 Hz using an AGICO MFK1-FA Kappabridge magnetic susceptibility meter. χ-T curves were measured in an argon atmosphere from room temperature to 700 °C.

IRM acquisition curves and FORCs were measured using a MicroMag Model 3900 vibrating sample magnetometer with a maximum 1 T applied field and 300 ms averaging time. IRM acquisition curves were acquired from 0 to 1 T in 100 steps with logarithmically spaced field steps and were then decomposed with the method of Robertson and France (1994). A total of 120 FORCs were measured for each sample, with B_u between -40 and 40 mT, B_c between 0 and 100 mT, and field spacing of approximately 1.6 mT. FORC diagrams were processed using the FORCinel software v3.05 (Harrison and Feinberg, 2008) with VARIFORC (Egli, 2013) smoothing parameters of $S_{c,0} = S_{b,0} = 6$ and $S_{c,1} = S_{b,1} = 9$.

3.1.3. Radiocarbon dating

Radiocarbon dating was performed with an accelerator mass spectrometer at Beta Analytic Inc. on selected planktonic foraminifera (*N. pachyderma* sinistral). The Marine13 curve (1σ range) was used for calibration (Reimer et al., 2013) with a reservior age (ΔR) correction of 400 ± 50 years based on Yoneda et al. (2007). Distributions of calibrated ages were analyzed using the Bayesian highest posterior density method of Lougheed and Obrochta (2016) to estimate calendar age ranges.

3.1.4. Trace element and REE analyses

Samples were freeze-dried, and were then digested with HNO_3-HF (1:1) in closed Teflon beakers to dissolve residual phases prior to geochemical measurements. Measurements were made on powder samples (0.05 g) using a Thermo Scientific XSERIES 2 inductively coupled plasma mass spectrometer (ICP-MS). Data were calibrated with the GSD-9 reference material.

3.1.5. Clay mineral analysis

Samples were treated with 15% H_2O_2 to remove organic matter, and were then treated with 5% HCl to remove carbonate. Particles with grain sizes less than 2 μm were extracted, concentrated, and smeared on glass slides. Analysis was performed using a Rigaku D/max 2500 diffractometer with CuKα radiation at 40 kV working voltage and 100 mA current intensity. Data were processed according to the description of Biscaye (1965). Clay mineral contents were estimated semi-quantitatively according to peak positions at 1.7 nm (smectite), 1 nm (illite), and 0.7 nm (kaolinite+chlorite). Relative contents of kaolinite and chlorite were discriminated based on the relative ratio of peak areas at 0.357 nm/0.354 nm.

3.1.6. Electron probe microanalysis

Volcanic glass shards, which were selected from tephra-containing samples, were treated with H_2O_2, and were subsequently mounted, ground, and polished to prepare for electron probe microanalysis. Major element compositions were measured using a JEOL JXA 8100 at 15 kV accelerating voltage. Electron beam diameters ranged from 5 to 10 μm, and the beam current was 6 nA. Na contents were determined first to minimize its mobilization effect. Overall, valid data were gained from 34 glass shards, which were normalized to an anhydrous basis (i.e., 100% total oxides).

3.2. The SCS

3.2.1. Core description

SCS samples are from Hole U1431D, which was drilled during IODP Expedition 349. Site U1431 is located in the central SCS, which is near the relict spreading ridge. Hole U1431D (15.38° N, 117.00° E; 4,240.5 m water depth) is the longest sedimentary sequence among the five holes drilled at this site. In total, 165.61 m and 236.50 m of sediment were recovered by advanced piston corer and extended core barrel corer, respectively. Sediments are composed of dark greenish grey clay, silty clay, silty sand, with occasional grey nannofossil oozes and volcanic ash layers (Li et al., 2015b). The upper 435 m of sediment have good recovery, and 991 cubic samples (8 cm^3) were sampled at 0.1-0.7 m intervals from core working halves. All samples were stored after sampling in a magnetically shielded environment.

3.2.2. Magnetic measurements

Magnetic susceptibility and anisotropy of magnetic susceptibility (AMS) were measured with a KLY-4S Kappabridge magnetic susceptibility meter. Magnetic susceptibility was normalized by sample mass and is expressed as χ. AMS is described by an ellipsoid with three orthogonal principal axes, which are defined as the maximum (K_1), intermediate (K_2), and minimum susceptibility axes (K_3), respectively.

Sample NRMs were measured using a 2-G Enterprises RAPID cryogenic magnetometer system equipped with an inline AF demagnetizer, and were then stepwise demagnetized to a maximum peak applied field of 100 mT with step intervals of 2.5-10 mT. ChRM directions were calculated with at least 5 successive demagnetization points using the PCA method of Kirschvink (1980). ARM and IRM were measured with a 2-G Enterprises Model 760R cryogenic magnetometer. An ARM was imparted in a 100 mT peak AF with a 0.05 mT DC bias field, which was then normalized by the DC field to give the ARM susceptibility (χ_{ARM}). An IRM was imparted in a 1 T DC field, which is defined as the SIRM.

Hysteresis loops, IRM acquisition curves, and FORCs were measured using a MicroMag Model 3900 vibrating sample magnetometer at applied fields between +1 T and -1 T with 300 ms averaging time. Hysteresis parameters and IRM acquisition curve measurements were conducted on every fourth sample. M_s, M_{rs}, and B_c were derived from hysteresis loops, and B_{cr} was acquired from backfield demagnetization curves. IRM acquisition curves were acquired with a maximum peak field of 1 T in 100 steps with logarithmically spaced field steps and were then decomposed into different magnetic mineral components following Robertson and France (1994). A total of 100 FORCs were measured for each sample, with B_u between -50 and 50 mT, B_c between 0 and 120 mT, and field spacing of approximately 3.2 mT. FORC diagrams were processed using the FORCinel software v1.19 with conventional FORC processing of Pike et al. (1999) using a smoothing factor of 5 (Harrison and Feinberg, 2008).

χ-T curves and stepwise thermal demagnetization of three-axis IRMs were measured for representative samples. χ-T curves were measured using an AGICO MFK1-FA Kappabridge equipped with a CS-3 furnace in an argon atmosphere with temperatures ranging from room temperature to 700 °C. Stepwise thermal demagnetization of three-axis IRMs was measured to characterize magnetic minerals with different coercivities (Lowrie, 1990). High-, medium-, and low- coercivity IRM fractions were imparted along three orthogonal sample axes with DC fields of 2.7 T, 0.5 T, and 0.05 T, respectively, and was then demagnetized thermally using a MMTDSC furnace with step intervals of 10-50 °C, and measured using a 2-G Enterprises Model 760R cryogenic magnetometer.

3.2.3. Diffuse reflectance spectroscopy (DRS) measurements

DRS measurements were conducted at wavelengths from 200 to 2000 nm in 0.5 nm steps at a scan rate of 250 nm/min on every second sample using a Cary 5000 UV-vis-IR spectrophotometer equipped with a $BaSO_4$-coated integrating sphere. According to the general theory of diffuse reflection developed by Kubelka (1948), if a sample is too thick to influence reflectance, the reflectance (R_∞) can be given by:

$$F(R_\infty) = (1 - R_\infty)^2/2R_\infty = K/S, \tag{3.1}$$

where K and S are the absorption and scattering coefficients of the sample, respectively, and $F(R_\infty)$ is called the remission of the Kubelka-Munk (K-M) function. DRS data were transformed into the K-M function, and the characteristic bands of hematite (Hm) and goethite (Gt) are indicated by second-derivative minima at ~535 nm and ~425 nm, respectively. Given that the amplitudes of hematite and goethite bands are proportional to their concentrations (Liu et al., 2011; Jiang et al., 2013), respectively, the relative concentrations of hematite and goethite in this thesis are estimated as I_{535}/I_{425}.

3.2.4. Time series analysis

Power spectra and evolutionary spectrograms of χ were obtained using the Acycle software v2.1 (Li et al., 2019), with a 4π multi-taper method and a Fast Fourier transform method, respectively (Thomson, 1982; Kodama and Hinnov, 2014). A cross-spectrum between χ and the LR04 $\delta^{18}O$ record (Lisiecki and Raymo, 2005) was obtained with the AnalySeries software v2.0 using a Blackman-Tukey algorithm with a Bartlett window (Paillard et al., 1996).

Chapter 4

East Asian monsoon evolution since the late Miocene from the South China Sea

This chapter was published in *Earth and Planetary Science Letters*, Volume 530, Paper 115960, Gai, C., Liu, Q., Roberts, A.P., Chou, Y., Zhao, X., Jiang, Z., Liu, J., 2020. East Asian monsoon evolution since the late Miocene from the South China Sea, doi: 10.1016/j.epsl.2019.115960.

Abstract The SCS has become a global focus for paleoclimatic and paleoceanographic studies due to its location, which makes it highly sensitive to the East Asian monsoon and to Pacific Ocean changes. We present here a refined magnetostratigraphy for the last 6.5 Ma for Hole U1431D, which was recovered during IODP Expedition 349 in the central SCS. Magnetic analyses demonstrate that magnetite is the dominant magnetic carrier except for within a greigite-bearing layer at 130.5-132.0 metres below sea floor. The greigite layer coincides with the timing of intensification of northern hemisphere glaciation and records an oceanographic response to this event. Environmental magnetic results indicate that the East Asian summer and winter monsoon were stable from 6.5 to 5 Ma. The summer monsoon intensified at 5 Ma, and then weakened gradually since 3.8 Ma. In contrast, the winter monsoon weakened at 5 Ma, and has then been enhanced since 3.8 Ma and more stable from 0.6 Ma. Spectral analysis indicates that the East Asian summer monsoon was driven directly by low-latitude insolation changes before ~3.2 Ma, and that it has been affected by both low-latitude insolation and high-latitude ice volume changes since ~3.2 Ma.

4.1. Introduction

The SCS, which is located at the junction of the Eurasian, Pacific, and Indo-Australian plates, is the largest marginal sea of the western Pacific Ocean (Li et al., 2014). The location of the SCS within the East Asian monsoon region makes it highly sensitive to changes in atmospheric-marine processes, terrigenous inputs (e.g., Webster, 1994; Tamburini et al., 2003; Liu et al., 2016), and water exchange with the Pacific Ocean through Luzon Strait (e.g., Wyrtki, 1961; Qu, 2000; Ludmann et al., 2005; Qu et al., 2006;

Tian et al., 2006). These factors have contributed to the SCS becoming a global focus in ocean-climate studies. Over the past two decades, at least 19 international research cruises and >2,000 exploratory boreholes have been drilled in the SCS (Wang et al., 2014a). A 33-Ma stratigraphic sequence recovered at ODP Site 1148 on the northern SCS slope provides the longest record for studies of paleoceanographic evolution and variations of orbital-forcing over periods ranging from 10^4 yr to 10^5 – 10^6 yr (Li et al., 2006; Tian et al., 2008). Long-term 400-500 ka $\delta^{13}C$ variations indicate major global ocean carbon reservoir reorganizations (P. Wang et al., 2003a, 2003b; Wang et al., 2004, 2010). East Asian monsoonal climates have been studied systematically at different scales, including at centennial-, millennial-, orbital-, and tectonic-scales (e.g., Wang et al., 1999; Higginson et al., 2003; Liu et al., 2003; M. Li et al., 2018), and the East Asian monsoon has been found to have a multi-stage history (Clift et al., 2002; Wehausen and Brumsack, 2002; Jian et al., 2003; Wan et al., 2007; Tian et al., 2011).

Precise age models are a prerequisite for robust determination of event sequences in geological history. Paleomagnetism is a commonly used and effective method for achieving this goal in marine sediments (e.g., Channell et al., 2013; Liu et al., 2014), including in the SCS. For example, Wang et al. (1993) reported that sedimentation rates decreased as water-depth deepened based on paleomagnetic analysis of three cores near the Nansha Islands. Based on oxygen isotopes and magnetostratigraphy, Kissel et al. (2003) revealed a pattern of low/high magnetic mineral contents and coarser/finer magnetic grain-size that coincided with cold/warm periods. Yang et al. (2009) presented a geomagnetic relative paleointensity record from two piston cores in Xisha Trough that suggests a pattern similar to that observed by Kissel et al. (2003) for the past ~85 ka. Wu et al. (2014, 2017) established new magnetostratigraphic frameworks for ODP sites 1148 and 1143 to provide records for precise global correlations back to 23 Ma and 4.6 Ma, respectively.

Most of these previous studies were restricted to the continental shelf and slope. Records of long and older SCS sedimentary sequences are less abundant, which limits understanding of long-term regional paleoenvironmental evolution, SCS formation mechanisms, and East Asian tectonic history (Li et al., 2014). Five sites in the deep SCS basin were drilled during IODP Expedition 349 to address such questions. In particular, Hole U1431D recovered the longest sediment sequence from this expedition, with a geological record since the late Miocene (Li et al., 2015b). The long and continuous sequence provides an opportunity to study multi-stage East Asian monsoon and paleoclimate variations in relation to orbital configurations. In this study, we construct a magnetic polarity stratigraphy for Hole U1431D and identify magnetic mineral variations that provide new insights into long-term East Asian monsoon evolution.

4.2. Sampling and methods

4.2.1. Core description and sampling

Site U1431 is located in the east sub-basin of the SCS near the relict spreading ridge with the youngest marine magnetic anomalies and is surrounded by seamounts and abyssal highs (Figure 4.1). Hole U1431D is the longest among the five holes drilled at this site, and is located at 15°22.54′ N, 117°00.01′ E (4,240.46 m water depth). Overall, 402.11 m of core was recovered from a 617.0 m interval (65.2% recovery), with 165.61 m of sediment recovered in 19 advanced piston corer (APC) cores at the top of the hole (98.1% recovery); 236.50 m of sediment was recovered over a 448.1 m interval from 48 extended core barrel (XCB) cores from the lower part of the hole (52.8% recovery). The sediments are dominated by clay, clayey silt, and silty sand, with occasional nannofossil ooze or volcanic ash (Li et al., 2015b).

Overall, 991 cubic samples (8 cm^3) were taken from the working halves of cores from the upper 435 m of the sequence for paleomagnetic and rock magnetic analysis at ~0.1-0.7 m sampling intervals. All samples were stored in a low magnetic field environment to minimize viscous remanent magnetization acquisition.

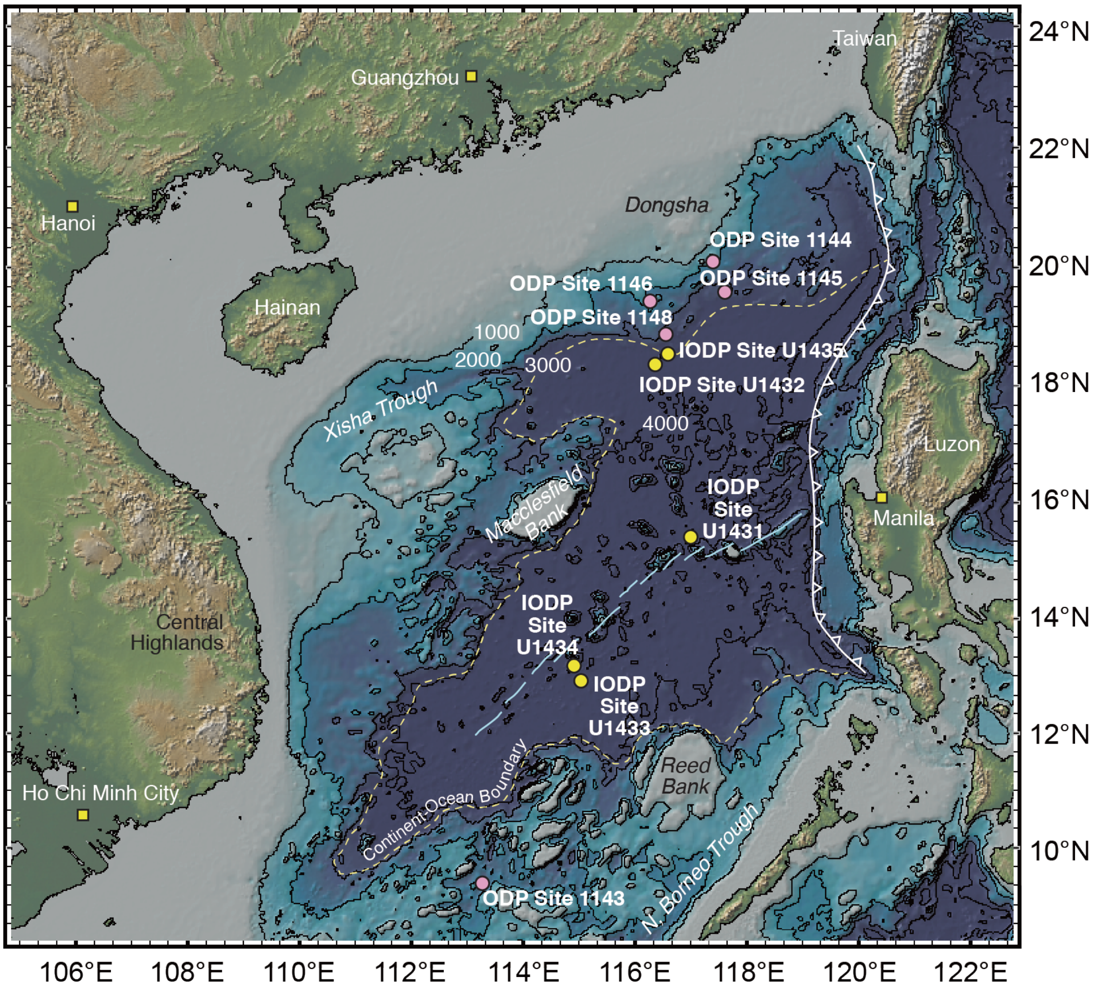

Figure 4.1 Schematic map of the SCS (modified from Li et al. (2015)). IODP sites from Expedition 349 (yellow dots) and from ODP Leg 184 (pink dots) are indicated. The yellow dashed line is the inferred continent/ocean boundary, the blue dashed lines are the fossil SCS spreading center, and the white line with teeth represents the present-day subduction plate boundary.

4.2.2. Methods

χ (mass-specific) and AMS were measured for all cubic samples using a Kappabridge KLY-4S system (1 × 10^{-8} SI sensitivity, AGICO Ltd., Brno, Czech Republic). AMS is a susceptibility ellipsoid with three orthogonal principal axes (maximum, intermediate, and minimum susceptibility axes, i.e., K_1, K_2, and K_3, respectively). Lineation ($L = K_1/K_2$) and foliation ($F = K_2/K_3$) are the AMS parameters discussed here (Tarling and Hrouda, 1993).

The NRM of all samples was measured followed by stepwise AF demagnetization up to peak applied fields of 100 mT, which were increased in 2.5-10 mT intervals using a 2-G Enterprises RAPID cryogenic magnetometer with inline AF demagnetization system. ChRM directions were determined by principal component analysis (Kirschvink, 1980) with at least 5 successive demagnetization points that define vectors directed to the origin of orthogonal vector component plots (Zijderveld, 1967). Samples with maximum angular deviation (MAD) values >15° were excluded.

Rock magnetic measurements were made on the paleomagnetic samples. An ARM was acquired in a 100-mT peak AF with 0.05 mT DC bias field, which is normalized by the DC field to give the ARM susceptibility (χ_{ARM}). An IRM was induced in 1 T DC field, which is defined as the SIRM. ARM and IRM were measured on a 2-G Enterprises Model 760R cryogenic magnetometer with in-line AF demagnetizer. Stepwise thermal demagnetization of an IRM imparted to three orthogonal sample axes with DC fields of 2.7 T, 0.5 T, and 0.05 T (Lowrie, 1990) was carried out with a MMTDSC furnace, with IRM measurements on the 2-G Enterprises Model 760R magnetometer. Temperature steps of 25-50 °C were used below 500 °C and 10 °C steps were used from 500 to 680 °C.

Every fourth sample was subjected to hysteresis loop and IRM acquisition analysis, and representative samples were subjected to FORC measurements (Pike et al., 1999) using a MicroMag Model 3900 vibrating sample magnetometer. The magnetic field was applied between +1 T and –1 T. M_s, M_{rs}, and B_c were obtained from hysteresis loops, and B_{cr} was obtained from backfield demagnetization curves. IRM acquisition curves were measured in non-linear field steps to 1 T and were decomposed into magnetic components following Robertson and France (1994). FORC diagrams were processed using the FORCinel software v. 1.19 (Harrison and Feinberg, 2008) with a smoothing factor of 5. χ-T (mass specific) curves were acquired in an argon atmosphere at a 976 Hz frequency from room temperature to 700 °C, using an AGICO Kappabridge MFK1-FA system equipped with a CS-3 furnace. DRS measurements were made on every second sample with a Cary 5000 UV–vis–IR spectrophotometer equipped with a $BaSO_4$-coated integrating sphere. The second derivative of the Kubelka-Munk (K-M) remission function spectrum is used to describe goethite (Gt) and hematite (Hm) concentrations at the 425 nm (I_{425}) and 535 nm (I_{535}) band intensities, respectively (Scheinost et al., 1998). Hm/Gt is given by: Hm/Gt = I_{535}/I_{425}.

4.3. Results

4.3.1. AMS

For most samples, K_3 axes are nearly perpendicular to the bedding plane (Figure 4.2a). K_3 inclinations for 94% of samples are > 60° (Figure 4.2b). In a Flinn Diagram (Flinn, 1962), the foliation for ~96% of samples exceeds the lineation (Figure 4.2c), which indicates that AMS ellipsoids are dominantly oblate, as expected for undisturbed sedimentary fabrics. Samples with K_3 inclinations < 60° or with prolate AMS ellipsoids were excluded from our paleomagnetic analysis because the horizons sampled may have been disturbed by coring and/or by turbidites.

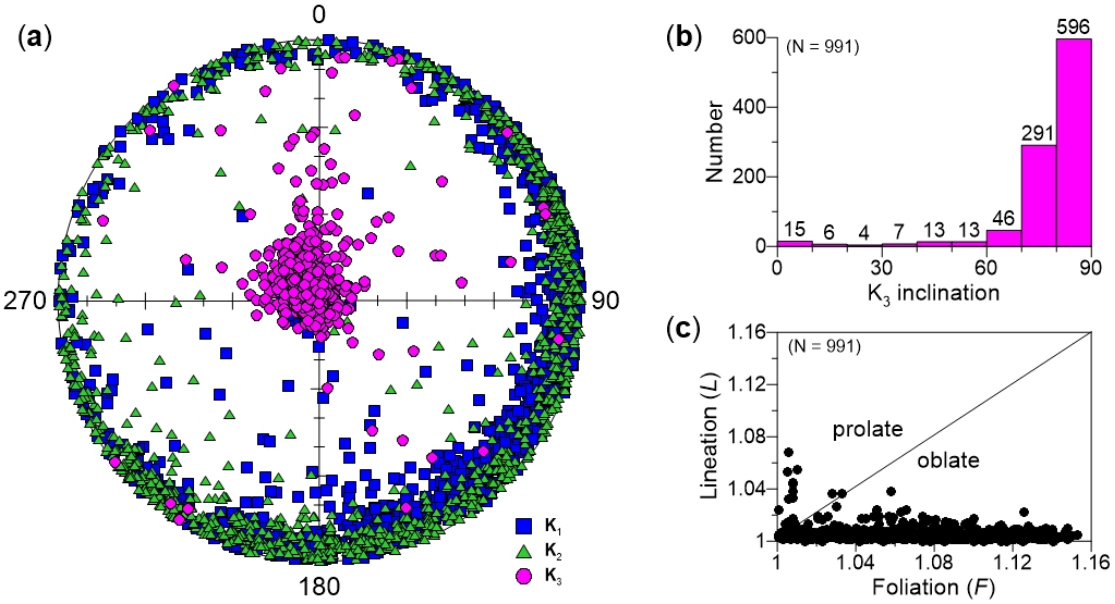

Figure 4.2 Anisotropy of magnetic susceptibility (AMS) data for sediments from Hole U1431D. (a) Projection of maximum (K_1), intermediate (K_2), and minimum (K_3) susceptibility axes; (b) distribution of K_3 inclinations; and (c) a Flinn (1962) diagram.

4.3.2. Paleomagnetic results

Typical AF demagnetization results are shown in Figure 4.3. For APC-cores in the upper 168.87 metres below seafloor (mbsf), nearly vertical drilling-induced magnetizations are removed effectively in nearly all samples to 15 mT. For XCB-cored samples below 168.87 mbsf, drilling-induced overprints for some samples cannot be removed completely even at 100 mT (Figures 4.3k and 4.3l). ChRMs are identified by components that are directed toward the origin of demagnetization diagrams, with near-complete demagnetization at 100 mT. Samples from the 130.5 to 132.0 mbsf depth interval acquire an obvious GRM above 50 mT (Figures 4.3i and 4.3j), with high

ΔGRM/ΔNRM values up to 2.25 (Fu et al., 2008) (Figure 4.4b), which are consistent with the behaviour of SSD greigite (Roberts et al., 2011).

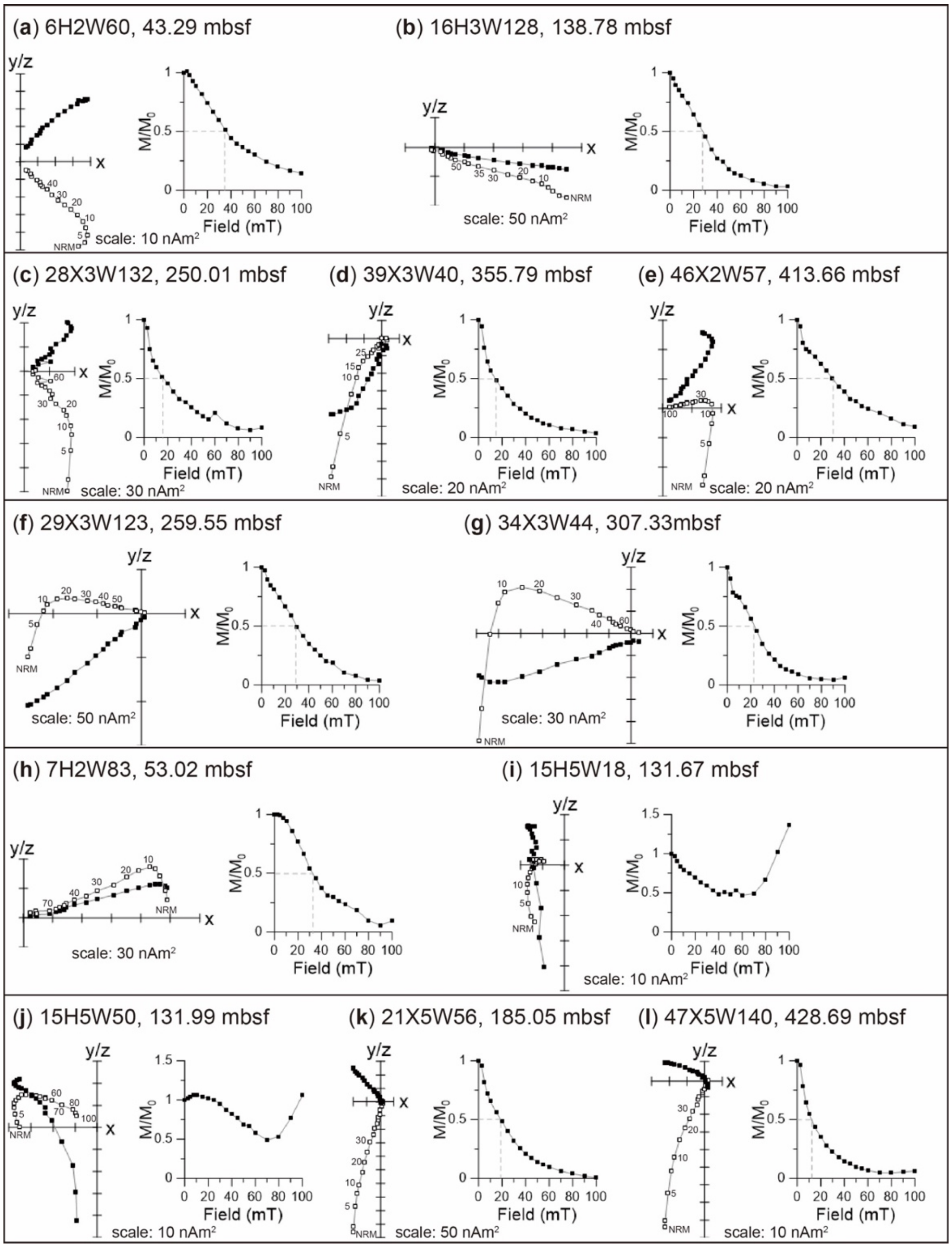

Figure 4.3 Representative orthogonal projections of AF demagnetization data for sediments from Hole U1431D (left) (Zijderveld, 1967) and remanence decay curves (right). Samples in (a-d) have normal polarity; those in (e-h) have reversed polarity; those in (i-j) acquired a gyroremanent magnetization; and those in (k-l) are affected by drilling-induced overprints that cannot be removed even at 100 mT. Solid (open) circles represent projections of the magnetization vector end-point onto horizontal (vertical) planes. Dashed lines in the remanence decay curves denote the median destructive field.

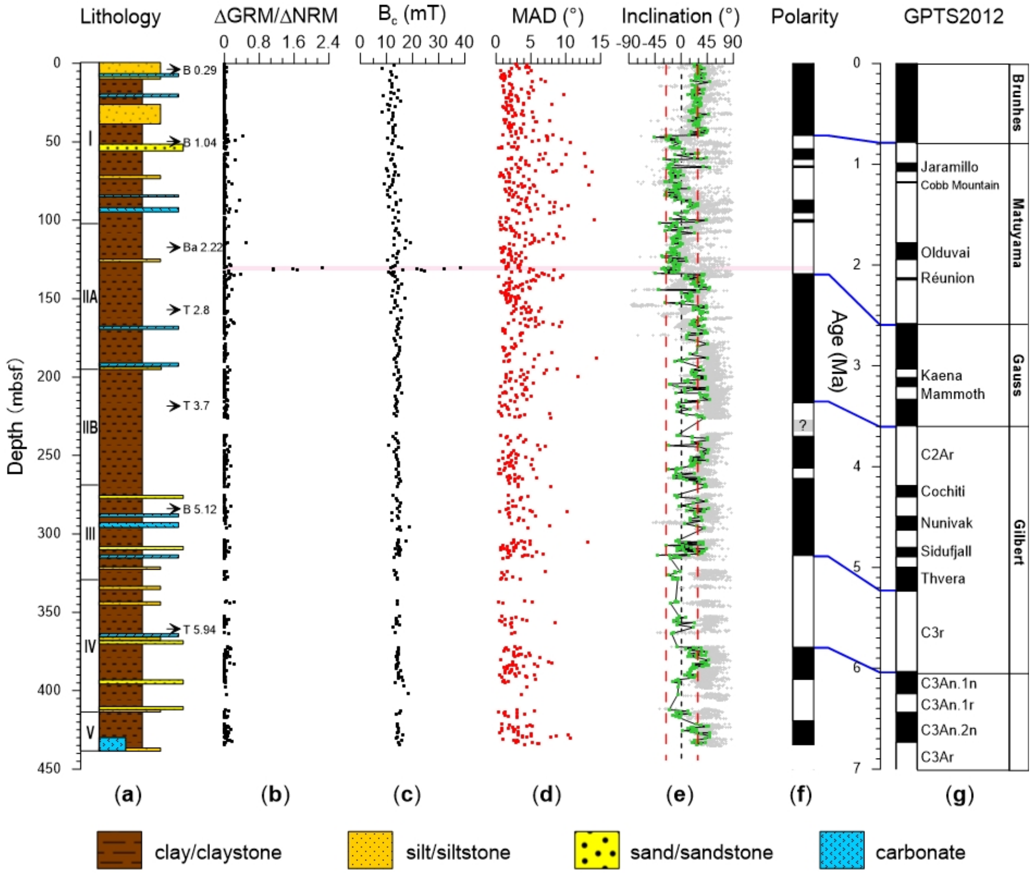

Figure 4.4 Magnetostratigraphy of Hole U1431D. (a) Sediment lithology (modified from Li et al. (2015)) and ages of representative calcareous nannofossil events. T = top/last appearance datum, B = base/first appearance datum, Ba = base acme; (b) ΔGRM/ΔNRM; (c) B_c; (d) MAD; (e) ChRM inclinations (green) and inclinations from shipboard 20 mT demagnetization (grey). Black and white intervals of (f) polarity and (g) geomagnetic polarity time scale (GPTS) (from Gradstein et al. (2012)), where black (white) intervals are normal (reversed) polarities. The grey interval indicates uncertain polarity. Red dashed lines in (e) denote the expected inclinations for a geocentric axial dipole field at the site latitude. Pink shading indicates the greigite-bearing layer.

Inclinations that are much steeper than the expected GAD value for this site (~±29°) (Li et al., 2015b) are associated either with samples within disturbed or turbiditic horizons with shallow K_3 inclinations, or with those affected by strong near-vertical drilling-induced overprints. Apart from this, positive inclination values vary more or less around the expected GAD inclination. In contrast, negative inclinations are much shallower than the expected value. This phenomenon has been observed in other SCS ODP/IODP cores (e.g., Kissel et al., 2003; Wu et al., 2014, 2017; Zhang et al., 2019); it is likely that the drilling-induced overprint has not been removed completely, but this does not affect the overall magnetostratigraphic pattern, which is further constrained by the biostratigraphy. Overall, samples with K_3 inclinations < 60°, inclinations > 50°, and/or MAD >10° were rejected. The SCS has been tectonically stable since ~15 Ma (Li et al., 2014), so positive (downward-directed) inclinations are interpreted to represent normal polarity, and *vice versa*.

4.3.3. Rock magnetic results

χ-T curves and stepwise thermal demagnetization of three-axis IRMs are used to characterize magnetic minerals (e.g., Lowrie, 1990; Hrouda, 1994). All measured χ-T heating curves decrease steeply to near-zero values at ~585 °C (Figures 4.5a$_1$-4.5a$_4$), which corresponds to the Curie temperature of magnetite (Dunlop and Özdemir, 1997). χ-T cooling curves have large magnetic susceptibility enhancements during heating, which indicate heating-induced ferrimagnetic mineral neoformation (Liu et al., 2005a). In Figure 4.5a$_1$, the heating curve continues to decrease above 585 °C, and finally reaches near-zero values at ~670 °C, which indicates the presence of hematite. A distinct χ increase at ~350 °C is evident in some heating curves (Figures 4.5a$_2$ and 4.5a$_3$), which suggests neoformation of strongly ferrimagnetic minerals that transformed from pyrite to magnetite (e.g., Passier et al., 2001). The low-coercivity component in stepwise thermal demagnetization of three-axis IRMs for selected samples has a maximum unblocking temperature of ~585 °C, which is indicative of magnetite (Figures 4.5b$_1$-4.5b$_4$). In the high-GRM layer, the intermediate-coercivity component decreases sharply below 350 °C

(Figures 4.5b$_2$ and 4.5b$_3$), which is indicative of greigite (Roberts, 1995; Roberts et al., 2011; Chang et al., 2008, 2014).

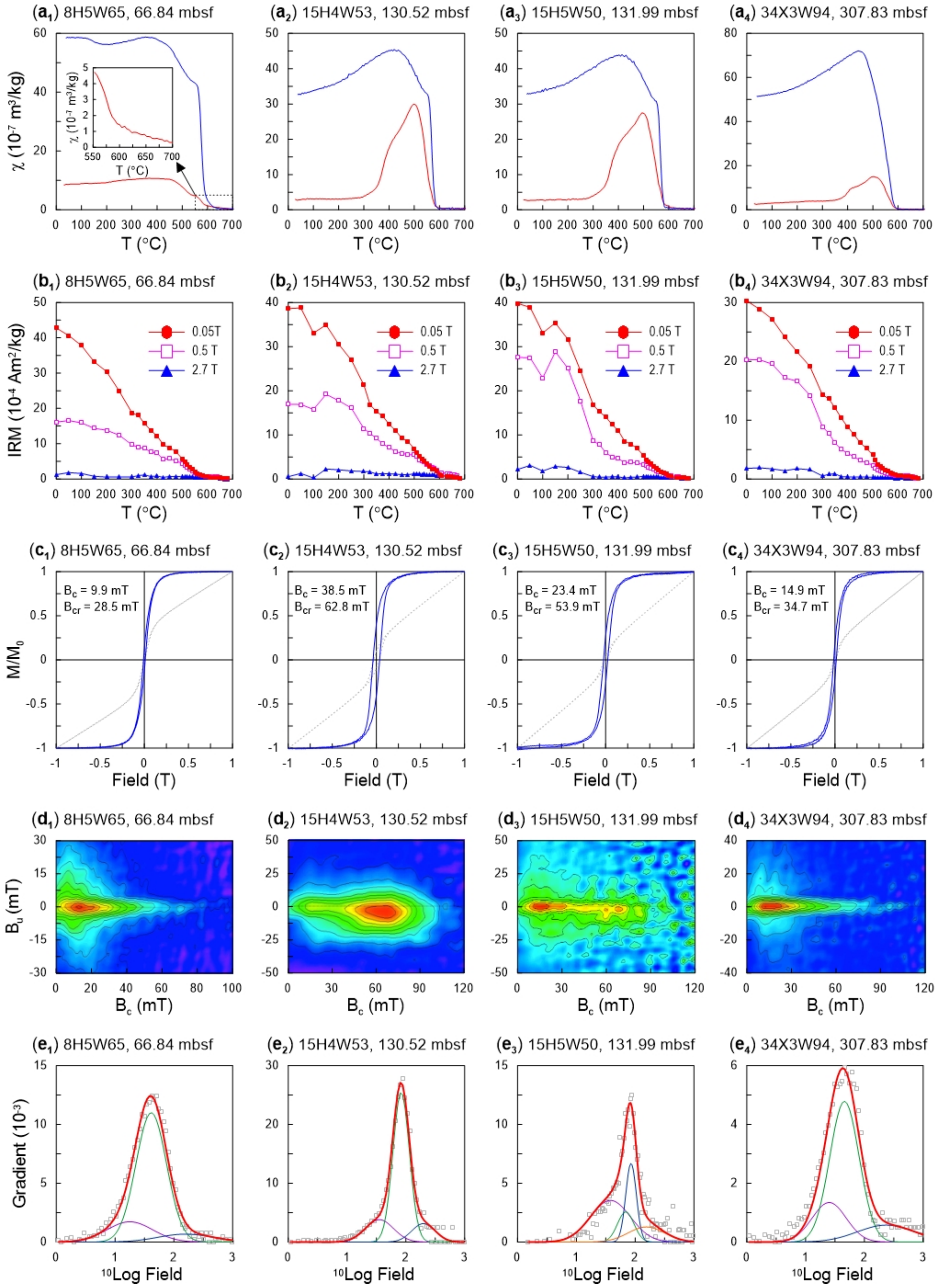

Figure 4.5 Magnetic properties of typical samples from Hole U1431D. (a$_1$-a$_4$) Temperature dependence of magnetic susceptibility (χ-T) curves, red (blue) lines are heating (cooling) curves; (b$_1$-b$_4$) thermal demagnetization of a three-component IRM; (c$_1$-c$_4$) hysteresis loops; (d$_1$-d$_4$) first-order reversal curve (FORC) diagrams (smoothing factor = 5); (e$_1$-e$_4$) IRM acquisition curve decomposition (purple, green, dark blue, orange, and red curves are for components 1, 2, 3, 4, and the sum of components, respectively).

Hysteresis parameters and FORC diagrams generally provide information about bulk magnetic properties and contributions from different components in magnetic mineral assemblages, respectively (Day et al., 1977; Roberts et al., 2000). In general, hysteresis loops are closed below 0.5 T (Figure $4.5c_1$), which indicates a dominance of low-coercivity magnetic minerals. FORC diagrams for many samples have a peak at ~17 mT, with horizontally elongated inner contours with small vertical spread, which indicate the presence of SD particles, while diverging outer contours indicate vortex state particles (Muxworthy and Dunlop, 2002; Roberts et al., 2017; Lascu et al., 2018) (Figure $4.5d_1$). In the high-GRM layer, B_c values (21.6-38.5 mT) are higher than in other layers (Figures 4.4c, $4.5c_2$, and $4.5c_3$). The respective FORC diagrams (Figures $4.5d_2$ and $4.5d_3$) have concentric contours that are shifted to negative interaction fields with a coercivity peak at 60-70 mT, which is indicative of SD greigite (Roberts et al., 2006, 2011). The peak at ~15 mT in Figure $4.5d_3$ indicates the existence of low-coercivity minerals such as SD magnetite. Some samples have weakly wasp-waisted hysteresis loops (Figure $4.5c_4$), which indicate the coexistence of at least two magnetic components with strongly contrasting B_c (Roberts et al., 1995). The respective FORC diagram indicates that the two components are low-coercivity SD magnetite with a B_c peak at ~20 mT and high-coercivity hematite with contours that extend to 90-110 mT, respectively (Figure $4.5d_4$). IRM acquisition curve decomposition is useful for discriminating magnetic phases with different coercivities (Kruiver et al., 2001; Heslop et al., 2002). Three components are identified in most samples (Figures $4.5e_1$, $4.5e_4$, and Table 4.1). Components 1 ($B_{1/2}$ ~17.8-25.1 mT, DP = 0.29-0.39) and 2 ($B_{1/2}$ ~35.5-45.7 mT, DP = 0.25-0.34) dominate with >85% total contributions. We infer that the two low coercivity components are due to magnetite in different domain states. Component 3 ($B_{1/2}$ ~158.5-234.4 mT, DP = 0.47-0.49) appears to be hematite. In the high-GRM layers (Figures $4.5e_2$, $4.5e_3$, and Table

4.1), low- ($B_{1/2}$ ~35.5-38 mT, DP = 0.25-0.34) and high-coercivity components ($B_{1/2}$ ~154.9-199.5 mT, DP = 0.2-0.31) are interpreted as due to magnetite and hematite, along with an intermediate-coercivity component due to greigite ($B_{1/2}$ ~69.2-85.1 mT, DP = 0.09-0.14). Magnetite is dominant throughout the hole, while the high-GRM layer (130.5-132.0 mbsf) contains greigite.

Table 4.1 Details of IRM acquisition curve decomposition for selected samples from Hole U1431D. $B_{1/2}$ is the field at which half of the SIRM is reached, and DP is the dispersion parameter.

Sample	Depth (mbsf)	Component 1			Component 2			Component 3			Component 4		
		$B_{1/2}$ (mT)	DP	IRM contribution (%)	$B_{1/2}$ (mT)	DP	IRM contribution (%)	$B_{1/2}$ (mT)	DP	IRM contribution (%)	$B_{1/2}$ (mT)	DP	IRM contribution (%)
8H5W65	66.84	17.8	0.39	17	41.2	0.26	74	158.5	0.47	8			
15H4W53	130.52	35.5	0.25	18	83.2	0.14	70	199.5	0.2	12			
15H5W50	130.97	38	0.34	47	69.2	0.14	14	85.1	0.09	23	154.9	0.31	16
34X3W94	307.83	25.1	0.29	21	45.7	0.25	64	234.4	0.49	15			

4.3.4. Magnetic parameters

Magnetic susceptibility mainly depends on the mineralogy and concentration of magnetic minerals. χ and SIRM correlate linearly with $R^2 = 0.78$ (Figure 4.6), which indicates an almost uniform magnetic mineral grain size throughout the studied sequence (Evans and Heller, 2003), where χ is controlled mainly by magnetite abundance. Thus, χ is used here as a proxy for magnetite concentration. ARM is also a concentration-

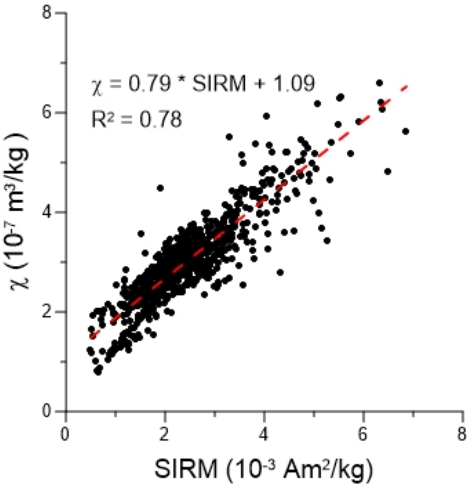

Figure 4.6 Correlation diagram of χ and SIRM for sediments from Hole U1431D.

dependent parameter that is sensitive to the fine magnetic mineral concentration. Down-core χ and ARM variations tend to change relatively gradually with occasional peaks. ARM/SIRM and χ_{ARM}/χ are indicative of grain-size variations, with high values indicating fine grains and *vice versa* (e.g., King et al., 1982; Deng et al., 2005). Based on general down-core trends, these parameters can be divided into three parts (Figures 4.7c and 4.7d). Below 300 mbsf, ARM/SIRM and χ_{ARM}/χ are relatively stable with minor fluctuations. From 300 to 230 mbsf, ARM/SIRM and χ_{ARM}/χ increase, which reflects finer magnetic grain sizes. Above 230 mbsf, they decline gradually, which indicates magnetic coarsening.

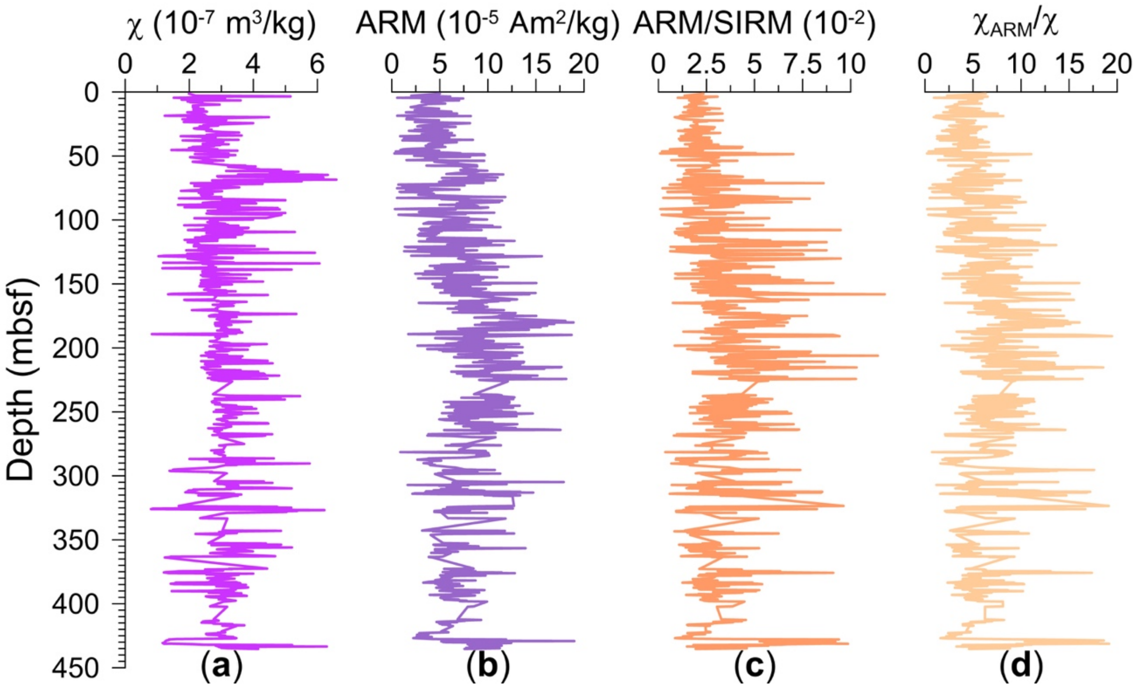

Figure 4.7 Down-core magnetic parameter variations for sediments from Hole U1431D. (a) χ, (b) ARM, (c) ARM/SIRM, and (d) χ_{ARM}/χ.

4.4. Discussion

4.4.1. Magnetostratigraphy

Preliminary paleomagnetic studies were conducted shipboard. Archive-halves of cores were AF-demagnetized to 20 mT with NRM measurements at 2.5-cm intervals (Li et al., 2015b). Inclinations are much steeper than expected at the site latitude, which indicates that ChRMs are not fully isolated at such fields due to a significant drilling-induced overprint. For XCB-cored sediments from below 168.87 mbsf, strong magnetic overprints preclude reliable polarity subchron identification (Figure 4.4e). Therefore, shipboard results cannot be used to establish a complete magnetic polarity zonation. Our post-cruise work presented here, therefore, improves the magnetostratigraphy for this site significantly.

Constrained by biostratigraphy (Table 4.2), our magnetostratigraphy is constructed by correlating the recorded polarity pattern to a reference GPTS (Gradstein et al., 2012). Ages of calcareous nannofossil events range from 0.29 to 1.04 Ma between 3.15 and 50.9 mbsf; thus, the upper normal polarity zone is interpreted as the Brunhes Chron, and the Matuyama/Brunhes boundary (0.781 Ma) is identified clearly at 45.96 mbsf (Figures 4.4e-4.4g). The interval between 45.96 and 134.14 mbsf has dominantly reversed polarity with four thin normal polarity zones; calcareous nannofossil events indicate ages from 1.04 to 2.22 Ma (Li et al., 2015b), so we identify this interval as the Matuyama Chron. The four normal polarity zones correspond to the Jaramillo (54.39-61.14 mbsf), Cobb Mountain (65.30-66.42 mbsf), Olduvai (87.09-95.15 mbsf), and Réunion (99.54-101.22 mbsf) subchrons, respectively. The last appearance datum (LAD) of the calcareous nannofossil *Reticulofenestra pseudoumbilicus* (3.7 Ma) at 217.07 mbsf allows us to interpret the normal polarity zone between 134.14 and 216.44 mbsf as the Gauss Chron.

The LAD of the calcareous nannofossil *Nicklithus amplificus* (5.94 Ma) at 361.67 mbsf helps to constrain this part of the record to the lower Gilbert Chron. In the interval between 216.44 and 244.17 mbsf, there is a ~10-metre-long core gap, which makes it difficult to define the polarity of this interval in which we infer C2Ar to occur. The first appearance datum (FAD) of the calcareous nannofossil *Ceratolithus rugosus* (5.12 Ma) at 284.6 mbsf constrains the lower boundary of the normal polarity zone at 313.88 mbsf as the lower boundary of the Thvera subchron. The immediately underlying reversed polarity interval is interpreted as C3r. The FAD of the calcareous nannofossil *Nicklithus amplificus* (6.91 Ma) at 527.31 mbsf suggests that the interval between 372.32 and the base of the hole at 434.77 mbsf corresponds to the top of Chron C3A. Therefore, we interpret the three polarity zones in this interval as C3An.1n (356.11-392.87 mbsf), C3An.1r (392.87-419.17mbsf), and C3An.2n (419.17-434.77 mbsf), respectively.

Table 4.2 Depths and ages of calcareous nannofossil datums for Hole U1431D (data from Li et al. (2015)). T = top/last appearance datum; B = base/first appearance datum; Ba = base acme; Bc = base common.

Calcareous nannofossil event	Age (Ma)	Depth (mbsf)
B *Emiliania huxleyi*	0.29	3.15
T *Pseudoemiliania lacunosa*	0.44	12.15
T *Gephyrocapsa* sp. 3	0.61	32.08
B *Gephyrocapsa* sp. 3	1.02	39.67
B *Gephyrocapsa* spp. >4 μm	1.04	50.9
T *Gephyrocapsa* spp. >5.5 μm	1.24	60.7
T *Calcidiscus macintyrei*	1.6	89.01
B *Gephyrocapsa* spp. >5.5 μm	1.62	96.1
T *Discoaster brouweri*	1.93	107.57
Ba *Discoaster triradiatus*	2.22	116.85
T *Discoaster surculus*	2.49	135.2
T *Discoaster tamalis*	2.8	157.4
T *Sphenolithus* spp.	3.54	188.3
T *Reticulofenestra pseudoumbilicus*	3.7	217.07
T *Amaurolithus tricorniculatus*	3.92	245.87
Bc *Discoaster asymmetricus*	4.13	255.38
T *Amaurolithus primus*	4.5	265.21
B *Ceratolithus rugosus*	5.12	284.6
B *Ceratolithus acutus*	5.35	298.56
T *Nicklithus amplificus*	5.94	361.67
B *Nicklithus amplificus*	6.91	527.31

Assuming a relatively constant sedimentation rate, the basal age of the sequence (434.77 mbsf) is estimated at ~6.5 Ma. From our magnetostratigraphy, the late Miocene sedimentation rate was ~115.6 m/Myr, which then decreased abruptly to ~61.8 m/Myr at ~6 Ma and remained stable (Figure 4.8). A sedimentation rate decrease at ~6 Ma is also observed in the northern SCS continental slope (Wu et al., 2014).

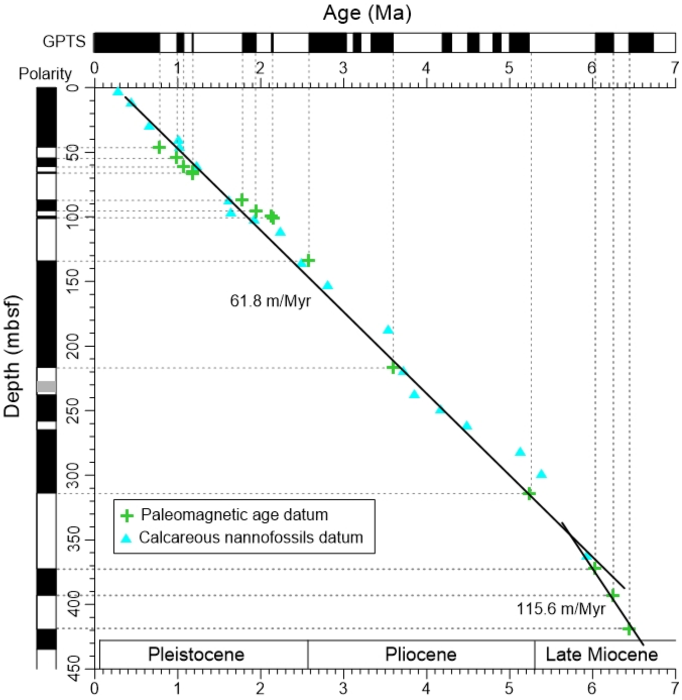

Figure 4.8 Age-depth plot for Hole U1431D.

4.4.2. Formation and preservation mechanism of the greigite-bearing layer

Greigite is an iron sulphide mineral that forms under sulphidic redox conditions (Berner, 1984; Wilkin and Barnes, 1997; Benning et al., 2000; Roberts, 2015) and that is often identified in fine-grained lacustrine and marine sediments (e.g., Kao et al., 2004; Rowan and Roberts, 2006; Liu et al., 2014). Greigite can form at any time during diagenesis if the necessary reactants are present, not only during early diagenesis (Roberts and Weaver, 2005; Roberts, 2015). The supply of organic matter, reactive iron, and sulphate are the dominant factors that control its formation and preservation (Morse et al., 1987; Roberts, 2015). Based on rock magnetic and paleomagnetic results, a greigite-bearing layer (130.5-132.0 mbsf) is recognised in the central SCS at Hole U1431D. From our magnetobiostratigraphic age model, the age of this layer is inferred to be 2.53-2.55 Ma, which slightly postdates intensification of northern hemisphere glaciation (iNHG) (Shackleton et al., 1984), when the subarctic Pacific Ocean became permanently stratified (Haug et al., 1999, 2005). Intrusion of colder Pacific Ocean waters into the SCS caused shoaling and enhancement of the thermocline (Huang et al., 2005). Therefore, vertical water exchange and deep-sea ventilation would have been impeded so that bottom waters became more stagnant. At ~2.7-2.5 Ma, surface nutrient contents increased significantly in the northern SCS (Jian et al., 2003), so that primary productivity and organic matter delivery to the seafloor increased. Inter-arc gateways in Luzon Strait are also important for water exchange between the SCS and the Pacific Ocean. The Loho remnant forearc basin, whose position is connected to the inter-arc passage between volcanic islands, deformed, uplifted, and closed, so that the Loho inter-arc water gateway disappeared at ~3 Ma (Chen et al., 2015). Consequently, less water flowed into the SCS and the SCS became progressively less well ventilated. Increasing sedimentary organic matter contents and restricted bottom water ventilation led to oxygen depletion. Therefore, organic matter had more chance to be preserved, which favoured iron sulphide formation.

Greigite has been reported in the southwest SCS sub-basin and from the northwestern SCS slope (Duan et al., 2017; M. Li et al., 2018). However, greigite is interbedded with magnetite in the southwest SCS, while there is a single greigite-bearing layer at a specific depth in Hole U1431D in the central SCS. These differences between the southwest and central SCS probably resulted from oceanographic variations over the respective time intervals. In the southwest SCS, connection with the Indian Ocean was cut off during glacial periods, and the continental shelf was exposed, so that terrigenous deposition increased rapidly, and anoxic conditions were produced that favoured greigite formation. Therefore, greigite prevailed during glacial periods and magnetite prevailed during interglacial periods (Duan et al., 2017). In contrast, Pacific Deep Water is always present in the central SCS (Wang and Sun, 1994), so it is not easy to form greigite-bearing layers. The thick greigite-bearing layer in Hole U1431D indicates that Pacific Deep-Water intrusion weakened in association with the iNHG event so that ventilation of the central SCS weakened, which led to authigenic greigite formation. The greigite-bearing layer in the northwestern SCS slope is an event deposit associated with delivery of an organic-rich turbidite during the last glacial maximum (M. Li et al., 2018).

4.4.3. Paleoclimatic implications of magnetic parameter variations

The East Asian monsoon regime is the dominant climatic feature in the SCS. At suborbital and millennial timescales, SCS monsoon evolution is associated tightly with glacial/interglacial cycles. The summer monsoon prevails during interglacial periods, and *vice versa* (e.g., Wang et al., 1999; Kissel et al., 2003; M. Li et al., 2018). However, monsoon evolution at tectonic and orbital scales remains controversial. For example, in the northern SCS slope, Kissel et al. (2003) suggested a weak summer monsoon from 1.2 to 0.7 Ma while Liu et al. (2003) argued that the summer monsoon prevailed during the same period. In addition, monsoon records from the southern and northern SCS have different trends since the Miocene. While several studies have focused on the SCS slope and the southwestern sub-basin (Wan et al., 2006, 2007; Tian et al., 2011; Liu et al., 2019), long-term monsoon evolution in the east sub-basin remains unclear. To better understand

SCS monsoon records, magnetic methods are applied to sediments from Hole U1431D in the east sub-basin since ~6.5 Ma.

Monsoon proxies

The concentration, grain size, and mineralogy of magnetic particles are related to primary geological or subsequent environmental processes (Liu et al., 2012); thus, magnetic parameters can be used to decipher environmental evolution. However, proxies can be ambiguous, and climatic signals can be suppressed, distorted, or masked by other geological processes. When interpreting sedimentary paleoclimatic records, potential complicating processes must be considered. Effects of sediment provenance and transportation changes should be considered because they can cause magnetic property changes in addition to environmental changes. The SCS is dominated by fluvial sediments, with more than 700 million metric tons of fluvial sediments received annually. The sediments come from several of the largest rivers in the world (i.e., the Pearl, Red, and Mekong Rivers) and small mountainous rivers (e.g., in SW Taiwan) (Liu and Stattegger, 2014; Liu et al., 2016). In the central SCS, sediments are mainly derived from fluvial systems in Taiwan and Luzon (Liu et al., 2016). Taiwan is tectonically active, with oblique arc-continent collision since ~6.5 Ma (Huang et al., 1997, 2000). Formation of the Taiwan orogen has increased terrigenous supply from SW Taiwan to the northern SCS since 3 Ma (Wan et al., 2010). However, few studies have focused on terrigenous flux changes to the central SCS influenced by tectonic activity in Taiwan. Based on the relatively stable sedimentation rate in Hole U1431D (Figure 4.8), we assume that tectonic activity in Taiwan had little impact on terrigenous fluxes to the central SCS. Apart from terrigenous sediments, volcanic ash layers occur in Hole U1431D above 194.95 mbsf.

Samples from identified ash layers were not included in further analyses because of the non-climatic origin of these layers.

Due to land-sea configuration changes caused by sea level fluctuations, sediment transportation can differ between late Quaternary interglacial and glacial periods. With exposure of large continental shelves, delivery of coarser sediments can occur during glacial periods in contrast to interglacial periods. For example, an exposed glacial continental shelf reduced the distance from the Pearl River to Core MD12-3432 on the northern SCS slope, which caused delivery of coarser magnetite and pyrrhotite to this site (Q. Chen et al., 2017). A similar situation is also recorded on the northwestern continental slope, where significantly increased hematite concentrations over the ~32-15 ka interval are interpreted as due to Red River-sourced sediment migration over shorter distances when sea level was ~90 m lower than present (M. Li et al., 2018). Compared to the northern and northwestern SCS, continental shelves in the northeastern SCS are much narrower, and the short sediment transport distance is largely unaffected by sea level changes (Liu et al., 2008, 2009). Therefore, the changing land-sea configuration did not likely have much effect on deposition in the central SCS.

Post-depositional diagenetic effects should always be considered in sediment magnetism studies. Magnetic minerals are sensitive to diagenetic oxidation and reduction reactions, and diagenetic modification of magnetic minerals in sediments can vary from subtle to pervasive (Roberts, 2015). In Hole U1431D, the mineral magnetic signature is dominated by detrital magnetic minerals. The influence of significant diagenetic alteration is restricted to a short-lived interval of sulfidic diagenesis at ~2.53-2.55 Ma, which suggests that sediments cannot be used to reconstruct monsoon evolution during this period (Section 4.4.2). Overall, magnetic parameter variations are controlled mainly by climatic changes in the central SCS, so they can be used as paleoclimate indicators for Hole U1431D.

Hematite prevails in warmer and drier climates while goethite forms preferentially under more humid conditions; the Hm/Gt ratio is, therefore, used as a climate indicator (e.g., Kämpf and Schwertmann, 1983; Maher, 1986). In the central SCS, nearly 85-90% of annual rainfall occurs during the summer monsoon season, while the annual average temperature is stable (Z. Liu et al., 2007). Therefore, Hm/Gt is mainly controlled by precipitation and can be employed as a proxy for monsoon-induced precipitation and weathering conditions (Clift, 2006; Y. Zhang et al., 2007; Liu et al., 2019). Decreasing/increasing Hm/Gt ratios indicate a strong/weak summer monsoon. In the SCS, magnetic susceptibility is proportional to terrigenous material input (Tian et al., 2005), and monsoon rainfall is expected to increase run-off and, thus, terrigenous inputs (Clift et al., 2002). Therefore, magnetic susceptibility can be a useful summer monsoon proxy. ARM is also used as a summer monsoon proxy because it is sensitive to fine magnetic particle variations. Higher χ and ARM values indicate stronger summer monsoons. Coarser ferrimagnetic particles in SCS sediments correspond to enhanced winter monsoons with arid conditions and greater physical erosion (Kissel et al., 2003; M. Li et al., 2018). Therefore, magnetic mineral grain size is used as a winter monsoon indicator here. Lower ARM/SIRM and χ_{ARM}/χ values indicate coarser magnetic grain sizes, and thus a stronger winter monsoon.

East Asian monsoon evolution

For Hole U1431D, magnetic parameter variations have large amplitudes (Figures 4.9a-4.9d), but with no obvious trends before 5 Ma. χ, ARM, and Hm/Gt variations indicate a stronger summer monsoon from 5 to 3.8 Ma (Figures 4.9a, 4.9b, and 4.9e), which then weakened gradually to the present. In concert, ARM/SIRM and χ_{ARM}/χ suggest that the winter monsoon weakened from 5 to 3.8 Ma (Figures 4.9c and 4.9d). The winter monsoon then strengthened until 0.6 Ma and became stable since then.

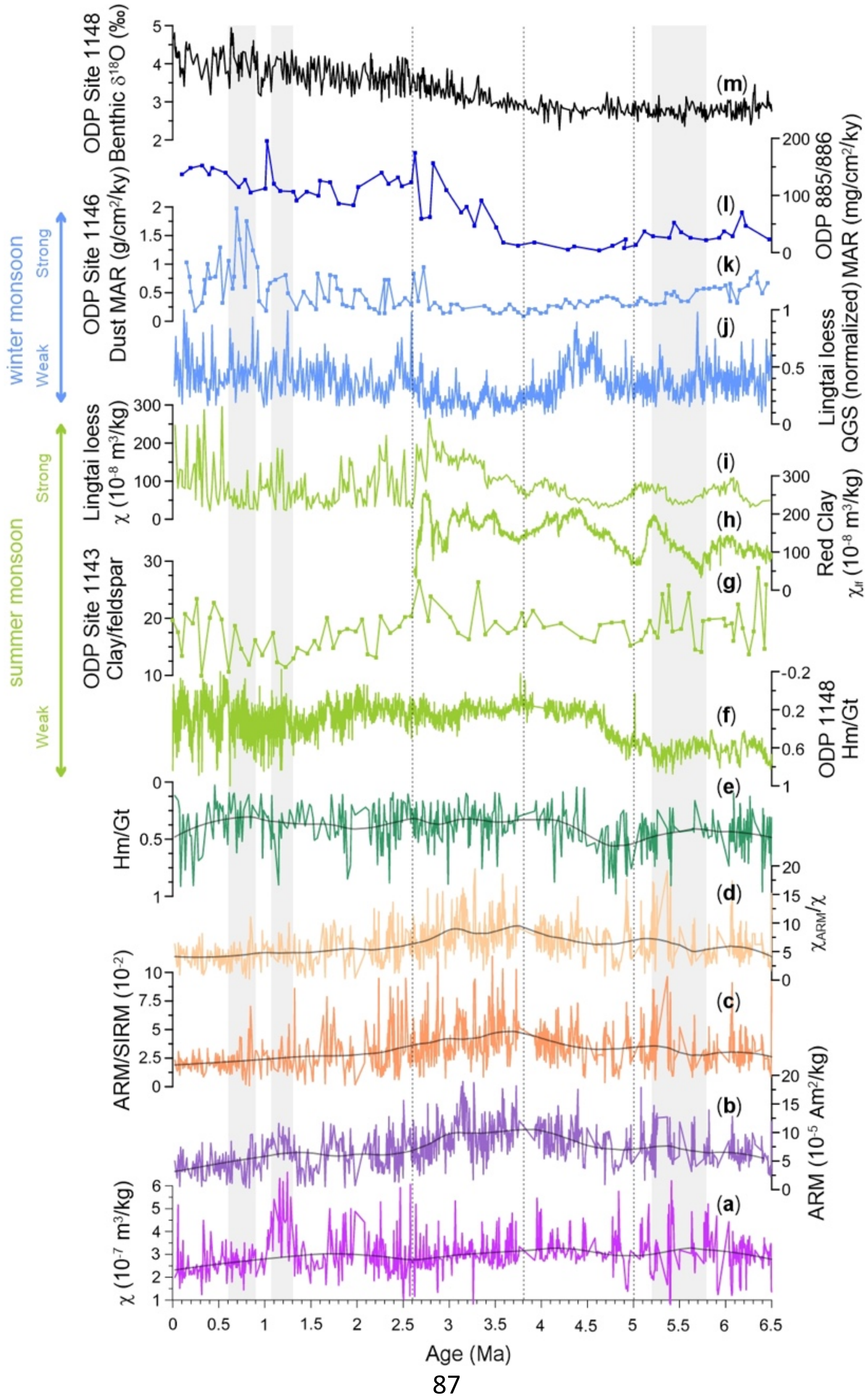

Figure 4.9 Marine and terrestrial records of climate variability in the South China Sea region since 6.5 Ma. (a-e) χ, ARM, ARM/SIRM, χ_{ARM}/χ, and Hm/Gt records for sediments from Hole U1431D, central South China Sea. (f) Hm/Gt record from ODP Site 1148, northern South China Sea (Clift, 2006). (g) Clay/feldspar record from ODP Site 1143, southwestern South China Sea (Wan et al., 2006). (h) χ_{lf} record from Shilou Red Clay, Chinese Loess Plateau (Ao et al., 2016). (i-j) χ and quartz grain size (QGS) records from Lingtai Loess, Chinese Loess Plateau (Sun et al., 2010). (k) Dust mass accumulation rate (MAR) at ODP Site 1146, northern South China Sea (Wan et al., 2007). (l) Eolian MAR at ODP Site 885/886, North Pacific Ocean (Rea et al., 1998). (m) Benthic $\delta^{18}O$ of *Uvigerina sp.* from ODP Site 1148, northern South China Sea (Tian et al., 2008). The grey lines in (a-e) are LOESS smoothed curves.

Loess-paleosol-Red Clay sequences on the CLP preserve thick continental archives for East Asian monsoon studies. Magnetic susceptibility and quartz grain size (QGS) are used widely as summer and winter monsoon proxies in the CLP, respectively (An et al., 1991; Heller and Evans, 1995; Xiao et al., 1995). Comparison of our record with those from the CLP and other SCS sites indicates some similarities and differences. Significant pedogenesis-induced χ_{lf} enhancements are recorded in Red Clay sequences on the CLP across the Miocene-Pliocene transition (Figure 4.9h), which are interpreted to reflect increased summer monsoon precipitation (Ao et al., 2016, 2018). Enhanced summer monsoons are also recorded in the southwest SCS, as indicated by increased clay/feldspar ratios (Figure 4.9g). However, summer monsoon patterns are obscured in Hole U1431D at this time by a lack of data caused by abundant calcareous turbidite deposits and drilling disturbances.

From 5 to 3.8 Ma, consistent trends from SCS and CLP records indicate an intensified summer monsoon and weakened winter monsoon. This extensive climate shift in East Asia was nearly synchronous with gradual closure of the Central American Seaway from the late Miocene to early Pliocene, which caused a significant ocean circulation reorganization (Keigwin, 1982; Haug and Tiedemann, 1998). Shoaling of the seaway limited heat exchange between the Pacific and Atlantic Oceans. The Gulf Stream then intensified and transported more warm and saline water to high northern latitudes, which favoured Pliocene warmth (Haug and Tiedemann, 1998; Haug et al., 2001). Model simulations suggest that Central American Seaway closure enhanced Atlantic meridional overturning circulation and led to a warmer northern and cooler southern hemisphere (Lunt et al., 2008; Steph et al., 2010). Increased meridional temperature gradients forced the Intertropical Convergence Zone northward, and transported more moisture to East Asia, thereby strengthening the summer monsoon.

Since 3.8 Ma, coarser magnetic particles and higher dust mass accumulation rates (MARs) in the SCS, and larger QGS on the CLP indicate that the winter monsoon strengthened over East Asia. In contrast, discrepancies exist in summer monsoon records from 3.8 to 2.6 Ma. In the SCS, decreasing magnetic mineral content (Figures 4.9a and 4.9b) and increasing Hm/Gt (Figures 4.9e and 4.9f) indicate a weakened summer monsoon in the northern and central SCS while increasing clay/feldspar values indicate an enhanced summer monsoon in the southwestern SCS (Figure 4.9g). An intensified winter monsoon and a weakened summer monsoon probably resulted from stronger glacial conditions (Prell and Kutzbach, 1992). The northern and central SCS are affected significantly by the North Pacific Ocean. Larger eolian dust fluxes to the North Pacific usually occur in glacial periods (Hovan et al., 1989, 1991). From 3.8 to 2.6 Ma, increasing eolian dust MAR in the Pacific Ocean suggests climate cooling (Figure 4.9l). Increasing benthic foraminiferal $\delta^{18}O$ (Figure 4.9m) and decreasing sea surface temperatures in the northern SCS also document the cooling trend (Huang et al., 2005; Tian et al., 2008). Therefore, cooling conditions dominate the SCS monsoon pattern, which resulted in a weakened summer monsoon and intensified winter monsoon. Similar conditions also appeared at ~2.6 Ma. Over the iNHG event, global cooling strengthened the Siberian High to enhance the winter monsoon while weakening the summer monsoon in East Asia. In the southwestern SCS, the contrasting trend during the 3.8-2.6 Ma interval may have been a response to final formation of the western Pacific "warm pool" (WPWP) (Figure 4.9g). The southwestern SCS is situated within the northern margin of the WPWP, and its hydrography is sensitive to tropical climate and WPWP development (Wang, 1998). Final formation of the WPWP at ~4 Ma made the southwestern SCS warmer than the northern SCS (Chaisson and Ravelo, 2000; Li et al., 2004; Jian et al., 2006). An intensified Equatorial Current and easterly trade winds also brought more precipitation to the south China region, which would have strengthened chemical weathering of terrigenous minerals, as reflected by increased clay/feldspar values (Figure 4.9g). Compared to the SCS, CLP records indicate an enhanced summer monsoon during the 3.8-2.6 Ma interval. Cooling is unlikely to intensify the summer monsoon, so this change is likely to have been caused by a different mechanism, such as intense phased Tibetan Plateau uplift (An et al., 2001; Sun et al., 2010).

Apart from defining long-term climate evolution, some short-term events can also be recognized from Hole U1431D. In the 1.3-1.06 Ma interval, χ and ARM have abnormally high values compared with neighbouring parts (Figures 4.9a and 4.9b). Sediments in this interval are mainly composed of silt turbidites, probably derived from Taiwan or other surrounding blocks (Li et al., 2015b). During the final stage of the mid-Pleistocene transition, which was accompanied by major northern hemisphere ice sheet expansion and global CO_2 reduction (Clark et al., 2006), decreasing ARM/SIRM and χ_{ARM}/χ values (Figures 4.9c and 4.9d) indicate an intensified winter monsoon as expected, which is consistent with the northern SCS and CLP records (Figures 4.9j and 4.9k).

Orbital forcing of the East Asian summer monsoon

Orbital forcing impacts the monsoon system significantly. Compared with the influence of the widely explored precession cycle for the East Asian monsoon (e.g., Tian et al., 2011; Su et al., 2013), longer cycles, especially the 400-kyr long-eccentricity cycle, have not been investigated extensively in monsoon-related proxies due to a lack of long, continuous proxy records (Tian et al., 2008; Wang et al., 2014b, 2010). Our relatively continuous magnetic records provide an opportunity to explore long orbital cycles and their evolution since 6.5 Ma. Spectral analysis of the χ record over the past 6.5 Ma was performed. The 4π multi-taper method and the Fast Fourier transform method were applied to produce a power spectrum and evolutionary spectrogram, respectively (Thomson, 1982; Kodama and Hinnov, 2014). At the 99% confidence level, the power spectrum has peaks at the orbital cyclicities of 404-, 39- to 43-, and 22- to 24-kyr, which correspond to the long eccentricity, obliquity, and precession cycles, respectively (Figure 4.10a). Moreover, the power spectrum also contains non-orbital approximately 143- and 30-kyr cycles (Figure 4.10a). Sampling intervals for ~12% of samples are smaller than the Nyquist frequency for precession cyclicity, which explains why the precession signal is less strong compared to longer orbital cycles. We note that 39- to 43-kyr cycles are observed rather than the expected 41-kyr orbital cycle, which reflects age model imprecisions due to the imperfectly defined magnetobiochronology and/or to potential sedimentation rate changes in Hole U1431D; such situations are encountered commonly when investigating long-term climate forcing in geological records. Moreover, other factors can affect the accuracy of spectral results. For example, gravity flow deposits and bioturbation are common throughout the sediments cored at Hole U1431D (Li et al., 2015b). Turbidite sequences could have different magnetic properties (e.g., higher χ)

compared to sediments controlled by monsoon variations. Thus, signals induced by turbidites could cause spectral distortions. Additionally, coring gaps in Hole U1431D introduce noise, which can make detection of regular cycles more difficult, especially for higher frequency signals. Nevertheless, orbital signals are evidently present.

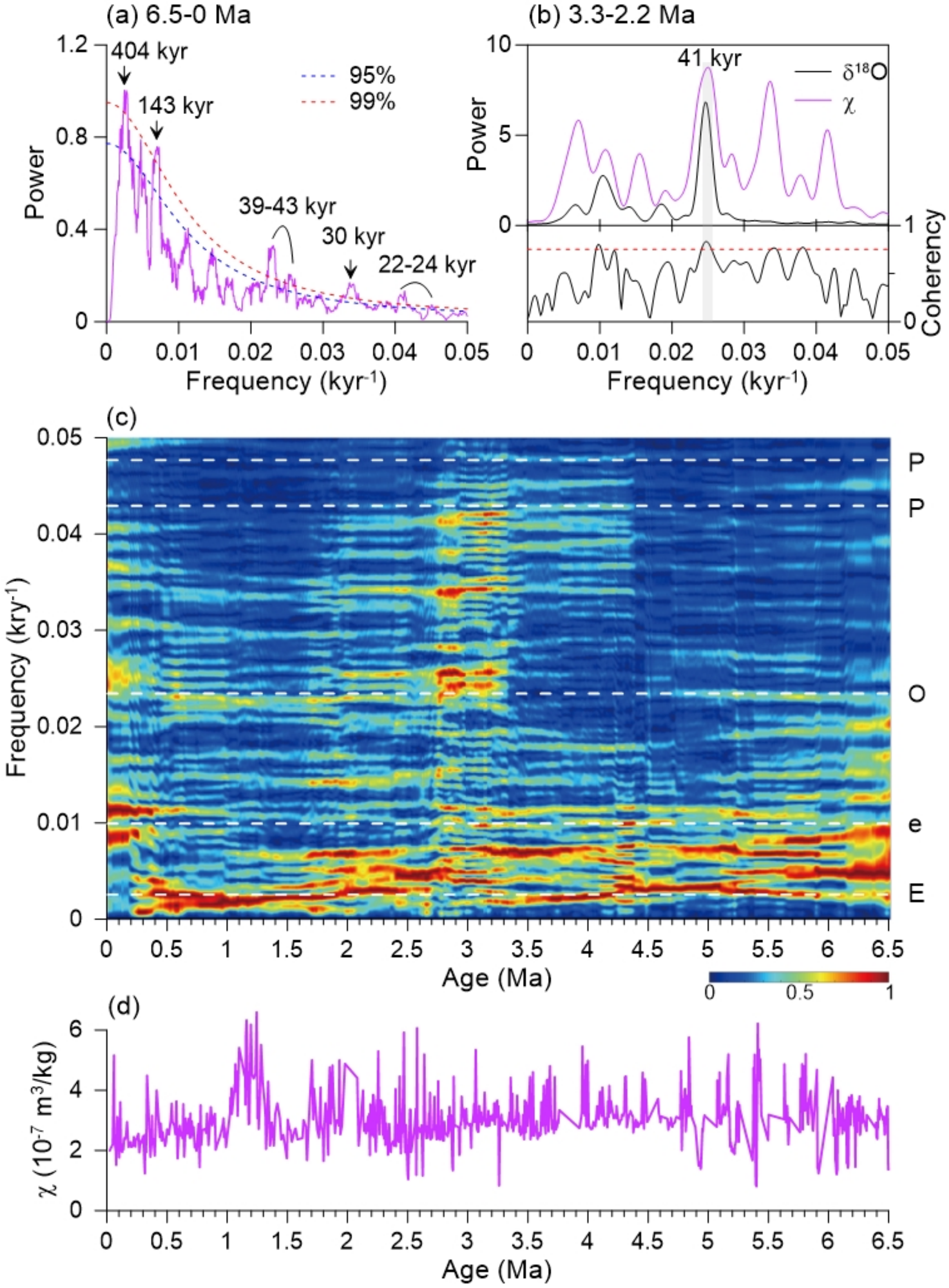

Figure 4.10 Spectral analysis of the χ record from Hole U1431D. (a) Power spectrum for the past 6.5 Ma; (b) cross-spectrum and coherency between the χ record and the LR04 benthic δ^{18}O record (Lisiecki and Raymo, 2005); (c) evolutionary spectrogram over the past 6.5 Ma; and (d) the χ record.

An evolutionary spectrum for the χ record reveals strong spectral densities at low frequencies, while cycles with higher frequencies are less obvious (Figure 4.10c). Precession cycles (21-23 kyr) are nearly indistinguishable except for weak signals from 4.4 to 2.6 Ma. In contrast, precession cycles are always significant in other SCS monsoon proxies (e.g., Tian et al., 2006; Huang et al., 2018), because precession plays a prominent role in modulating low-latitude daily insolation. We attribute the poor resolution of precession signals to coring gaps that preclude detection of precession cycles.

Obliquity cycles (41 kyr) are identified before ~4.7 Ma and from 3.3 to 0.5 Ma, while short-eccentricity cycles (95 and 125 kyr) disappear at ~2.6 Ma, appear again at ~1 Ma, then amplify gradually and finally stabilize after 0.7 Ma. For obliquity cycles, signals before ~4.7 Ma are less reliable because of frequent coring gaps. Obliquity cycles emerge at about the same time as early NHG at 3.2 Ma (Shackleton and Opdyke, 1977), which was associated with increased global ice volume for which variations were forced orbitally by obliquity cycles since the Pliocene (Lisiecki and Raymo, 2005, 2007). To further test whether χ variations were affected by global ice volume, cross-spectral analysis with a Bartlett window was performed between the χ record and the LR04 benthic $\delta^{18}O$ record (Lisiecki and Raymo, 2005). The time interval between 3.2 and 2.2 Ma is selected because the χ record during this time interval is more continuous and less affected by factors other than the summer monsoon. The identified 41-kyr cycle in the χ record correlates strongly with the benthic $\delta^{18}O$ spectrum (Figure 4.10b), which suggests that global ice volume had a significant effect on East Asian summer monsoon evolution during this period. The presence of turbidites precludes use of evolutionary spectra from 1.3 to 1.06 as straightforward climatic signals, so the MPT onset is not evident at Hole U1431D. However, gradual establishment of short-eccentricity cycles is as expected for the MPT, which suggests that the sediment magnetic properties record environmental changes, and further verify the fidelity of the magnetobiochronology during this time interval. Long-eccentricity cycles (400 kyr) have strong spectral densities throughout the past 6.5 Ma, which suggests that 400-kyr forcing is significant for the East Asian summer monsoon system. To further investigate the long-eccentricity magnetic cyclicity, Gaussian band-pass filtering was applied to the χ dataset (Figure 4.11). The filtered ~400-kyr cycles in the χ record are generally in phase with eccentricity before ~3.2 Ma, with high χ values corresponding to long-eccentricity maxima. Eccentricity affects the climate

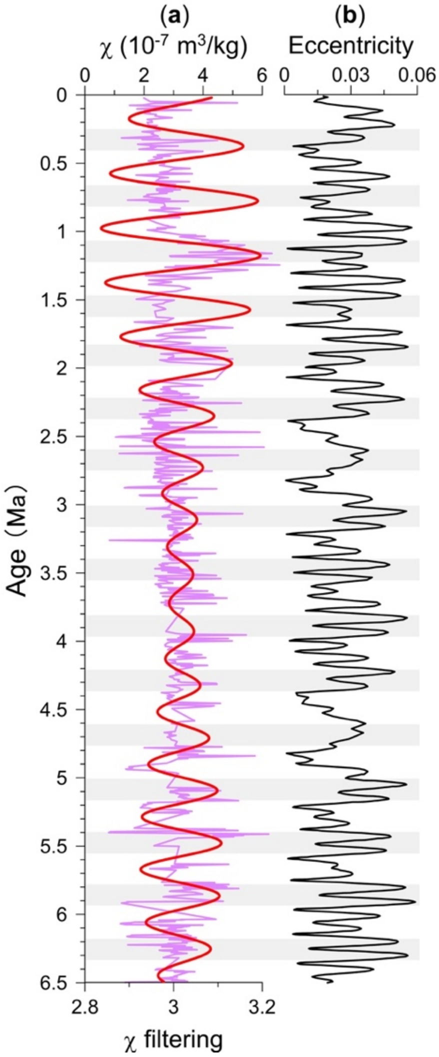

Figure 4.11 Comparison of χ with orbital eccentricity over the last 6.5 Ma. (a) The χ record (pink) and its filtered signal (red) for Hole U1431D; and (b) orbital eccentricity variations (Laskar et al., 2004). The band-pass filter has a 0.0025 kyr^{-1} central frequency.

system through modulation of the precession-driven low-latitude process, therefore, ~400-kyr cyclicity in the χ record is interpreted as a direct linear response to low-latitude insolation changes. That is, for maximum long-eccentricity values, summer insolation has maximum values at low latitudes, and enhanced seasonal variation leads to monsoon intensification and increased precipitation. This promotes weathering and river runoff, so that more terrigenous material (high χ values) is transported to the SCS. Since ~3.2 Ma, with the onset of early NHG, global ice volume changes have an increasing impact on summer monsoon evolution, which produces both 400- and 41-kyr cycles in the χ record.

4.5. Conclusions

1) Based on detailed rock magnetic analysis, magnetite is the dominant magnetic mineral in Hole U1431D in the central SCS. We present a magnetobiostratigraphy for Hole U1431D since ~6.5 Ma, which is the longest record available from the deep SCS basin.

2) A greigite-bearing layer occurs at 2.53-2.55 Ma. Intensification of northern hemisphere glaciation may have played an important role in the formation/preservation of greigite. Cooling of Pacific Ocean waters and arc-continent collision in Taiwan and the Philippines restricted water exchange between the SCS and the Pacific Ocean, which reduced bottom water ventilation, and favoured a short-lived period of greigite formation.

3) Sedimentary magnetic parameters provide effective proxies for East Asian monsoon variations. The East Asian summer and winter monsoons were stable from 6.5 to 5 Ma. The summer monsoon strengthened at 5 Ma, followed by a gradual weakening since 3.8 Ma. The winter monsoon weakened at 5 Ma, and then strengthened at 3.8 Ma until it stabilized at 0.6 Ma. Spectral analysis indicates that orbital forcing played an

important role in regional paleoclimatic evolution. Before ~3.2 Ma, the East Asian summer monsoon responded directly to low-latitude insolation changes; since ~3.2 Ma, the East Asian summer monsoon was driven by both low-latitude insolation and high-latitude ice volume changes.

Chapter 5

Recording fidelity of relative paleointensity characteristics in the North Pacific Ocean

---

Abstract NPO sediments are important archives of geomagnetic field evolution, yet late Quaternary geomagnetic field behaviour in the NPO is less explored because of generally low sedimentation rates and the challenge of dating sediments deposited below the calcite compensation depth. Core NP02 sediments from the NPO contain three visible tephra layers, which are identified as the To-Of, Spfa-1, and Kt-3 tephra, respectively. An age model for core NP02 is established based on tephra correlation and one radiocarbon date, which gives a mean sedimentation rate of ~11.6 cm/kyr. Magnetic analyses suggest the dominance of two remanence carriers; detrital vortex state and biogenic SD magnetite. Variable depth offsets between the RPI signals carried by the two remanence carriers adds a negligible age error (<0.5 kyr) to the core NP02 RPI record. Pronounced RPI amplitude variations are observed, and the Rockall and Laschamp excursions are identified in the core NP02 RPI record based on the age model. The fidelity of the core NP02 RPI record is further verified by comparison with other RPI stacks and records, and we demonstrate that the RPI variations can assist in chronology refinement.

5.1. Introduction

The geomagnetic field plays an important role in shielding Earth from cosmic radiation (Lal and Peters, 1967; Heinrich and Spill, 1979). Observational and geological records suggest that the geomagnetic field varies over a range of timescales from micropulsations to superchrons (e.g., Jacobs, 1959; Valet and Meynadier, 1993; St-Onge et al., 2003; Biggin et al., 2008; Granot et al., 2012; Demetrescu and Dobrica, 2014). As the largest ocean in the world, the Pacific Ocean preserves abundant information about geomagnetic field evolution (e.g., Doell and Cox, 1971; Roberts et al., 1997; Lanci et al., 2004; Channell and Lanci, 2014; Yamazaki and Yamamoto, 2018). However, studies of late Quaternary geomagnetic field variations from the NPO remain relatively sparse. From post-depositional remanent magnetization lock-in models, Roberts and Winklhofer (2004) suggested that detailed geomagnetic field behaviour, such as geomagnetic excursions and short-term non-dipole behaviour, can be recorded adequately at sedimentation rates >10 cm/kyr. In contrast, sedimentation rates in the NPO are generally low (e.g., Ninkovich et al., 1966; Prince et al., 1980; Kyte et al., 1993; Rea et al., 1998; Pettke et al., 2000; Korff et al., 2016), which impedes high-resolution geomagnetic field behaviour studies on orbital and sub-orbital time scales. Also, NPO sediments are usually deposited below the CCD, which impedes development of radiocarbon dating and continuous oxygen-isotope stratigraphy to construct precise age models to assist understanding of past geomagnetic field evolution.

RPI variations of Earth's magnetic field have been used as a chronological tool in marine sediments (e.g., Guyodo and Valet, 1996, 1999; Valet et al., 2005; Yamamoto et al., 2007; Channell et al., 2009, 2016a). This makes RPI variations valuable in environments like the deep NPO (Roberts et al., 1997; Yamazaki, 1999; Yamamoto et al., 2007; Shin et al., 2019). The main advantage of the RPI approach is that dipole geomagnetic variations are recorded synchronously around the world and represent a geophysical measurement that is independent of seawater chemistry and that can be used to develop independent age constraints (Roberts et al., 2013). Paleointensity-assisted chronology studies are based on the assumption that sedimentary magnetic records contain information about the magnetic field intensity at the time of sediment deposition (Tauxe, 1993). To ensure that RPI records are not contaminated by other sedimentary magnetic signals, magnetite should be the dominant remanence carrier, the concentration of magnetite should vary down-core by less than one order of magnitude, and the grain size of magnetite should be in the 1-15 μm range (King et al., 1983; Tauxe, 1993). However, these requirements are based on the assumption that sediments contain a single magnetic mineral component rather than a mixture of several components. Recent studies suggest that magnetite with different grain-sizes responds differently to the geomagnetic field during paleomagnetic signal acquisition in sediments (Roberts et al., 2012, 2013; Yamazaki et al., 2013b; Ouyang et al., 2014; L. Chen et al., 2017). Biogenic and terrestrial magnetite co-occur pervasively in NPO sediments (Yamazaki and Ioka, 1997; Yamazaki and Shimono, 2013; Zhang et al., 2018). Given that biogenic and terrestrial magnetite have different grain-size distributions, potential complexities in magnetic recording need to be considered, including the possible presence of different remanence acquisition mechanisms with different lock-in depths. Therefore, detailed assessment of magnetic grain-size characteristics should be made to test the fidelity of sedimentary RPI records. In this study, we use an independent age model for NPO core NP02 to assess whether RPI correlations based on magnetite components with different grain-size distributions can be used to refine the core chronology.

5.2. Sampling and methods

5.2.1. Core description and sampling

Core NP02 is a 4.35 m gravity piston core from 40.48° N, 150.1° E. It was recovered from the NPO abyssal plain at a water depth of 5,177 m. This location lies below the CCD, so few foraminifera are preserved. The core site is downwind of Asian dust source areas and many volcanoes in the Japanese archipelago and Kamchatka Peninsula (Weber et al., 1996) (Figure 5.1). Therefore, the studied sediments are composed mainly of clay with occasionally intercalated tephra layers. Cubic samples (8 cm^3) were taken continuously from the working half of core NP02 for paleomagnetic and rock magnetic analyses.

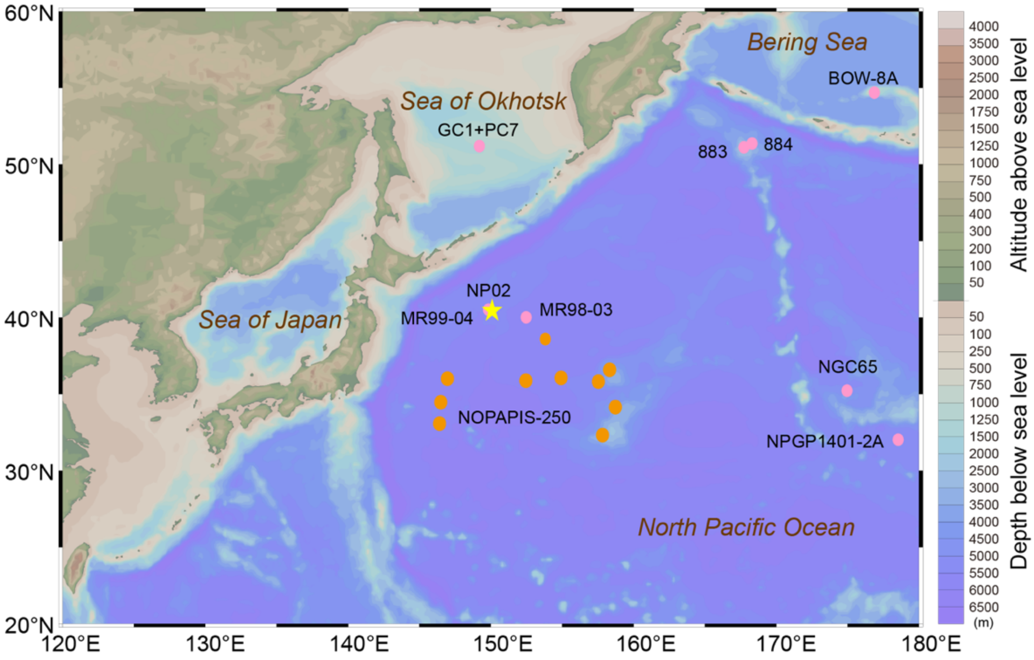

Figure 5.1 Map of the NPO with locations of core NP02 (yellow star), cores used to develop the NOPAPIS-250 stack (orange circles) (Yamamoto et al., 2007), and other Pacific cores (pink circles) relevant to this study (cores GC1+PC7, Inoue and Yamazaki, 2010, Yamazaki et al., 2013a; core BOW-8A, Okada et al., 2005; Site 883/884, Roberts et al., 1997, Roberts, 2008; MR99-04 and MR98-03, Aoki et al., 2000; core NGC65, Yamazaki, 1999; NPGP1401-2A, Shin et al., 2019).

5.2.2. Methods

Magnetic measurements

Magnetic remanence measurements were made using a 2-G Enterprises Model 760R cryogenic magnetometer with an in-line AF demagnetizer. The NRM was measured and stepwise demagnetized to a peak field of 100 mT, in logarithmically increasing field steps of 0.1-7.7 mT. ChRM directions were determined by PCA with successive demagnetization points that define vectors directed toward the origin of demagnetization diagrams (Kirschvink, 1980). Core NP02 is not oriented, therefore, the mean ChRM declination was calculated by making a constant azimuthal rotation to all samples to yield an adjusted mean declination of 0°. An ARM was imparted in a 100 mT peak field with a 0.05 mT DC bias field, and was then demagnetized with applied fields of 10, 20, 30, 40, 50, 60, 70, 80, 90, and 100 mT. IRMs were imparted in a DC field of 1 T, which is defined here as the SIRM.

Magnetic susceptibility (χ, mass specific) was measured at a frequency of 976 Hz. Temperature-dependent magnetic susceptibility (χ-T) curves for representative samples were measured in an argon atmosphere from room temperature to 700 °C. χ and χ-T curves were measured using an AGICO Kappabridge MFK 1-FA system equipped with a CS-3 furnace in an argon atmosphere.

IRM acquisition curves and FORCs (Pike et al., 1999; Roberts et al., 2000) were measured to a maximum field of 1 T using a MicroMag Model 3900 vibrating sample magnetometer. FORC diagrams were processed with the FORCinel software v3.05 (Harrison and Feinberg, 2008), and IRM acquisition curves were decomposed following Robertson and France (1994).

^{14}C dating

^{14}C dates were obtained using accelerator mass spectrometry on planktonic foraminifera (*N. pachyderma* sinistral). A probability density function of calibrated ages was calculated using ^{14}C determinations and the 1σ range from the Marine13 calibration curve (Reimer et al., 2013) with a reservoir age of ΔR = 400±50 years based on Yoneda et al. (2007). This calibrated age distribution was analyzed subsequently using the

Bayesian highest posterior density method to produce a calibrated age range determination following Lougheed and Obrochta (2016).

Volcanic glass shard analysis

Samples from the identified tephra layers were treated with H_2O_2, and then volcanic glass shards were selected, mounted, ground, and polished for electron probe microanalysis. Major element compositions were measured with a JEOL JXA-8100 electron microprobe at 15 kV accelerating voltage with 5-10 μm beam diameter and 6 nA beam current. Na contents were determined first to reduce the impact of its mobilization. For comparison, all data were normalized to an anhydrous basis (i.e., 100% total oxides).

5.3. Results

5.3.1. Paleomagnetic stability

The NRM is demagnetized almost completely at 100 mT (Figure 5.2a), which suggests that the NRM is carried mainly by low-coercivity magnetic minerals. A secondary remanent magnetization is present in some samples and can be removed by AF demagnetization to 10 mT. ChRMs can be identified as components directed toward the origin of demagnetization diagrams up to 100 mT. MAD values were calculated by PCA (Kirschvink, 1980) and are generally < 5° (Figure 5.2b), which suggests that the ChRMs are stable and well-defined. ChRM inclinations vary about an average value of 52°, which is slightly shallower than the expected geocentric axial dipole value for this site (±59.6°). Shallower inclinations may be associated with acquisition of a depositional remanent magnetization or sediment compaction (e.g., Anson and Kodama, 1987; Arason and Levi, 1990; Tauxe and Kent, 2004; Roberts et al., 2013). Three successive reversed polarity inclination values are identified at depths of 39 to 45 cm, which are interpreted to represent a geomagnetic excursion.

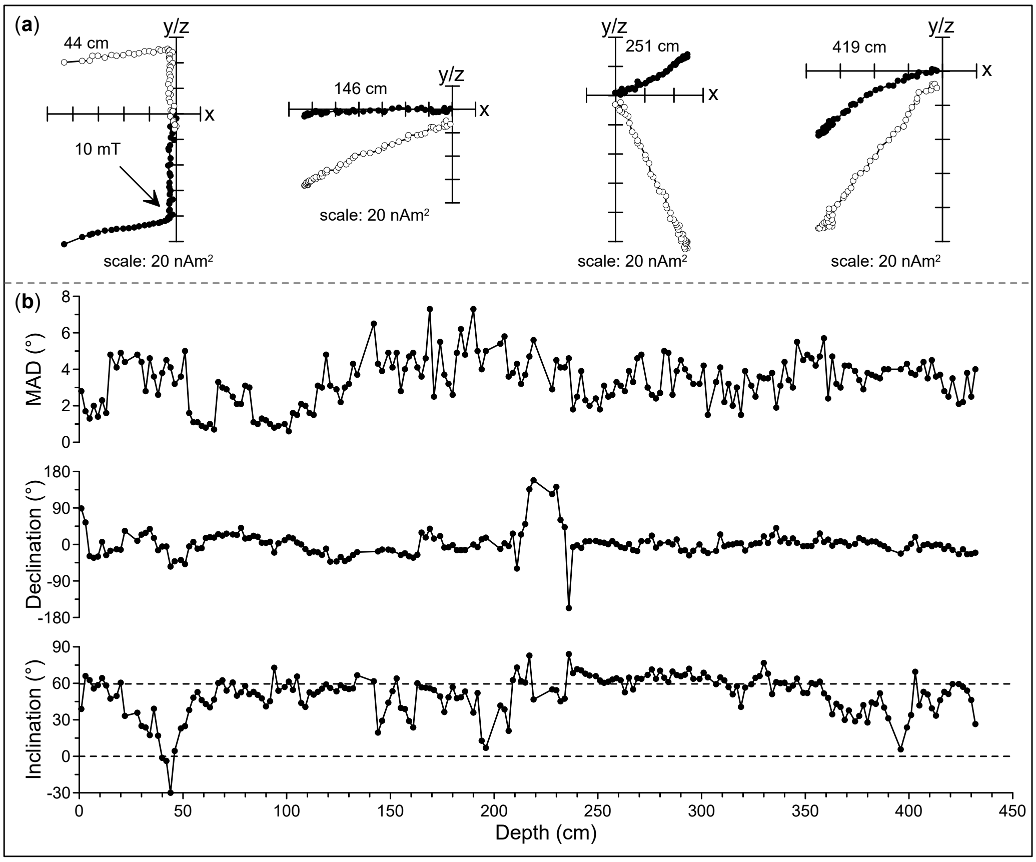

Figure 5.2 (a) Representative orthogonal projections of AF demagnetization data for sediments from core NP02. Solid (open) circles denote projections of the magnetization vector onto horizontal (vertical) planes. (b) ChRM inclinations, declinations, and MAD values. Dashed lines represent the expected inclination for a geocentric axial dipole field at the site latitude and inclination = 0°, respectively.

5.3.2. Mineral magnetic properties of the sediment

Bulk rock magnetic results are shown in Figure 5.3. χ-T heating curves increase steadily from room temperature to ~300-400 °C (Figure 5.3a), which indicates gradual unblocking of SD particles and/or heating-induced ferrimagnetic mineral neoformation. χ-T curves for tephra-containing samples (i.e., at depths of 141 and 393 cm in Figure 5.3a) have larger χ values than other curves during both heating and cooling. The heating curve for one tephra-containing sample (141 cm) reaches a near-zero value at ~660 °C, which suggests the presence of hematite. Otherwise, all heating curves decrease to near-zero values at ~580 °C, which corresponds to the Curie temperature of magnetite (Dunlop and Özdemir, 1997). Down-core variations of concentration-dependent magnetic parameters (χ, ARM, and SIRM) are shown in Figure 5.3b. Tephra-containing samples are distinguished by anomalously high χ, SIRM, and ARM values, and high elemental Zr contents (unpublished data), and were removed from our paleomagnetic record. Once these tephra-dominated intervals are removed, χ, ARM, and SIRM values vary within a factor of 5.5, 5.5, and 6.8, respectively, which suggests that the magnetite concentration is relatively homogeneous (i.e. variation of less than one order of magnitude) throughout core NP02. ARM/SIRM is used widely as a magnetic grain-size proxy. However, ARM acquisition can be affected strongly by the magnetic mineral concentration, with higher magnetite concentrations reducing ARM acquisition efficiency (Sugiura, 1979; King et

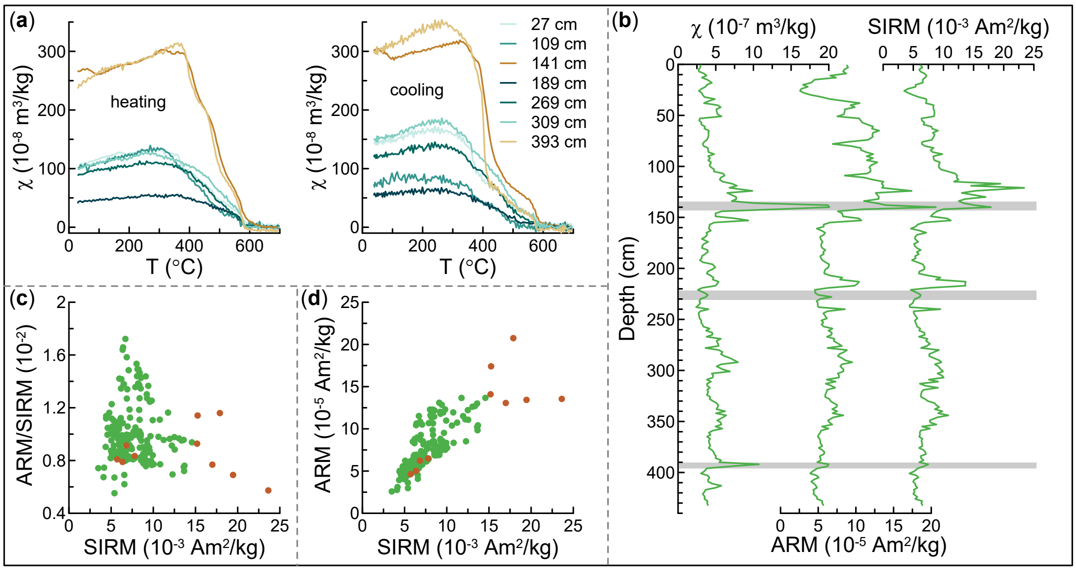

Figure 5.3 Rock magnetic results from core NP02. (a) Temperature dependence of magnetic susceptibility (χ-T) curves; left (right) are heating (cooling) curves (the depths of the representative samples are indicated in the legend); (b) down-core concentration parameter variations for χ, ARM, and SIRM; major ash layers are indicated by grey shaded areas; bi-plots of (c) SIRM and ARM/SIRM and (d) SIRM and ARM. Brown circles in (c) and (d) represent volcanic ash-containing samples.

al., 1983). If SIRM is used to represent the magnetic mineral concentration, a higher SIRM should produce lower ARM/SIRM values. A bi-plot of ARM/SIRM and SIRM for core NP02 does not have such a trend (Figure 5.3c), which indicates that the magnetite concentration has no significant effect on ARM acquisition efficiency. Therefore, ARM/SIRM can be employed here as a magnetic grain-size proxy. A bi-plot of ARM and SIRM has a linear trend with little scatter (Figure 5.3d), which suggests that changes in bulk magnetite grain size are relatively minor.

Although the bulk magnetic properties are relatively homogenous, FORC diagrams and IRM acquisition curve decomposition analyses suggest the presence of mixed magnetic signatures in core NP02. FORC diagrams contain a ridge-like distribution along the B_c axis with little vertical spreading, along with an asymmetrically distributed component that diverges toward the B_u axis (Figures 5.4a$_1$-5.4a$_6$). The former component together with a negative contribution along the B_u axis (Figures 5.4a$_2$-5.4a$_4$) is due to SD particles with uniaxial anisotropy (Muxworthy et al., 2004; Newell, 2005), which is often associated with non-interacting biogenic SD particles (Egli et al., 2010), while the latter component is typical of detrital particles in the magnetic vortex state (Lascu et al., 2018; Muxworthy and Dunlop, 2002; Roberts et al., 2017). Some FORC diagrams also contain a secondary peak near the origin (Figures 5.4a$_1$, 5.4a$_2$, and 5.4a$_4$), which indicates viscous behaviour associated with particles near the SP/SSD threshold size (Pike et al., 2001b; Roberts et al., 2000). The gradient of corresponding IRM acquisition curves is asymmetric (Figures 5.4b$_1$-5.4b$_6$), which suggests a mixing of multiple coercivity/mineral phases that is consistent with indications from the FORC diagrams. For the selected 51 samples, four components are identified through IRM acquisition curve decomposition (Table 5.1). Component 1 ($B_{1/2}$ = 24-33 mT, DP = 0.20-0.22) and component 2 ($B_{1/2}$ = 54-69 mT, DP = 0.19-0.21), which together contribute more than 75% of the IRM, can

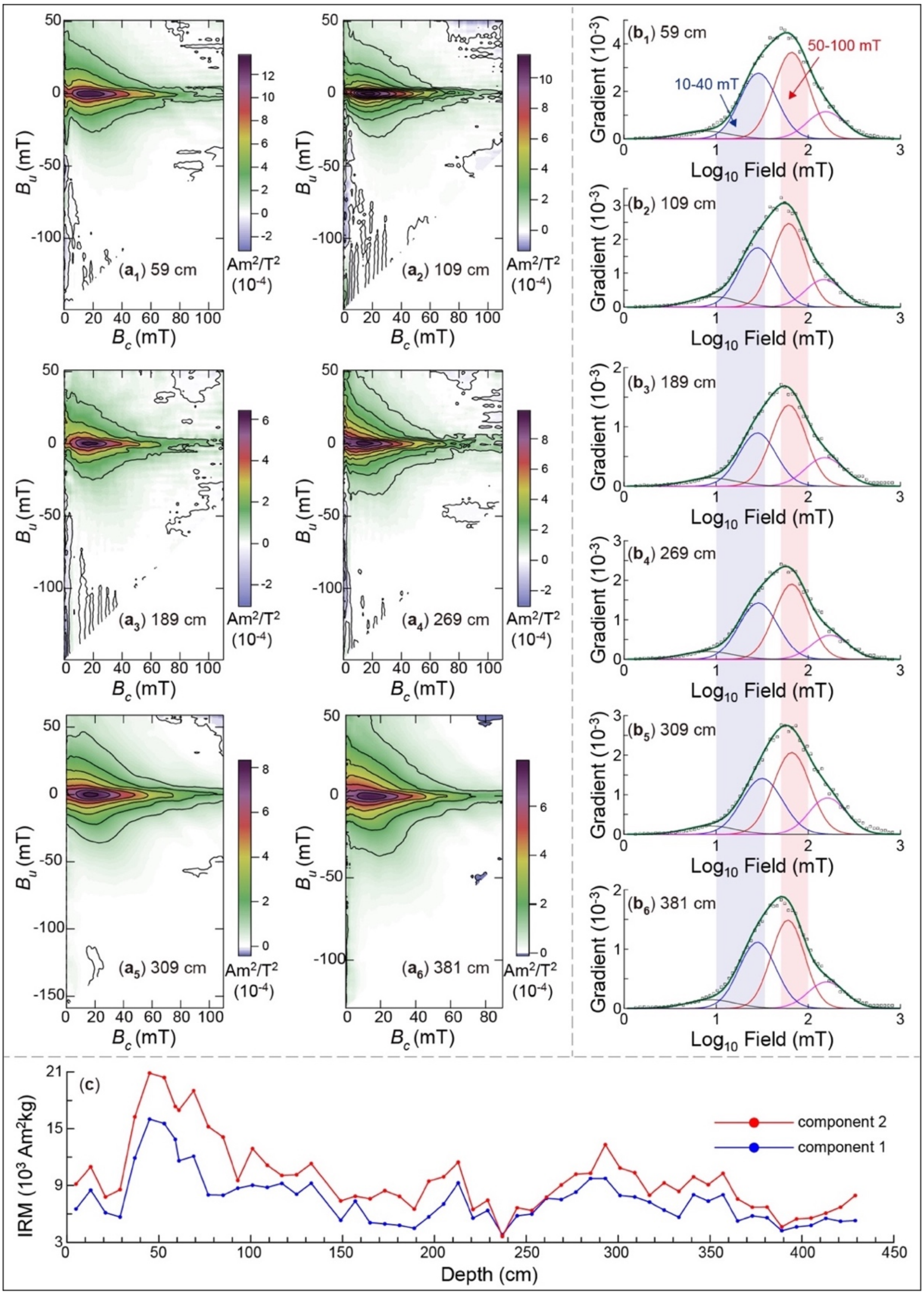

Figure 5.4 Magnetic properties of typical samples from core NP02. (a_1-a_6) FORC diagrams with VARIFORC (Egli, 2013) smoothing parameters of $S_{c,0} = 6$, $S_{c,1} = 9$, $S_{b,0} = 6$, and $S_{b,1} = 9$; (b_1-b_6) IRM acquisition curve decomposition. Blue, red, purple, grey, and green curves are for components 1, 2, 3, 4, and the sum of components, respectively; light blue and pink bands represent 10-40 and 50-100 mT field windows, respectively; and (c) down-core variations of IRM for components 1 and 2 derived from IRM acquisition curve decomposition.

Table 5.1 IRM decomposition results for 51 samples from core NP02.

Sample	Component 1			Component 2			Component 3			Component 4		
	$B_{1/2}$ (mT)	DP	contri.	$B_{1/2}$ (mT)	DP	contri.	$B_{1/2}$ (mT)	DP	contri.	$B_{1/2}$ (mT)	DP	contri.
5	28.2	0.21	32.9	67.6	0.19	46.2	169.8	0.2	14.6	9.8	0.27	6.3
13	27.5	0.22	34.9	69.2	0.2	45	173.8	0.2	13.2	8.3	0.27	7
21	25.7	0.22	33.8	61.7	0.21	42.9	162.2	0.2	14.4	9.8	0.27	8.9
29	27.5	0.21	31.3	60.3	0.2	47.2	166	0.21	13.4	9.5	0.26	8.1
37	28.2	0.2	33.9	66.1	0.18	46.2	177.8	0.2	12.3	9.8	0.27	7.6
45	27.5	0.2	33.3	64.6	0.18	43.4	169.8	0.2	17.1	7.2	0.27	6.2
53	28.2	0.21	33.2	64.6	0.18	43.6	162.2	0.2	17	7.2	0.27	6.2
59	28.8	0.2	35.5	66.1	0.19	44.3	154.9	0.2	14.7	7.6	0.27	5.5
61	26.3	0.21	32	58.9	0.19	46.7	151.4	0.2	15.5	9.1	0.27	5.8
69	26.9	0.21	29.9	60.3	0.2	47.1	151.4	0.21	16.4	9.5	0.27	6.6
77	26.3	0.21	27.8	56.2	0.19	52.8	151.4	0.21	12.3	9.5	0.27	7.1
85	26.9	0.21	28.6	55	0.18	50.7	147.9	0.22	13.7	8.3	0.27	7
93	28.8	0.21	38	57.5	0.19	41.6	151.4	0.22	13.4	9.5	0.27	7
101	26.9	0.2	32.5	57.5	0.19	46.4	151.4	0.21	14.8	10	0.27	6.3
109	28.2	0.2	33.8	61.7	0.18	42.9	147.9	0.2	15.7	9.5	0.26	7.6
117	28.8	0.22	38.3	61.7	0.2	41.8	158.5	0.22	13.3	8.5	0.27	6.6
125	26.3	0.22	35.7	61.7	0.19	44.9	158.5	0.21	15.1	7.9	0.27	4.2
133	27.5	0.21	35.2	61.7	0.18	43.2	154.9	0.21	15.8	8.1	0.27	5.8
149	25.1	0.22	33.5	53.7	0.18	46.3	151.4	0.22	14.5	7.6	0.27	5.7
157	28.8	0.22	37.4	63.1	0.2	40	158.5	0.22	15.7	7.9	0.26	6.9
165	26.9	0.21	30.7	61.7	0.19	46	158.5	0.2	17.1	8.3	0.27	6.1
173	25.1	0.21	28.8	60.3	0.19	49.3	158.5	0.2	16.2	8.7	0.27	5.8
181	25.7	0.21	29.3	58.9	0.2	48	154.9	0.22	17.6	9.3	0.26	5.2
189	28.2	0.2	31.1	61.7	0.19	45.1	151.4	0.21	17.5	8.9	0.27	6.2
197	24	0.22	30.4	57.5	0.21	50.5	158.5	0.22	13.6	7.2	0.27	5.5
205	25.1	0.21	32.3	57.5	0.2	45.4	151.4	0.21	14.8	8.9	0.26	7.6
213	29.5	0.21	35.6	60.3	0.2	44	154.9	0.21	15.3	9.1	0.26	5.1
221	27.5	0.21	37.6	60.3	0.18	43.8	154.9	0.21	13.5	8.1	0.27	5.1
229	30.9	0.21	36.5	69.2	0.2	42.7	182	0.2	13	9.1	0.27	7.8
237	33.1	0.22	40.3	69.2	0.21	38.4	177.8	0.2	12.7	9.1	0.27	8.6
245	31.6	0.22	37.5	69.2	0.21	43	177.8	0.2	11.7	9.1	0.27	7.8
253	29.5	0.22	36.6	64.6	0.19	38.8	166	0.22	18.7	8.7	0.27	6
261	29.5	0.22	39	67.6	0.19	39.6	166	0.21	16.8	8.7	0.27	4.6
269	28.8	0.21	35.9	66.1	0.19	43.2	173.8	0.2	14.6	8.1	0.27	6.3
277	28.2	0.22	35.4	64.6	0.19	43.6	166	0.2	14.7	8.7	0.27	6.3
285	28.2	0.22	39.4	66.1	0.19	41.7	169.8	0.2	12.4	8.7	0.27	6.4
293	26.3	0.22	36.8	66.1	0.21	50.2	158.5	0.22	9.1	6.3	0.26	4
301	28.2	0.21	32.6	67.6	0.18	44.6	173.8	0.22	17.4	8.7	0.27	5.4
309	31.6	0.22	32.2	66.1	0.2	42.9	162.2	0.2	19.2	8.7	0.26	5.7
317	29.5	0.2	36.1	64.6	0.19	39.7	158.5	0.21	18	9.5	0.27	6.2
325	26.9	0.21	33	63.1	0.2	47.7	173.8	0.22	14.2	7.9	0.27	5.1
333	26.9	0.21	31.8	58.9	0.18	47.2	162.2	0.22	15.3	7.9	0.27	5.7
341	28.8	0.2	34.1	63.1	0.19	42.2	158.5	0.21	16.1	9.8	0.27	7.6
349	28.8	0.2	33.5	64.6	0.19	41.4	151.4	0.21	16.5	9.8	0.27	8.7
357	26.9	0.22	35.6	64.6	0.2	45.7	177.8	0.2	13.2	7.6	0.27	5.5
365	26.9	0.2	31.9	61.7	0.19	46	162.2	0.21	16.6	7.9	0.27	5.5
373	28.2	0.21	37.5	64.6	0.18	43.4	173.8	0.21	14	8.1	0.27	5
381	28.2	0.2	36.1	60.3	0.18	43.4	158.5	0.2	14.5	8.9	0.26	6
389	25.1	0.21	39.6	58.9	0.2	43.3	173.8	0.21	9.7	8.9	0.27	7.5
397	25.1	0.21	36.8	60.3	0.19	43.4	173.8	0.21	12.5	8.9	0.27	7.4
405	25.7	0.21	36.8	61.7	0.2	42.9	173.8	0.21	12.8	8.3	0.27	7.5

be associated with the detrital vortex state and biogenic SD components indicated in FORC diagrams, respectively. Component 3 ($B_{1/2}$ = 148-182 mT, DP = 0.20-0.23) is similar to the low- and medium-coercivity components identified in Chinese loess-paleosol sequences (Spassov et al., 2003; Hu et al., 2013; R. Zhang et al., 2016), which is interpreted to represent detrital maghemite and/or pedogenic hematite. Component 4 ($B_{1/2}$ <10 mT, DP = 0.26-0.27) may represent pedogenic magnetic particles just above the SP/SSD threshold size, which correspond to the component indicated by the secondary peak at the origin of FORC diagrams. Downcore, IRMs of components 1 and 2 vary within a factor of 4.2 and 5.8, respectively (Figure 5.4c).

5.3.3. Normalized remanence records

RPI values can be estimated by normalizing the NRM by a laboratory-induced magnetization, such as IRM or ARM, to compensate for magnetic mineral concentration changes. Selection of a suitable RPI normalizer depends largely on the grain size distribution of the remanence carrier. ARM is mainly carried by finer magnetic particles, while IRM is also carried by coarser MD particles. Core NP02 samples are dominated by fine (SD and vortex state) magnetic particles, so ARM is chosen as the normalizer.

Our paleomagnetic and rock magnetic results satisfy conventional criteria for RPI studies (King et al., 1983; Tauxe, 1993), and further indicate that two components (hypothesized to be detrital and biogenic magnetite) with different magnetic grain size distributions dominate the magnetic mineral assemblage. The coercivities of the detrital and biogenic components do not overlap strongly over the 10-40 and 50-100 mT windows (blue and pink bands, respectively, in Figures 5.4b_1-5.4b_6). Therefore, demagnetization intervals of 10-40 and 50-100 mT are chosen to evaluate RPI signals recorded by the detrital and biogenic components, respectively. Due to the logarithmic spacing of demagnetization steps, the 10-40 mT and 50-100 mT demagnetization intervals are represented by the 10.7-41.6 mT and 52.8-100 mT measurements, respectively. The slopes of NRM/ARM derived for the detrital and biogenic components have similar RPI variations (Figure 5.5a), which indicates that a robust RPI signal is likely to have been recorded in core NP02 sediments, despite the presence of two magnetite sub-populations.

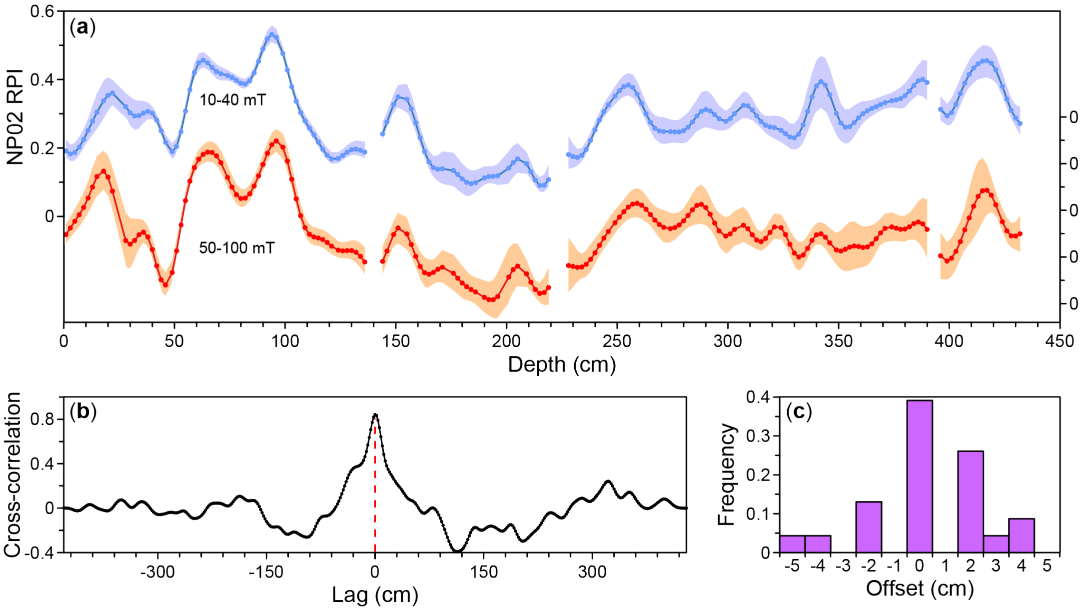

Figure 5.5 RPI estimates in core NP02. (a) RPI estimates from the detrital (10-40 mT, blue curve) and biogenic (50-100 mT, red curve) components with 95% confidence interval, respectively (filtered with a 15 cm cutoff); (b) cross-correlation results for the detrital and biogenic RPI estimates; and (c) distribution of relative offsets between the positions of peaks and troughs in detrital and biogenic RPI estimates.

5.3.4. Major element composition of glass shards

Three visible tephra layers are identified at depths of 137-143 cm, 220-227 cm, and 391-395 cm. Each tephra layer has homogeneous glass populations with relatively narrow compositional ranges (Figure 5.6), which excludes the possibility of tephra mixing due to bioturbation and/or simultaneous deposition. Major element compositions of the 34 analyzed glass shards fall into the rhyolite field (Figure 5.6a). In terms of potassium contents, tephra layers 1 (137-143 cm) and 3 (391-395 cm) belong to the low-K field while tephra layer 2 (220-227 cm) falls into the medium-K field (Figure 5.6b).

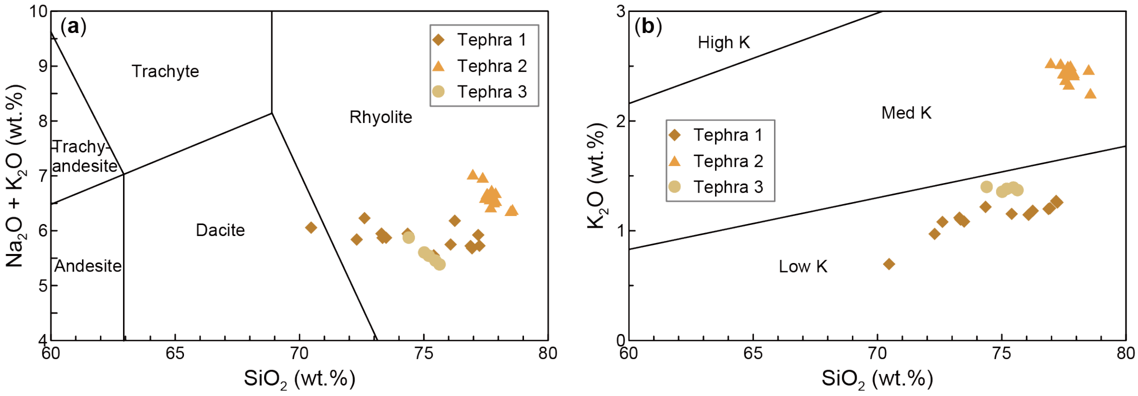

Figure 5.6 Geochemical characteristics of the glass shards from core NP02. (a) Classification of the total alkali-silica (TAS) diagram with composition fields from Le Bas et al. (1986); and (b) SiO_2-K_2O diagram with boundaries of high-, moderate-, and low-K rocks according to Gill (1981).

5.4. Discussion

5.4.1. Age model construction

Age models are often constructed using classical interpolation/regression techniques, which assume symmetrically/normally distributed age errors (Blaauw, 2010). However, ^{14}C calibrations often result in asymmetrical and multi-peaked calendar age uncertainties (Ramsey, 1995; Buck et al., 1999; Blaauw, 2010), and such asymmetrical distributions can lead to problems for age model construction. Consideration of full probability density functions can avoid such issues when estimating age-depth models (e.g., Blaauw and Christen, 2005; Ramsey, 2008; Lougheed and Obrochta, 2019). There is also an inherent depth uncertainty in sampling geological archives. For core NP02, an age model was constructed following Lougheed and Obrochta (2019) using age constraints provided by the tephra correlation and one calibrated ^{14}C age in which probability density functions are used, with incorporation of realistic errors for both age and depth.

Tephra are a product of large and explosive volcanic eruptions, which spread widely over land, sea, and ice. Unless a volcanic ash has been reworked long after deposition, the same tephra layer in different depositional sinks has effectively an identical age — an isochron — to within about a year and is considered to be geologically synchronous (Lowe, 2011). Therefore, tephra layers are excellent stratigraphic markers and are used widely for correlating and dating sedimentary successions (e.g., Grönvold et al., 1995; Mangerud et al., 1984; Smith et al., 2013; Matsu'ura et al., 2014; Rutledal et al., 2020). In the western NPO, tephra layers are generally dominated by vitric material from high-SiO_2 magmas that originated in subduction-related volcanic events from the Japanese archipelago or the Kamchatka Peninsula (Ninkovich et al., 1966; Horn et al., 1969). The Kamchatka Peninsula has the largest number of Quaternary calderas per unit of arc length in the world (Hughes and Mahood, 2008). Medium-K_2O glass shards with K_2O ~ 3 wt.% are common, while low-K shards are rarer in the late Pleistocene (Volynets, 1994; Portnyagin et al., 2019). Considering the relatively lower K_2O contents (< 2.52 wt.%) of glass shards from core NP02 (Figure 5.6b), it is unlikely that tephra layers in this core are from the Kamchatka Peninsula. In contrast, volcanoes in the Japanese archipelago produced late Quaternary tephra with typical K_2O contents of 1.0-3.0 wt.% (Machida and Arai, 2003; Aoki and Machida, 2006), so we focus correlation efforts on volcanic events in the Japanese archipelago.

By comparing glass shard chemistry results with data reported in previous studies, each tephra layer from core NP02 has been identified and correlated with tephra markers. Although Na_2O contents do not overlap perfectly, major element compositions of 14 analyzed glass shards for tephra layer 1 are in good agreement with that of the To-Of tephra, which has been dated to occur in late MIS 3 (32-40 ka) (Smith et al., 2013; Matsu'ura et al., 2014). The glass shard chemistry of tephra layers 2 and 3 are highly similar to that of the Spfa-1 and Kt-3 tephra, respectively (Table 5.2). The Spfa-1 tephra has an AMS ^{14}C age of 45.105 – 46.560 cal. ka BP (Uesawa et al., 2016), while Kt-3 has an uncalibrated AMS ^{14}C age of 54.616 ± 0.857 ka BP (Amma-Miyasaka et al., 2020). These tephra markers have been reported widely in the NPO; co-occurrences of To-Of and Spfa-1 have been reported in cores MR99-K04 and MR98-03 (Aoki, 2000), which are close to core NP02 (Figure 5.1).

Table 5.2 Average major-element compositions of glass shards from core NP02 and correlative tephra markers (normalized).

	Tephra 1		Tephra 2		Tephra 3		To-Of[a]		Spfa-1[a]		Kt-3[a]	
	Avg.	±1σ	Avg.	±1σ	Avg.	±1σ	Avg.	±1σ	Avg.	±1σ	Avg.	±1σ
SiO_2	74.52	2.16	77.74	0.40	75.14	0.48	77.1	0.74	77.36	0.75	74.73	0.45
TiO_2	0.37	0.07	0.14	0.01	0.35	0.02	0.42	0.07	0.15	0.04	0.35	0.03
Al_2O_3	13.83	1.2	12.31	0.24	12.84	0.22	12.65	0.29	12.37	0.48	12.92	0.39
FeO	1.92	0.32	1.48	0.09	2.84	0.04	1.97	0.23	1.47	0.16	2.76	0.16
MnO	0.08	0.08	0.05	0.07	0.08	0.07	0.08	0.06	0.06	0.02	0.1	0.02
MgO	0.51	0.14	0.16	0.03	0.44	0.03	0.4	0.07	0.18	0.06	0.46	0.05
CaO	2.66	0.69	1.45	0.03	2.68	0.04	2.22	0.21	1.57	0.22	2.69	0.21
Na_2O	4.76	0.27	4.2	0.15	4.19	0.18	3.91	0.12	4.1	0.19	4.37	0.17
K_2O	1.12	0.15	2.44	0.07	1.38	0.02	1.25	0.06	2.7	0.12	1.56	0.12
P_2O_5	0.05	0.05	0.03	0.02	0.06	0.03			0.03	0.03	0.06	0.03
Total	100		100		100		100		100		100	
n	14		15		5		15		114		30	

[a] Average composition of the To-Of tephra is from Machida and Arai (2003); Spfa-1 and Kt-3 are from Amma-Miyasaka et al. (2019).

The To-Of tephra does not provide a suitable age constraint for core NP02 because of its large age uncertainty. However, its occurrence suggests that sediments above this layer were deposited after 40 ka, a time when radiocarbon can play a role in chronology development. Therefore, discrete samples (3 cm in length) were taken continuously from the upper 137 cm of core NP02, and were then washed, sieved, and observed under the microscope to seek foraminifera. Foraminifera are generally preserved poorly in sediments deposited below the CCD, and foraminifera (*N. pachyderma* sinistral) were only identified at a depth of 49-52 cm. A sample from this depth yielded a radiocarbon date of 28.413 (28.077-28.714, 2σ) cal. ka BP.

Ages for the upper (above 50 cm) and lower (below 395 cm) parts of core NP02 are estimated by polynomial fitting and linear regression, respectively. Based on upward extrapolation, the age estimate for the core-top (0 cm) is 21.07 ka. An absence of surficial sediments is common for gravity coring where the surface layer is removed by impact of the core on the seafloor (e.g., Adelseck and Anderson, 1978; Karlin, 1990; Skinner and McCave, 2003). After removal of 17 cm for the three tephra-containing sediment intervals, which are considered as instantaneous deposits, the mean sedimentation rate for core NP02 based on our age model is ~11.6 cm/kyr (Figure 5.7).

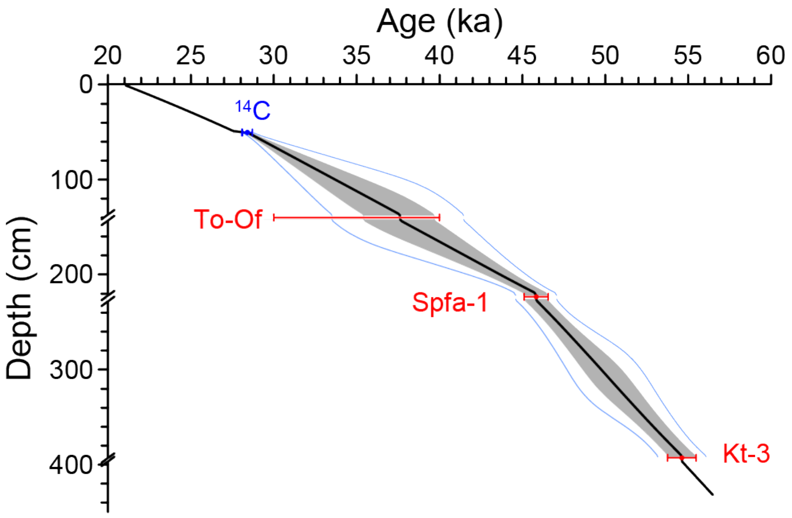

Figure 5.7 Age-depth model for core NP02. Ages for the upper (<50 cm), intermediate (50-395 cm), and lower (>395 cm) parts are estimated from polynomial fitting, probability density functions (Lougheed and Obrochta, 2019), and linear regression, respectively. Grey shaded areas and blue lines indicate the 1σ and 2σ confidence intervals, respectively. The radiocarbon date and tephra layers with age errors are also indicated.

5.4.2. Core NP02 RPI characteristics and recording fidelity

Remanence lock-in in sediments can lead to depth offsets between the sediment/water interface and the recorded remanence (Verosub, 1977; Tauxe, 1993). Recent analyses of remanences carried by detrital and biogenic components indicate that there is no relative lock-in depth offset between RPI signals recorded by these components within marine sediments (Ouyang et al., 2014; L. Chen et al., 2017). For core NP02, cross-correlation results for the detrital and biogenic components suggest no phase lag for the whole sediment sequence (Figure 5.5b). When comparing the depth positions of all RPI maxima and minima in the sequence, the distribution of relative lock-in depth offsets is centered on zero offset (Figure 5.5c), which is consistent with the cross-correlation results. However, relative lock-in variations produce a maximum depth error of 5 cm (Figure 5.5c). For continuous high-resolution RPI studies, any relative lock-in depth offsets could be a crucial limitation when assessing leads and lags between millennial scale climatic variations and, therefore, should be considered as part of the age uncertainty (Roberts et al., 2013). The relative depth offset induces an age error <0.5 kyr for points in the RPI record from core NP02, which should have little effect on comparisons with other RPI stacks/records.

Core NP02 RPI estimates are plotted with respect to age in Figure 5.8a. The RPI minima centered at ~27 ka and ~43 ka in core NP02 are accompanied by aberrant inclinations, which are likely associated with the Rockall and Laschamp excursions (Bonhommet and Babkine, 1967; Bonhommet and Zähringer, 1969; Channell et al., 2016b). The Laschamp excursion is the most pervasively documented and studied Quaternary geomagnetic excursion, which occurred at ~41 ka and lasted less than 3 kyr (Laj et al., 2000; Wagner et al., 2000). During the Laschamp excursion, inclination directional changes have been observed from locations with a broad geographical coverage (e.g., Laj et al., 2006 and references therein; Ferk and Leonhardt, 2009; Nowaczyk et al., 2012; Caricchi et al., 2019). However, geomagnetic field behaviour during the Laschamp excursion over the NPO seems to have been different from that over the rest of the world; reversed polarity inclinations have not been recorded in NP02

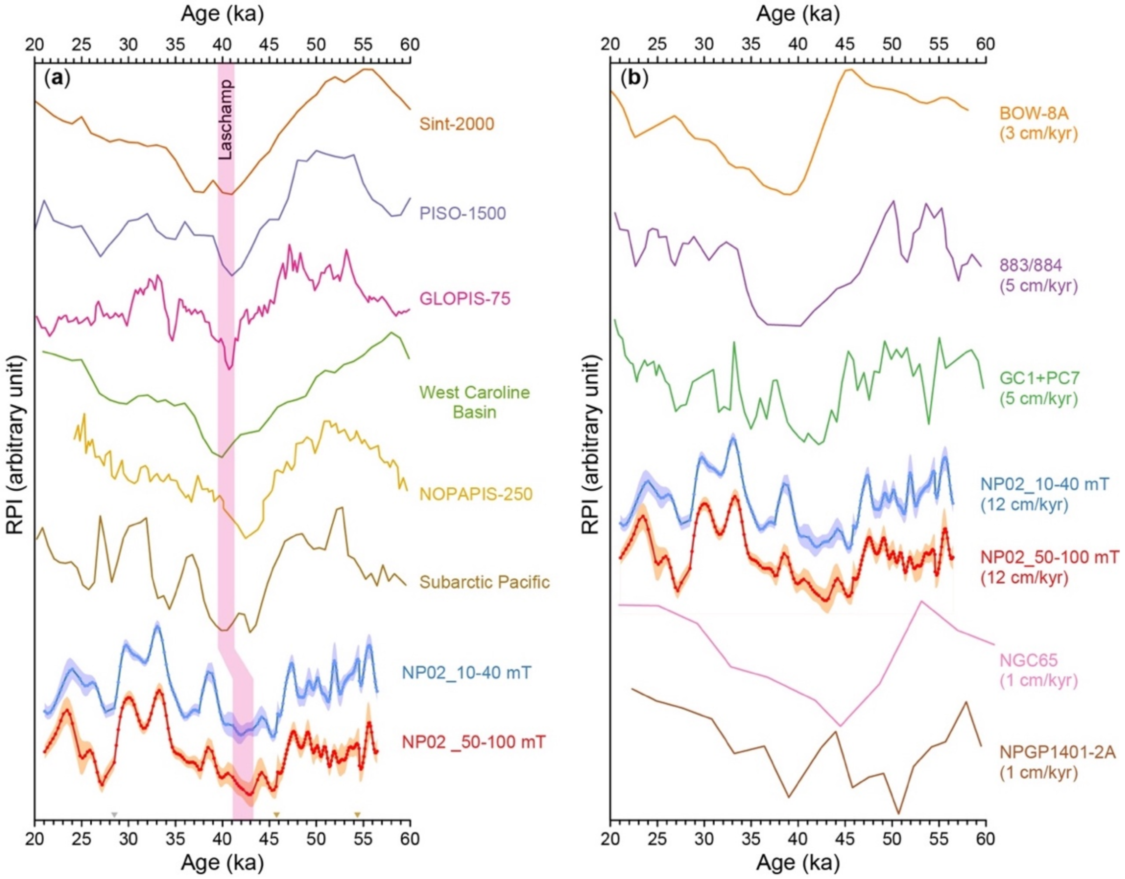

Figure 5.8 Comparisons of core NP02 RPI estimates with (a) global stacks (Sint-2000 (Valet et al., 2005), PISO-1500 (Channell et al., 2009), and GLOPIS (Laj et al., 2004)); regional stacks from the equatorial (West Caroline Basin stack, Yamazaki et al., 2008), mid-latitude (NOPAPIS-250, Yamamoto et al., 2007), and subarctic Pacific Ocean (Zhong et al., 2020); and (b) individual RPI records of core BOW-8A (Okada et al., 2005), Site 883/884 (Roberts et al., 1997; Roberts, 2008), core GC1+PC7 (Inoue and Yamazaki, 2010; Yamazaki et al., 2013a), core NGC65 (Yamazaki, 1999), and core NPGP1401-2A (Shin et al., 2019). The Laschamp excursion is denoted by the pink shaded area. Positions of the radiocarbon date (grey triangle) and tephra layers (brown triangle) from core NP02 are indicated in (a). All stacks and RPI records are rescaled to the 0-1 range.

(Figure 5.9) and other NPO cores (e.g., Roberts et al., 1997; Okada et al., 2005; Inoue and Yamazaki, 2010; Shin et al., 2019; Xiao et al., 2020; Zhong et al., 2020). Also, a model for the Laschamp excursion predicts that the field intensity over the Pacific Ocean remained relatively high compared to most locations on Earth (Leonhardt et al., 2009). The different geomagnetic field behaviour over the NPO during the Laschamp excursion may have resulted from a relatively large non-dipole to dipole field ratio, which remains to be explored with the aid of higher-resolution records.

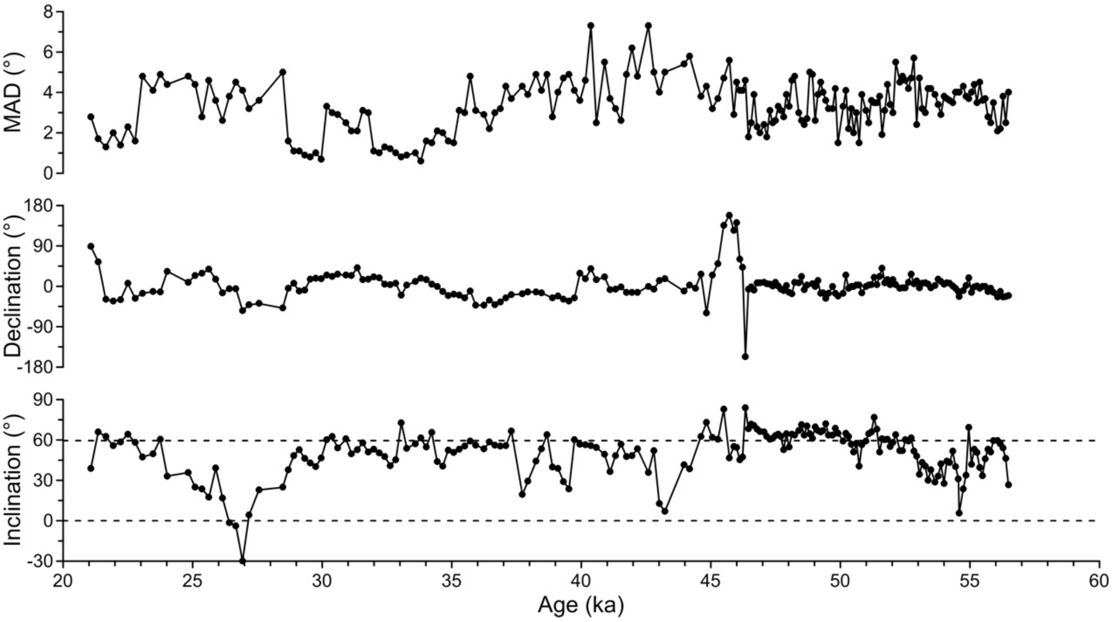

Figure 5.9 Temporal variations of ChRM inclinations, declinations, and MAD values.

Core NP02 RPI variations are compared with global RPI stacks (Sint-2000, PISO-1500, and GLOPIS-75) and regional stacks from the equatorial (West Caroline Basin stack), mid-latitude (the NOPAPIS-250 stack), and subarctic Pacific Ocean (Laj et al., 2004; Valet et al., 2005; Yamamoto et al., 2007; Yamazaki, 2008; Channell et al., 2009; Zhong et al., 2020) (Figure 5.8a). The RPI minimum centered at ~43 ka in core NP02 correlates with the marked RPI Laschamp excursion minimum at ~40-42 ka identified in all other stacks. The lag in recording of this RPI minimum in core NP02 may be due to age model imprecision (Figure 5.7) and variable sedimentation rates. Before the Laschamp excursion, all records have broad RPI maxima in the ~47-55 ka interval. After the Laschamp excursion, the records have a generally increasing trend to ~30 ka. Although the reference stacks generally suggest a similar overall pattern, there are still differences in their fine detail. For example, two peaks at ~47 ka and 53 ka occur in the GLOPIS-75 stack, which are not observed in the other stacks that have a broad maximum at ~47-55 ka. Also, the subarctic Pacific stack has larger variations after the Laschamp excursion than the other stacks, particularly compared to the other regional Pacific stacks. Zhong et al. (2020) attributed the contrasting subarctic North Pacific RPI pattern to regionally variable geomagnetic field behaviour. However, this large variability is not observed in the geomagnetic model of Ziegler and Constable (2015), which covers a longer time duration and suggests lower variability and less significant recording of excursions in the Pacific Ocean compared to the Atlantic Ocean (Ziegler and Constable, 2015). Given that stacking of multiple records with variable resolution can distort amplitude features and smooth high-frequency and local geomagnetic variations, we further compare individual RPI records from the NPO and its marginal seas (Roberts et al., 1997; Yamazaki, 1999; Okada et al., 2005; Roberts, 2008; Inoue and Yamazaki, 2010; Yamazaki et al., 2013a; Shin et al., 2019) (Figure 5.8b). To aid comparison, only records with geomagnetism-independent age models are considered. The RPI record of core NP02 resembles that of GC1+PC7, which validates the core NP02 RPI signal. Apart from this comparison, consistency among individual records is less obvious than among the stacks, which may be associated with age model imprecisions and variable sedimentation rates. Nevertheless, pronounced RPI amplitude variations are recorded at Site 883/884, core GC1+PC7, and core NP02 from mid to high latitudes. In contrast, core BOW-8A from the Bering Sea and cores from latitudes lower than 40° N have less significant amplitude variations, and it is difficult to ascertain whether the lower variability is a result of genuine geomagnetic field behaviour or imperfect recording that smooths the large variability due to low sedimentation rates. The model of Ziegler and Constable (2015) is based mainly on records from the equatorial Pacific Ocean, so their documented low field variability over the Pacific Ocean could be biased; more records from the mid to high latitude Pacific Ocean are required to improve our understanding of Pacific geomagnetic field behaviour.

5.5. Conclusions

Dating of Quaternary NPO sediments is challenging because they were usually deposited below the CCD. A geomagnetism-independent age model for NPO core NP02 is established with the aid of tephra correlation (using the To-Of, Spfa-1, and Kt-3 tephra layers) and one radiocarbon date. Detrital vortex state and biogenic SD magnetite in sediments from core NP02 both record RPI variations faithfully, which indicates that RPI-assisted chronology is a promising dating tool for NPO sediments. To assess the reliability of RPI determinations, apart from the common criteria suggested by Tauxe (1993), assessment of component-specific magnetic properties, as presented here, is also required. For sediments that contain more than one magnetic mineral component, the RPI record should be checked to ensure that each component records consistent RPI variations. Moreover, relative depth offsets in recording of components needs to be checked to assess whether this provides further age uncertainties that should be taken into consideration.

Chapter 6

Latitudinal shifts of northern hemisphere westerlies linked to the Atlantic meridional overturning circulation

Abstract Westerlies are a major component of the global atmospheric circulation system and understanding their long-term dynamics is essential for assessing interactions within the climate system. However, little is known about their long-term variability and underlying driving mechanisms. Marine sediments from the NPO preserve relatively continuous dust records and, thus, provide sensitive archives of past changes in the northern hemisphere westerlies. NPO core NP02 is located downwind of Asian dust source areas, and is sensitive to meridional westerly shifts. Relatively constant *L*-ratio values and stable Al substitution indicate that HIRM variations reflect changes in the absolute concentration of high-coercivity magnetic minerals. We demonstrate that HIRM is dominated by the hematite concentration in core NP02, and that it can be used as a proxy for dust content. We reconstructed a dust record from core NP02 for the ~21-57 ka interval, and identify abrupt dust content decreases at ~25, 39, 48, and 55 ka that can be linked to Heinrich events 2, 4, 5, and 5a. The low dust contents are interpreted to have been caused by southward shifts of the westerlies in association with slowdown of the Atlantic meridional overturning circulation (AMOC). AMOC slowdown during Heinrich events reduces ocean heat transport to high latitudes and increases the meridional temperature gradient, which leads to a strengthening and southward shift of the westerlies. The main westerly axis, thus, shifts away from the core NP02 site during Heinrich events and, therefore, low dust contents are recorded in core NP02. In contrast, a small AMOC reduction during Heinrich event 3 (H_3) did not change the meridional temperature gradient markedly; therefore, the westerly shift was not significant, and there was no abrupt dust content decrease in core NP02 during H_3.

6.1. Introduction

Westerlies are the prevailing winds that blow from west to east between latitudes of 30° and 60° (Toggweiler, 2009). Westerlies are a major component of the global atmospheric circulation system and play an essential role in transporting heat and moisture, and in balancing the energy distribution between low- and high-latitude regions (e.g., Shao et al., 2011; An et al., 2012; Boex et al., 2013; Mölg et al., 2014). The southern hemisphere westerlies are modulated by precession (Lamy et al., 2019), and observations and climate modelling indicate that they have shifted poleward since the 1960s and that this trend is correlated with modern global warming (Thompson and Solomon, 2002; Chen and Held, 2007; Archer and Caldeira, 2008; Chavaillaz et al., 2013). However, much less is known about the long-term variability of the northern hemisphere westerlies and the mechanisms that drive them.

Studies of long-term northern hemisphere westerly variations rely mainly on terrestrial and marginal sea sediments. For example, increased sediment grain size in the central CLP suggests intensified westerlies over the late Cenozoic, which has been linked to development of northern hemisphere ice sheets (Sun et al., 2008). Westerly (grain size >25 μm) and summer monsoon (normalized and averaged carbonate content and total organic carbon flux) records from Lake Qinghai have an anti-phase relationship since 32 ka, which indicates that westerlies dominated the last glaciation, while the Asian summer monsoon prevailed in the Holocene (An et al., 2012). Sediment provenance shifts in the Japan Sea over the past 60 ka suggest that the main westerly axis was located to the south and north of the Tibetan Plateau during stadials and interstadials, respectively (Nagashima et al., 2011). However, unambiguous proxy indicators for the westerlies are not easy to obtain because these regions are also affected by monsoon circulation (e.g., Tian et al., 2013; Seo et al., 2014; Wang et al., 2018).

Relatively continuously deposited and undisturbed deep-sea sediments in the NPO preserve environmental records from which past westerly behaviour can be inferred. Eolian dust, which originates from arid regions of the Asian interior, is transported to the NPO by the westerlies (Rea et al., 1985; Rea and Leinen, 1988; Rea, 1994; Zhao et al., 2006; Maher et al., 2010), and dominates the major detrital component of NPO sediments (Windom, 1969; Ferguson et al., 1970). Studies from the NPO indicate that larger dust fluxes usually occurred in glacial stages (e.g., Hovan et al., 1989, 1991; Serno et al., 2017), with coarser grain sizes associated with stronger westerlies (Rea, 1994). Periodic changes have been recognized in Quaternary dust records, such as Milankovitch periodicities (eccentricity, obliquity, and precession), and 52 kyr signals (Janecek and Rea, 1984; Pisias and Leinen, 1984; Morley et al., 1987; Hovan et al., 1991). The 100-kyr and 41-kyr signals dominate the dust flux and grain size records, respectively (Rea, 1994), while the 52 kyr signal has been interpreted to result from nonlinear interactions between external insolation forcing and internal climate feedback mechanisms (Hovan et al., 1991). However, NPO sediments are usually deposited below the CCD, which prevents development of continuous oxygen isotope records. Therefore, most studies are not constrained by precise time frameworks, which hampers further understanding of westerly forcing mechanisms on sub-orbital and millennial timescales.

Core NP02 is situated downwind of Asian source areas, and adjacent to the main westerly axis. This location is, therefore, expected to be sensitive to shifts in the westerlies. In this chapter, a dust record is presented for core NP02 over the ~21-57 kyr interval to discuss potential driving factors for recorded dust content changes.

6.2. Material and methods

6.2.1. Core description

Core NP02 is a 4.35 m gravity piston core raised at 40.48°N, 150.10°E. It was recovered from the NPO abyssal plain at a water depth of 5,177 m, downwind of Asian interior dust source areas (Figure 6.1). Sediments are composed mainly of clay with three tephra layers, which are identified as the To-Of, Spfa-1, and Kt-3 tephra (Section 5.4.1).

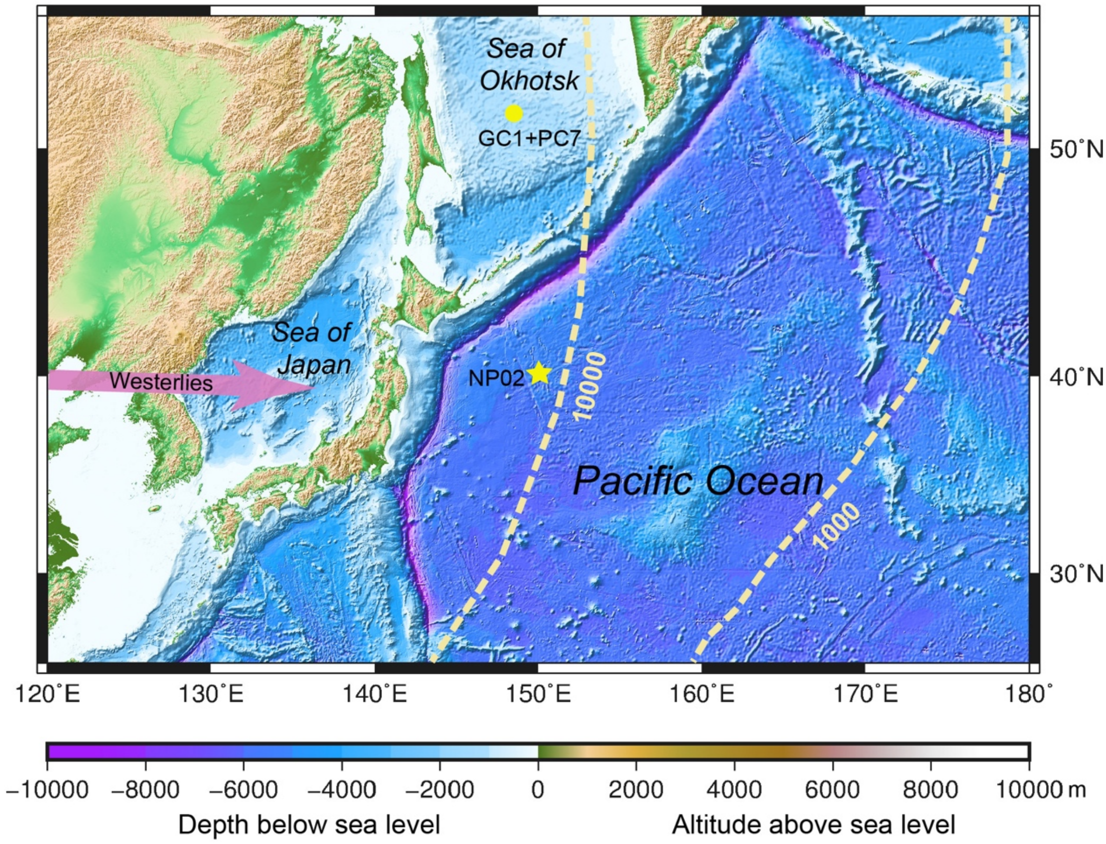

Figure 6.1 Schematic map of the NPO. The locations of core NP02 (yellow star) and cores GC1+ PC7 (yellow circle) are indicated. The arrow represents the direction of the main modern westerly axis (Merrill et al., 1989); dashed lines represent mineral aerosol fluxes to the NPO (in mg/m^2/yr, from Duce et al. (1991)).

6.2.2. Methods

Magnetic remanences were measured for cubic samples (8 cm^3) with a 2-G Enterprises Model 760R cryogenic magnetometer. IRMs were imparted in DC fields of 1 T, -0.1 T, and -0.3 T, which are defined as the saturation IRM (SIRM), $IRM_{-0.1\,T}$, and $IRM_{-0.3\,T}$, respectively. The HIRM is defined as HIRM = (SIRM + $IRM_{-0.3\,T}$)/2 (Robinson, 1986); the $HIRM_{-0.1\,T}$ and the L-ratio are defined as $HIRM_{-0.1\,T}$ = (SIRM + $IRM_{-0.1\,T}$)/2 and L-ratio= HIRM/[0.5 * (SIRM +$IRM_{-0.1\,T}$)] (Q. Liu et al., 2007), respectively.

Trace element and rare earth element (REE) analyses were made using a Thermo Scientific XSERIES 2 ICP-MS. Samples were freeze-dried and digested with HF-HNO_3 (1:1) in closed Teflon bottles before ICP-MS analysis. Analytical accuracy was assessed with the GSD-9 standard, blank, and replicate measurements.

Clay minerals were determined by X-ray diffraction. Prior to measurement, samples were treated with 15% H_2O_2 and then 5% HCl to remove organic matter and carbonate, respectively. Clay-sized particles (< 2 μm) were extracted and concentrated with a centrifuge, and were subsequently smeared on glass slides. The analysis was performed using a Rigaku D/max 2500 diffractometer with CuKα radiation at 40 kV voltage and 100 mA current intensity. Peak parameters were estimated semi-quantitatively following the description of Biscaye (1965). Relative contents of smectite, illite, and kaolinite + chlorite were estimated based on peak positions at 1.7 nm, 1 nm, and 0.7 nm, respectively (Holtzapffel, 1985). Relative contents of kaolinite and chlorite were separated according to the relative 0.357 nm and 0.354 nm peak areas.

6.3. Results

6.3.1. Age model

The initial age model for core NP02 was constructed based on tephra correlation and one radiocarbon date (Chapter 5). Here, we tuned the core NP02 RPI record to RPI variations from subarctic Pacific Ocean cores GC1+PC7 (Figure 6.2), which have age models based on oxygen isotope stratigraphy (Inoue and Yamazaki, 2010; Yamazaki et al., 2013a). Then, RPI age tie points, together with age constraints based on tephra correlation and one radiocarbon date (Chapter 5), were used to construct a refined age model following Lougheed and Obrochta (2019). Ages for the upper and lower parts of core NP02 were extrapolated by polynomial fitting and linear regression, respectively. The core NP02 RPI record is estimated to span the 21-57 ka interval.

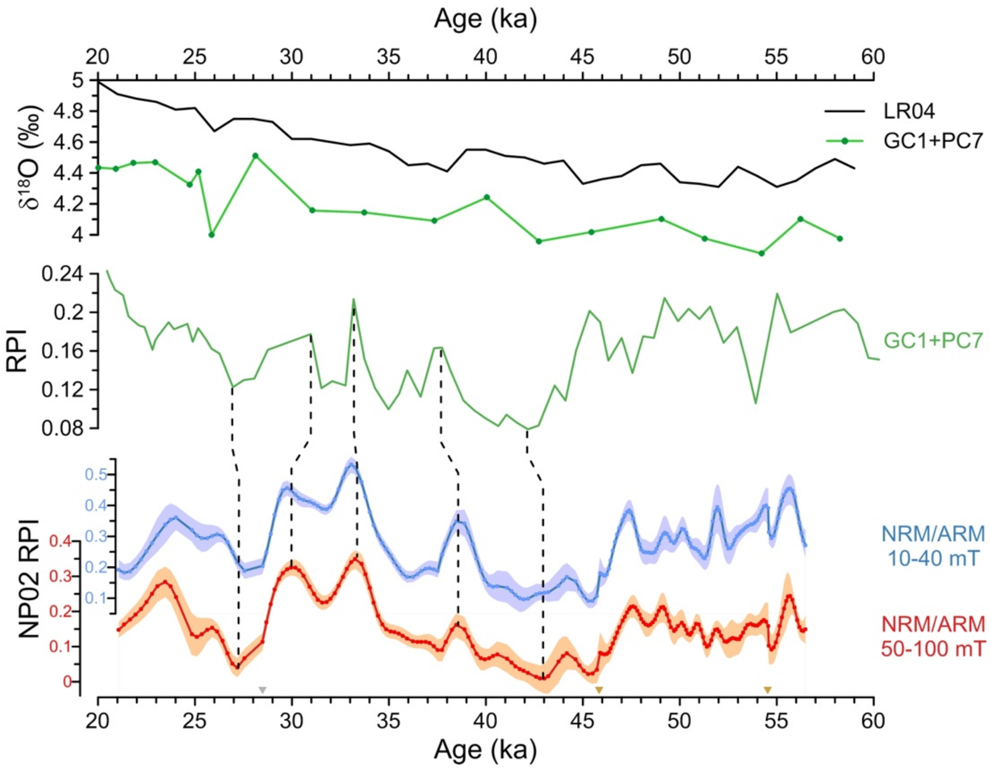

Figure 6.2 Correlation of RPI estimates from core NP02 with the RPI record of cores GC1+PC7 (Inoue and Yamazaki, 2010; Yamazaki et al., 2013). Grey and brown triangles indicate the radiocarbon date and tephra correlations discussed in Chapter 5; black dashed lines indicate RPI tie points.

6.3.2. Rock magnetic results

HIRM is used widely to evaluate the concentration of high-coercivity magnetic minerals (e.g., Robinson, 1986; Bloemendal et al., 1992; Yamazaki and Ioka, 1997; Itambi et al., 2009; Ortega-Guerrero et al., 2020). However, its interpretation can be complicated by changes in the properties of high-coercivity magnetic minerals, such as the coercivity distribution and isomorphous cation substitution (Wells et al., 1999; Q. Liu et al., 2007; Jiang et al., 2012). The *L*-ratio enables semi-quantitative identification of coercivity variations (Q. Liu et al., 2007). Samples from the Spfa-1 and Kt-3 tephra layers have relatively high and low *L*-ratio values, respectively; some neighbouring samples also have abnormal *L*-ratio values (i.e., samples near the Spfa-1 and Kt-3 tephra layers have relatively high and low values, respectively). This is likely to result from contamination by volcanic ash. After excluding the tephra samples and samples with abnormal *L*-ratio values, *L*-ratio variations fall within a relatively narrow band of values (shaded area in Figure 6.3a), which indicates that the Al substitution degree is relatively stable (Figure 6.3b). Therefore, HIRM values can be interpreted as a proxy for the absolute concentration of high-coercivity magnetic minerals.

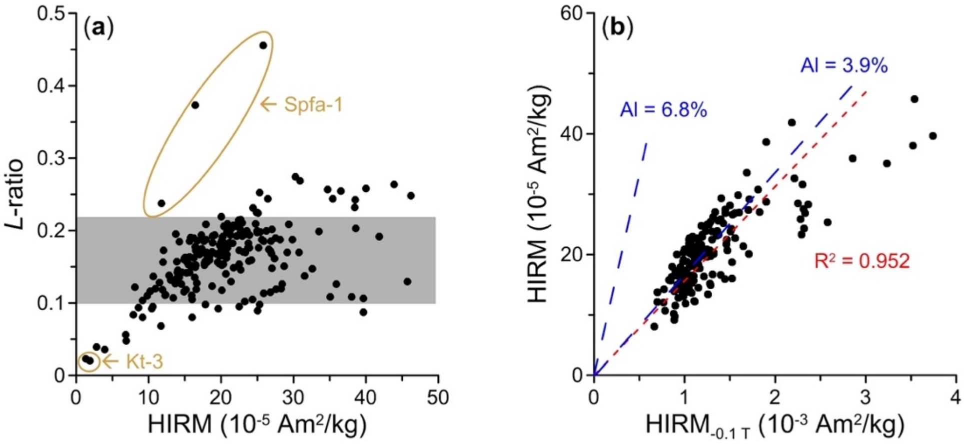

Figure 6.3 (a) Correlations between the *L*-ratio and HIRM for samples from core NP02; and (b) relationship between HIRM and $HIRM_{-0.1\ T}$. Red and blue dashed lines in (b) denote the regression fitting curve and hematite with different Al substitution from Hu et al. (2016), respectively.

6.3.3. Non-magnetic results

Clay mineral assemblages from core NP02 are mainly composed of smectite (14.9-62.4%), illite (25.7-60.5%), chlorite (6.0-23.9%), and kaolinite (0.1-3.8%) (Figures 6.4a-6.4d). The relative proportion of smectite increased gradually in the ~54-45 ka and ~41-30 ka intervals, before declining at ~27 ka. The relative proportion of illite has an opposite trend to that of smectite. The relative proportion of chlorite decreased in the ~55-45 ka

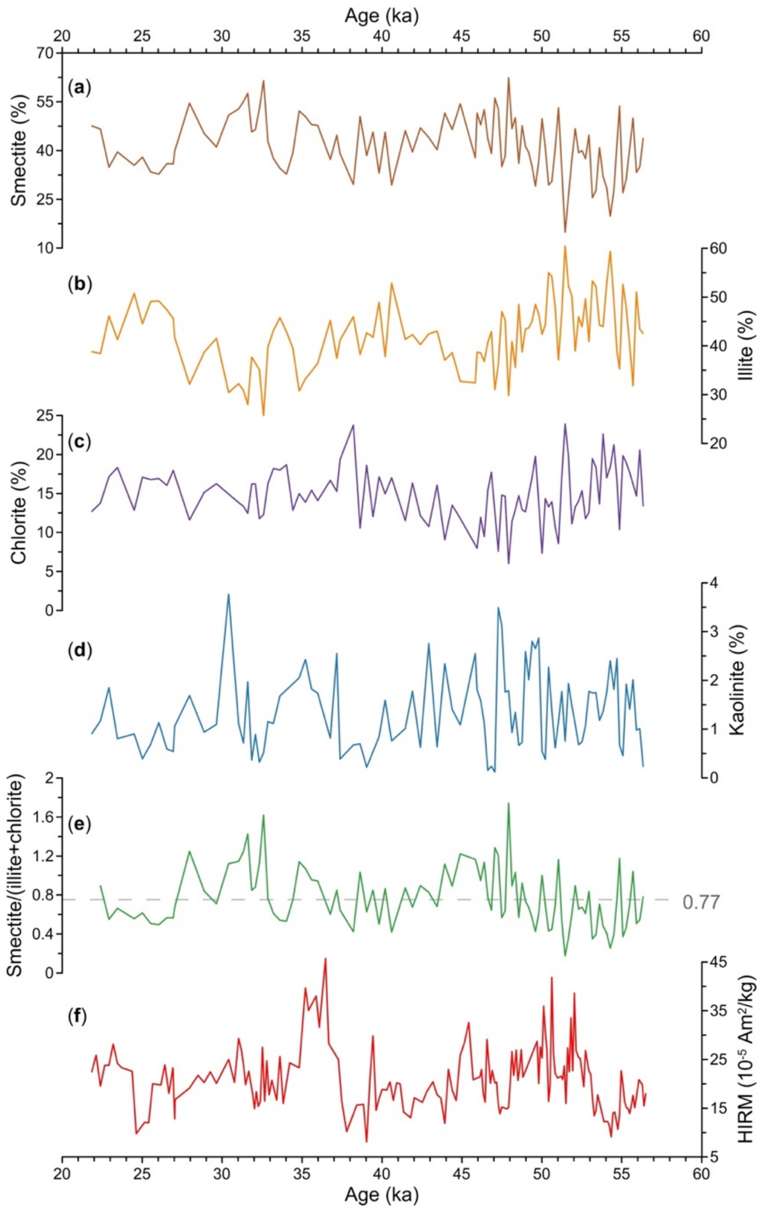

Figure 6.4 Temporal variations of (a-d) the relative proportions of smectite, illite, chlorite, and kaolinite, respectively; (e) smectite/(illite + chlorite); and (f) HIRM. The dashed line in (e) is the mean smectite/(illite+ chlorite) value.

interval, and was then relatively stable. Compared to the other three clay minerals, kaolinite makes a negligible contribution to the clay mineral assemblage. In a lanthanum-thorium-scandium (La-Th-Sc) ternary diagram (Figure 6.5), core NP02 data fall in the same area as data for material from Asian interior areas, which indicates that the sediment is sourced mainly from the Asian interior.

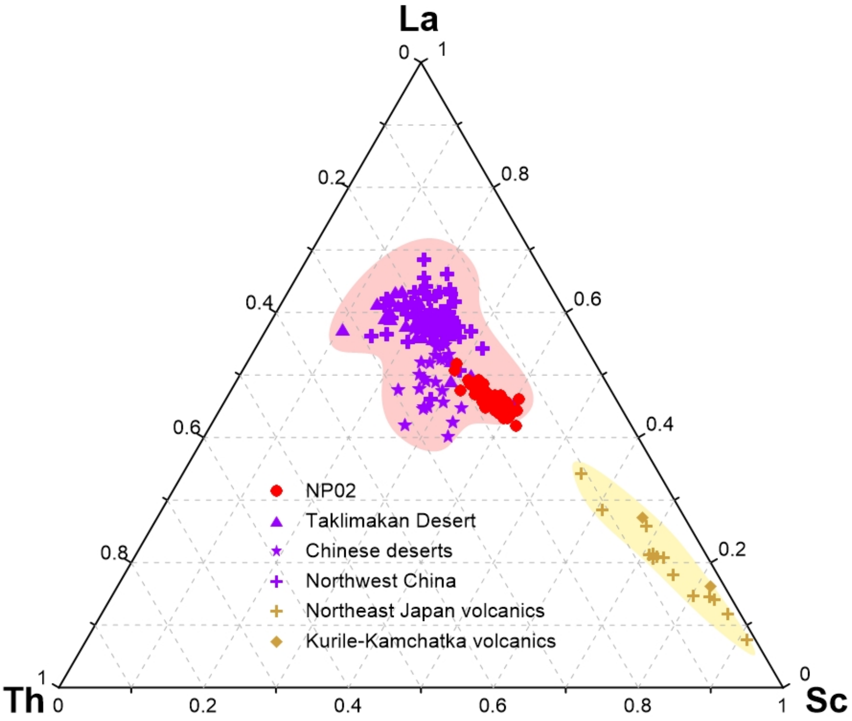

Figure 6.5 La-Th-Sc ternary diagram for the siliciclastic fraction of samples from core NP02. Desert samples are from the Tarim Basin (Yang et al., 2007), northwestern China (Hu and Yang, 2016), and other Chinese deserts (W. Zhang et al., 2016); results for volcanic rocks from northeastern Japan (Masuda and Aoki, 1979) and the Kurile-Kamchatka peninsulas (Weber et al., 1996) are shown for comparison.

6.4. Discussion

6.4.1. Proxy interpretation

Hematite and goethite are magnetically weak, but stable, imperfect antiferromagnetic minerals that usually occur as nanoparticles in the Asian interior. They have long atmospheric residence times and can be transported over long distances (Maher et al., 2010; Maher, 2011); therefore, they have been studied widely in relation to dust contents (e.g., Yamazaki and Ioka, 1997; Larrasoaña et al., 2003; Watkins and Maher, 2003; Dorfman et al., 2015; Zhang et al., 2020). HIRM provides an indication of the hematite and goethite concentration (Forster and Heller, 1997; Thompson and Oldfield, 1986). Goethite is often volumetrically more abundant than hematite in sediments. For example, the goethite concentration is 2 to 3 times higher than that of hematite in loess-paleosol sequences on the CLP (Ji et al., 2004). However, goethite concentration is difficult to measure because less than 20% of its IRM can be acquired at applied fields of up to 2 T (France and Oldfield, 2000; Rochette et al., 2005). Therefore, HIRM provides more information about the concentration of hematite than goethite. In core NP02, the occurrence of hematite has been identified by IRM acquisition curve decomposition (Section 5.3.2). Considering that hematite cannot have an authigenic origin in the NPO (Yamazaki and Ioka, 1997), it is assumed that it has been transported entirely as dust. The magnetization acquired above 300 mT has a linear relationship with IRM carried by component 3 of the IRM decomposition results presented in Section 5.3.2 (Figure 6.6). Therefore, HIRM is used here as a proxy for hematite concentration, similar to the interpretation of Doh et al. (1988), and so to indicate the dust content of core NP02.

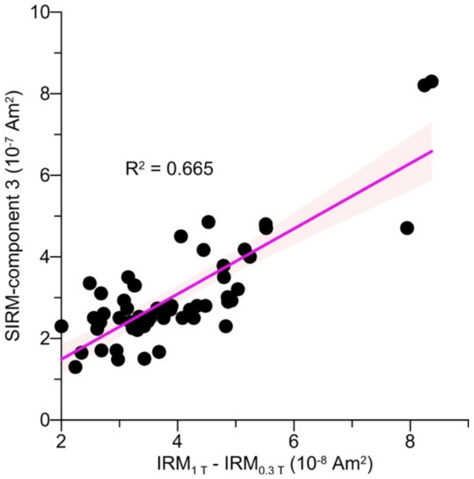

Figure 6.6 Correlation between IRM acquired above 300 mT and the SIRM of component 3.

Clay minerals are continental weathering products, whose compositional changes are influenced dominantly by sedimentary provenance and climatic conditions (e.g., Arnold et al., 1995; Liu et al., 2016). Given that core NP02 sediments are sourced mainly from the Asian interior, clay mineral assemblage variations are interpreted to reflect Asian interior climatic conditions. Smectite forms by chemical weathering under temperate to humid climates, while illite and chlorite result from physical erosion and/or weak hydrolysis under cold and arid conditions (Chamley, 1989). Kaolinite is a product of intense chemical weathering under warm and humid climates with good drainage conditions (Chamley, 1989). The extremely low kaolinite contents (< 4%) in core NP02 are consistent with the lack of intense chemical weathering in Asian interior dust (Shen et al., 2005). Considering the dilution effect of individual clay minerals, the smectite/(illite + chlorite) ratio is employed to indicate weathering conditions, with higher values indicating more humid conditions.

6.4.2. Dust content changes in the North Pacific Ocean and potential mechanisms for dust variability

On millennial timescales, abrupt dust content decreases are identified at approximately 25, 39, 48, and 55 ka, and can be linked to Heinrich (H) events 2, 4, 5, and 5a, as recorded in Greenland ice cores (Figure 6.7). Dust content variations to the NPO are influenced by the location and areal extent of dust source regions and/or the westerly dust transportation pathway. The NPO is sedimentologically more simple than other oceans, with the Asian interior serving as a major dust source throughout the Cenozoic (Janecek and Rea, 1983; Janecek, 1985; Rea et al., 1985), as verified by the La-Th-Sc ternary diagram for the core NP02 siliciclastic fraction (Figure 6.5). For core NP02 sediments, the smectite/(illite + chlorite) ratio does not have an obvious overall trend, with variations more or less around 0.77 (Figure 6.4e). This relatively limited variability indicates that Asian interior climate over the 21-57 ka interval was relatively stable and arid. Interpretations of the relationship between source regions and the climatic significance of dust remain controversial. Increased eolian dust contents are often attributed to increased aridity. For example, increased hematite contents at ~2.5 Ma and over the past 800 ka have been attributed to progressive Asian continental aridification (Yamazaki and Ioka, 1997; Yamazaki, 2009). In contrast, Zhang et al. (2020) suggested that enhanced dust contents are caused by increased sediment availability associated with increased snow and glacial meltwater that resulted from climatic cooling. In this case, increased eolian dust inputs are due to provision of renewable sources of erodible silt that could be deflated as dust during arid climatic phases. Given that the source area weathering regime was relatively unchanged and that HIRM and smectite/(illite + chlorite) do not suggest any evident relationship as indicated by Yamazaki and Ioka (1997) or Zhang et al. (2020), dust source regions cannot be the primary driver of dust content changes recorded in core NP02.

An alternative possibility is that the westerly transportation pathway should be considered as a potential explanation for dust variations in core NP02. Warming of the tropical troposphere or cooling of the polar stratosphere are expected to increase the meridional temperature gradient (Chen et al., 2007). Such a change will affect the location of baroclinic instability, and finally affect westerly strength and movement (Chen et al., 2007; Kidston and Vallis, 2012; Vallis et al., 2015). Both climate simulations and geological reconstructions suggest that the main northern westerly axis lies at around 38° to 40°N over the NPO (Rea and Leinen, 1988; Zhao et al., 2006), and that the main axis of westerlies shifts southward during winter/glacial periods, while it moves poleward during summer/interglacial periods (Barry and Chorly, 1976; Hovan et al., 1991; Janecek and Rea, 1985). Moreover, westerly strength has no obvious effect on dust contents over the NPO (Hovan et al., 1991; Rea, 1994). Therefore, dust content changes in core NP02 are expected to be sensitive to meridional shifts in the westerly path. Many abrupt climate changes during the last glacial period were caused by changes in Atlantic meridional overturning circulation (AMOC) conditions (Broecker et al., 1985; Rahmstorf, 2002). The AMOC is a fundamental and important component of the climate system that transports heat from low to high latitudes. AMOC slowdowns during Heinrich events reduce meridional ocean heat transport, including a ~60% reduction north of 40° N (Sun et al., 2012), which increases the meridional temperature gradient and eventually leads to strengthened and southward-shifted westerlies. At the same time, dust contents in core NP02 decline, as reflected by low HIRM values (Figure 6.7c), which indicate that less

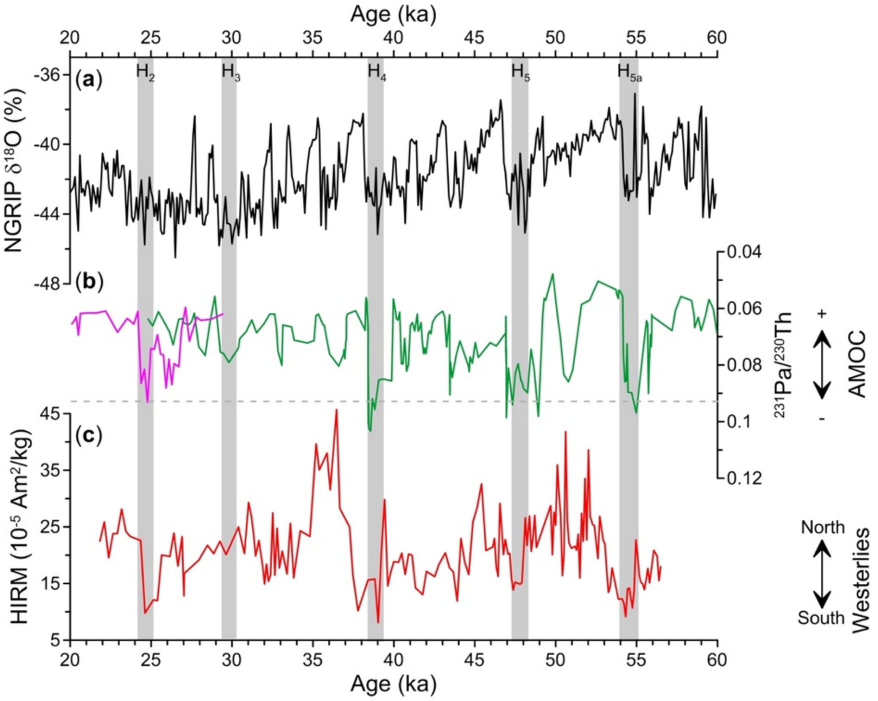

Figure 6.7 Westerly and North Atlantic climate records over the 60-20 ka interval. (a) NGRIP $\delta^{18}O$ (Andersen et al., 2004); (b) $^{231}Pa/^{230}Th$; pink and green curves represent the ODP Site 1063 record over the 20-30 ka interval (Böhm et al., 2015) and the core CDH19 record over the 25-60 ka interval (Henry et al., 2016), respectively; and (c) HIRM from core NP02. The dashed line in (b) denotes the $^{231}Pa/^{230}Th$ production ratio of 0.093 in sea water (Yu et al., 1996).

eolian material was transported to and deposited in the studied area. This implies that the main westerly axis moved away from the core NP02 site. Therefore, we suggest that the main westerly axis was situated south of the core NP02 site, at least during these Heinrich events.

Atlantic-to-Pacific atmospheric teleconnections have been tested by water-hosing simulations, which indicate that AMOC slowdowns deepen the Aleutian low and intensify midlatitude westerlies over the extratropical NPO (Wu et al., 2008). Therefore, it is likely that the abrupt dust content decrease during Heinrich events 2, 4, 5, and 5a in core NP02 was caused by southward westerly shifts associated with AMOC slowdowns. However, dust contents during H_3 did not decrease obviously (Figure 6.7c). In contrast to the other mentioned Heinrich events, ice-rafted debris identified in H_3 is related to surges from the European rather than the Laurentide ice sheet, which leads to smaller iceberg inputs to the North Atlantic and has less influence on the AMOC (Grousset et al., 1993; Gwiazda et al., 1996; Hemming, 2004; Peck et al., 2007). As expected, $^{231}Pa/^{230}Th$ ratios, which provide a measure of AMOC strength, did not reach a production ratio of 0.093 during H_3 (Figure 6.7b) (Yu et al., 1996; Henderson and Anderson, 2003), which indicates that there was only a small AMOC reduction at that time. Consistent with this observation, the AMOC during H_3 has been interpreted to have been relatively deep and vigorous (Henry et al., 2016; Turney et al., 2016; Lynch-Stieglitz, 2017), so that there was no abrupt meridional temperature gradient change to cause a southward westerly shift as during other Heinrich events. In turn, there was no abrupt dust content decrease in core NP02 during H_3 (Figure 6.7c).

6.5. Conclusions

Dust contents in the NPO are usually linked to Asian interior source region climate conditions. Situated near the main axis of the westerly path, dust content variations at the midlatitude location of core NP02 appear to be more sensitive to meridional westerly shifts. Our dust record for the ~21-57 ka interval has low dust contents during Heinrich events 2, 4, 5, and 5a, which indicates that the AMOC influences westerlies on millennial timescales. AMOC slowdowns increase the meridional temperature gradient and lead to a strengthened, southward westerly shift, which increases the distance between the main westerly axis and the study area and transports less dust to the core NP02 site.

Chapter 7

Conclusions and future work

7.1. Conclusions

The NPO and its largest marginal sea, the SCS, have different environmental settings. In this Ph.D. thesis, 435 m and 4.35 m sedimentary sequences were studied from SCS Hole U1431D and NPO core NP02, respectively. The main conclusions of these paleomagnetic and rock magnetic studies are summarized below.

Terrigenous magnetite is the dominant magnetic mineral throughout SCS Hole U1431D, with a single authigenic greigite-bearing interval identified at 130.5-132.0 mbsf. Thus, terrigenous magnetite underpins a magnetostratigraphic time framework spanning the past ~6.5 Ma, which is the longest record available from the deep SCS basin. According to this age framework, the greigite-bearing layer has an estimated age of 2.53-2.55 Ma and its formation/preservation appears to be associated with intensification of northern hemisphere glaciation. Cooling of Pacific deep water and closure of Loho inter-arc water gateways led to sluggish water exchange between the SCS and the NPO, which reduced SCS bottom water ventilation and benefitted organic matter preservation and, therefore, favoured greigite formation.

The environmental magnetic properties of Hole U1431D are controlled predominantly by the East Asian monsoon and can be used to reconstruct monsoon evolution over the past 6.5 Ma. χ, ARM, and Hm/Gt are used as rainfall-related summer monsoon proxies, while ARM/SIRM and χ_{ARM}/χ are used as wind-related winter monsoon proxies. Variations in these parameters indicate that the East Asian summer and winter monsoons were stable before 5 Ma. The summer monsoon intensified from 5 to 3.8 Ma, and then weakened gradually. In contrast, the winter monsoon weakened at 5 Ma, underwent prolonged intensification from 3.8 Ma, and finally stabilized at 0.6 Ma. Spectral analyses were employed to explore East Asian summer monsoon forcing mechanisms on orbital timescales. For the Hole U1431D χ record, 400-kyr long-eccentricity periodicity prevails over the past 6.5 Ma, which indicates that low-latitude insolation exerts a significant control over the East Asian summer monsoon system. The in-phase relationship between χ and long-eccentricity before 3.2 Ma demonstrates that the summer monsoon responded directly to low-latitude insolation between 6.5 and 3.2 Ma. Since 3.2 Ma, there is a high coherency between χ and global ice volume, which suggests that global ice volume exerted an increasing impact on summer monsoon evolution.

Dating of late Quaternary NPO sediments is challenging because deposition usually occurs below the CCD. Magnetic polarity reversals are not recorded in core NP02, and the shallow CCD precludes development of an oxygen isotope stratigraphy. Therefore, I examined the feasibility of RPI-assisted chronology based on an initial paleomagnetically-independent age model. Three visible tephra layers were identified in core NP02, which can be correlated to the To-Of, Spfa-1, and Kt-3 tephra layers (Machida and Arai, 2003; Amma-Miyasaka et al., 2020). Together with a radiocarbon date, an initial age model was reconstructed over the ~22-57 ka interval. Paleomagnetic analyses suggest that the natural remanent magnetization of the NP02 sediments is carried by detrital vortex state magnetite and biogenic SD magnetite, which record similar RPI patterns. Based on this initial age model, we compared core NP02 RPI estimates with global RPI stacks, regional Pacific RPI stacks from different latitudes, and individual RPI records from the NPO and its marginal seas (Roberts et al., 1997; Yamazaki, 1999; Laj et al., 2004; Okada et al., 2005; Valet et al., 2005; Yamamoto et al., 2007; Roberts, 2008; Yamazaki et al., 2008, 2013; Channell et al., 2009; Inoue and Yamazaki, 2010; Shin et al., 2019; Zhong et al., 2020). Consistent RPI patterns validate the core NP02 RPI record, and I demonstrate that RPI-assisted chronology has the potential to date NPO sediments.

I then refined the initial age model by tuning the reconstructed RPI variations to RPI records from cores GC1+PC7 (Inoue and Yamazaki, 2010; Yamazaki et al., 2013a) to explore the paleoclimatic significance of observed rock magnetic variations. HIRM in core NP02 sediments is shown to be a proxy for hematite concentration and is used to reconstruct variations in Asian-sourced dust content. Given the location of core NP02 and the relative stability of Asian interior climate during the studied time interval, dust content variations are attributed to meridional shifts in the westerlies. Dust minima coincide with Heinrich events 2, 4, 5, and 5a, and were likely caused by southward westerly shifts associated with AMOC slowdowns.

7.2. Future work

Based on the findings of this Ph.D. study, future work following three main objectives is recommended. The first objective is to construct high-quality regional RPI reference stacks and to develop a method for RPI correlation. The geomagnetic field can have a non-dipolar geometry, such as during geomagnetic excursions (Roberts, 2008), and regional geomagnetic characteristics can be smoothed during construction of global stacks. Thus, chronological artifacts may occur when attempting to correlate a regional RPI record in the depth domain to a global RPI reference stack in the time domain. To better understand regional geomagnetic field characteristics and to improve the robustness of RPI correlation, it is essential to construct high-quality regional RPI reference stacks. Moreover, techniques for RPI correlation have been “arbitrary” for several decades, with correlations based on matching minima, maxima, and slopes of RPI curves. Such “wiggle matching” without robust statistical/probabilistic uncertainty assessment cannot always be robust. Therefore, it is essential to develop a robust probabilistic method for RPI correlation.

A second suggested avenue for future work is to explore temporal and spatial westerly variations. This requires a suite of sediment cores along a meridian with respect to the westerlies, which can be used to study dust content, grain size, and source region variations. Such records will enable exploration of relationships between westerly forcing mechanisms and global climate changes, and will provide new insights into land-sea climate coupling processes.

A third and final pathway for future work is to explore the interplay between the East Asian monsoon and the westerlies. SCS sediments record East Asian monsoon evolution, while NPO sediments record westerly evolution. Therefore, sediments that span the same time interval from these two regions can be used to study coupling mechanisms and phase relationships between the East Asian monsoon and the westerlies. When combined with climate simulations, such comparisons will enable researchers to explore how high-latitude climate signals, such as AMOC changes, exert control over the mid-latitude NPO and low-latitude SCS.

References

Adelseck Jr, C.G., Anderson, T.F., 1978. The late Pleistocene record of productivity fluctuations in the eastern equatorial Pacific Ocean. *Geology* 6, 388–391. https://doi.org/10.1130/0091-7613(1978)6<388:TLPROP>2.0.CO;2

Aksu, A.E., Mudie, P.J., 1985. Magnetostratigraphy and palynology demonstrate at least 4 million years of Arctic Ocean sedimentation. *Nature* 318, 280–283. https://doi.org/10.1038/318280a0

Amma-Miyasaka, M., Miura, D., Nakagawa, M., Uesawa, S., Furukawa, R., 2020. Stratigraphy and chronology of silicic tephras in the Shikotsu-Toya volcanic field, Japan: evidence of a late Pleistocene ignimbrite flare-up in southwestern Hokkaido. *Quat. Int.* 35. https://doi.org/10.1016/j.quaint.2019.11.019

An, Z., Kukla, G.J., Porter, S.C., Xiao, J., 1991. Magnetic susceptibility evidence of monsoon variation on the Loess Plateau of central China during the last 130,000 years. *Quat. Res.* 36, 29–36. https://doi.org/10.1016/0033-5894(91)90015-W

An, Z., Kutzbach, J.E., Prell, W.L., Porter, S.C., 2001. Evolution of Asian monsoons and phased uplift of the Himalaya - Tibetan Plateau since Late Miocene times. *Nature* 411, 62–66. https://doi.org/10.1038/35075035

An, Z., Colman, S.M., Zhou, W., Li, X., Brown, E.T., Jull, A.J.T., Cai, Y., Huang, Y., Lu, X., Chang, H., Song, Y., Sun, Y., Xu, H., Liu, W., Jin, Z., Liu, X., Cheng, P., Liu, Y., Ai, L., Li, X., Liu, X., Yan, L., Shi, Z., Wang, X., Wu, F., Qiang, X., Dong, J., Lu, F., Xu, X., 2012. Interplay between the westerlies and Asian monsoon recorded in Lake Qinghai sediments since 32 ka. *Sci. Rep.* 2, 305–307. https://doi.org/10.1038/srep00619

Anderson, D.M., Prell, W.L., 1993. A 300 kyr record of upwelling off Oman during the late Quaternary: evidence of the Asian southwest monsoon. *Paleoceanography* 8, 193–208. https://doi.org/10.1029/93PA00256

Andersen, K.K., Azuma, N., Barnola, J.M., Bigler, M., Biscaye, P., Caillon, N., Chappellaz, J., Clausen, H.B., Dahl-Jensen, D., Fischer, H., Flückiger, J., Fritzsche, D., Fujii, Y., Goto-Azuma, K., Grønvold, K., Gundestrup, N.S., Hansson, M., Huber, C., Hvidberg, C.S., Johnsen, S.J., Jonsell, U., Jouzel, J., Kipfstuhl, S., Landais, A., Leuenberger, M., Lorrain, R., Masson-Delmotte, V., Miller, H., Motoyama, H., Narita, H., Popp, T., Rasmussen, S.O., Raynaud, D., Rothlisberger, R., Ruth, U., Samyn, D., Schwander, J., Shoji, H., Siggard-Andersen, M.L., Steffensen, J.P., Stocker, T., Sveinbjörnsdóttir, A.E., Svensson, A., Takata, M., Tison, J.L., Thorsteinsson, T., Watanabe, O., Wilhelms, F., White, J.W.C., 2004. High-resolution record of northern hemisphere climate extending into the last interglacial period. *Nature* 431, 147–151. https://doi.org/10.1038/nature02805

Anson, G.L., Kodama, K.P., 1987. Compaction-induced inclination shallowing of the post-depositional remanent magnetization in a synthetic sediment. *Geophys. J. Int.* 88, 673–692. https://doi.org/10.1111/j.1365-246X.1987.tb01651.x

Ao, H., Roberts, A.P., Dekkers, M.J., Liu, X., Rohling, E.J., Shi, Z., An, Z., Zhao, X., 2016. Late Miocene-Pliocene Asian monsoon intensification linked to Antarctic ice-sheet growth. *Earth Planet. Sci. Lett.* 444, 75–87. https://doi.org/10.1016/j.epsl.2016.03.028

Ao, H., Dekkers, M.J., Roberts, A.P., Rohling, E.J., An, Z., Liu, X., Jiang, Z., Qiang, X., Xu, Y., Chang, H., 2018. Mineral magnetic record of the Miocene-Pliocene climate transition on the Chinese Loess Plateau, North China. *Quat. Res.* 89, 619–628. https://doi.org/10.1017/qua.2017.77

Aoki, K., 2000. Late Quaternary tephrostratigraphy of marine cores collected during "Mirai" MR98-03 and MR99-K04 cruises. *Rep. Japan Mar. Sci. Technol. Cent.* 41, 49–55.

Aoki, K., Machida, H., 2006. Major element composition of volcanic glass shards in the late Quaternary widespread tephras in Japan — distinction of tephras using K_2O-TiO_2 diagrams. *Bull. Geol. Surv. Jpn.* 57, 239–258.

Arason, P., Levi, S., 1990. Compaction and inclination shallowing in deep-sea sediments from the Pacific Ocean. *J. Geophys. Res.* 95, 4501–4510. https://doi.org/10.1029/JB095iB04p04501

Archer, C.L., Caldeira, K., 2008. Historical trends in the jet streams. *Geophys. Res. Lett.* 35. https://doi.org/10.1029/2008GL033614

Arnold, E., Leinen, M., King, J., 1995. Paleoenvironmental variation based on the mineralogy and rock-magnetic properties of sediment from Sites 885 and 886. *Proc. Ocean Drill. Progr. Sci. Res.* 145, 231–245. https://doi.org/10.2973/odp.proc.sr.145.113.1995

Banerjee, S.K., 1971. New grain size limits for palaeomagnetic stability in haematite. *Nat. Phys. Sci.* 232, 15. https://doi.org/10.1038/physci232015a0

Barkley, R.A., 1970. The Kuroshio Current. *Sci. J.* 6, 54–60.

Barry, R.G., Chorly, R.J., 1976. *Atmosphere, Weather and Climate*. Routledge.

Benning, L.G., Wilkin, R.T., Barnes, H.L., 2000. Reaction pathways in the Fe-S system below 100°C. *Chem. Geol.* 167, 25–51. https://doi.org/10.1016/S0009-2541(99)00198-9

Berner, R.A., 1970. Sedimentary pyrite formation. *Am. J. Sci.* 268, 1–23. https://doi.org/10.2475/ajs.268.1.1

Berner, R.A., 1984. Sedimentary pyrite formation: an update. *Geochim. Cosmochim. Acta* 48, 605–615. https://doi.org/10.1016/0016-7037(84)90089-9

Biggin, A.J., Strik, G.H.M.A., Langereis, C.G., 2008. Evidence for a very-long-term trend in geomagnetic secular variation. *Nat. Geosci.* 1, 395–398. https://doi.org/10.1038/ngeo181

Biscaye, P.E., 1965. Mineralogy and sedimentation of recent deep-sea clay in the Atlantic Ocean and adjacent seas and oceans. *Bull. Geol. Soc. Am.* 76, 803–832. https://doi.org/10.1130/0016-7606(1965)76[803:MASORD]2.0.CO;2

Blaauw, M., 2010. Methods and code for "classical" age-modelling of radiocarbon sequences. *Quat. Geochron.* 5, 512–518. https://doi.org/10.1016/j.quageo.2010.01.002

Blaauw, M., Christen, J.A., 2005. Radiocarbon peat chronologies and environmental change. *J. R. Stat. Soc. C* 54, 805–816. https://doi.org/10.1111/j.1467-9876.2005.00516.x

Blake, R.L., Hessevick, R.E., Zoltai, T., Finger, L.W., 1966. Refinement of the hematite structure. *Am. Mineral.* 51, 123–129. https://doi.org/10.1016.2010.01.025

Blanchet, C.L., Thouveny, N., Vidal, L., 2009. Formation and preservation of greigite (Fe_3S_4) in sediments from the Santa Barbara Basin: implications for paleoenvironmental changes during the past 35 ka. *Paleoceanography* 24. https://doi.org/10.1029/2008PA001719

Bloemendal, J., King, J.W., Hall, F.R., Doh, S.J., 1992. Rock magnetism of late Neogene and Pleistocene deep-sea sediments: relationship to sediment source, diagenetic processes, and sediment lithology. *J. Geophys. Res.* 97, 4361–4375. https://doi.org/10.1029/91JB03068

Boex, J., Fogwill, C., Harrison, S., Glasser, N.F., Hein, A., Schnabel, C., Xu, S., 2013. Rapid thinning of the late Pleistocene Patagonian ice sheet followed migration of the southern westerlies. *Sci. Rep.* 3, 2118. https://doi.org/10.1038/srep02118

Böhm, E., Lippold, J., Gutjahr, M., Frank, M., Blaser, P., Antz, B., Fohlmeister, J., Frank, N., Andersen, M.B., Deininger, M., 2015. Strong and deep Atlantic meridional overturning circulation during the last glacial cycle. *Nature* 517, 73–76. https://doi.org/10.1038/nature14059

Bonhommet, N., Babkine, J., 1967. Sur la presence d'aimentation inverse dans la Chaine des Puys. *C. R. Acad. Sci. B* 264, 92–94.

Bonhommet, N., Zähringer, J., 1969. Paleomagnetism and potassium argon age determinations of the Laschamp geomagnetic polarity event. *Earth Planet. Sci. Lett.* 6, 43–46. https://doi.org/10.1016/0012-821X(69)90159-9

Borradaile, G.J., Lagroix, F., 2000. Magnetic characterization using a three-dimensional hysteresis projection, illustrated with a study of limestones. *Geophys. J. Int.* 141, 213–226. https://doi.org/10.1046/j.1365-246X.2000.00066.x

Broecker, W.S., Peteet, D.M., Rind, D., 1985. Does the ocean-atmosphere system have more than one stable mode of operation? *Nature* 315, 21–26. https://doi.org/10.1038/315021a0

Brunhes, B., 1906. Recherches sur la direction d'aimantation des roches volcaniques. *J. Phys. Théorique Appliquée* 5, 705–724. https://doi.org/10.1051/jphystap:019060050070500

Buck, C., Christen, A., James, G.N., 1999. BCal: an on-line Bayesian radiocarbon calibration tool. *Internet Archaeol.* 7. https://doi.org/10.11141/ia.7.1

Butler, R.F., 1992. *Paleomagnetism: Magnetic Domains to Geologic Terranes*. Blackwell Scientific Publications. https://doi.org/10.5860/choice.29-5708

Cande, S.C., Kent, D. V., 1995. Revised calibration of the geomagnetic polarity timescale for the late Cretaceous and Cenozoic. *J. Geophys. Res.* 100, 6093–6095. https://doi.org/10.1029/94JB03098

Canfield, D.E., Raiswell, R., Bottrell, S., 1992. The reactivity of sedimentary iron minerals toward sulfide. *Am. J. Sci.* 292, 659–683. https://doi.org/10.2475/ajs.292.9.659

Caricchi, C., Lucchi, R.G., Sagnotti, L., Macrì, P., Di Roberto, A., Del Carlo, P., Husum, K., Laberg, J.S., Morigi, C., 2019. A high-resolution geomagnetic relative paleointensity record from the Arctic Ocean deep-water gateway deposits during the last 60 kyr. *Geochem. Geophys. Geosyst.* 20, 2355–2377. https://doi.org/10.1029/2018GC007955

Centurioni, L.R., Niiler, P.P., Lee, D.K., 2004. Observations of inflow of Philippine sea surface water into the South China Sea through the Luzon strait. *J. Phys. Oceanogr.* 34, 113–121. https://doi.org/10.1175/1520-0485(2004)034<0113:OOIOPS>2.0.CO;2

Chaisson, W.P., Ravelo, A.C., 2000. Pliocene development of the east-west hydrographic gradient in the equatorial Pacific. *Paleoceanography* 15, 497–505. https://doi.org/10.1029/1999PA000442

Chamley, H., 1989. *Clay Sedimentology*. Springer. https://doi.org/10.1007/978-3-642-85916-8

Champion, D.E., Lanphere, M.A., Kuntz, M.A., 1988. Evidence for a new geomagnetic reversal from lava flows in Idaho: discussion of short polarity reversals in the Brunhes and late Matuyama polarity chrons. *J. Geophys. Res.* 93, 11667–11680. https://doi.org/10.1029/jb093ib10p11667

Chang, C.P., Zhang, Y., Li, T., 2000. Interannual and interdecadal variations of the East Asian summer monsoon and tropical pacific SSTs. Part I: roles of the subtropical ridge. *J. Clim.* 13, 4310–4325. https://doi.org/10.1175/1520-

0442(2000)013<4310:IAIVOT>2.0.CO;2

Chang, L., Roberts, A.P., Tang, Y., Rainford, B.D., Muxworthy, A.R., Chen, Q., 2008. Fundamental magnetic parameters from pure synthetic greigite (Fe_3S_4). *J. Geophys. Res. Solid Earth* 113. https://doi.org/10.1029/2007JB005502

Chang, L., Vasiliev, I., van Baak, C., Krijgsman, W., Dekkers, M.J., Roberts, A.P., Fitz Gerald, J.D., van Hoesel, A., Winklhofer, M., 2014. Identification and environmental interpretation of diagenetic and biogenic greigite in sediments: a lesson from the Messinian Black Sea. *Geochem. Geophys. Geosyst.* 15, 3612–3627. https://doi.org/10.1002/2014GC005411

Chang, L., Heslop, D., Roberts, A.P., Rey, D., Mohamed, K.J., 2016a. Discrimination of biogenic and detrital magnetite through a double Verwey transition temperature. *J. Geophys. Res. Solid Earth* 12, 3–14. https://doi.org/10.1002/2015JB012485

Chang, L., Roberts, A.P., Heslop, D., Hayashida, A., Li, J., Zhao, X., Tian, W., Huang, Q., 2016b. Widespread occurrence of silicate-hosted magnetic mineral inclusions in marine sediments and their contribution to paleomagnetic recording. *J. Geophys. Res. Solid Earth* 121, 8415–8431. https://doi.org/10.1002/2016JB013109

Channell, J.E.T., Lanci, L., 2014. Oligocene-Miocene relative (geomagnetic) paleointensity correlated from the equatorial Pacific (IODP Site U1334 and ODP Site 1218) to the South Atlantic (ODP Site 1090). *Earth Planet. Sci. Lett.* 387, 77–88. https://doi.org/10.1016/j.epsl.2013.11.028

Channell, J.E.T., Erba, E., Nakanishi, M., Tamaki, K., 1995. Late Jurassic - early Cretaceous time scales and oceanic magnetic anomaly block models, in: Berggren, W.A., Kent, D.V., Aubry, M.-P., Hardenbol, J. (Eds.), *Geochronology, Time Scales and Global Stratigraphic Correlations*. pp. 51–63.

Channell, J.E.T., Xuan, C., Hodell, D.A., 2009. Stacking paleointensity and oxygen isotope data for the last 1.5 Myr (PISO-1500). *Earth Planet. Sci. Lett.* 283, 10–23. https://doi.org/10.1016/j.epsl.2009.03.012

Channell, J.E.T., Ohneiser, C., Yamamoto, Y., Kesler, M.S., 2013. Oligocene-Miocene magnetic stratigraphy carried by biogenic magnetite at sites U1334 and U1335 (equatorial Pacific Ocean). *Geochem. Geophys. Geosyst.* 14, 265–282. https://doi.org/10.1029/2012GC004429

Channell, J.E.T., Hodell, D.A., Curtis, J.H., 2016a. Relative paleointensity (RPI) and oxygen isotope stratigraphy at IODP Site U1308: North Atlantic RPI stack for 1.2-2.2 Ma (NARPI-2200) and age of the Olduvai Subchron. *Quat. Sci. Rev.* 131, 1–19. https://doi.org/10.1016/j.quascirev.2015.10.011

Channell, J.E.T., Harrison, R.J., Lascu, I., McCave, I.N., Hibbert, F.D., Austin, W.E.N., 2016b. Magnetic record of deglaciation using FORC-PCA, sortable-silt grain size, and magnetic excursion at 26 ka, from the Rockall Trough (NE Atlantic). *Geochem. Geophys. Geosyst.* 17, 1823–1841. https://doi.org/10.1002/2016GC006300

Chao, S.Y., Shaw, P.T., Wu, S.Y., 1996. Deep water ventilation in the South China Sea. *Deep. Res. I* 43, 445–466. https://doi.org/10.1016/0967-0637(96)00025-8

Chavaillaz, Y., Codron, F., Kageyama, M., 2013. Southern westerlies in LGM and future (RCP4.5) climates. *Clim. Past* 9, 517–524. https://doi.org/10.5194/cp-9-517-2013

Chen, C.-T.A., Wang, S.L., Wang, B.J., Pai, S.C., 2001. Nutrient budgets for the South China Sea basin. *Mar. Chem.* 75, 281–300. https://doi.org/10.1016/S0304-4203(01)00041-X

Chen, G., Held, I.M., 2007. Phase speed spectra and the recent poleward shift of southern hemisphere surface westerlies. *Geophys. Res. Lett.* 34, 4641–4645. https://doi.org/10.1029/2007GL031200

Chen, G., Held, I.M., Robinson, W.A., 2007. Sensitivity of the latitude of the surface westerlies to surface friction. *J. Atmos. Sci.* 64, 2899–2915. https://doi.org/10.1175/JAS3995.1

Chen, L., Heslop, D., Roberts, A.P., Chang, L., Zhao, X., McGregor, H. V., Marino, G., Rodriguez-Sanz, L., Rohling, E.J., Pälike, H., 2017. Remanence acquisition efficiency in biogenic and detrital magnetite and recording of geomagnetic paleointensity. *Geochem. Geophys. Geosyst.* 18, 1435–1450. https://doi.org/10.1002/2016GC006753

Chen, Q., Kissel, C., Liu, Z., 2017. Late Quaternary climatic forcing on the terrigenous supply in the northern South China Sea: input from magnetic studies. *Earth Planet. Sci. Lett.* 471, 160–171. https://doi.org/10.1016/j.epsl.2017.04.047

Chen, W.H., Huang, C.Y., Lin, Y.J., Zhao, Q., Yan, Y., Chen, D., Zhang, X., Lan, Q., Yu, M., 2015. Depleted deep South China Sea δ^{13}C paleoceanographic events in response to tectonic evolution in Taiwan-Luzon Strait since middle Miocene. *Deep-Sea Res. II* 122, 195–225. https://doi.org/10.1016/j.dsr2.2015.02.005

Cheng, H., Edwards, R.L., Sinha, A., Spötl, C., Yi, L., Chen, S., Kelly, M., Kathayat, G., Wang, X., Li, X., Kong, X., Wang, Y., Ning, Y., Zhang, H., 2016. The Asian monsoon over the past 640,000 years and ice age terminations. *Nature* 534, 640–646. https://doi.org/10.1038/nature18591

Chevallier, R., Mathieu, S., 1943. Propriétés magnétiques des poudres d'hématites - influence des dimensions des grains. *Ann. Phys. (Paris).* 11, 258–288.

Clift, P.D., 2006. Controls on the erosion of Cenozoic Asia and the flux of clastic sediment to the ocean. *Earth Planet. Sci. Lett.* 241, 571–580. https://doi.org/10.1016/j.epsl.2005.11.028

Clift, P., Lee, J., Clark, M.K., Blusztajn, J., 2002. Erosional response of South China to arc rifting and monsoonal strengthening; a record from the South China Sea. *Mar. Geol.* 184, 207–226. https://doi.org/10.1016/S0025-3227(01)00301-2

Collinson, D.W., 1965. Depositional remanent magnetization in sediments. *J. Geophys. Res.* 70, 4663–4668. https://doi.org/10.1029/jz070i018p04663

Cornell, R.M., Schwertmann, U., 2003. *The Iron Oxides: Structure, Properties, Reactions, Occurrences and Uses*. John Wiley & Sons. https://doi.org/10.1002/3527602097

Cox, A., 1968. Lengths of geomagnetic polarity intervals. *J. Geophys. Res.* 73, 3247–3260. https://doi.org/10.1029/jb073i010p03247

Cox, A., 1969. Geomagnetic reversals. *Science* 164, 237–245. https://doi.org/10.1126/science.163.3864.237

Cox, A., Doell, R.R., Dalrymple, G.B., 1963. Geomagnetic polarity epochs and Pleistocene geochronometry. *Nature* 198, 1049–1051. https://doi.org/10.1038/1981049a0

Davis, B.A.S., Brewer, S., 2009. Orbital forcing and role of the latitudinal insolation/temperature gradient. *Clim. Dyn.* 32, 143–165. https://doi.org/10.1007/s00382-008-0480-9

Day, R., Fuller, M., Schmidt, V.A., 1977. Hysteresis properties of titanomagnetites: grain-size and compositional dependence. *Phys. Earth Planet. Inter.* 13, 260–267. https://doi.org/10.1016/0031-9201(77)90108-X

de Boer, C.B., Dekkers, M.J., 1998. Thermomagnetic behaviour of haematite and goethite as a function of grain size in various non-saturating magnetic fields. *Geophys. J. Int.* 133, 541–552. https://doi.org/10.1046/j.1365-246X.1998.00522.x

Dearing, J.A., Dann, R.J.L., Hay, K., Lees, J.A., Loveland, P.J., Maher, B.A., O'Grady, K., 1996. Frequency-dependent susceptibility measurements of environmental materials. *Geophys. J. Int.* 124, 228–240. https://doi.org/10.1111/j.1365-246X.1996.tb06366.x

Dekkers, M.J., Linssen, J.H., 1989. Rock magnetic properties of fine-grained natural low-temperature haematite with reference to remanence acquisition mechanisms in red beds. *Geophys. J. Int.* 99, 1–18. https://doi.org/10.1111/j.1365-246X.1989.tb02012.x

deMenocal, P.B., 1995. Plio-Pleistocene African climate. *Science* 270, 53–59. https://doi.org/10.1126/science.270.5233.53

Demetrescu, C., Dobrica, V., 2014. Multi-decadal ingredients of the secular variation of the geomagnetic field. Insights from long time series of observatory data. *Phys. Earth Planet. Inter.* 231, 39–55. https://doi.org/10.1016/j.pepi.2014.03.001

Dempster, A.P., Laird, N.M., Rubin, D.B., 1977. Maximum likelihood from incomplete data via the EM algorithm. *J. R. Stat. Soc. B* 39, 1–22. https://doi.org/10.1111/j.2517-6161.1977.tb01600.x

Deng, C., Vidic, N.J., Verosub, K.L., Singer, M.J., Liu, Q., Shaw, J., Zhu, R., 2005. Mineral magnetic variation of the Jiaodao Chinese loess/paleosol sequence and its bearing on long-term climatic variability. *J. Geophys. Res. Solid Earth* 110. https://doi.org/10.1029/2004JB003451

Doell, R.R., Cox, A., 1971. Pacific geomagnetic secular variation. *Science* 171, 248–254. https://doi.org/10.1126/science.171.3968.248

Doh, S.J., King, J.W., Leinen, M., 1988. A rock-magnetic study of giant piston core LL44-GPC3 from the central North Pacific and its paleoceanographic implications. *Paleoceanography* 3, 89–111. https://doi.org/10.1029/PA003i001p00089

Dorfman, J.M., Stoner, J.S., Finkenbinder, M.S., Abbott, M.B., Xuan, C., St-Onge, G., 2015. A 37,000-year environmental magnetic record of aeolian dust deposition from Burial Lake, Arctic Alaska. *Quat. Sci. Rev.* 128, 81–97. https://doi.org/10.1016/j.quascirev.2015.08.018

Duce, R.A., Liss, P.S., Merrill, J.T., Atlas, E.L., Buat-Menard, P., Hicks, B.B., Miller, J.M., Prospero, J.M., Arimoto, R., Church, T.M., Ellis, W., Galloway, J.N., Hansen, L., Jickells, T.D., Knap, A.H., Reinhardt, K.H., Schneider, B., Soudine, A., Tokos, J.J., Tsunogai, S., Wollast, R., Zhou, M., 1991. The atmospheric input of trace species to the world ocean. *Global Biogeochem. Cycles* 5, 193–259. https://doi.org/10.1029/91GB01778

Dunlop, D.J., 1984. A method of determining demagnetizing factor from multidomain hysteresis. *J. Geophys. Res.* 89, 553–558. https://doi.org/10.1029/JB089iB01p00553

Dunlop, D.J., Özdemir, Ö., 1997. *Rock Magnetism: Fundamentals and Frontiers*. Cambridge University Press.

Dupont-Nivet, G., Vasiliev, I., Langereis, C.G., Krijgsman, W., Panaiotu, C., 2005. Neogene tectonic evolution of the southern and eastern Carpathians constrained by paleomagnetism. *Earth Planet. Sci. Lett.* 236, 374–387. https://doi.org/10.1016/j.epsl.2005.04.030

Dytłow, S., Winkler, A., Górka-Kostrubiec, B., Sagnotti, L., 2019. Magnetic, geochemical and granulometric properties of street dust from Warsaw (Poland). *J. Appl. Geophys.* 169, 58–73. https://doi.org/10.1016/j.jappgeo.2019.06.016

Eaton, J.A., Morrish, A.H., 1969. Magnetic domains in hematite at and above the Morin transition. *J. Appl. Phys.* 40, 3180–3185. https://doi.org/10.1063/1.1658162

Egli, R., 2003. Analysis of the field dependence of remanent magnetization curves. *J. Geophys. Res. Solid Earth* 108. https://doi.org/10.1029/2002jb002023

Egli, R., 2004a. Characterization of individual rock magnetic components by analysis of remanence curves, 1. Unmixing natural sediments. *Stud. Geophys. Geod.* 48, 391–446. https://doi.org/10.1023/B:SGEG.0000020839.45304.6d

Egli, R., 2004b. Characterization of individual rock magnetic components by analysis of remanence curves. 2. Fundamental properties of coercivity distributions. *Phys. Chem. Earth* 29, 851–867. https://doi.org/10.1016/j.pce.2004.04.001

Egli, R., 2004c. Characterization of individual rock magnetic components by analysis of remanence curves. 3. Bacterial magnetite and natural processes in lakes. *Phys. Chem. Earth* 29, 869–884. https://doi.org/10.1016/j.pce.2004.03.010

Egli, R., 2013. VARIFORC: an optimized protocol for calculating non-regular first-order reversal curve (FORC) diagrams. *Glob. Planet. Change* 110, 302–320. https://doi.org/10.1016/j.gloplacha.2013.08.003

Egli, R., Chen, A.P., Winklhofer, M., Kodama, K.P., Horng, C.-S., 2010. Detection of noninteracting single domain particles using first-order reversal curve diagrams. *Geochem. Geophys. Geosyst.* 11. https://doi.org/10.1029/2009gc002916

Enkin, R.J., Yang, Z., Yan, C., Courtillot, V., 1992. Paleomagnetic constraints on the geodynamic history of the major blocks of China from the Permian to the present. *J. Geophys. Res.* 97, 13953–13989. https://doi.org/10.1029/92jb00648

Evans, M., Heller, F., 2003. *Environmental Magnetism: Principles and Applications of Enviromagnetics*. Academic Press.

Fabian, K., 2003. Some additional parameters to estimate domain state from isothermal magnetization measurements. *Earth Planet. Sci. Lett.* 213, 337–345. https://doi.org/10.1016/S0012-821X(03)00329-7

Fang, G., Fang, W., Fang, Y., Wang, K., 1998. A survey of studies on the South China Sea upper ocean circulation. *Acta Oceanogr. Taiwanica* 37, 1–16.

Farina, M., Esquivel, D.M.S., De Barros, H.G.P.L., 1990. Magnetic iron-sulphur crystals from a magnetotactic microorganism. *Nature* 342, 256–258. https://doi.org/10.1038/343256a0

Ferguson, W.S., Griffin, J.J., Goldberg, E.D., 1970. Atmospheric dusts from the North Pacific — a short note on a long-range eolian transport. *J. Geophys. Res.* 75, 1137–1139. https://doi.org/10.1029/2009GC002916

Ferk, A., Leonhardt, R., 2009. The Laschamp geomagnetic field excursion recorded in Icelandic lavas. *Phys. Earth Planet. Inter.* 177, 19–30. https://doi.org/10.1016/j.pepi.2009.07.011

Fisher, R., 1953. Dispersion on a sphere. *Proc. R. Soc. Lond. A* 217, 295–305. https://doi.org/10.1098/rspa.1953.0064

Florindo, F., Karner, D.B., Marra, F., Renne, P.R., Roberts, A.P., Weaver, R., 2007. Radioisotopic age constraints for Glacial Terminations IX and VII from aggradational sections of the Tiber River delta in Rome, Italy. *Earth Planet. Sci. Lett.* 256, 61–80. https://doi.org/10.1016/j.epsl.2007.01.014

Forster, T., Heller, F., 1997. Magnetic enhancement paths in loess sediments from Tajikistan, China and Hungary. *Geophys. Res. Lett.* 24, 17–20. https://doi.org/10.1029/96GL03751

France, D.E., Oldfield, F., 2000. Identifying goethite and hematite from rock magnetic measurements of soils and sediments. *J. Geophys. Res. Solid Earth* 105, 2781–2795. https://doi.org/10.1029/1999jb900304

Fu, Y., von Dobeneck, T., Franke, C., Heslop, D., Kasten, S., 2008. Rock magnetic identification and geochemical process models of greigite formation in Quaternary marine sediments from the Gulf of Mexico (IODP Hole U1319A). *Earth Planet. Sci. Lett.* 275, 233–245. https://doi.org/10.1016/j.epsl.2008.07.034

Gai, C., Liu, Q., Roberts, A.P., Chou, Y., Zhao, X., Jiang, Z., Liu, J., 2020. East Asian monsoon evolution since the late Miocene from the South China Sea. *Earth Planet. Sci. Lett.* 530, 115960. https://doi.org/10.1016/j.epsl.2019.115960

Gao, Y., Arimoto, R., Zhou, M.Y., Merrill, J.T., Duce, R.A., 1992. Relationships between the dust concentrations over eastern Asia and the remote North Pacific. *J. Geophys. Res.* 97, 9867–9872. https://doi.org/10.1029/92JD00714

García, J., Subías, G., 2004. The Verwey transition - a new perspective. *J. Phys. Condens. Matter* 16, R145. https://doi.org/10.1088/0953-8984/16/7/R01

Gersonde, R., 2012. The expedition of the research vessel “Sonne” to the subpolar North Pacific and the Bering Sea in 2009 (SO202-INOPEX). *Repts. Polar Mar. Res.* 643, 1–323.

Gill, J.B., 1981. *Orogenic Andesites and Plate Tectonics.* Springer-Verlag. https://doi.org/10.1016/0377-0273(82)90060-9

Gorter, E.W., 1954. Saturation magnetization and crystal chemistry of ferrimagnetic oxides. *Philips Res. Rep.* 9, 295–355.

Gradstein, F.M., Ogg, J.G., Schmitz, M.D., Ogg, G.M., 2012. *The Geologic Time Scale 2012*. Elsevier. https://doi.org/10.1016/C2011-1-08249-8

Graham, K.W.T., 1961. The re-magnetization of a surface outcrop by lightning currents. *Geophys. J. R. Astron. Soc.* 6, 85–102. https://doi.org/10.1111/j.1365-246X.1961.tb02963.x

Granot, R., Dyment, J., Gallet, Y., 2012. Geomagnetic field variability during the Cretaceous Normal Superchron. *Nat. Geosci.* 5, 220–223. https://doi.org/10.1038/ngeo1404

Grönvold, K., Óskarsson, N., Johnsen, S.J., Clausen, H.B., Hammer, C.U., Bond, G., Bard, E., 1995. Ash layers from Iceland in the Greenland GRIP ice core correlated with oceanic and land sediments. *Earth Planet. Sci. Lett.* 135, 149–155. https://doi.org/10.1016/0012-821X(95)00145-3

Grousset, F.E., Labeyrie, L., Sinko, J.A., Cremer, M., Bond, G., Duprat, J., Cortijo, E., Huon, S., 1993. Patterns of ice-rafted detritus in the glacial North Atlantic (40–55° N). *Paleoceanography* 8, 175–192. https://doi.org/10.1029/92PA02923

Guo, Z.T., Ruddiman, W.F., Hao, Q.Z., Wu, H.B., Qiao, Y.S., Zhu, R.X., Peng, S.Z., Wei, J.J., Yuan, B.Y., Liu, T.S., 2002. Onset of Asian desertification by 22 Myr ago inferred from loess deposits in China. *Nature* 416, 159–163. https://doi.org/10.1038/416159a

Guyodo, Y., Valet, J.P., 1996. Relative variations in geomagnetic intensity from sedimentary records: the past 200,000 years. *Earth Planet. Sci. Lett.* 143, 23–36. https://doi.org/10.1016/0012-821x(96)00121-5

Guyodo, Y., Valet, J.P., 1999. Global changes in intensity of the Earth’s magnetic field during the past 800 kyr. *Nature* 399, 249–252. https://doi.org/10.1038/20420

Gwiazda, R.H., Hemming, S.R., Broecker, W.S., 1996. Provenance of icebergs during Heinrich event 3 and the contrast to their sources during other Heinrich episodes. *Paleoceanography* 11, 371–378. https://doi.org/10.1029/96PA01022

Hadley, G., 1735. Concerning the cause of the general trade-winds. *Philos. Trans. R. Soc. Lond.* 39, 58–62. https://doi.org/10.1098/rstl.1735.0014

Halley, E., 1687. An historical account of the trade winds, and monsoons, observable in the seas between and near the Tropicks, with an attempt to assign the physical cause of the said winds. *Philos. Trans. R. Soc. Lond.* 16, 153–168. https://doi.org/10.1098/rstl.1686.0026

Harrison, R.J., Feinberg, J.M., 2008. FORCinel: an improved algorithm for calculating first-order reversal curve distributions using locally weighted regression smoothing. *Geochem. Geophys. Geosyst.* 9. https://doi.org/10.1029/2008GC001987

Harrison, R.J., Lascu, I., 2014. FORCulator: a micromagnetic tool for simulating first-order reversal curve diagrams. *Geochem. Geophys. Geosyst.* 15, 4671–4691. https://doi.org/10.1002/2014GC005582

Harrison, R.J., Muraszko, J., Heslop, D., Lascu, I., Muxworthy, A.R., Roberts, A.P., 2018. An improved algorithm for unmixing first-order reversal curve diagrams using principal component analysis. *Geochem. Geophys. Geosyst.* 19, 1595–1610. https://doi.org/10.1029/2018GC007511

Haug, G.H., Tiedemann, R., 1998. Effect of the formation of the Isthmus of Panama on Atlantic Ocean thermohaline circulation. *Nature* 393, 673.

Haug, G.H., Sigman, D.M., Tiedemann, R., Pedersen, T.F., Sarnthein, M., 1999. Onset of permanent stratification in the subarctic Pacific Ocean. *Nature* 401, 779–782. https://doi.org/10.1038/44550

Haug, G.H., Tiedemann, R., Zahn, R., Ravelo, A.C., 2001. Role of Panama uplift on oceanic freshwater balance. *Geology* 29, 207–210.

Haug, G.H., Ganopolski, A., Sigman, D.M., Rosell-Mele, A., Swann, G.E.A., Tiedemann, R., Jaccard, S.L., Bollmann, J., Maslin, M.A., Leng, M.J., Eglinton, G., 2005. North Pacific seasonality and the glaciation of North America 2.7 million years ago. *Nature* 433, 821–825. https://doi.org/10.1038/nature03332

Heider, F., Zitzelsberger, A., Fabian, K., 1996. Magnetic susceptibility and remanent coercive force in grown magnetite crystals from 0.1 µm to 6 mm. *Phys. Earth Planet. Inter.* 93, 239–256. https://doi.org/10.1016/0031-9201(95)03071-9

Heinrich, W., Spill, A., 1979. Geomagnetic shielding of cosmic rays for different satellite orbits. *J. Geophys. Res.* 84, 4401–4404. https://doi.org/10.1029/JA084iA08p04401

Heller, F., Evans, M.E., 1995. Loess magnetism. *Rev. Geophys.* 33, 211–240. https://doi.org/10.1029/95RG00579

Hemming, S.R., 2004. Heinrich events: massive late Pleistocene detritus layers of the North Atlantic and their global climate imprint. *Rev. Geophys.* 42. https://doi.org/10.1029/2003RG000128

Henderson, G.M., Anderson, R.F., 2003. The U-series toolbox for paleoceanography. *Rev. Mineral. Geochem.* 52, 493–531. https://doi.org/10.2113/0520493

Henry, L.G., McManus, J.F., Curry, W.B., Roberts, N.L., Piotrowski, A.M., Keigwin, L.D., 2016. North Atlantic ocean circulation and abrupt climate change during the last glaciation. *Science* 353, 470–474. https://doi.org/10.1126/science.aaf5529

Heslop, D., Dillon, M., 2007. Unmixing magnetic remanence curves without *a priori* knowledge. *Geophys. J. Int.* 170, 556–566.

Heslop, D., Dekkers, M.J., Kruiver, P.P., van Oorschot, I.H.M., 2002. Analysis of isothermal remanent magnetization acquisition curves using the expectation-maximization algorithm. *Geophys. J. Int.* 148, 58–64.

Heslop, D., McIntosh, G., Dekkers, M.J., 2004. Using time- and temperature-dependent Preisach models to investigate the limitations of modelling isothermal remanent magnetization acquisition curves with cumulative log Gaussian functions. *Geophys. J. Int.* 157, 55–63. https://doi.org/10.1111/j.1365-246X.2004.02155.x

Higginson, M.J., Maxwell, J.R., Altabet, M.A., 2003. Nitrogen isotope and chlorin paleoproductivity records from the northern South China Sea: remote vs. local forcing of millennial- and orbital-scale variability. *Mar. Geol.* 201, 223–250. https://doi.org/10.1016/S0025-3227(03)00218-4

Holtzapffel, T., 1985. *Les minéraux argileux, préparation, analyse diffractométrique et* *détermination*. Société géologique du Nord Publication.

Horn, D.R., Delach, M.N., Horn, B.M., 1969. Distribution of volcanic ash layers and turbidites in the North Pacific. *Bull. Geol. Soc. Am.* 80, 1715–1724. https://doi.org/10.1130/0016-7606(1969)80[1715:DOVALA]2.0.CO;2

Horn, D.R., Horn, B.M., Delach, M.N., 1970. Sedimentary provinces of the North Pacific, in: Hays, J.D. (Ed.), *Geological Investigations of the North Pacific*. pp. 1–21. https://doi.org/10.1130/MEM126-p1

Horng, C.S., Chen, K.H., 2006. Complicated magnetic mineral assemblages in marine sediments offshore of southwestern Taiwan: possible influence of methane flux on the early diagenetic process. *Terr. Atmos. Ocean. Sci.* 17, 1009. https://doi.org/10.3319/TAO.2006.17.4.1009(GH)

Horng, C.S., Roberts, A.P., 2006. Authigenic or detrital origin of pyrrhotite in sediments?: Resolving a paleomagnetic conundrum. *Earth Planet. Sci. Lett.* 241, 750–762. https://doi.org/10.1016/j.epsl.2005.11.008

Horng, C.S., Huh, C.A., 2011. Magnetic properties as tracers for source-to-sink dispersal of sediments: a case study in the Taiwan Strait. *Earth Planet. Sci. Lett.* 309, 141–152. https://doi.org/10.1016/j.epsl.2011.07.002

Horng, C.S., Huh, C.A., Chen, K.H., Lin, C.H., Shea, K.S., Hsiung, K.H., 2012. Pyrrhotite as a tracer for denudation of the Taiwan orogen. *Geochem. Geophys. Geosyst.* 13. https://doi.org/10.1029/2012GC004195

Hovan, S.A., Rea, D.K., Pisias, N.G., Shackleton, N.J., 1989. A direct link between the China loess and marine $\delta^{18}O$ records: aeolian flux to the North Pacific. *Nature* 340, 296–298. https://doi.org/10.1038/340296a0

Hovan, S.A., Rea, D.K., Pisias, N.G., 1991. Late Pleistocene continental climate and oceanic variability recorded in northwest Pacific sediments. *Paleoceanography* 6, 349–370. https://doi.org/10.1029/91PA00559

Hrouda, F., 1994. A technique for the measurement of thermal changes of magnetic susceptibility of weakly magnetic rocks by the CS-2 apparatus and KLY-2 Kappabridge. *Geophys. J. Int.* 118, 604–612. https://doi.org/10.1111/j.1365-246X.1994.tb03987.x

Hu, F., Yang, X., 2016. Geochemical and geomorphological evidence for the provenance of aeolian deposits in the Badain Jaran Desert, northwestern China. *Quat. Sci. Rev.* 131, 179–192. https://doi.org/10.1016/j.quascirev.2015.10.039

Hu, P., Liu, Q., Torrent, J., Barrón, V., Jin, C., 2013. Characterizing and quantifying iron oxides in Chinese loess/paleosols: implications for pedogenesis. *Earth Planet. Sci. Lett.* 369, 271–283. https://doi.org/10.1016/j.epsl.2013.03.033

Hu, P.X., Zhao, X., Roberts, A.P., Heslop, D., Viscarra Rossel, R.A., 2018. Magnetic domain state diagnosis in soils, loess, and marine sediments from multiple first-order reversal curve-type diagrams. *J. Geophys. Res. Solid Earth* 132, 998–1017. https://doi.org/10.1002/2017JB015195

Huang, B., Jian, Z., Wang, P., 2005. Paleoceanographic evolution recorded in the northern South China Sea since 4 Ma. *Sci. China D* 48, 2166–2173. https://doi.org/10.1360/03yd0564

Huang, C.Y., Wu, W.Y., Chang, C.P., Tsao, S., Yuan, P.B., Lin, C.W., Xia, K.-Y., 1997. Tectonic evolution of accretionary prism in the arc-continent collision terrane of Taiwan. *Tectonophysics* 281, 31–51. https://doi.org/10.1016/S0040-1951(97)00157-1

Huang, C.Y., Yuan, P.B., Lin, C.W., Wang, T.K., Chang, C.P., 2000. Geodynamic processes of Taiwan arc-continent collision and comparison with analogs in Timor, Papua New Guinea, Urals and Corsica. *Tectonophysics* 325, 1–21. https://doi.org/10.1016/S0040-1951(00)00128-1

Huang, E., Chen, Y., Schefuß, E., Steinke, S., Liu, J., Tian, J., Martínez-Méndez, G., Mohtadi, M., 2018. Precession and glacial-cycle controls of monsoon precipitation isotope changes over East Asia during the Pleistocene. *Earth Planet. Sci. Lett.* 494, 1–11. https://doi.org/10.1016/j.epsl.2018.04.046

Hughes, G.R., Mahood, G.A., 2008. Tectonic controls on the nature of large silicic calderas in volcanic arcs. *Geology* 36, 627–630. https://doi.org/10.1130/G24796A.1

Hunt, C.P., Singer, M.J., Kletetschka, G., TenPas, J., Verosub, K.L., 1995. Effect of citrate-bicarbonate-dithionite treatment on fine-grained magnetite and maghemite. *Earth Planet. Sci. Lett.* 130, 87–94. https://doi.org/10.1016/0012-821X(94)00256-X

Inoue, S., Yamazaki, T., 2010. Geomagnetic relative paleointensity chronostratigraphy of sediment cores from the Okhotsk Sea. *Palaeogeogr. Palaeoclimatol. Palaeoecol.* 291, 253–266. https://doi.org/10.1016/j.palaeo.2010.02.037

Irurzun, M.A., Palermo, P., Gogorza, C.S.G., Sinito, A.M., Aldana, M., Costanzo-Álvarez, V., Ohlendorf, C., Zolitschka, B., 2020. Testing lake-level reconstructions based on rock magnetic proxies for the sediment record of Laguna Cháltel (Patagonia, Argentina). *Quat. Res.* 95, 113–128. https://doi.org/10.1017/qua.2020.15

Itambi, A.C., von Dobeneck, T., Mulitza, S., Bickert, T., Heslop, D., 2009. Millennial-scale northwest African droughts related to Heinrich events and Dansgaard-Oeschger cycles: evidence in marine sediments from offshore Senegal. *Paleoceanography* 24, PA1205. https://doi.org/10.1029/2007PA001570

Jackson, M., Worm, H.U., Banerjee, S.K., 1990. Fourier analysis of digital hysteresis data: rock magnetic applications. *Phys. Earth Planet. Inter.* 65, 78–87. https://doi.org/10.1016/0031-9201(90)90077-B

Jacobs, J.A., 1959. Geomagnetic micropulsations. *Nature* 183, 381. https://doi.org/10.1038/183381a0

Janecek, T.R., 1985. Eolian sedimentation in the northwest Pacific Ocean: a preliminary examination of the data from Deep Sea Drilling Project Sites 576 and 578. *Init. Rep. Deep Sea Drill. Proj.* 86, 589–603. https://doi.org/10.2973/dsdp.proc.86.126.1985

Janecek, T.R., Rea, D.K., 1983. Eolian deposition in the northeast Pacific Ocean: Cenozoic history of atmospheric circulation. *Geol. Soc. Am. Bull.* 94, 730–738. https://doi.org/10.1130/0016-7606(1983)94<730:EDITNP>2.0.CO;2

Janecek, T.R., Rea, D.K., 1984. Pleistocene fluctuations in northern hemisphere tradewinds and westerlies, in: Berger, I., Imbrie, J., Hays, J., Kukla, G., Saltzman, B. (Eds.), *Milankovitch and Climate, Understanding the Response to Orbital Forcing, Part 1*. D. Reidel, Norwell, pp. 331–347.

Janecek, T.R., Rea, D.K., 1985. Quaternary fluctuations in the northern hemisphere trade winds and westerlies. *Quat. Res.* 24, 150–163. https://doi.org/10.1016/0033-5894(85)90002-X

Ji, J., Chen, J., Balsam, W., Lu, H., Sun, Y., Xu, H., 2004. High resolution hematite/goethite records from Chinese loess sequences for the last glacial-interglacial cycle: rapid climatic response of the East Asian monsoon to the tropical Pacific. *Geophys. Res. Lett.* 31. https://doi.org/10.1029/2003GL018975

Jian, Z., Zhao, Q., Cheng, X., Wang, J., Wang, P., Su, X., 2003. Pliocene-Pleistocene stable isotope and paleoceanographic changes in the northern South China Sea. *Palaeogeogr. Palaeoclimatol. Palaeoecol.* 3–4, 425–442. https://doi.org/10.1016/S0031-0182(03)00259-1

Jian, Z., Yu, Y., Li, B., Wang, J., Zhang, X., Zhou, Z., 2006. Phased evolution of the south-north hydrographic gradient in the South China Sea since the middle Miocene. *Palaeogeogr. Palaeoclimatol. Palaeoecol.* 230, 251–263. https://doi.org/10.1016/j.palaeo.2005.07.018

Jiang, W.T., Horng, C.S., Roberts, A.P., Peacor, D.R., 2001. Contradictory magnetic polarities in sediments and variable timing of neoformation of authigenic greigite. *Earth Planet. Sci. Lett.* 193, 1–12. https://doi.org/10.1016/S0012-821X(01)00497-6

Jiang, Z., Liu, Q., Barrón, V., Torrent, J., Yu, Y., 2012. Magnetic discrimination between Al-substituted hematites synthesized by hydrothermal and thermal dehydration methods and its geological significance. *J. Geophys. Res. Solid Earth* 117. https://doi.org/10.1029/2011JB008605

Johnson, H.P., Kinoshita, H., Merrill, R.T., 1975. Rock magnetism and paleomagnetism of some North Pacific deep-sea sediments. *Bull. Geol. Soc. Am.* 86, 412–420. https://doi.org/10.1130/0016-7606(1975)86<412:RMAPOS>2.0.CO;2

Jolliffe, I.T., 2002. *Principal Component Analysis*. Springer-Verlag.

Jones, C.E., Halliday, A.N., Rea, D.K., Owen, R.M., 2000. Eolian inputs of lead to the North Pacific. *Geochim. Cosmochim. Acta* 64, 1405–1416. https://doi.org/10.1016/S0016-7037(99)00439-1

Kämpf, N., Schwertmann, U., 1983. Goethite and hematite in a climosequence in southern Brazil and their application in classification of kaolinitic soils. *Geoderma* 29, 27–39. https://doi.org/10.1016/0016-7061(83)90028-9

Kao, S.J., Horng, C.S., Roberts, A.P., Liu, K.K., 2004. Carbon-sulfur-iron relationships in sedimentary rocks from southwestern Taiwan: influence of geochemical environment on greigite and pyrrhotite formation. *Chem. Geol.* 203, 153–168. https://doi.org/10.1016/j.chemgeo.2003.09.007

Karlin, R., 1990. Magnetite diagenesis in marine sediments from the Oregon continental margin. *J. Geophys. Res.* 95, 4405–4419. https://doi.org/10.1029/JB095iB04p04405

Katari, K., Bloxham, J., 2001. Effects of sediment aggregate size on DRM intensity: a new theory. *Earth Planet. Sci. Lett.* 186, 113–122. https://doi.org/10.1016/S0012-821X(00)00386-1

Katz, B., Elmore, R.D., Engel, M.H., 1998. Authigenesis of magnetite in organic-rich sediment next to a dike: implications for thermoviscous and chemical remagnetizations. *Earth Planet. Sci. Lett.* 163, 221–234. https://doi.org/10.1016/S0012-821X(98)00189-7

Kawahata, H., Ohkushi, K.I., Hatakeyama, Y., 1999. Comparative late Pleistocene paleoceanographic changes in the mid latitude boreal and austral western Pacific. *J. Oceanogr.* 55, 747–761. https://doi.org/10.1023/A:1007824415499

Keigwin, L., 1982. Isotopic paleoceanography of the Caribbean and east Pacific: role of Panama uplift in late Neogene time. *Science* 217, 350–353. https://doi.org/10.1126/science.217.4557.350

Kent, D.V., Lowrie, W., 1974. Origin of magnetic instability in sediment cores from the central North Pacific. *J. Geophys. Res.* 79, 2987–3000. https://doi.org/10.1029/JB079i020p02987

Kidston, J., Vallis, G.K., 2012. The relationship between the speed and the latitude of an eddy-driven jet in a stirred barotropic model. *J. Atmos. Sci.* 69, 3251–3263. https://doi.org/10.1175/JAS-D-11-0300.1

Kiefer, T., Sarnthein, M., Erlenkeuser, H., Grootes, P.M., Roberts, A.P., 2001. North Pacific response to millennial-scale changes in ocean circulation over the last 60 kyr. *Paleoceanography* 16, 179–189. https://doi.org/10.1029/2000PA000545

King, J., Banerjee, S.K., Marvin, J., Özdemir, Ö., 1982. A comparison of different magnetic methods for determining the relative grain size of magnetite in natural materials: some results from lake sediments. *Earth Planet. Sci. Lett.* 59, 404–419. https://doi.org/10.1016/0012-821X(82)90142-X

King, J.W., Banerjee, S.K., Marvin, J., 1983. A new rock-magnetic approach to selecting sediments for geomagnetic paleointensity studies: application to paleointensity for the last 4000 years. *J. Geophys. Res.* 88, 5911–5921. https://doi.org/10.1029/JB088iB07p05911

Kirschvink, J.L., 1980. The least-squares line and plane and the analysis of palaeomagnetic data. *Geophys. J. R. Astron. Soc.* 62, 699–718. https://doi.org/10.1111/j.1365-246X.1980.tb02601.x

Kissel, C., Laj, C., Clemens, S., Solheid, P., 2003. Magnetic signature of environmental changes in the last 1.2 Myr at ODP Site 1146, South China Sea. *Mar. Geol.* 201, 119–132. https://doi.org/10.1016/S0025-3227(03)00212-3

Kissel, C., Liu, Z., Li, J., Wandres, C., 2016. Magnetic minerals in three Asian rivers draining into the South China Sea: Pearl, Red, and Mekong Rivers. *Geochem. Geophys. Geosyst.* 17, 1678–1693. https://doi.org/10.1002/2016GC006283

Kissel, C., Liu, Z., Li, J., Wandres, C., 2017. Magnetic signature of river sediments drained into the southern and eastern part of the South China Sea (Malay Peninsula, Sumatra, Borneo, Luzon and Taiwan). *Sediment. Geol.* 347, 10–20. https://doi.org/10.1016/j.sedgeo.2016.11.007

Kissel, C., Sarnthein, M., Laj, C., Wang, P.X., Wandres, C., Egli, R., 2018. Magnetic fingerprints of modern sediments in the South China Sea resulting from source-to-sink processes. *Geochem. Geophys. Geosyst.* 19, 1979–1993. https://doi.org/10.1029/2018GC007571

Kletetschka, G., Wasilewski, P.J., 2002. Grain size limit for SD hematite. *Phys. Earth Planet. Inter.* 129, 173–179. https://doi.org/10.1016/S0031-9201(01)00271-0

Kodama, K.P., Hinnov, L.A., 2014. *Rock Magnetic Cyclostratigraphy*. John Wiley & Sons. https://doi.org/10.1002/9781118561294

Korff, L., von Dobeneck, T., Frederichs, T., Kasten, S., Kuhn, G., Gersonde, R., Diekmann, B., 2016. Cyclic magnetite dissolution in Pleistocene sediments of the abyssal northwest Pacific Ocean: evidence for glacial oxygen depletion and carbon trapping. *Paleoceanography* 31, 600–624. https://doi.org/10.1002/2015PA002882

Kosterov, A., 2003. Low-temperature magnetization and AC susceptibility of magnetite: effect of thermomagnetic history. *Geophys. J. Int.* 154, 58–71. https://doi.org/10.1046/j.1365-246X.2003.01938.x

Krs, M., Novák, F., Krsová, M., Pruner, P., Kouklíková, L., Jansa, J., 1992. Magnetic properties and metastability of greigite-smythite mineralization in brown-coal basins of the Krušné hory Piedmont, Bohemia. *Phys. Earth Planet. Inter.* 70, 273–287. https://doi.org/10.1016/0031-9201(92)90194-Z

Kruiver, P.P., Dekkers, M.J., Heslop, D., 2001. Quantification of magnetic coercivity components by the analysis of acquisition curves of isothermal remanent magnetisation. *Earth Planet. Sci. Lett.* 189, 269–276. https://doi.org/10.1016/S0012-821X(01)00367-3

Kyte, F.T., Leinen, M., Heath, G.R., Zhou, L., 1993. Cenozoic sedimentation history of the central North Pacific: inferences from the elemental geochemistry of core LL44-GPC3. *Geochim. Cosmochim. Acta* 57, 1719–1740. https://doi.org/10.1016/0016-7037(93)90109-A

Laj, C., Kissel, C., Mazaud, A., Channell, J.E.T., Beer, J., 2000. North Atlantic palaeointensity stack since 75 ka (NAPIS-75) and the duration of the Laschamp event. *Philos. Trans. R. Soc. Lond. A* 358, 1009–1025. https://doi.org/10.1098/rsta.2000.0571

Laj, C., Kissel, C., Beer, J., 2004. High resolution global paleointensity stack since 75 kyr (GLOPIS-75) calibrated to absolute values, in: Channell, J.E.T., Kent, D.V., Lowrie, W., Meerts, J. (Eds.), *AGU Geophysical Monograph Series*: *Timescales of the Paleomagnetic Field.* pp. 255–265. https://doi.org/10.1029/145GM19

Laj, C., Kissel, C., Roberts, A.P., 2006. Geomagnetic field behavior during the Iceland Basin and Laschamp geomagnetic excursions: a simple transitional field geometry? *Geochem. Geophys. Geosyst.* 7. https://doi.org/10.1029/2005GC001122

Lal, D., Peters, B., 1967. Cosmic ray produced radioactivity on the Earth, in: Flügge, D. (Ed.), *Handbuch Der Physik*. Springer, pp. 551–612. https://doi.org/10.1007/978-3-642-46079-1_7

Lamy, F., Chiang, J.C.H., Martínez-Méndez, G., Thierens, M., Arz, H.W., Bosmans, J., Hebbeln, D., Lambert, F., Lembke-Jene, L., Stuut, J.B., 2019. Precession modulation of the South Pacific westerly wind belt over the past million years. *Proc. Natl. Acad. Sci. USA* 116, 23455–23460. https://doi.org/10.1073/pnas.1905847116

Lanci, L., Pares, J.M., Channell, J.E.T., Kent, D. V., 2004. Miocene magnetostratigraphy from equatorial Pacific sediments (ODP Site 1218, Leg 199). *Earth Planet. Sci. Lett.* 226, 207–224. https://doi.org/10.1016/j.epsl.2004.07.025

Lanci, L., Parés, J.M., Channell, J.E.T., Kent, D.V., 2005. Oligocene magnetostratigraphy from equatorial Pacific sediments (ODP Sites 1218 and 1219, Leg 199). *Earth Planet. Sci. Lett.* 237, 617–634. https://doi.org/10.1016/j.epsl.2005.07.004

Larrasoaña, J.C., Roberts, A.P., Rohling, E.J., Winklhofer, M., Wehausen, R., 2003. Three million years of monsoon variability over the northern Sahara. *Clim. Dyn.* 21, 689–698. https://doi.org/10.1007/s00382-003-0355-z

Lascu, I., Banerjee, S.K., Berquó, T.S., 2010. Quantifying the concentration of ferrimagnetic particles in sediments using rock magnetic methods. *Geochem. Geophys. Geosyst.* 11. https://doi.org/10.1029/2010GC003182

Lascu, I., Harrison, R.J., Li, Y., Muraszko, J.R., Channell, J.E.T., Piotrowski, A.M., Hodell, D.A., 2015. Magnetic unmixing of first-order reversal curve diagrams using principal component analysis. *Geochem. Geophys. Geosyst.* 16, 2900–2915. https://doi.org/10.1002/2015GC005909

Lascu, I., Einsle, J.F., Ball, M.R., Harrison, R.J., 2018. The vortex state in geologic materials: a micromagnetic perspective. *J. Geophys. Res. Solid Earth* 123, 7285–7304. https://doi.org/10.1029/2018JB015909

Laskar, J., Robutel, P., Joutel, F., Gastineau, M., Correia, A.C.M., Levrard, B., 2004. A long-term numerical solution for the insolation quantities of the Earth. *Astron. Astrophys.* 428, 261–285. https://doi.org/10.1051/0004-6361:20041335

Le Bas, M.J., Le Maitre, R.W., Streckeisen, A., Zanettin, B., 1986. A chemical classification of volcanic rocks based on the total alkali-silica diagram. *J. Petrol.* 27, 745–750. https://doi.org/10.1093/petrology/27.3.745

Lee, D.D., Seung, H.S., 2001. Algorithms for non-negative matrix factorization, in: *Advances in Neural Information Processing Systems*. pp. 556–562.

Leonhardt, R., Fabian, K., Winklhofer, M., Ferk, A., Laj, C., Kissel, C., 2009. Geomagnetic field evolution during the Laschamp excursion. *Earth Planet. Sci. Lett.* 278, 87–95. https://doi.org/10.1016/j.epsl.2008.11.028

Levi, S., Banerjee, S.K., 1976. On the possibility of obtaining relative paleointensities from lake sediments. *Earth Planet. Sci. Lett.* 29, 219–226.

https://doi.org/10.1016/0012-821X(76)90042-X

Li, B., Wang, J., Huang, B., Li, Q., Jian, Z., Zhao, Q., Su, X., Wang, P., 2004. South China Sea surface water evolution over the last 12 Myr: a south-north comparison from Ocean Drilling Program Sites 1143 and 1146. *Paleoceanography* 19, PA1009. https://doi.org/10.1029/2003PA000906

Li, C., Xu, X., Lin, J., Sun, Z., Zhu, J., Yao, Y., Zhao, X., Liu, Q., Kulhanek, D.K., Wang, J., Song, T., Zhao, J., Qiu, N., Guan, Y., Zhou, Z., Williams, T., Bao, R., Briais, A., Brown, E.A., Chen, Y., Clift, P.D., Colwell, F.S., Dadd, K.A., Ding, W., Almeida, I.H., Huang, X., Hyun, S., Jiang, T., Koppers, A.A.P., Li, Q., Liu, C., Liu, Z., Nagai, R.H., Peleo-Alampay, A., Su, X., Tejada, M.L.G., Trinh, H.S., Yeh, Y.C., Zhang, C., Zhang, F., Zhang, G., 2014. Ages and magnetic structures of the South China Sea constrained by deep tow magnetic surveys and IODP Expedition 349. *Geochem. Geophys. Geosyst.* 15, 4958–4983. https://doi.org/10.1002/2014GC005567

Li, C., Lin, J., Kulhanek, D.K., Williams, T., Bao, R., Briais, A., Brown, E.A., Chen, Y., Clift, P.D., Colwell, F.S., Dadd, K.A., Ding, W.-W., Hernández-Almeida, I., Huang, X.-L., Hyun, S., Jiang, T., Koppers, A.A.P., Li, Q., Liu, C., Liu, Q., Liu, Z., Nagai, R.H., Peleo-Alampay, A., Su, X., Sun, Z., Tejada, M.L.G., Trinh, H.S., Yeh, Y.-C., Zhang, C., Zhang, F., Zhang, G.-L., Zhao, X., 2015a. Expedition 349 summary. *Proc. Int. Ocean Disc. Progr.* 349, 1–43. https://doi.org/10.14379/iodp.proc.349.101.2015

Li, C, Lin, J., Kulhanek, D.K., Williams, T., Bao, R., Briais, A., Brown, E.A., Chen, Y., Clift, P.D., Colwell, F.S., Dadd, K.A., Ding, W., Hernández-Almeida, I., Huang, X.-L., Hyun, S., Jiang, T., Koppers, A.A.P., Li, Q., Liu, C., Liu, Q., Liu, Z., Nagai, R.H., Peleo-Alampay, A., Su, X., Sun, Z., Tejada, M.L.G., Trinh, H.S., Yeh, Y.-C., Zhang, C., Zhang, F., Zhang, G.-L., Zhao, X., 2015b. Site U1431. *Proc. Int. Ocean Disc. Progr.* 349. https://doi.org/http://dx.doi.org/10.14379/iodp.proc.349.103.2015

Li, J., Yue, L., Roberts, A.P., Hirt, A.M., Pan, F., Guo, L., Xu, Y., Xi, R., Guo, L., Qiang, X., Gai, C., Jiang, Z., Sun, Z., Liu, Q., 2018. Global cooling and enhanced Eocene Asian mid-latitude interior aridity. *Nat. Commun.* 9, 1–8. https://doi.org/10.1038/s41467-018-05415-x

Li, M., Ouyang, T., Roberts, A.P., Heslop, D., Zhu, Z., Zhao, X., Tian, C., Peng, S., Zhong, H., Peng, X., Qiu, Y., 2018. Influence of sea level change and centennial East Asian monsoon variations on northern South China Sea sediments over the past 36 kyr. *Geochem. Geophys. Geosyst.* 19, 1674–1689. https://doi.org/10.1029/2017GC007321

Li, M., Hinnov, L., Kump, L., 2019. Acycle: time-series analysis software for paleoclimate research and education. *Comput. Geosci.* 127, 12–22. https://doi.org/10.1016/j.cageo.2019.02.011

Li, Q., Wang, P., Zhao, Q., Shao, L., Zhong, G., Tian, J., Cheng, X., Jian, Z., Su, X., 2006. A 33 Ma lithostratigraphic record of tectonic and paleoceanographic evolution of the South China Sea. *Mar. Geol.* 230, 217–235. https://doi.org/10.1016/j.margeo.2006.05.006

Lisiecki, L.E., Raymo, M.E., 2005. A Pliocene-Pleistocene stack of 57 globally distributed benthic $\delta^{18}O$ records. *Paleoceanography* 20. https://doi.org/10.1029/2004PA001071

Lisiecki, L.E., Raymo, M.E., 2007. Plio-Pleistocene climate evolution: trends and transitions in glacial cycle dynamics. *Quat. Sci. Rev.* 26, 56–69. https://doi.org/10.1016/j.quascirev.2006.09.005

Liu, C., Clift, P.D., Giosan, L., Miao, Y., Warny, S., Wan, S., 2019. Paleoclimatic evolution of the SW and NE South China Sea and its relationship with spectral reflectance data over various age scales. *Palaeogeogr. Palaeoclimatol. Palaeoecol.* 525, 25–43. https://doi.org/10.1016/j.palaeo.2019.02.019

Liu, J., Chen, Z., Chen, M., Yan, W., Xiang, R., Tang, X., 2010. Magnetic susceptibility variations and provenance of surface sediments in the South China Sea. *Sediment. Geol.* 230, 77–85. https://doi.org/10.1016/j.sedgeo.2010.07.001

Liu, J., Shi, X., Liu, Q., Ge, S., Liu, Y., Yao, Z., Zhao, Q., Jin, C., Jiang, Z., Liu, S., Qiao, S., Li, X., Li, C., Wang, C., 2014. Magnetostratigraphy of a greigite-bearing core from the south Yellow Sea: implications for remagnetization and sedimentation. *J. Geophys. Res. Solid Earth* 119, 7425–7441. https://doi.org/10.1002/2014JB011206

Liu, Q., Deng, C., Yu, Y., Torrent, J., Jackson, M.J., Banerjee, S.K., Zhu, R., 2005a. Temperature dependence of magnetic susceptibility in an argon environment: implications for pedogenesis of Chinese loess/palaeosols. *Geophys. J. Int.* 161, 102–112. https://doi.org/10.1111/j.1365-246X.2005.02564.x

Liu, Q., Torrent, J., Maher, B.A., Yu, Y., Deng, C., Zhu, R., Zhao, X., 2005b. Quantifying grain size distribution of pedogenic magnetic particles in Chinese loess and its significance for pedogenesis. *J. Geophys. Res. Solid Earth* 110, B11. https://doi.org/10.1029/2005JB003726

Liu, Q., Yu, Y., Pan, Y., Zhu, R., Zhao, X., 2005c. Partial anhysteretic remanent magnetization (pARM) of synthetic single- and multi-domain magnetites and its paleoenvironmental significance. *Chin. Sci. Bull.* 50, 2381–2384. https://doi.org/10.1360/982005-178

Liu, Q., Roberts, A.P., Torrent, J., Horng, C.S., Larrasoaña, J.C., 2007. What do the HIRM and S-ratio really measure in environmental magnetism? *Geochem. Geophys. Geosyst.* 8. https://doi.org/10.1029/2007GC001717

Liu, Q., Roberts, A.P., Larrasoaña, J.C., Banerjee, S.K., Guyodo, Y., Tauxe, L., Oldfield, F., 2012. Environmental magnetism: principles and applications. *Rev. Geophys.* 50. https://doi.org/10.1029/2012RG000393

Liu, Z., Stattegger, K., 2014. South China Sea fluvial sediments: an introduction preface. *J. Asian Earth Sci.* 79, 507–508. https://doi.org/10.1016/j.jseaes.2013.11.003

Liu, Z., Alain, T., Clemens, S.C., Wang, P., 2003. Quaternary clay mineralogy in the northern South China Sea (ODP Site 1146). *Sci. China D* 46, 1223–1235. https://doi.org/10.1360/02yd0107

Liu, Z., Colin, C., Huang, W., Phon Le, K., Tong, S., Chen, Z., Trentesaux, A., 2007. Climatic and tectonic controls on weathering in south China and Indochina Peninsula: clay mineralogical and geochemical investigations from the Pearl, Red, and Mekong drainage basins. *Geochem. Geophys. Geosyst.* 8. https://doi.org/10.1029/2006GC001490

Liu, Z., Tuo, S., Colin, C., Liu, J.T., Huang, C.Y., Selvaraj, K., Chen, C.T.A., Zhao, Y., Siringan, F.P., Boulay, S., Chen, Z., 2008. Detrital fine-grained sediment contribution from Taiwan to the northern South China Sea and its relation to regional ocean circulation. *Mar. Geol.* 255, 149–155. https://doi.org/10.1016/j.margeo.2008.08.003

Liu, Z., Zhao, Y., Colin, C., Siringan, F.P., Wu, Q., 2009. Chemical weathering in Luzon, Philippines from clay mineralogy and major-element geochemistry of river sediments. *Appl. Geochemistry* 24, 2195–2205. https://doi.org/10.1016/j.apgeochem.2009.09.025

Liu, Z., Colin, C., Li, X., Zhao, Y., Tuo, S., Chen, Z., Siringan, F.P., Liu, J.T., Huang, C.Y., You, C.F., Huang, K.F., 2010. Clay mineral distribution in surface sediments of the northeastern South China Sea and surrounding fluvial drainage basins: source and transport. *Mar. Geol.* 227, 48–60. https://doi.org/10.1016/j.margeo.2010.08.010

Liu, Z., Zhao, Y., Colin, C., Stattegger, K., Wiesner, M.G., Huh, C.-A., Zhang, Y., Li, X., Sompongchaiyakul, P., You, C.-F., 2016. Source-to-sink transport processes of fluvial sediments in the South China Sea. *Earth-Sci. Rev.* 153, 238–273. https://doi.org/10.1016/j.earscirev.2015.08.005

Lougheed, B.C., Obrochta, S.P., 2016. MatCal: open source Bayesian ^{14}C age calibration in Matlab. *J. Open Res. Softw.* 4. https://doi.org/10.5334/jors.130

Lougheed, B.C., Obrochta, S.P., 2019. A rapid, deterministic age-depth modeling routine for geological sequences with inherent depth uncertainty. *Paleoceanogr. Paleoclimatol.* 34, 122–133. https://doi.org/10.1029/2018PA003457

Lowe, D.J., 2011. Tephrochronology and its application: a review. *Quat. Geochron.* 6, 107–153. https://doi.org/https://doi.org/10.1016/j.quageo.2010.08.003

Lowrie, W., 1990. Identification of ferromagnetic minerals in a rock by coercivity and unblocking temperature properties. *Geophys. Res. Lett.* 17, 159–162. https://doi.org/10.1029/GL017i002p00159

Lowrie, W., Kent, D.V., 2004. Geomagnetic polarity timescales and reversal frequency regimes, in: Channell, J.E.T., Kent, D.V., Lowrie, W., Meerts, J. (Eds.), *AGU Geophysical Monograph Series: Timescales of the Paleomagnetic Field*. pp. 117–129. https://doi.org/10.1029/145GM09

Lunt, D.J., Valdes, P.J., Haywood, A., Rutt, I.C., 2008. Closure of the Panama Seaway during the Pliocene: implications for climate and northern hemisphere glaciation. *Clim. Dyn.* 30, 1–18. https://doi.org/10.1007/s00382-007-0265-6

Lynch-Stieglitz, J., 2017. The Atlantic meridional overturning circulation and abrupt climate change. *Ann. Rev. Mar. Sci.* 9, 83–104. https://doi.org/10.1146/annurev-marine-010816-060415

Machida, H., Arai, F., 2003. *The Atlas of Volcanic Ash*. University of Tokyo Press.

Maher, B.A., 1986. Characterisation of soils by mineral magnetic measurements. *Phys. Earth Planet. Inter.* 42, 76–92. https://doi.org/10.1016/S0031-9201(86)80010-3

Maher, B.A., 1988. Magnetic properties of some synthetic sub-micron magnetites. *Geophys. J.* 94, 83–96. https://doi.org/10.1111/j.1365-246X.1988.tb03429.x

Maher, B.A., 2011. The magnetic properties of Quaternary aeolian dusts and sediments, and their palaeoclimatic significance. *Aeolian Res.* 3, 87–144. https://doi.org/10.1016/j.aeolia.2011.01.005

Maher, B.A., Thompson, R., 2012. Oxygen isotopes from chinese caves: records not of monsoon rainfall but of circulation regime. *J. Quat. Sci.* 27, 615–624. https://doi.org/10.1002/jqs.2553

Maher, B.A., Prospero, J.M., Mackie, D., Gaiero, D., Hesse, P.P., Balkanski, Y., 2010. Global connections between aeolian dust, climate and ocean biogeochemistry at the present day and at the last glacial maximum. *Earth-Sci. Rev.* 99, 61–97. https://doi.org/10.1016/j.earscirev.2009.12.001

Mangerud, J., Lie, S.E., Furnes, H., Kristiansen, I.L., Lømo, L., 1984. A Younger Dryas ash bed in western Norway, and its possible correlations with tephra in cores from the Norwegian Sea and the North Atlantic. *Quat. Res.* 21, 85–104. https://doi.org/10.1016/0033-5894(84)90092-9

Mann, S., Sparks, N.H.C., Frankel, R.B., Bazylinski, D.A., Jannasch, H.W., 1990. Biomineralization of ferrimagnetic greigite (Fe_3S_4) and iron pyrite (FeS_2) in a magnetotactic bacterium. *Nature* 343, 258–261. https://doi.org/10.1038/343258a0

Martin, J.H., Fitzwater, S.E., 1988. Iron deficiency limits phytoplankton growth in the north-east Pacific subarctic. *Nature* 31, 341–343. https://doi.org/10.1038/331341a0

Masuda, Y., Aoki, K.I., 1979. Trace element variations in the volcanic rocks from the Nasu zone, northeast Japan. *Earth Planet. Sci. Lett.* 44, 139–149. https://doi.org/10.1016/0012-821X(79)90014-1

Matsu'ura, T., Furusawa, A., Shimogama, K., Goto, N., Komatsubara, J., 2014. Late Quaternary tephrostratigraphy and cryptotephrostratigraphy of deep-sea sequences (Chikyu C9001C cores) as tools for marine terrace chronology in NE Japan. *Quat. Geochron.* 23, 67–79. https://doi.org/10.1016/j.quageo.2014.06.001

Matsuzaki, H., Kobayashi, K., Momose, K., 1954. On the anomalously strong natural remanent magnetism of the lava of Mt. Utsukushi-ga-hara. *J. Geomagn. Geoelectr.* 6, 53–56. https://doi.org/10.5636/jgg.6.53

Matuyama, M., 1929. On the direction of magnetisation of basalt in Japan, Tyôsen and Manchuria. *Proc. Imp. Acad.* 5, 203–205. https://doi.org/10.2183/pjab1912.5.203

Mayergoyz, I.D., 1986. Mathematical models of hysteresis. *IEEE Trans. Magn.* 22, 603–608. https://doi.org/10.1109/TMAG.1986.1064347

McDonough, W.F., Sun, S.S., 1995. The composition of the Earth. *Chem. Geol.* 120, 223–253. https://doi.org/10.1016/0009-2541(94)00140-4

McElhinny, M.W., 1973. *Palaeomagnetism and Plate Tectonics*. Cambridge University Press. https://doi.org/10.2307/1795057

Meena, N.K., Maiti, S., Shrivastava, A., 2011. Discrimination between anthropogenic (pollution) and lithogenic magnetic fraction in urban soils (Delhi, India) using environmental magnetism. *J. Appl. Geophys.* 73, 121–129. https://doi.org/10.1016/j.jappgeo.2010.12.003

Meert, J.G., 2009. In GAD we trust. *Nat. Geosci.* 2, 673–674. https://doi.org/10.1038/ngeo635

Mehra, O.P., Jackson, M.L., 1958. Iron oxide removal from soils and clays by a dithionite–citrate system buffered with sodium bicarbonate. *Clays Clay Miner.* 7, 317–327. https://doi.org/10.1016/b978-0-08-009235-5.50026-7

Merrill, J.T., Uematsu, M., Bleck, R., 1989. Meteorological analysis of long range transport of mineral aerosols over the North Pacific. *J. Geophys. Res.* 94, 8584–8598. https://doi.org/10.1029/JD094iD06p08584

Mizuno, K., White, W.B., 1983. Annual and interannual variability in the Kuroshio Current system. *J. Phys. Oceanogr.* 13, 1847–1867. https://doi.org/10.1175/1520-0485(1983)013<1847:aaivit>2.0.co;2

Mölg, T., Maussion, F., Scherer, D., 2014. Mid-latitude westerlies as a driver of glacier variability in monsoonal High Asia. *Nat. Clim. Change* 4, 68–73. https://doi.org/10.1038/nclimate2055

Morin, F.J., 1950. Magnetic susceptibility of α-Fe_2O_3 and α-Fe_2O_3 with added titanium. *Phys. Rev.* 78, 819. https://doi.org/10.1103/PhysRev.78.819.2

Morley, J.J., Pisias, N.G., Leinen, M., 1987. Late Pleistocene time series of atmospheric and oceanic variables recorded in sediments from the subarctic Pacific. *Paleoceanography* 2, 49–62. https://doi.org/10.1029/PA002i001p00049

Morse, J.W., Millero, F.J., Cornwell, J.C., Rickard, D., 1987. The chemistry of the hydrogen sulfide and iron sulfide systems in natural waters. *Earth-Sci. Rev.* 24, 1–42. https://doi.org/10.1016/0012-8252(87)90046-8

Moskowitz, B.M., Frankel, R.B., Bazylinski, D.A., 1993. Rock magnetic criteria for the detection of biogenic magnetite. *Earth Planet. Sci. Lett.* 120, 283–300. https://doi.org/10.1016/0012-821X(93)90245-5

Mullins, C.E., Tite, M.S., 1973. Magnetic viscosity, quadrature susceptibility, and frequency dependence of susceptibility in single-domain assemblies of magnetite and maghemite. *J. Geophys. Res.* 78, 804–809. https://doi.org/10.1029/jb078i005p00804

Musgrave, R.J., Kars, M., Vega, M.E., 2019. Progressive and punctuated magnetic mineral diagenesis: the rock magnetic record of multiple fluid inputs and progressive pyritization in a volcano-bounded basin, IODP Site U1437, Izu Rear Arc. *J. Geophys. Res. Solid Earth* 124, 5357–5378. https://doi.org/10.1029/2018JB017277

Muxworthy, A.R., Dunlop, D.J., 2002. First-order reversal curve (FORC) diagrams for pseudo-single-domain magnetites at high temperature. *Earth Planet. Sci. Lett.* 203, 369–382. https://doi.org/10.1016/S0012-821X(02)00880-4

Muxworthy, A.R., Heslop, D., Williams, W., 2004. Influence of magnetostatic interactions on first-order-reversal-curve (FORC) diagrams: a micromagnetic approach. *Geophys. J. Int.* 158, 888–897. https://doi.org/10.1111/j.1365-246X.2004.02358.x

Nagashima, K., Tada, R., Tani, A., Sun, Y., Isozaki, Y., Toyoda, S., Hasegawa, H., 2011. Millennial-scale oscillations of the westerly jet path during the last glacial period. *J. Asian Earth Sci.* 40, 1214–1220. https://doi.org/10.1016/j.jseaes.2010.08.010

Nagy, L., Williams, W., Muxworthy, A.R., Fabian, K., Almeida, T.P., Conbhuí, P.Ó., Shcherbakov, V.P., 2017. Stability of equidimensional pseudo-single-domain magnetite over billion-year timescales. *Proc. Natl. Acad. Sci. U. S. A.* 114, 10356–10360. https://doi.org/10.1073/pnas.1708344114

Néel, L., 1955a. Remarques sur la théorie des propriétés magnétiques des substances dures. *Appl. Sci. Res. B* 4, 13–24. https://doi.org/10.1007/BF02316465

Néel, L., 1955b. Some theoretical aspects of rock-magnetism. *Adv. Phys.* 4, 191–243. https://doi.org/10.1080/00018735500101204

Newell, A.J., 2005. A high-precision model of first-order reversal curve (FORC) functions for single-domain ferromagnets with uniaxial anisotropy. *Geochem. Geophys. Geosyst.* 6. https://doi.org/10.1029/2004GC000877

Ninkovich, D., Opdyke, N., Heezen, B.C., Foster, J.H., 1966. Paleomagnetic stratigraphy, rates of deposition and tephrachronology in North Pacific deep-sea sediments. *Earth Planet. Sci. Lett.* 1, 476–492. https://doi.org/10.1016/0012-821X(66)90052-5

Nowaczyk, N.R., Arz, H.W., Frank, U., Kind, J., Plessen, B., 2012. Dynamics of the Laschamp geomagnetic excursion from Black Sea sediments. *Earth Planet. Sci. Lett.* 351–352, 54–69. https://doi.org/10.1016/j.epsl.2012.06.050

Okada, M., Takagi, M., Narita, H., Takahashi, K., 2005. Chronostratigraphy of sediment cores from the Bering Sea and the subarctic Pacific based on paleomagnetic and oxygen isotopic analyses. *Deep-Sea Res. II* 52, 2092–2109. https://doi.org/10.1016/j.dsr2.2005.08.004

Oldfield, F., 1991. Environmental magnetism - a personal perspective. *Quat. Sci. Rev.* 10, 73–85. https://doi.org/10.1016/0277-3791(91)90031-O

Oldfield, F., Yu, L., 1994. The influence of particle size variations on the magnetic properties of sediments from the north-eastern Irish Sea. *Sedimentology* 41, 1093–1108. https://doi.org/10.1111/j.1365-3091.1994.tb01443.x

Opdyke, N.D., Henry, K.W., 1969. A test of the dipole hypothesis. *Earth Planet. Sci. Lett.* 6, 139–151. https://doi.org/10.1016/0012-821X(69)90132-0

Opdyke, N.D., Foster, J.H., 1970. Paleomagnetism of cores from the North Pacific. *Mem. Geol. Soc. Am.* 126, 83–119. https://doi.org/10.1130/MEM126-p83

Opdyke, N.D., Channell, J.E.T., 1996. *Magnetic Stratigraphy*. Academic Press.

Ortega-Guerrero, B., Avendaño, D., Caballero, M., Lozano-García, S., Brown, E.T., Rodríguez, A., García, B., Barceinas, H., Soler, A.M., Albarrán, A., 2020. Climatic control on magnetic mineralogy during the late MIS 6 - early MIS 3 in Lake Chalco, central Mexico. *Quat. Sci. Rev.* 230, 106163. https://doi.org/10.1016/j.quascirev.2020.106163

Ouyang, T., Heslop, D., Roberts, A.P., Tian, C., Zhu, Z., Qiu, Y., Peng, X., 2014. Variable remanence acquisition efficiency in sediments containing biogenic and detrital magnetites: implications for relative paleointensity signal recording. *Geochem. Geophys. Geosyst.* 15, 2780–2796. https://doi.org/10.1002/2014GC005301

Özdemir, Ö., Dunlop, D.J., 2014. Hysteresis and coercivity of hematite. *J. Geophys. Res. Solid Earth* 119, 2582–2594. https://doi.org/10.1002/2013JB010739

Paillard, D., Labeyrie, L., Yiou, P., 1996. Macintosh program performs time-series analysis. *Eos, Trans. Am. Geophys. Union* 77, 379–379. https://doi.org/10.1029/96eo00259

Pan, Y., Petersen, N., Davila, A.F., Zhang, L., Winklhofer, M., Liu, Q., Hanzlik, M., Zhu, R., 2005. The detection of bacterial magnetite in recent sediments of Lake Chiemsee (southern Germany). *Earth Planet. Sci. Lett.* 232, 109–123. https://doi.org/10.1016/j.epsl.2005.01.006

Passier, H.F., de Lange, G.J., Dekkers, M.J., 2001. Magnetic properties and geochemistry of the active oxidation front and the youngest sapropel in the eastern Mediterranean Sea. *Geophys. J. Int.* 145, 604–614. https://doi.org/10.1046/j.0956-540X.2001.01394.x

Patton, B.J., Fitch, J.L., 1962. Anhysteretic remanent magnetization in small steady fields. *J. Geophys. Res.* 67, 307–311. https://doi.org/10.1029/jz067i001p00307

Pauling, L., Hendricks, S.B., 1925. The crystal structures of hematite and corundum. *J. Am. Chem. Soc.* 47, 781–790. https://doi.org/10.1021/ja01680a027

Pausata, F.S.R., Battisti, D.S., Nisancioglu, K.H., Bitz, C.M., 2011. Chinese stalagmite δ^{18}O controlled by changes in the Indian monsoon during a simulated Heinrich event. *Nat. Geosci.* 4, 474–480. https://doi.org/10.1038/ngeo1169

Peck, V.L., Hall, I.R., Zahn, R., Scourse, J.D., 2007. Progressive reduction in NE Atlantic intermediate water ventilation prior to Heinrich events: response to NW European ice sheet instabilities? *Geochem. Geophys. Geosyst.* 8. https://doi.org/10.1029/2006GC001321

Pettke, T., Halliday, A.N., Hall, C.M., Rea, D.K., 2000. Dust production and deposition in Asia and the North Pacific Ocean over the past 12 Myr. *Earth Planet. Sci. Lett.* 178, 397–413. https://doi.org/10.1016/S0012-821X(00)00083-2

Pickard, G.L., Emery, W.J., 1964. *Descriptive Physical Oceanography: An Introduction*. Oxford: Butterworth. https://doi.org/10.1016/C2009-0-24322-4

Pike, C.R., Fernandez, A., 1999. An investigation of magnetic reversal in submicron-scale Co dots using first order reversal curve diagrams. *J. Appl. Phys.* 85, 6668–6676. https://doi.org/10.1063/1.370177

Pike, C.R., Roberts, A.P., Verosub, K.L., 1999. Characterizing interactions in fine magnetic particle systems using first order reversal curves. *J. Appl. Phys.* 85, 6660–6667. https://doi.org/10.1063/1.370176

Pike, C.R., Roberts, A.P., Dekkers, M.J., Verosub, K.L., 2001a. An investigation of multi-domain hysteresis mechanisms using FORC diagrams. *Phys. Earth Planet. Inter.* 126, 11–25. https://doi.org/10.1016/S0031-9201(01)00241-2

Pike, C.R., Roberts, A.P., Verosub, K.L., 2001b. First-order reversal curve diagrams and thermal relaxation effects in magnetic particles. *Geophys. J. Int.* 145, 721–730. https://doi.org/10.1046/j.0956-540X.2001.01419.x

Pisias, N.G., Leinen, M., 1984. Milankovitch forcing of the oceanic system: evidence from the northwest Pacific, in: Berger, I., Imbrie, J., Hays, J., Kukla, G., Saltzman, B. (Eds.), *Milankovitch and Climate, Understanding the Response to Orbital Forcing, Part 1*. pp. 307–330.

Portnyagin, M., Ponomareva, V., Zelenin, E., Bazanova, L., Pevzner, M., Plechova, A., Rogozin, A., Garbe-Schönberg, D., 2019. TephraKam: geochemical database of glass compositions in tephra and welded tuffs from the Kamchatka volcanic arc (NW Pacific). *Earth Syst. Sci. Data Discuss.* https://doi.org/10.5194/essd-2019-202

Pósfai, M., Cziner, K., Márton, E., Márton, P., Buseck, P.R., Frankel, R.B., Bazylinski, D.A., 2001. Crystal-size distributions and possible biogenic origin of Fe sulfides. *Eur. J. Mineral.* 13, 691–703. https://doi.org/10.1127/0935-1221/2001/0013-0691

Preisach, F., 1935. Über die magnetische Nachwirkung. *Z. Phys.* 94, 227–302. https://doi.org/10.1007/BF01349418

Prell, W.L., Kutzbach, J.E., 1992. Sensitivity of the Indian monsoon to forcing parameters and implications for its evolution. *Nature* 360, 647–652. https://doi.org/10.1038/360647a0

Prince, R.A., Heath, G.R., Kominz, M., 1980. Paleomagnetic studies of central North Pacific sediment cores: stratigraphy, sedimentation rates, and the origin of magnetic instability. *Geol. Soc. Am. Bull.* 91, 1789–1835. https://doi.org/10.1130/0016-7606(1980)91<447:PSOCNP>2.0.CO;2

Qiu, B., 2002. The Kuroshio Extension system: its large-scale variability and role in the midlatitude ocean-atmosphere interaction. *J. Oceanogr.* 58, 57–75. https://doi.org/10.1023/A:1015824717293

Qu, T., Mitsudera, H., Yamagata, T., 2000. Intrusion of the North Pacific waters into the South China Sea. *J. Geophys. Res. Oceans.* 105, 6415–6424. https://doi.org/10.1029/1999jc900323

Qu, T., Girton, J.B., Whitehead, J.A., 2006. Deepwater overflow through Luzon Strait. *J. Geophys. Res. Oceans.* 111. https://doi.org/10.1029/2005JC003139

Rahmstorf, S., 2002. Ocean circulation and climate during the past 120,000 years. *Nature* 419, 207–241. https://doi.org/10.1038/nature01090

Ramsey, C.B., 1995. Radiocarbon calibration and analysis of stratigraphy: the OxCal program. *Radiocarbon* 37, 425–430. https://doi.org/10.1017/s0033822200030903

Ramsey, C.B., 2008. Deposition models for chronological records. *Quat. Sci. Rev.* 27, 42–60. https://doi.org/10.1016/j.quascirev.2007.01.019

Rea, D.K., 1994. The paleoclimatic record provided by eolian deposition in the deep sea: the geologic history of wind. *Rev. Geophys.* 32, 159–195. https://doi.org/10.1029/93RG03257

Rea, D.K., Leinen, M., 1988. Asian aridity and the zonal westerlies: late Pleistocene and Holocene record of eolian deposition in the northwest Pacific Ocean. *Palaeogeogr. Palaeoclimatol. Palaeoecol.* 66, 1–8. https://doi.org/10.1016/0031-0182(88)90076-4

Rea, D.K., Leinen, M., Janecek, T.R., 1985. Geologic approach to the long-term history of atmospheric circulation. *Science* 227, 721–725. https://doi.org/10.1126/science.227.4688.721

Rea, D.K., Snoeckx, I., Joseph, L.H., 1998. Late Cenozoic eolian deposition in the North Pacific: Asian drying, Tibetan uplift, and cooling of the northern hemisphere. *Paleoceanography* 13, 215–224. https://doi.org/10.1029/98PA00123

Reimer, P.J., Bard, E., Bayliss, A., Beck, J.W., Blackwell, P.G., Ramsey, C.B., Buck, C.E., Cheng, H., Edwards, R.L., Friedrich, M., Grootes, P.M., Guilderson, T.P., Haflidason, H., Hajdas, I., Hatté, C., Heaton, T.J., Hoffmann, D.L., Hogg, A.G., Hughen, K.A., Kaiser, K.F., Kromer, B., Manning, S.W., Niu, M., Reimer, R.W., Richards, D.A., Scott, E.M., Southon, J.R., Staff, R.A., Turney, C.S.M., van der Plicht, J., 2013. IntCal13 and Marine13 radiocarbon age calibration curves 0–50,000 years cal BP. *Radiocarbon* 55, 1869–1887. https://doi.org/10.2458/azu_js_rc.55.16947

Reinholdsson, M., Snowball, I., Zillén, L., Lenz, C., Conley, D.J., 2013. Magnetic enhancement of Baltic Sea sapropels by greigite magnetofossils. *Earth Planet. Sci. Lett.* 366, 137–150. https://doi.org/10.1016/j.epsl.2013.01.029

Rivière, G., 2011. A dynamical interpretation of the poleward shift of the jet streams in global warming scenarios. *J. Atmos. Sci.* 68, 1253–1272. https://doi.org/10.1175/2011JAS3641.1

Roberts, A.P., 1995. Magnetic properties of sedimentary greigite (Fe_3S_4). *Earth Planet. Sci. Lett.* 134, 227–236. https://doi.org/10.1016/0012-821X(95)00131-U

Roberts, A.P., 2008. Geomagnetic excursions: knowns and unknowns. *Geophys. Res. Lett.* 35. https://doi.org/10.1029/2008GL034719

Roberts, A.P., 2015. Magnetic mineral diagenesis. *Earth-Sci. Rev.* 151, 1–47. https://doi.org/10.1016/j.earscirev.2015.09.010

Roberts, A.P., Turner, G.M., 1993. Diagenetic formation of ferrimagnetic iron sulphide minerals in rapidly deposited marine sediments, South Island, New Zealand. *Earth Planet. Sci. Lett.* 115, 257–273. https://doi.org/10.1016/0012-821X(93)90226-Y

Roberts, A.P., Winklhofer, M., 2004. Why are geomagnetic excursions not always recorded in sediments? Constraints from post-depositional remanent magnetization lock-in modelling. *Earth Planet. Sci. Lett.* 227, 345–359. https://doi.org/10.1016/j.epsl.2004.07.040

Roberts, A.P., Weaver, R., 2005. Multiple mechanisms of remagnetization involving sedimentary greigite (Fe_3S_4). *Earth Planet. Sci. Lett.* 231, 263–277. https://doi.org/10.1016/j.epsl.2004.11.024

Roberts, A.P., Cui, Y., Verosub, K.L., 1995. Wasp-waisted hysteresis loops: mineral magnetic characteristics and discrimination of components in mixed magnetic systems. *J. Geophys. Res.* 100, 17909–17924. https://doi.org/10.1029/95jb00672

Roberts, A.P., Lehman, B., Weeks, R.J., Verosub, K.L., Laj, C., 1997. Relative paleointensity of the geomagnetic field over the last 200,000 years from ODP Sites 883 and 884, North Pacific Ocean. *Earth Planet. Sci. Lett.* 152, 11–23. https://doi.org/10.1016/s0012-821x(97)00132-5

Roberts, A.P., Pike, C.R., Verosub, K.L., 2000. First-order reversal curve diagrams: a new tool for characterizing the magnetic properties of natural samples. *J. Geophys. Res. Solid Earth* 105, 28461–28475. https://doi.org/10.1029/2000jb900326

Roberts, A.P., Liu, Q., Rowan, C.J., Chang, L., Carvallo, C., Torrent, J., Horng, C.S., 2006. Characterization of hematite (α-Fe_2O_3), goethite (α-FeOOH), greigite (Fe_3S_4), and pyrrhotite (Fe_7S_8) using first-order reversal curve diagrams. *J. Geophys. Res. Solid Earth* 111. https://doi.org/10.1029/2006JB004715

Roberts, A.P., Chang, L., Rowan, C.J., Horng, C.S., Florindo, F., 2011. Magnetic properties of sedimentary greigite (Fe_3S_4): an update. *Rev. Geophys.* 49. https://doi.org/10.1029/2010RG000336

Roberts, A.P., Chang, L., Heslop, D., Florindo, F., Larrasoaña, J.C., 2012. Searching for single domain magnetite in the “pseudo-single-domain” sedimentary haystack: implications of biogenic magnetite preservation for sediment magnetism and relative paleointensity determinations. *J. Geophys. Res. Solid Earth* 117. https://doi.org/10.1029/2012JB009412

Roberts, A.P., Tauxe, L., Heslop, D., 2013. Magnetic paleointensity stratigraphy and high-resolution Quaternary geochronology: successes and future challenges. *Quat. Sci. Rev.* 61, 1–16. https://doi.org/10.1016/j.quascirev.2012.10.036

Roberts, A.P., Heslop, D., Zhao, X., Pike, C.R., 2014. Understanding fine magnetic particle systems through use of first-order reversal curve diagrams. *Rev. Geophys.* 52, 557–602. https://doi.org/10.1002/2014RG000462

Roberts, A.P., Almeida, T.P., Church, N.S., Harrison, R.J., Heslop, D., Li, Y., Li, J., Muxworthy, A.R., Williams, W., Zhao, X., 2017. Resolving the origin of pseudo-single domain magnetic behavior. *J. Geophys. Res. Solid Earth* 122, 9534–9558. https://doi.org/10.1002/2017JB014860

Roberts, A.P., Zhao, X., Harrison, R.J., Heslop, D., Muxworthy, A.R., Rowan, C.J., Larrasoaña, J.C., Florindo, F., 2018a. Signatures of reductive magnetic mineral diagenesis from unmixing of first-order reversal curves. *J. Geophys. Res. Solid Earth* 123, 4500–4522. https://doi.org/10.1029/2018JB015706

Roberts, A.P., Tauxe, L., Heslop, D., Zhao, X., Jiang, Z., 2018b. A critical appraisal of the "Day" diagram. *J. Geophys. Res. Solid Earth* 123, 2618–2644. https://doi.org/10.1002/2017JB015247

Roberts, A.P., Hu, P., Harrison, R.J., Heslop, D., Muxworthy, A.R., Oda, H., Sato, T., Tauxe, L., Zhao, X., 2019. Domain state diagnosis in rock magnetism: evaluation of potential alternatives to the Day diagram. *J. Geophys. Res. Solid Earth* 124, 5286–5314. https://doi.org/10.1029/2018JB017049

Roberts, A.P., Zhao, X., Heslop, D., Abrajevitch, A., Chen, Y.H., Hu, P., Jiang, Z., Liu, Q., Pillans, B.J., 2020. Hematite (α-Fe_2O_3) quantification in sedimentary magnetism: limitations of existing proxies and ways forward. *Geosci. Lett.* 7, 1–11. https://doi.org/10.1186/s40562-020-00157-5

Robertson, D.J., France, D.E., 1994. Discrimination of remanence-carrying minerals in mixtures, using isothermal remanent magnetisation acquisition curves. *Phys. Earth Planet. Inter.* 82, 223–234. https://doi.org/10.1016/0031-9201(94)90074-4

Robinson, S.G., 1986. The late Pleistocene palaeoclimatic record of North Atlantic deep-sea sediments revealed by mineral-magnetic measurements. *Phys. Earth Planet. Inter.* 42, 22–47. https://doi.org/10.1016/S0031-9201(86)80006-1

Rochette, P., Mathé, P.E., Esteban, L., Rakoto, H., Bouchez, J.L., Liu, Q., Torrent, J., 2005. Non-saturation of the defect moment of goethite and fine-grained hematite up to 57 Teslas. *Geophys. Res. Lett.* 32. https://doi.org/10.1029/2005GL024196

Rowan, C.J., Roberts, A.P., 2006. Magnetite dissolution, diachronous greigite formation, and secondary magnetizations from pyrite oxidation: unravelling complex magnetizations in Neogene marine sediments from New Zealand. *Earth Planet. Sci. Lett.* 241, 119–137. https://doi.org/10.1016/j.epsl.2005.10.017

Rutledal, S., Berben, S.M.P., Dokken, T.M., van der Bilt, W.G.M., Cederstrøm, J.M., Jansen, E., 2020. Tephra horizons identified in the western North Atlantic and Nordic Seas during the Last Glacial Period: extending the marine tephra framework. *Quat. Sci. Rev.* 240, 106247. https://doi.org/10.1016/j.quascirev.2020.106247

Sagnotti, L., Rochette, P., Jackson, M., Vadeboin, F., Dinarès-Turell, J., Winkler, A., Maher, B., Moreno, E., Hanesch, M., Scholger, R., Jude, R., Shaw, J., McIntosh, G., Osete, M.L., Matzka, J., Petersen, N., Larrasoaña, J.C., O'Reagan, M., Roberts, A.P., Mullender, T., Peters, C., Mohamed, K.J., Rey, D., Hannam, J., Heller, F., Frederichs, T., Bleil, U., 2003. Inter-laboratory calibration of low-field magnetic and anhysteretic susceptibility measurements. *Phys. Earth Planet. Inter.* 138, 25–38. https://doi.org/10.1016/S0031-9201(03)00063-3

Sagnotti, L., Roberts, A.P., Weaver, R., Verosub, K.L., Florindo, F., Pike, C.R., Clayton, T., Wilson, G.S., 2005. Apparent magnetic polarity reversals due to remagnetization resulting from late diagenetic growth of greigite from siderite. *Geophys. J. Int.* 160, 89–100. https://doi.org/10.1111/j.1365-246X.2005.02485.x

Sakamoto, T.T., Hasumi, H., Ishii, M., Emori, S., Suzuki, T., Nishimura, T., Sumi, A., 2005. Responses of the Kuroshio and the Kuroshio Extension to global warming in a high-resolution climate model. *Geophys. Res. Lett.* 32. https://doi.org/10.1029/2005GL023384

Scheinost, A.C., Chavernas, A., Barrón, V., Torrent, J., 1998. Use and limitations of second-derivative diffuse reflectance spectroscopy in the visible to near-infrared range to identify and quantify Fe oxide minerals in soils. *Clays Clay Miner.* 46, 528–536. https://doi.org/10.1346/CCMN.1998.0460506

Schneider, D.A., Kent, D. V., 1990. The time-averaged paleomagnetic field. *Rev. Geophys.* 28, 71–96. https://doi.org/10.1029/RG028i001p00071

Seo, I., Lee, Y.I., Yoo, C.M., Kim, H.J., Hyeong, K., 2014. Sr-Nd isotope composition and clay mineral assemblages in eolian dust from the central Philippine Sea over the last 600 kyr: implications for the transport mechanism of Asian dust. *J. Geophys. Res.* 119, 11492–11504. https://doi.org/10.1002/2014JD022025

Serno, S., Winckler, G., Anderson, R.F., Jaccard, S.L., Kienast, S.S., Haug, G.H., 2017. Change in dust seasonality as the primary driver for orbital-scale dust storm variability in East Asia. *Geophys. Res. Lett.* 44, 3796–3805. https://doi.org/10.1002/2016GL072345

Seton, M., Müller, R.D., Zahirovic, S., Gaina, C., Torsvik, T., Shephard, G., Talsma, A., Gurnis, M., Turner, M., Maus, S., Chandler, M., 2012. Global continental and ocean basin reconstructions since 200 Ma. *Earth-Sci. Rev.* 113, 212–270. https://doi.org/10.1016/j.earscirev.2012.03.002

Sha, Y., Ren, X., Shi, Z., Zhou, P., Li, X., Liu, X., 2020. Influence of the Tibetan Plateau and its northern margins on the mid-latitude westerly jet over Central Asia in summer. *Palaeogeogr. Palaeoclimatol. Palaeoecol.* 544, 109611. https://doi.org/10.1016/j.palaeo.2020.109611

Shackleton, N.J., Opdyke, N.D., 1977. Oxygen isotope and palaeomagnetic evidence for early northern hemisphere glaciation. *Nature* 270, 216–219. https://doi.org/10.1038/270216a0

Shackleton, N.J., Backman, J., Zimmerman, H., Kent, D.V., Hall, M.A., Roberts, D.G., Schnitker, D., Baldauf, J.G., Desprairies, A., Homrighausen, R., Huddlestun, P., Keene, J.B., Kaltenback, A.J., Krumsiek, K.A.O., Morton, A.C., Murray, J.W., Westberg-Smith, J., 1984. Oxygen isotope calibration of the onset of ice-rafting and history of glaciation in the North Atlantic region. *Nature* 307, 620–623. https://doi.org/10.1038/307620a0

Shao, Y., Wyrwoll, K.H., Chappell, A., Huang, J., Lin, Z., McTainsh, G.H., Mikami, M., Tanaka, T.Y., Wang, X., Yoon, S., 2011. Dust cycle: an emerging core theme in Earth system science. *Aeolian Res.* 2, 181–204. https://doi.org/10.1016/j.aeolia.2011.02.001

Shaw, P.T., Chao, S.Y., 1994. Surface circulation in the South China Sea. *Deep-Sea Res. I* 41, 1663–1683. https://doi.org/10.1016/0967-0637(94)90067-1

Shen, Z., Li, X., Cao, J., Caquineau, S., Wang, Y., Zhang, X., 2005. Characteristics of clay minerals in Asian dust and their environmental significance. *China Part.* 3, 260–264. https://doi.org/10.1016/s1672-2515(07)60198-5

Shin, J.Y., Yu, Y., Kim, W., 2019. Wavelet-based verification of a relative paleointensity record from the North Pacific. *Earth Planets Space* 71, 88. https://doi.org/10.1186/s40623-019-1067-x

Skinner, B.J., Erd, R.C., Grimaldi, F.S., 1964. Greigite, the thio-spinel of iron; a new mineral. *Am. Mineral.* 49, 543–555.

Skinner, L.C., McCave, I.N., 2003. Analysis and modelling of gravity- and piston coring based on soil mechanics. *Mar. Geol.* 199, 181–204. https://doi.org/10.1016/S0025-3227(03)00127-0

Smirnov, D., Newman, M., Alexander, M.A., 2014. Investigating the role of ocean-atmosphere coupling in the North Pacific Ocean. *J. Clim.* 27, 592–606. https://doi.org/10.1175/JCLI-D-13-00123.1

Smith, V.C., Staff, R.A., Blockley, S.P.E., Ramsey, C.B., Nakagawa, T., Mark, D.F., Takemura, K., Danhara, T., 2013. Identification and correlation of visible tephras in the Lake Suigetsu SG06 sedimentary archive, Japan: chronostratigraphic markers for synchronising of east Asian/west Pacific palaeoclimatic records across the last 150 ka. *Quat. Sci. Rev.* 67, 121–137. https://doi.org/10.1016/j.quascirev.2013.01.026

Snowball, I.F., 1997. Gyroremanent magnetization and the magnetic properties of greigite-bearing clays in southern Sweden. *Geophys. J. Int.* 129, 624–636. https://doi.org/10.1111/j.1365-246X.1997.tb04498.x

Son, S.W., Lee, S., 2005. The response of westerly jets to thermal driving in a primitive equation model. *J. Atmos. Sci.* 62, 3741–3757. https://doi.org/10.1175/JAS3571.1

Spassov, S., Heller, F., Kretzschmar, R., Evans, M.E., Yue, L.P., Nourgaliev, D.K., 2003. Detrital and pedogenic magnetic mineral phases in the loess/palaesol sequence at Lingtai (central Chinese Loess Plateau). *Phys. Earth Planet. Inter.* 140, 255–275. https://doi.org/10.1016/j.pepi.2003.09.003

St-Onge, G., Stoner, J.S., Hillaire-Marcel, C., 2003. Holocene paleomagnetic records from the St. Lawrence Estuary, eastern Canada: centennial- to millennial-scale geomagnetic modulation of cosmogenic isotopes. *Earth Planet. Sci. Lett.* 209, 113–130. https://doi.org/10.1016/S0012-821X(03)00079-7

Stacey, F.D., 1963. The physical theory of rock magnetism. *Adv. Phys.* 12, 45–133. https://doi.org/10.1080/00018736300101263

Stacey, F.D., 1972. On the role of Brownian motion in the control of detrital remanent magnetization of sediments. *Pure Appl. Geophys.* 98, 139–145. https://doi.org/10.1007/BF00875588

Steph, S., Tiedemann, R., Prange, M., Groeneveld, J., Schulz, M., Timmermann, A., Nürnberg, D., Rühlemann, C., Saukel, C., Haug, G.H., 2010. Early Pliocene increase in thermohaline overturning: a precondition for the development of the modern equatorial Pacific cold tongue. *Paleoceanography* 25. https://doi.org/10.1029/2008PA001645

Stober, J.C., Thompson, R., 1979. An investigation into the source of magnetic minerals in some Finnish lake sediments. *Earth Planet. Sci. Lett.* 45, 464–474. https://doi.org/10.1016/0012-821X(79)90145-6

Stoner, E.C., Wohlfarth, E.P., 1948. A mechanism of magnetic hysteresis in heterogeneous alloys. *Philos. Trans. R. Soc. Lond. A* 240, 599–642. https://doi.org/10.1098/rsta.1948.0007

Su, X., Liu, C., Beaufort, L., Tian, J., Huang, E., 2013. Late Quaternary coccolith records in the South China Sea and East Asian monsoon dynamics. *Glob. Planet. Change* 111, 88–96. https://doi.org/10.1016/j.gloplacha.2013.08.016

Sugiura, N., 1979. ARM, TRM and magnetic interactions: concentration dependence.

Earth Planet. Sci. Lett. 42, 451–455. https://doi.org/10.1016/0012-821X(79)90054-2

Sun, D., Su, R., Bloemendal, J., Lu, H., 2008. Grain-size and accumulation rate records from late Cenozoic aeolian sequences in northern China: implications for variations in the East Asian winter monsoon and westerly atmospheric circulation. *Palaeogeogr. Palaeoclimatol. Palaeoecol.* 264, 39–53. https://doi.org/10.1016/j.palaeo.2008.03.011

Sun, Y., An, Z., Clemens, S.C., Bloemendal, J., Vandenberghe, J., 2010. Seven million years of wind and precipitation variability on the Chinese Loess Plateau. *Earth Planet. Sci. Lett.* 297, 525–535. https://doi.org/10.1016/j.epsl.2010.07.004

Sun, Y., Clemens, S.C., Morrill, C., Lin, X., Wang, X., An, Z., 2012. Influence of Atlantic meridional overturning circulation on the East Asian winter monsoon. *Nat. Geosci.* 5, 46–49. https://doi.org/10.1038/ngeo1326

Sverdrup, H.U., Johnson, M.W., Fleming, R.H., 1942. *The Oceans: Their Physics, Chemistry, and General Biology*. Prentice-Hall. https://doi.org/10.2307/210609

Talley, L.D., 1993. Distribution and formation of North Pacific Intermediate Water. *J. Phys. Oceanogr.* 23, 517–537. https://doi.org/10.1175/1520-0485(1993)023<0517:DAFONP>2.0.CO;2

Tamburini, F., Adatte, T., Föllmi, K., Bernasconi, S.M., Steinmann, P., 2003. Investigating the history of East Asian monsoon and climate during the last glacial-interglacial period (0-140000 years): mineralogy and geochemistry of ODP Sites 1143 and 1144, South China Sea. *Mar. Geol.* 201, 147–168. https://doi.org/10.1016/S0025-3227(03)00214-7

Tarling, D., Hrouda, F., 1993. *The Magnetic Anisotropy of Rocks*. Chapman & Hall, London.

Tauxe, L., 1993. Sedimentary records of relative paleointensity of the geomagnetic field: theory and practice. *Rev. Geophys.* 31, 319–354. https://doi.org/10.1029/93RG01771

Tauxe, L., 2010. *Essentials of Paleomagnetism*. University of California Press.

Tauxe, L., Kent, D.V., 2004. A simplified statistical model for the geomagnetic field and the detection of shallow bias in paleomagnetic inclinations: was the ancient magnetic field dipolar?, in: Channell, J.E.T., Kent, D.V., Lowrie, W., Meerts, J. (Eds.), *AGU Geophysical Monograph Series: Timescales of the Paleomagnetic Field*. pp. 101–115. https://doi.org/10.1029/145GM08

Tauxe, L., Yamazaki, T., 2015. Paleointensities, in: *Treatise on Geophysics*. Elsevier, pp. 510–563. https://doi.org/10.1016/B978-0-444-53802-4.00107-X

Tauxe, L., Mullender, T.A.T., Pick, T., 1996. Potbellies, wasp-waists, and superparamagnetism in magnetic hysteresis. *J. Geophys. Res. Solid Earth* 101, 571–583. https://doi.org/10.1029/95jb03041

Tauxe, L., Steindorf, J.L., Harris, A., 2006. Depositional remanent magnetization: toward an improved theoretical and experimental foundation. *Earth Planet. Sci. Lett.* 244, 515–529. https://doi.org/10.1016/j.epsl.2006.02.003

Thellier, E., 1938. Sur l'aimantation des terres cuites et ses applications géophysique. *Ann. Inst. Phys. Globe Univ. Paris* 16, 157–302.

Thompson, D.W.J., Solomon, S., 2002. Interpretation of recent southern hemisphere climate change. *Science* 296, 895–899. https://doi.org/10.1126/science.1069270

Thompson, R., Oldfield, F., 1986. *Environmental Magnetism*. Allen & Unwin Ltd, London. https://doi.org/10.1007/978-94-011-8036-8

Thomson, D.J., 1982. Spectrum estimation and harmonic analysis. *Proc. IEEE* 70, 1055–

1096. https://doi.org/10.1109/PROC.1982.12433

Tian, F., Herzschuh, U., Dallmeyer, A., Xu, Q., Mischke, S., Biskaborn, B.K., 2013. Environmental variability in the monsoon-westerlies transition zone during the last 1200 years: lake sediment analyses from central Mongolia and supra-regional synthesis. *Quat. Sci. Rev.* 73, 31–47. https://doi.org/10.1016/j.quascirev.2013.05.005

Tian, J., Wang, P.X., Cheng, X.R., Li, Q.Y., 2005. Astronomically tuned time scale 12 Ma to 18.3 Ma, ODP Site 1148, northern South China Sea. *Earth Sci. - J. China Univ. Geosci.* 30, 513–518.

Tian, J., Pak, D.K., Wang, P., Lea, D., Cheng, X., Zhao, Q., 2006. Late Pliocene monsoon linkage in the tropical South China Sea. *Earth Planet. Sci. Lett.* 252, 72–81. https://doi.org/10.1016/j.epsl.2006.09.028

Tian, J., Zhao, Q., Wang, P., Li, Q., Cheng, X., 2008. Astronomically modulated Neogene sediment records from the South China Sea. *Paleoceanography* 23. https://doi.org/10.1029/2007PA001552

Tian, J., Xie, X., Ma, W., Jin, H., Wang, P., 2011. X-ray fluorescence core scanning records of chemical weathering and monsoon evolution over the past 5 Myr in the southern South China Sea. *Paleoceanography* 26. https://doi.org/10.1029/2010PA002045

Toggweiler, J.R., 2009. Shifting westerlies. *Science* 323, 1434–1435. https://doi.org/10.1126/science.1169823

Turney, C.S.M., Palmer, J., Bronk Ramsey, C., Adolphi, F., Muscheler, R., Hughen, K.A., Staff, R.A., Jones, R.T., Thomas, Z.A., Fogwill, C.J., Hogg, A., 2016. High-precision dating and correlation of ice, marine and terrestrial sequences spanning Heinrich event 3: testing mechanisms of interhemispheric change using New Zealand ancient kauri (Agathis australis). *Quat. Sci. Rev.* 137, 126–134. https://doi.org/10.1016/j.quascirev.2016.02.005

Uesawa, S., Nakagawa, M., Umetsu, A., 2016. Explosive eruptive activity and temporal magmatic changes at Yotei Volcano during the last 50,000 years, southwest Hokkaido, Japan. *J. Volcanol. Geotherm. Res.* 325, 27–44. https://doi.org/10.1016/j.jvolgeores.2016.06.008

Valet, J.P., Meynadier, L., 1993. Geomagnetic field intensity and reversals during the past four million years. *Nature* 366, 234–238. https://doi.org/10.1038/366234a0

Valet, J.P., Meynadier, L., Guyodo, Y., 2005. Geomagnetic dipole strength and reversal rate over the past two million years. *Nature* 435, 802–805. https://doi.org/10.1038/nature03674

Vallis, G.K., Zurita-Gotor, P., Cairns, C., Kidston, J., 2015. Response of the large-scale structure of the atmosphere to global warming. *Q. J. R. Meteorol. Soc.* 141, 1479–1501. https://doi.org/10.1002/qj.2456

Van der Voo, R., 1990. Phanerozoic paleomagnetic poles from Europe and North America and comparisons with continental reconstructions. *Rev. Geophys.* 28, 167–206. https://doi.org/10.1029/RG028i002p00167

van Peer, T.E., Xuan, C., Lippert, P.C., Liebrand, D., Agnini, C., Wilson, P.A., 2017. Extracting a detailed magnetostratigraphy from weakly magnetized, Oligocene to early Miocene sediment drifts recovered at IODP Site U1406 (Newfoundland Margin, Northwest Atlantic Ocean). *Geochem. Geophys. Geosyst.* 18, 3910–3928. https://doi.org/10.1002/2017GC007185

Verosub, K.L., 1977. Depositional and postdepositional processes in the magnetization of sediments. *Rev. Geophys.* 15, 129–143.

https://doi.org/10.1029/RG015i002p00129

Verosub, K.L., Fine, P., Singer, M.J., Tenpas, J., 1993. Pedogenesis and paleoclimate: interpretation of the magnetic susceptibility record of Chinese loess-paleosol sequences. *Geology* 21, 1011–1014. https://doi.org/10.1130/0091-7613(1993)021<1011:PAPIOT>2.3.CO;2

Verwey, E.J.W., 1939. Electronic conduction of magnetite (Fe_3O_4) and its transition point at low temperatures. *Nature* 144, 327–328. https://doi.org/10.1038/144327b0

Vogt, P.R., Anderson, C.N., Bracey, D.R., 1971. Mesozoic magnetic anomalies, sea-floor spreading, and geomagnetic reversals in the southwestern North Atlantic. *J. Geophys. Res.* 76, 4796–4823. https://doi.org/10.1029/jb076i020p04796

Volynets, O.N., 1994. Geochemical types, petrology, and genesis of late Cenozoic volcanic rocks from the Kurile-Kamchatka island-arc system. *Int. Geol. Rev.* 36, 393–405. https://doi.org/10.1080/00206819409465467

Wagner, G., Beer, J., Laj, C., Kissel, C., Masarik, J., Muscheler, R., Synal, H.A., 2000. Chlorine-36 evidence for the Mono Lake event in the summit GRIP ice core. *Earth Planet. Sci. Lett.* 181, 1–6. https://doi.org/10.1016/S0012-821X(00)00196-5

Wan, S., Li, A., Clift, P.D., Jiang, H., 2006. Development of the East Asian summer monsoon: evidence from the sediment record in the South China Sea since 8.5 Ma. *Palaeogeogr. Palaeoclimatol. Palaeoecol.* 241, 139–159. https://doi.org/10.1016/j.palaeo.2006.06.013

Wan, S., Li, A., Clift, P.D., Stuut, J.B.W., 2007. Development of the East Asian monsoon: mineralogical and sedimentologic records in the northern South China Sea since 20 Ma. *Palaeogeogr. Palaeoclimatol. Palaeoecol.* 254, 561–582. https://doi.org/10.1016/j.palaeo.2007.07.009

Wan, S., Li, A., Clift, P.D., Wu, S., Xu, K., Li, T., 2010. Increased contribution of terrigenous supply from Taiwan to the northern South China Sea since 3Ma. *Mar. Geol.* 278, 115–121. https://doi.org/10.1016/j.margeo.2010.09.008

Wan, S., Sun, Y., Nagashima, K., 2020. Asian dust from land to sea: processes, history and effect from modern observation to geological records. *Geol. Mag.* 157, 701–706. https://doi.org/10.1017/S0016756820000333

Wang, B., Clemens, S.C., Liu, P., 2003. Contrasting the Indian and East Asian monsoons: implications on geologic timescales. *Mar. Geol.* 201, 5–21. https://doi.org/10.1016/S0025-3227(03)00196-8

Wang, B., Huang, F., Wu, Z., Yang, J., Fu, X., Kikuchi, K., 2009. Multi-scale climate variability of the South China Sea monsoon: a review. *Dyn. Atmos. Ocean.* 47, 15–37. https://doi.org/10.1016/j.dynatmoce.2008.09.004

Wang, B., Zhang, G., Li, S., Yang, Z., Roberts, A.P., Zhao, Q., Wang, Z., 2016. Early Carboniferous paleomagnetic results from the northeastern margin of the Qinghai-Tibetan plateau and their implications. *Gondwana Res.* 36, 57–64. https://doi.org/10.1016/j.gr.2016.04.007

Wang, B.G., Tang, X.Z., Hou, H.M., Yuan, Y.R., 1993. A preliminary study on the magnetostratigraphy in waters of Nansha Islands. *Trop. Oceanol.* 12, 53–60.

Wang, F., Li, Z., Wang, X., Li, B., Chen, F., 2018. Variation and interplay of the Siberian High and westerlies in central-east Asia during the past 1200 kyr. *Aeolian Res.* 33, 62–81. https://doi.org/10.1016/j.aeolia.2018.05.003

Wang, G., Chen, D., Su, J., 2006. Generation and life cycle of the dipole in the South China Sea summer circulation. *J. Geophys. Res. Oceans.* 111. https://doi.org/10.1029/2005JC003314

Wang, L., Sarnthein, M., Erlenkeuser, H., Grimalt, J., Grootes, P., Heilig, S., Ivanova, E., Kienast, M., Pelejero, C., Pflaumann, U., 1999. East Asian monsoon climate during the late Pleistocene: high-resolution sediment records from the South China Sea. *Mar. Geol.* 156, 245–284. https://doi.org/10.1016/S0025-3227(98)00182-0

Wang, P., 1998. Western Pacific in glacial cycles: seasonality in marginal seas and variabilities of warm pool. *Sci. China D* 41, 35–41. https://doi.org/10.1007/BF02932418

Wang, P., Li, Q., 2009. *The South China Sea: Paleoceanography and Sedimentology*. Springer. https://doi.org/10.1029/2010eo080009

Wang, P., Tian, J., Cheng, X., Liu, C., Xu, J., 2003a. Carbon reservoir changes preceded major ice-sheet expansion at the mid-Brunhes event. *Geology* 31, 239–242. https://doi.org/10.1130/0091-7613(2003)031<0239:CRCPMI>2.0.CO;2

Wang, P., Tian, J., Cheng, X., Liu, Q., Xu, J., 2003b. Exploring cyclic changes of the ocean carbon reservoir. *Chin. Sci. Bull.* 48, 2536–2548. https://doi.org/10.1360/03wd0155

Wang, P., Tian, J., Cheng, X., Liu, C., Xu, J., 2004. Major Pleistocene stages in a carbon perspective: the South China Sea record and its global comparison. *Paleoceanography* 19, PA4005. https://doi.org/10.1029/2003PA000991

Wang, P., Clemens, S., Beaufort, L., Braconnot, P., Ganssen, G., Jian, Z., Kershaw, P., Sarnthein, M., 2005. Evolution and variability of the Asian monsoon system: state of the art and outstanding issues. *Quat. Sci. Rev.* 24, 595–629. https://doi.org/10.1016/j.quascirev.2004.10.002

Wang, P., Tian, J., Lourens, L.J., 2010. Obscuring of long eccentricity cyclicity in Pleistocene oceanic carbon isotope records. *Earth Planet. Sci. Lett.* 290, 319–330. https://doi.org/10.1016/j.epsl.2009.12.028

Wang, P., Li, Q., Tian, J., 2014a. Pleistocene paleoceanography of the South China Sea: progress over the past 20 years. *Mar. Geol.* 352, 381–396. https://doi.org/10.1016/j.margeo.2014.03.003

Wang, P., Li, Q., Tian, J., Jian, Z., Liu, C., Li, L., Ma, W., 2014b. Long-term cycles in the carbon reservoir of the Quaternary ocean: a perspective from the South China Sea. *Natl. Sci. Rev.* 1, 119–143. https://doi.org/10.1093/nsr/nwt028

Wang, P., Wang, B., Cheng, H., Fasullo, J., Guo, Z., Kiefer, T., Liu, Z., 2014c. The global monsoon across timescales: coherent variability of regional monsoons. *Clim. Past* 10. https://doi.org/10.5194/cp-10-2007-2014

Wang, Y.J., Cheng, H., Edwards, R.L., An, Z.S., Wu, J.Y., Shen, C.C., Dorale, J.A., 2001. A high-resolution absolute-dated late Pleistocene monsoon record from Hulu Cave, China. *Science* 294, 2345–2348. https://doi.org/10.1126/science.1064618

Wang, Y., Cheng, H., Edwards, R.L., Kong, X., Shao, X., Chen, S., Wu, J., Jiang, X., Wang, X., An, Z., 2008. Millennial- and orbital-scale changes in the East Asian monsoon over the past 224,000 years. *Nature* 451, 1090–1093. https://doi.org/10.1038/nature06692

Watkins, S.J., Maher, B.A., 2003. Magnetic characterisation of present-day deep-sea sediments and sources in the North Atlantic. *Earth Planet. Sci. Lett.* 214, 379–394. https://doi.org/10.1016/S0012-821X(03)00422-9

Watson, J.H.P., Cressey, B.A., Roberts, A.P., Ellwood, D.C., Charnock, J.M., Soper, A.K., 2000. Structural and magnetic studies on heavy-metal-adsorbing iron sulphide nanoparticles produced by sulphate-reducing bacteria. *J. Magn. Magn. Mater.* 214, 13–30. https://doi.org/10.1016/S0304-8853(00)00025-1

Weber, E.T., Owen, R.M., Dickens, G.R., Halliday, A.N., Jones, C.E., Rea, D.K., 1996. Quantitative resolution of eolian continental crustal material and volcanic detritus in

North Pacific surface sediment. *Paleoceanography* 11, 115–127. https://doi.org/10.1029/95PA02720

Webster, P.J., 1994. The role of hydrological processes in ocean-atmosphere interactions. *Rev. Geophys.* 32, 427–476. https://doi.org/10.1029/94RG01873

Wehausen, R., Brumsack, H.J., 2002. Astronomical forcing of the East Asian monsoon mirrored by the composition of Pliocene South China Sea sediments. *Earth Planet. Sci. Lett.* 201, 621–636. https://doi.org/10.1016/S0012-821X(02)00746-X

Weiss, B.P., Kim, S.S., Kirschvink, J.L., Kopp, R.E., Sankaran, M., Kobayashi, A., Komeili, A., 2004. Ferromagnetic resonance and low-temperature magnetic tests for biogenic magnetite. *Earth Planet. Sci. Lett.* 224, 73–89. https://doi.org/10.1016/j.epsl.2004.04.024

Weiss, P., 1907. L'hypothèse du champ moléculaire et la propriété ferromagnétique. *J. Phys. Théorique Appliquée* 6, 661–690. https://doi.org/10.1051/jphystap:019070060066100

Wells, M.A., Fitzpatrick, R.W., Gilkes, R.J., Dobson, J., 1999. Magnetic properties of metal-substituted haematite. *Geophys. J. Int.* 138, 571–580. https://doi.org/10.1046/j.1365-246X.1999.00840.x

Wilkin, R.T., Barnes, H.L., 1997. Formation processes of framboidal pyrite. *Geochim. Cosmochim. Acta* 61, 323–339. https://doi.org/10.1016/S0016-7037(96)00320-1

Windom, H.L., 1969. Atmospheric dust records in permanent snowfields: implications to marine sedimentation. *Bull. Geol. Soc. Am.* 80, 761–782. https://doi.org/10.1130/0016-7606(1970)81[3177:ADRIPS]2.0.CO;2

Winklhofer, M., Chang, L., Eder, S.H.K., 2014. On the magnetocrystalline anisotropy of greigite (Fe_3S_4). *Geochem. Geophys. Geosyst.* 15, 1558–1579. https://doi.org/10.1002/2013GC005121

Worm, H.U., 1998. On the superparamagnetic - stable single domain transition for magnetite, and frequency dependence of susceptibility. *Geophys. J. Int.* 133, 201–206. https://doi.org/10.1046/j.1365-246X.1998.1331468.x

Worne, S., Kender, S., Swann, G.E.A., Leng, M.J., Ravelo, A.C., 2019. Coupled climate and subarctic Pacific nutrient upwelling over the last 850,000 years. *Earth Planet. Sci. Lett.* 522, 87–97. https://doi.org/10.1016/j.epsl.2019.06.028

Wu, H., Zhao, X., Shi, M., Zhang, S., Li, H., Yang, T., 2014. A 23 Myr magnetostratigraphic time framework for Site 1148, ODP Leg 184 in South China Sea and its geological implications. *Mar. Petrol. Geol.* 58, 749–759. https://doi.org/10.1016/j.marpetgeo.2014.01.003

Wu, H., Shi, M., Zhao, X., Huang, B., Zhang, S., Li, H., Yang, T., Lin, C., 2017. Magnetostratigraphy of ODP Site 1143 in the South China Sea since the early Pliocene. *Mar. Geol.* 394, 133–142. https://doi.org/10.1016/j.margeo.2017.08.010

Wu, L., Li, C., Yang, C., Xie, S.P., 2008. Global teleconnections in response to a shutdown of the Atlantic meridional overturning circulation. *J. Clim.* 21, 3002–3019. https://doi.org/10.1175/2007JCLI1858.1

Wyrtki, K., 1961. *Physical Oceanography of the Southeast Asian Waters*. University of California, Scripps Institution of Oceanography, California. https://doi.org/10.1017/S0025315400054370

Xiao, C., Wang, Y., Lin, J., 2020. Constraints of magnetostratigraphic and mineralogical data on the provenance of sediments in the Parece Vela Basin of the western Pacific. *J. Asian Earth Sci.* 196, 104373. https://doi.org/10.1016/j.jseaes.2020.104373

Xiao, J., Porter, S.C., An, Z., Kumai, H., Yoshikawa, S., 1995. Grain size of quartz as an indicator of winter monsoon strength on the loess plateau of central China during the last 130,000 yr. *Quat. Res.* 43, 22–29. https://doi.org/10.1006/qres.1995.1003

Xie, S., Evershed, R.P., Huang, X., Zhu, Z., Pancost, R.D., Meyers, P.A., Gong, L., Hu, C., Huang, J., Zhang, S., Gu, Y., Zhu, J., 2013. Concordant monsoon-driven postglacial hydrological changes in peat and stalagmite records and their impacts on prehistoric cultures in central China. *Geology* 41, 827–830. https://doi.org/10.1130/G34318.1

Xie, Y., Wu, F., Fang, X., 2020. A major environmental shift by the middle Eocene in southern China: evidence from palynological records. *Rev. Palaeobot. Palynol.* 104226. https://doi.org/10.1016/j.revpalbo.2020.104226

Yamamoto, Y., Yamazaki, T., Kanamatsu, T., Ioka, N., Mishima, T., 2007. Relative paleointensity stack during the last 250 kyr in the northwest Pacific. *J. Geophys. Res. Solid Earth* 112. https://doi.org/10.1029/2006JB004477

Yamazaki, T., 1999. Relative paleointensity of the geomagnetic field during Brunhes Chron recorded in North Pacific deep-sea sediment cores: orbital influence? *Earth Planet. Sci. Lett.* 169, 23–35. https://doi.org/10.1016/S0012-821X(99)00064-3

Yamazaki, T., 2008. Magnetostatic interactions in deep-sea sediments inferred from first-order reversal curve diagrams: implications for relative paleointensity normalization. *Geochem. Geophys. Geosyst.* 9. https://doi.org/10.1029/2007GC001797

Yamazaki, T., 2009. Environmental magnetism of Pleistocene sediments in the North Pacific and Ontong-Java Plateau: temporal variations of detrital and biogenic components. *Geochem. Geophys. Geosyst.* 10. https://doi.org/10.1029/2009GC002413

Yamazaki, T., Ioka, N., 1997. Environmental rock-magnetism of pelagic clay: implications for Asian eolian input to the North Pacific since the Pliocene. *Paleoceanography* 12, 111–124. https://doi.org/10.1029/96PA02757

Yamazaki, T., Shimono, T., 2013. Abundant bacterial magnetite occurrence in oxic red clay. *Geology* 41, 1191–1194. https://doi.org/10.1130/G34782.1

Yamazaki, T., Yamamoto, Y., 2018. Relative paleointensity and inclination anomaly over the last 8 Myr obtained from the Integrated Ocean Drilling Program Site U1335 sediments in the eastern equatorial Pacific. *J. Geophys. Res. Solid Earth* 123, 7305–7320. https://doi.org/10.1029/2018JB016209

Yamazaki, T., Kanamatsu, T., Mizuno, S., Hokanishi, N., Gaffar, E.Z., 2008. Geomagnetic field variations during the last 400 kyr in the western equatorial Pacific: paleointensity-inclination correlation revisited. *Geophys. Res. Lett.* 35. https://doi.org/10.1029/2008GL035373

Yamazaki, T., Inoue, S., Shimono, T., Sakamoto, T., Sakai, S., 2013a. Sea-ice conditions in the Okhotsk Sea during the last 550 kyr deduced from environmental magnetism. *Geochem. Geophys. Geosyst.* 14, 5026–5040. https://doi.org/10.1002/2013GC004959

Yamazaki, T., Yamamoto, Y., Acton, G., Guidry, E.P., Richter, C., 2013b. Rock-magnetic artifacts on long-term relative paleointensity variations in sediments. *Geochem. Geophys. Geosyst.* 14, 29–43. https://doi.org/10.1002/ggge.20064

Yang, X., Zhu, B., White, P.D., 2007. Provenance of aeolian sediment in the Taklamakan Desert of western China, inferred from REE and major-elemental data. *Quat. Int.* 175, 71–85. https://doi.org/10.1016/j.quaint.2007.03.005

Yang, X., Heller, F., Wu, N., Yang, J., Su, Z., 2009. Geomagnetic paleointensity dating of South China Sea sediments for the last 130 kyr. *Earth Planet. Sci. Lett.* https://doi.org/10.1016/j.epsl.2009.04.035

Yasuda, I., 1997. The origin of the North Pacific Intermediate Water. *J. Geophys. Res.*

Oceans. 102, 893–909. https://doi.org/10.1029/96jc02938

Yoneda, M., Uno, H., Shibata, Y., Suzuki, R., Kumamoto, Y., Yoshida, K., Sasaki, T., Suzuki, A., Kawahata, H., 2007. Radiocarbon marine reservoir ages in the western Pacific estimated by pre-bomb molluscan shells. *Nucl. Instr. Methods Phys. Res. B* 259, 432–437. https://doi.org/10.1016/j.nimb.2007.01.184

You, Y., 2003. The pathway and circulation of North Pacific Intermediate Water. *Geophys. Res. Lett.* 30. https://doi.org/10.1029/2003GL018561

Yu, E.F., Francois, R., Bacon, M.P., 1996. Similar rates of modern and last-glacial ocean thermohaline circulation inferred from radiochemical data. *Nature* 379, 689–694. https://doi.org/10.1038/379689a0

Zhang, Q., Liu, Q., Li, J., Sun, Y., 2018. An integrated study of the eolian dust in pelagic sediments from the North Pacific Ocean based on environmental magnetism, transmission electron microscopy, and diffuse reflectance spectroscopy. *J. Geophys. Res. Solid Earth* 123, 3358–3376. https://doi.org/10.1002/2017JB014951

Zhang, Q., Liu, Q., Roberts, A.P., Larrasoaña, J.C., Shi, X., Jin, C., 2020. Mechanism for enhanced eolian dust flux recorded in North Pacific Ocean sediments since 4.0 Ma: aridity or humidity at dust source areas in the Asian interior? *Geology* 48, 77–81. https://doi.org/10.1130/G46862.1

Zhang, R.-C., Hanawa, K., 1993. Features of the water-mass front in the northwestern North Pacific. *J. Geophys. Res.* 98, 967–975. https://doi.org/10.1029/92jc01854

Zhang, R., Necula, C., Heslop, D., Nie, J., 2016. Unmixing hysteresis loops of the late Miocene-early Pleistocene loess-red clay sequence. *Sci. Rep.* 6, 1–8. https://doi.org/10.1038/srep29515

Zhang, W., Yu, L., Lu, M., Hutchinson, S.M., Feng, H., 2007. Magnetic approach to normalizing heavy metal concentrations for particle size effects in intertidal sediments in the Yangtze Estuary, China. *Environ. Pollut.* 147, 238–244. https://doi.org/10.1016/j.envpol.2006.08.003

Zhang, W., Chen, J., Ji, J., Li, G., 2016. Evolving flux of Asian dust in the North Pacific Ocean since the late Oligocene. *Aeolian Res.* 23, 11–20. https://doi.org/10.1016/j.aeolia.2016.09.004

Zhang, Y.G., Ji, J., Balsam, W.L., Liu, L., Chen, J., 2007. High resolution hematite and goethite records from ODP 1143, South China Sea: co-evolution of monsoonal precipitation and El Niño over the past 600,000 years. *Earth Planet. Sci. Lett.* 264, 136–150. https://doi.org/10.1016/j.epsl.2007.09.022

Zhang, Y., Yi, L., Ogg, J.G., 2019. Pliocene-Pleistocene magneto-cyclostratigraphy of IODP Site U1499 and implications for climate-driven sedimentation in the northern South China Sea. *Palaeogeogr. Palaeoclimatol. Palaeoecol.* 527, 118–132. https://doi.org/10.1016/j.palaeo.2019.04.029

Zhao, T.L., Gong, S.L., Zhang, X.Y., Blanchet, J.P., McKendry, I.G., Zhou, Z.J., 2006. A simulated climatology of Asian dust aerosol and its trans-Pacific transport. Part I: mean climate and validation. *J. Clim.* 19, 104–122. https://doi.org/10.1175/JCLI3605.1

Zhao, W., Zhou, C., Tian, J., Yang, Q., Wang, B., Xie, L., Qu, T., 2014. Deep water circulation in the Luzon Strait. *J. Geophys. Res. Oceans.* 119, 790–804. https://doi.org/10.1002/2013JC009587

Zhao, X., Roberts, A.P., Heslop, D., Paterson, G.A., Li, Y., Li, J., 2017. Magnetic domain state diagnosis using hysteresis reversal curves. *J. Geophys. Res. Solid Earth* 122, 4767–4789. https://doi.org/10.1002/2016JB013683

Zhong, Y., Liu, Y., Yang, X., Zhang, J., Liu, J., Bosin, A., Gorbarenko, S.A., Shi, X., Chen, T., Chou, Y.M., Liu, W., Wang, H., Gai, C., Liu, J., Derkachev, A.N., Qiang, X., Liu, Q., 2020. Do non-dipole geomagnetic field behaviors persistently exist in the subarctic Pacific Ocean over the past 140 ka? *Sci. Bull.* 65, 1505–1507. https://doi.org/10.1016/j.scib.2020.05.016

Ziegler, L.B., Constable, C.G., 2015. Testing the geocentric axial dipole hypothesis using regional paleomagnetic intensity records from 0 to 300 ka. *Earth Planet. Sci. Lett.* 423, 48–56. https://doi.org/10.1016/j.epsl.2015.04.022

Zijderveld, J.D.A., 1967. AC demagnetization of rocks: analysis of results, in: Collinson, D.W., Creer, K.M., Runcorn, S.K. (Eds.), *Methods in Paleomagnetism*. pp. 254–286.